



# IASI ammonia observations to study land-use change, soil-atmosphere exchange and the effect of meteorology

Rimal Abeed

## ► To cite this version:

Rimal Abeed. IASI ammonia observations to study land-use change, soil-atmosphere exchange and the effect of meteorology. Meteorology. Sorbonne Université, 2023. English. NNT : 2023SORUS274 . tel-04264523

**HAL Id: tel-04264523**

**<https://theses.hal.science/tel-04264523>**

Submitted on 30 Oct 2023

**HAL** is a multi-disciplinary open access archive for the deposit and dissemination of scientific research documents, whether they are published or not. The documents may come from teaching and research institutions in France or abroad, or from public or private research centers.

L'archive ouverte pluridisciplinaire **HAL**, est destinée au dépôt et à la diffusion de documents scientifiques de niveau recherche, publiés ou non, émanant des établissements d'enseignement et de recherche français ou étrangers, des laboratoires publics ou privés.



Sorbonne Université

École Doctorale des Sciences de l'Environnement d'Île-de-France (ED129)

*Laboratoire Atmosphères, Observations Spatiales (LATMOS)*

**IASI ammonia observations to study land–use change, soil –  
atmosphere exchange and the effect of meteorology**

Rimal Abeed

Thèse de doctorat d'observation et techniques spatiales pour l'océan, l'atmosphère  
et le climat

Dirigée par Sarah Safieddine et Cathy Clerbaux

Présentée et soutenue publiquement le 20 avril 2023

**Devant un jury composé de :**

Sébastien Payan	Président du jury
Jean-François Muller	Rapporteur
Eloise Marais	Rapporteuse
Didier Hauglustaine	Examineur
Gaëlle Dufour	Examinatrice
Martin Van Damme	Examineur
Jeffrey Geddes	Examineur
Sarah Safieddine	Co-encadrante de thèse (invitée)
Cathy Clerbaux	Directrice de thèse

*To Amer*





## Acknowledgement

Almost four years since I joined LATMOS, as an intern and later a PhD student. Those years were not easy, especially with the pandemic and a few turning points in my life. I was, however, lucky enough to be surrounded by individuals who made the heaviness lighter on my being. I would like to start by thanking my supervisor, Sarah Safieddine, for her constant involvement and devotion to supporting me on both the personal and professional levels. I thank her for her guidance, and for helping me realign with the thesis goals, through the roller coaster of life. Of course, Cathy Clerbaux, for her advices along the years and her unshakable positive attitude that made the hard seem easy. Camille Viatte, for our discussions about ammonia, and her availability whenever I needed help or an opinion regarding my work. And of course, Maya George, for her light company in the office, the chit-chats, technical and administrative support, and the laughs. Every and each person in the IASI team, for making me feel a part of a group, and not left alone. The fellow PhD students whom with I shared lunch during gloomy Parisian days in the kitchen, and in the *Les Arènes de Lutèce* park on sunny days. Thankful for the friendship of Natalie Brett, the spontaneous meet-ups for a chat. Ana Parracho, for her company, art and great sense of humor. I am grateful for the presence of my dear friend, Souhaib Ayoub, their support and love to get me through tough times. I thank Nayla Karamé Majdalani, for helping me transform into the strongest version of myself, thus far. My parents and siblings, for their love and support. I am grateful for my dear friends, the two women warriors, Tara Kenkhuis and Christine Lahens, I wouldn't have been here if it wasn't for them. Finally, I am also thankful for Wael Aboudahr, for his presence, and support.



## Résumé

L'ammoniac ( $\text{NH}_3$ ) est la forme d'azote utilisable la plus abondante dans l'environnement et l'un des gaz principaux émis par l'agriculture. Le  $\text{NH}_3$  contribue à la perte de biodiversité, aux épisodes de pollution par les particules fines ( $\text{PM}_{2.5}$ ) et à l'acidification des surfaces d'eau et des sols. Depuis la révolution industrielle, les émissions d'ammoniac ont augmenté en continu, accompagnées de l'intensification de l'agriculture et de l'augmentation de la demande alimentaire. Les concentrations atmosphériques devraient continuer à augmenter dans le futur, notamment à cause du réchauffement climatique. Dans les travaux de ma thèse, j'ai utilisé les mesures de la mission satellite IASI pour étudier l'évolution temporelle et spatiale de l'ammoniac dans des différentes régions agricoles. J'ai d'abord étudié l'effet des fluctuations météorologiques sur les concentrations atmosphériques associées à différentes pratiques agricoles. Je me suis ensuite concentrée sur les échanges sol – atmosphère, pour dériver un facteur d'émission de  $\text{NH}_3$ , pendant la saison de croissance agricole en Europe. Pour réaliser ces études, j'ai utilisé différents jeux de données : les données météorologiques provenant de la réanalyse (ERA5) de l'European Centre for Medium-Range Weather Forecasts (ECMWF), la couverture terrestre et la surface brûlée provenant du sondeur MODIS embarqué à bord des satellites Aqua et Terra, et des données de simulation de modèle provenant du modèle de chimie-transport GEOS-Chem. Enfin, j'ai étudié les fluctuations de l'ammoniac atmosphérique en Syrie, pour analyser l'impact du conflit sur les terres cultivées.



## Abstract

Ammonia ( $\text{NH}_3$ ) is the most abundant usable form of nitrogen in the environment, and one of the main gases emitted from agriculture.  $\text{NH}_3$  contributes to the loss in biodiversity, fine particulate matter ( $\text{PM}_{2.5}$ ) pollution episodes, and acidification of the water and soil bodies. Since the industrial revolution, ammonia emissions are constantly increasing, along with the increase in agricultural intensification and food demand. In my thesis I used measurements from the IASI mission to study the temporal and spatial evolution of ammonia in different agricultural regions. I first studied the effect of meteorological fluctuations on atmospheric concentrations linked to agricultural practices. I then focused on the soil – atmosphere exchange to derive a soil emission factor of  $\text{NH}_3$  during the growing season in Europe. To perform these studies, I used a variety of datasets: meteorological data from the European Centre for Medium-Range Weather Forecasts (ECMWF) reanalysis (ERA5), land cover type and burned area from the sounder MODIS onboard the Aqua and Terra satellites, and model simulation data from the chemical-transport model GEOS-Chem. Finally, I studied the fluctuations of atmospheric ammonia in Syria, to analyze the effect of conflict on agricultural activities.



# Table of contents

---

<b>1</b>	<b>Introduction and research questions.....</b>	<b>5</b>
1.1	The nitrogen cycle.....	7
1.2	N <sub>r</sub> in the environment.....	9
1.2.1	Reactive N: sources, sinks, and impacts.....	10
1.2.2	Human fixation of N .....	11
1.3	NH <sub>3</sub> in the atmosphere .....	14
1.3.1	Historical evolution.....	14
1.3.2	Measuring NH <sub>3</sub> .....	15
1.3.3	NH <sub>3</sub> trends and mitigation measures .....	17
1.3.4	Future projections.....	19
1.4	Thesis objectives .....	20
<b>2</b>	<b>Data and methods .....</b>	<b>23</b>
2.1	IASI on Metop.....	23
2.1.1	The Metop satellite.....	24
2.1.2	Metop Orbit Characteristics .....	26
2.1.3	The IASI instrument.....	27
2.2	Remote sensing of ammonia from space.....	31
2.3	Ammonia from IASI .....	32
2.3.1	NH <sub>3</sub> retrieval methods .....	32
2.3.2	The Hyperspectral Index (HRI).....	33
2.3.3	Artificial neural networks for NH <sub>3</sub> retrieval.....	35
2.3.4	IASI NH <sub>3</sub> products used in this thesis .....	38
2.4	Meteorological data.....	38
2.4.1	Skin temperature .....	38
2.4.2	Air surface temperature .....	39
2.4.3	Total precipitation .....	39
2.4.4	Wind speed.....	39

2.4.5	Relative humidity .....	40
2.5	Land data .....	40
2.5.1	MODIS Land Cover type .....	40
2.5.2	MODIS burned area .....	41
<b>3</b>	<b>Ammonia – biosphere interactions .....</b>	<b>43</b>
3.1	NH <sub>3</sub> chemistry and transport .....	45
3.1.1	Fertilizer types and use .....	46
3.1.2	Urea hydrolysis in the soil .....	48
3.1.3	NH <sub>3</sub> volatilization to the near surface air .....	49
3.1.4	Transport and deposition .....	50
3.1.5	Formation of fine PM .....	51
3.2	Ammonia concentrations in Europe, Canada, and Mexico .....	53
3.2.1	The effect of skin temperature on NH <sub>3</sub> columns .....	54
3.2.2	The effect of air temperature on NH <sub>3</sub> total columns .....	60
3.2.3	The effect of relative humidity on NH <sub>3</sub> total columns .....	61
3.3	Other regions and climate zones around the world .....	63
3.3.1	Precipitation and climate zones .....	65
3.3.2	T skin and climate zones .....	68
3.3.3	Wind speed .....	70
3.4	Conclusion .....	71
<b>4</b>	<b>Ammonia volatilization from agricultural soils in Europe .....</b>	<b>73</b>
4.1	Introduction .....	74
4.2	Methods and datasets .....	76
4.2.1	Ammonia emission potential .....	76
4.2.2	Calculation of emission potential <i><b>f<sub>soil</sub></b></i> .....	77
4.2.3	MODIS Land Cover Type .....	81
4.2.4	GEOS-Chem chemistry transport model .....	81
4.2.5	EC-Earth climate model .....	82
4.3	Results .....	83
4.3.1	GEOS-Chem vs. IASI .....	83
4.3.2	Ammonia emissions, losses and lifetime in Europe .....	86
4.3.3	Mass transfer coefficient estimation .....	91



4.3.4	Emission potential in Europe .....	92
4.3.5	Case study: ammonia increase with temperature under future scenarios .....	98
4.4	Discussion and conclusions.....	102
4.5	Published article .....	104
<b>5</b>	<b>Industrial and agricultural changes during the Syrian war .....</b>	<b>132</b>
5.1	Regions of study.....	133
5.2	The war timeline.....	134
5.3	The industrial region .....	135
5.3.1	Ammonia changes due to the war events .....	135
5.3.2	Local air quality in Homs in relation to the industry.....	139
5.4	The agricultural region .....	141
5.5	Can we draw a link between both regions? .....	142
5.6	Conclusion.....	143
5.7	Published article .....	145
<b>6</b>	<b>Conclusions and discussions.....</b>	<b>158</b>
6.1	Thesis conclusions.....	159
6.2	Perspectives and future work .....	161
<b>A.</b>	<b>Regions for Chapter 3.....</b>	<b>165</b>
<b>B.</b>	<b>NH<sub>3</sub> – precipitation .....</b>	<b>167</b>
<b>C.</b>	<b>NH<sub>3</sub> – T skin binning .....</b>	<b>173</b>
<b>D.</b>	<b>NH<sub>3</sub> – T skin anomalies .....</b>	<b>176</b>
	<b>References</b>	<b>198</b>



# Chapter 1

## *1 Introduction and research questions*

The agricultural revolution that occurred ~10,000 years ago shaped today's economy and politics (Galloway et al., 2004). By selectively domesticating plants and animals, it allowed the human population to increase in count and prosper. In today's world and under the current dietary choices, the human race is not able to survive anymore without vast fields of cultivated/fertilized lands, and acres stacked with selected breeds of animals for slaughter and exploitation. Agricultural practices evolved with the passing years, introducing new methods and techniques to increase the yield or minimize the losses in case of natural disasters (e.g. floods, tsunami). For example, farmers used to burn fields prior to sowing after it was discovered that charcoal (carbon) increases the fertility of the soil. It was later explained that charcoal holds nutrients (e.g. ammonium ( $\text{NH}_4^+$ )) in the soil for a longer time than a soil without it. During the same period, a scientist discovered that ammonia ( $\text{NH}_3$ ) is a nutrient for plants and if manufactured synthetically, it can be applied as fertilizers to increase the yield. Several scientists tried to manufacture ammonia to no avail. Until the 20<sup>th</sup> century, Fritz Haber figured a way to produce ammonia by putting the non-reactive nitrogen ( $\text{N}_2$ ) and hydrogen ( $\text{H}_2$ ) gas under high pressure and temperature. Eventually, the chemical bonds linking the nitrogen (N) and hydrogen (H) atoms in  $\text{N}_2$  and  $\text{H}_2$  respectively will break, to form loose H and N that will later merge into ammonia. It was such a breakthrough in the world of agriculture, and it needed to be applied at an industrial scale. Later, Carl Bosch designed an industrial procedure that succeeded in producing huge amounts of ammonia. Together, they won a patent for the Haber – Bosch process, and changed the course of the world.

Synthetic fertilizers were the driver of the huge rise in population count by almost 2 folds from 1910 up until year 2000 (Erisman et al., 2008). The world consumption of synthetic fertilizers was found to increase by +300 %, mainly driven by Asia, Brazil and the United States (USDA, 2022a). One can argue that this is the result of agricultural intensification, while this is true to a certain extent, a part of the increase in fertilizers use is due to cropland expansion. For

example, in 2019 the global cropland area was estimated to be  $1,244.2 \pm 62.7$  million hectares (Mha) (compared to  $\sim 1090.3$  Mha average during [2000 – 2003]) (Potapov et al., 2022), this is roughly the size of both the united states (983.4 Mha) and Argentina (278 Mha) combined. The excess of N threw off the balance of the nitrogen cycle, one of the vital geochemical cycles on Earth, putting our survival on the stake (Rockström et al., 2009). Agriculture-emitted ammonia eventually get deposited in terrestrial ecosystems, leading to unintended fertilization of the natural habitats, and as a result, a loss in biodiversity (Erisman et al., 2008). In addition to that, ammonia is also one of the ignored contributors to air quality deterioration, its chemical reactivity with acidic species in the atmosphere leads to the formation of harmful particulate matter (PM). In intensive agricultural areas the inorganic  $\text{PM}_{2.5}$ <sup>1</sup> can be attributed to ammonia emissions (e.g. at least 50 % of the  $\text{PM}_{2.5}$  in California (Schiferl et al., 2014)). Its reduction, therefore is crucial to improve air quality. For instance, a decrease of ammonia emission in China by – 50 % can lead to a reduction of – 11 to – 17 % in  $\text{PM}_{2.5}$ , which will reduce haze pollution episodes (Liu et al., 2019).

Nitrogen related pollution episodes are a growing threat (Fields, 2004). At least since 2008, ammonia trends were seen to increase over a ten year period (Van Damme et al., 2021). The global population has been growing ever since the apparition of the Haber-Bosch process, and it will continue to do so. The United Nations (UN) expect a count of 9.7 billion in 2050 and 10.4 billion in 2100 (UN, 2022). With it, the food demand will rise by +35 % to +56 % in 2050, and if climate change is considered in the analysis, the numbers will change to +30 % to +62 % (van Dijk et al., 2021), due to the increase in ammonia emissions with temperature. The global respond to this growing demand is by intensifying agricultural practices and expanding the croplands surface area. Both of these strategies will eventually increase the nitrogen input in the environment. Thus, further increasing the loss in biodiversity, and leading to air quality degradation. It is therefore crucial to understand the factors that affect the loss of ammonia from agricultural soils, in order to be able to set a limit for the N applied especially under future climate scenarios. Reducing N

---

<sup>1</sup> Particulate matter with a diameter less than or equal to 2.5 microns.

input to soils will benefit both the environment and the economy; it is also proved to be beneficial on the longer run for a better yield (Chen et al., 2017).

In this chapter, I walk you through the different processes taking place in the nitrogen cycle, and the impacts of the excess N input from human intervention. I, then, discuss the history of atmospheric ammonia, the current trends and future projections. Finally, I list the thesis objectives aiming to understand the effects of multiple factors, such as meteorology and land use change on atmospheric ammonia.

## *1.1 The nitrogen cycle*

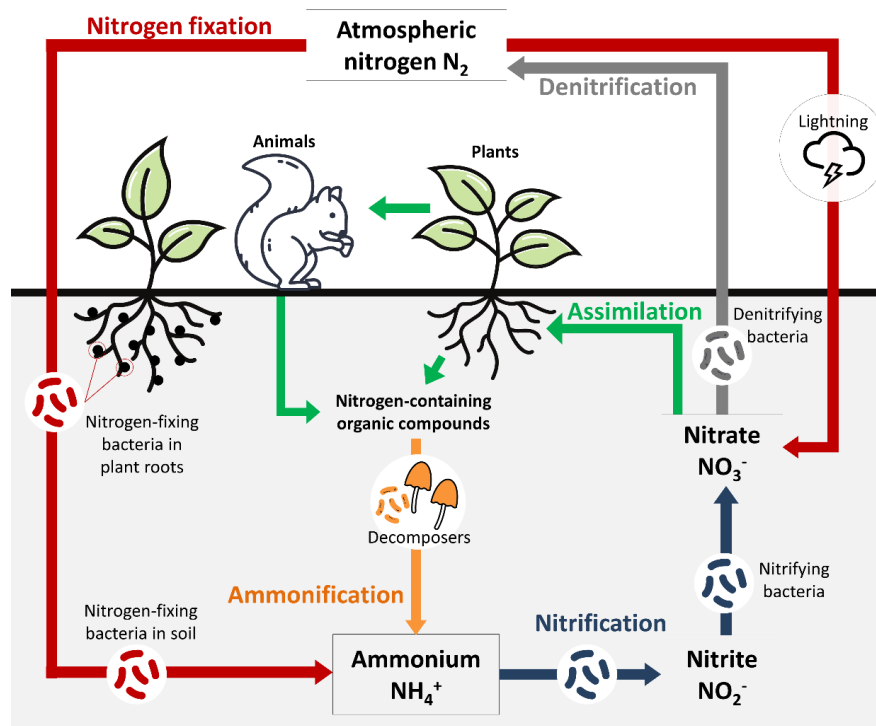
Nitrogen (N) is one of six most abundant elements (C, H, N, O, S, P)<sup>2</sup> that are considered the major building blocks of life on Earth (Chopra and Lineweaver, 2008). N is present in all living organisms as nucleic acids (DNA and RNA), proteins (amino acids), vitamins, and adenosine triphosphate (ATP) that is involved in metabolism (Takai, 2019). Although nitrogen consists of 78% of the terrestrial atmosphere, the vast majority of organisms (~99%) are not able to absorb it in its inert form ( $N_2$ ). This is due to the strong triple bond linking both nitrogen atoms; such a bond is hard to break (naturally) under ambient conditions except by lightning and some bacterial species in the soil and water bodies (Galloway et al., 2004).  $N_2$  is rather known to be the non-reactive form of nitrogen, and it forms the first pool of nitrogen on Earth. The second pool is that of the reactive nitrogen ( $N_r$ ), and it consists of all forms of nitrogen except  $N_2$ , such as: nitrate ( $NO_3^-$ ), ammonium/ammonia ( $NH_4^+/NH_3$ ), and organic nitrogen ( $N_{org}$ ). The latter is defined as nitrogen originating from living organisms. It can be made of animal and plant residues, in addition to manure and urea (Jacob, 1999). Living organisms can only assimilate nitrogen in its reactive form ( $N_r$ ). Atmospheric  $N_2$  is therefore unusable by these organisms unless transformed into  $N_r$ , this process is called “nitrogen fixation”. The interaction between the two large nitrogen pools on Earth is mainly governed by nitrogen fixation ( $N_2$  to  $N_r$ ), and denitrification ( $N_r$  to  $N_2$ ) (Takai, 2019).

Figure 1.1 is adapted from the Environmental Protection Agency (US EPA, 2015), and summarizes the main natural pathways of nitrogen in the environment.  $N_2$  is either fixed by

---

<sup>2</sup> Carbon, hydrogen, nitrogen, oxygen, sulfur, and phosphorous.

bacterial species (in the soil and in plant roots), lightning, or volcanic eruptions. The nitrogen-fixing bacteria turns  $N_2$  into a reduced form of nitrogen (ammonia  $NH_3$  and ammonium  $NH_4^+$ ). This pathway of  $N_2$  can also be referred as the biological nitrogen fixation (BNF). The produced ammonium and ammonia are then nitrified by bacteria to give nitrites  $NO_2^-$  and nitrates  $NO_3^-$ , this process is aerobic<sup>3</sup> and is called nitrification (blue arrows in Figure 1.1). These anions<sup>4</sup> ( $NO_2^-$  and nitrates  $NO_3^-$ ) do not exist alone in nature, rather they attach to positively charged ions (cations), e.g.  $H^+$  to form nitrous  $HNO_2$  and nitric  $HNO_3$  acids.



**Figure 1.1. The nitrogen cycle. The Figure is adapted from the US Environmental Protection Agency (US EPA, 2015).**

Plants can assimilate and absorb nitrogen in the form of ammonia/ammonium and nitrate (Lea, 1985). When lightning occurs, the triple bond of atmospheric  $N_2$  can be broken as well as the double bond of the two oxygen atoms ( $O_2$ ) in the atmosphere, the N and O can then produce nitrogen oxide NO (or nitric oxide). The oxidation of NO, by the hydroperoxyl radical ( $HO_2\cdot$ ) and hydroxyl radical ( $HO\cdot$ ) continues until nitrogen dioxide ( $NO_2$ ) and then nitrate ( $NO_3^-$ ) are formed. The nitrogen fixation pathway is shown in red arrows in Figure 1.1. Another pathway that can

<sup>3</sup> A process that requires the presence of oxygen.

<sup>4</sup> Negatively charged ions.

produce ammonia (and ammonium) is the decomposition of organic nitrogen by a group of bacterial species and fungi, the decomposers, the process is known as ammonification (shown in orange in Figure 1.1). The nitrogen cycle is finally closed by denitrification that turns  $N_r$  back into its non-reactive form ( $N_2$ ), this process is done by the denitrifying bacteria and is anaerobic<sup>5</sup> (grey arrows in Figure 1.1).

The total  $N_r$  fixed naturally is estimated to be at a rate of 65 Tg N yr<sup>-1</sup> (Erismann et al., 2015), and most of it (~90 %) is fixed by BNF (Fowler et al., 2013). Marine microorganisms also contribute to the nitrogen fixation. While most of the  $N_r$  produced in the oceans is stored in sediments (~140 Tg N yr<sup>-1</sup>), the rest of it is denitrified back to atmospheric  $N_2$  or nitrous oxide ( $N_2O$ ), the latter has a lifetime of 114 years and is the third most important greenhouse gas after methane ( $CH_4$ ) and carbon dioxide ( $CO_2$ ) (Erismann et al., 2015).

## 1.2 $N_r$ in the environment

Nitrogen is most abundant in the non-reactive form. However, its reactive form,  $N_r$ , is vital for life on Earth. Too much of it, though, is rather a damage than a benefit (Rockström et al., 2009; Steffen et al., 2015). This section highlights the different forms of  $N_r$  in the environment, the human fixation of N, and the main sources, sinks, and impacts of excess  $N_r$ .

Following  $N_2$  fixation,  $N_r$  can fall into three main categories (Jacob, 1999):

- (1) Reduced (inorganic) nitrogen, e.g. ammonia ( $NH_3$ ), and ammonium ( $NH_4^+$ ),
- (2) Oxidized (inorganic) nitrogen, e.g. nitrite ( $NO_2^-$ ), nitrate ( $NO_3^-$ ), nitrous oxide ( $N_2O$ ), and nitrogen oxides ( $NO_x = NO + NO_2$ ), and
- (3) Organic nitrogen, e.g. residues of animal and plant tissue, urea, and organo-nitrates (e.g.  $RONO_2$ , where R is an organyl<sup>6</sup> group).

Among all the forms of reactive N in the atmosphere, ammonia is known to be the most abundant form of  $N_r$  (Behera et al., 2013). Some other examples of atmospheric N-containing gases are:  $NO_x$ ,  $HNO_3$ , and  $N_2O$  (much less reactive than the other two). Naturally produced  $NO_x$  gases

<sup>5</sup> A process that takes place in the absence of oxygen.

<sup>6</sup> In organic chemistry, an organyl group is an organic substituent with one free valence at a carbon atom (e.g. an alkyl group –  $CH_3$ ).

(dominantly by lightning) also play a role in air quality, and in the formation of ozone in the upper troposphere (Bray et al., 2021; Murray, 2016; Myhre et al., 2013), however, these represent only 10 % to 15 % of the total  $\text{NO}_x$  emitted globally (Schumann and Huntrieser, 2007). Organo-nitrates are formed in the atmosphere via oxidation (photochemical and nocturnal) of volatile organic compounds (VOCs). The oxidation process is initiated by the two radicals OH and  $\text{NO}_3$  (Farmer et al., 2010). Organo-nitrates are known to be important for surface ozone formation in the stratosphere (Fiore et al., 2005), but also in the budget calculation of reactive nitrogen and aerosol formation in the lower troposphere (Foulds et al., 2021).

### 1.2.1 Reactive $N$ : sources, sinks, and impacts

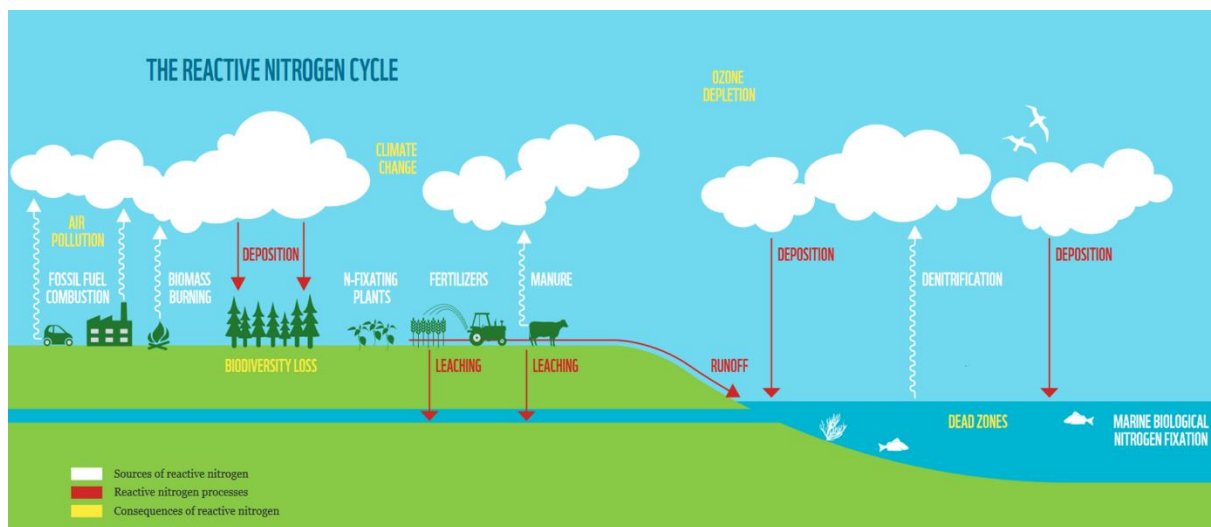


**Figure 1.2. The reactive nitrogen cycle. It summarizes the sources of N (white arrows), the processes taking place following  $N_r$  release to the environment (red), and the consequences that follow (yellow). Figure from Erisman et al. (2015).**

Excess  $N_r$  pollutes both marine and terrestrial ecosystems, deteriorates tropospheric air quality and contributes to ozone depletion in the stratosphere (Erisman et al., 2015). Figure 1.2 summarizes the sources of nitrogen (white arrows), the processes (sinks) that follow the  $N_r$  release (red arrows), and the damages (yellow) excess  $N_r$  causes to the environment. The industrial production of fertilizers (and other goods), along with traffic are major sources of  $NO_x$  gases (through fossil fuel combustion). Biomass burning and agricultural fires release  $N_r$  in the form of  $NO_x$  and  $NH_3$ , through the combustion of organic N (Bray et al., 2021; Whitburn et al., 2015). In



agricultural lands and livestock management facilities, ammonia is released following the application of fertilizers, throughout the management process and spreading of animal manure, and through the N-fixating plants that are cultivated in croplands (Chakraborty and Sen Gupta, 1959; Erisman et al., 2015; Sommer and Hutchings, 2001). In marine ecosystems N is fixed and stored in sediments, and the rest of it is denitrified and released back to the atmosphere as  $N_2$ . The emitted  $NO_x$  and  $NH_3$  end up: (1) on lands/plants through direct wet and/or dry deposition, and leaching in agricultural soil water, and (2) in oceans through groundwater, surface runoff and deposition (wet and dry, Figure 1.2).

Atmospheric  $N_r$  degrades air quality directly due to  $NO_x$  emissions (Jung et al., 2022), and indirectly through the cascade of reactions caused by  $NH_3$  molecules (Galloway et al., 2003), since the latter is a precursor for particulate matter formation  $PM_{2.5}$  (Fortems-Cheiney et al., 2016; Viatte et al., 2022, 2020). In addition to that, the excess in nutrients ( $NH_4^+$  and  $HNO_3$ ) in water bodies causes eutrophication<sup>7</sup>, resulting in loss in marine habitat and biodiversity, and the creation of dead zones (Selman et al., 2008). Excess  $N_r$  also results in acidic and nutrient-rich soils, such environments favor species that can survive acidic and highly nutritious media, and lead to the death of more fragile species, therefore reducing the overall resilience of ecosystems (Erisman et al., 2015). Globally, not all regions are affected to the same extent by excess  $N_r$ , for instance, the biodiversity loss is more apparent in parts of Africa and Southern America, Eastern U.S., South Asia and Central and Western Europe, than in the rest of the world (Erisman et al., 2015).

### *1.2.2 Human fixation of N*

During the 19<sup>th</sup> century, and following discovery of the Haber-Bosch process (the industrial conversion of  $N_2$  to  $NH_3$ ), the production of synthetic fertilizers played a major role in the perturbation of the N cycle (Fowler et al., 2013; Rockström et al., 2009). Since then, human activities started to play a role in  $N_2$  fixation, and eventually became the first driver of global environmental changes (Crutzen, 2002; IPCC, 2013). Rockström and colleagues (Rockström et

---

<sup>7</sup> Eutrophication is the excessive richness of nutrients in water bodies, due to excess (anthropogenic)  $N_r$  which causes a dense growth of cyanobacteria. This results in algal blooms (e.g. in lakes), which blocks sunlight in the water body and consumes the existing oxygen resulting in the creation of “dead zones”. The water body becomes inhabitable by fish, therefore causing loss in marine biodiversity.

al., 2009) introduced the concept of “planetary boundaries” for a safe operating space<sup>8</sup> for humanity. These boundaries are thresholds that should not be exceeded, and are often associated with biophysical processes on Earth (e.g. the boundary of the nitrogen cycle is the amount of  $N_r$  in the environment). In today’s world, the amount of fixed nitrogen by humans already exceeded the limit for a safe operating space. Anthropogenic activities produce  $N_r$  through several processes (Galloway et al., 2003):

- (1) Combustion of fossil fuel that produces  $NO_x$ ,
- (2) agricultural activities such as fertilizers production and application, and manure management, and,
- (3) N-fixating plants cultivated for food production purposes (soy, rice, beans, and other leguminous plants).

The use of fertilizers allowed the global population to increase in count, 50 % of the total population were estimated to be fed by the Haber-Bosch process in 2010 (Erisman et al., 2008). However, the excessive use of fertilizers caused a reduction in the resilience of agro-ecosystems (Erisman et al., 2015). Fertilizers production, and application, in general is the dominant source of the reactive nitrogen on Earth with an estimate of 70 % of the total terrestrial  $N_r$  (Battye et al., 2017), and most of it is in the form of ammonia  $NH_3$  (Galloway et al., 2004). Although, fossil fuel combustion is a source of  $N_r$ , the amount of agriculture-emitted  $N_r$  exceeds that from fossil fuels (mainly in the form of  $NO_x$  gases), and this is to the largest extent caused by the inefficient use of ammoniacal fertilizers, and the huge numbers of domesticated animals for food production purposes (Behera et al., 2013). Other anthropogenic and biogenic sources emit ammonia, however, agricultural activities are the main contributors in the  $NH_3$  global budget (Bouwman et al., 1997; Galloway et al., 2008; Sutton et al., 2013), and this includes a variety of agricultural activities (cultivation, fertilization, and manure management). While it is hard to quantify the exact amount of  $N_r$  fixed naturally, it is estimated that the total  $N_r$  input from fertilizers is double (or triple) the amount fixed by BNF (Fowler et al., 2013; Galloway et al., 2013). The meat and poultry industries alone account to one-third of the total anthropogenic nitrogen loss to the terrestrial ecosystem, which is roughly  $65 \text{ Tg N yr}^{-1}$  (Uwizeye et al., 2020). Regions that are

---

<sup>8</sup> The “safe operating space” is the state of environmental wellbeing that allows for sustainable development with respect to the earth system (e.g. substantial loss in biodiversity).

dominated by manure management and cropping are the ones that show the highest annual emissions of ammonia, sometimes exceeding  $25 \text{ kg N ha}^{-1}$ , such as in Northern Europe (Sutton et al., 2013) (Figure 1.3).

As stated earlier, other sources of ammonia contribute to the total  $\text{NH}_3$  budget. For instance, the least addressed sources emit 15 % of the total ammonia emissions, and these include: sewage management, traffic (catalytic converters), pets, fish ponds, wild animals, and combustion (Gross et al., 1999; Sutton et al., 2000).

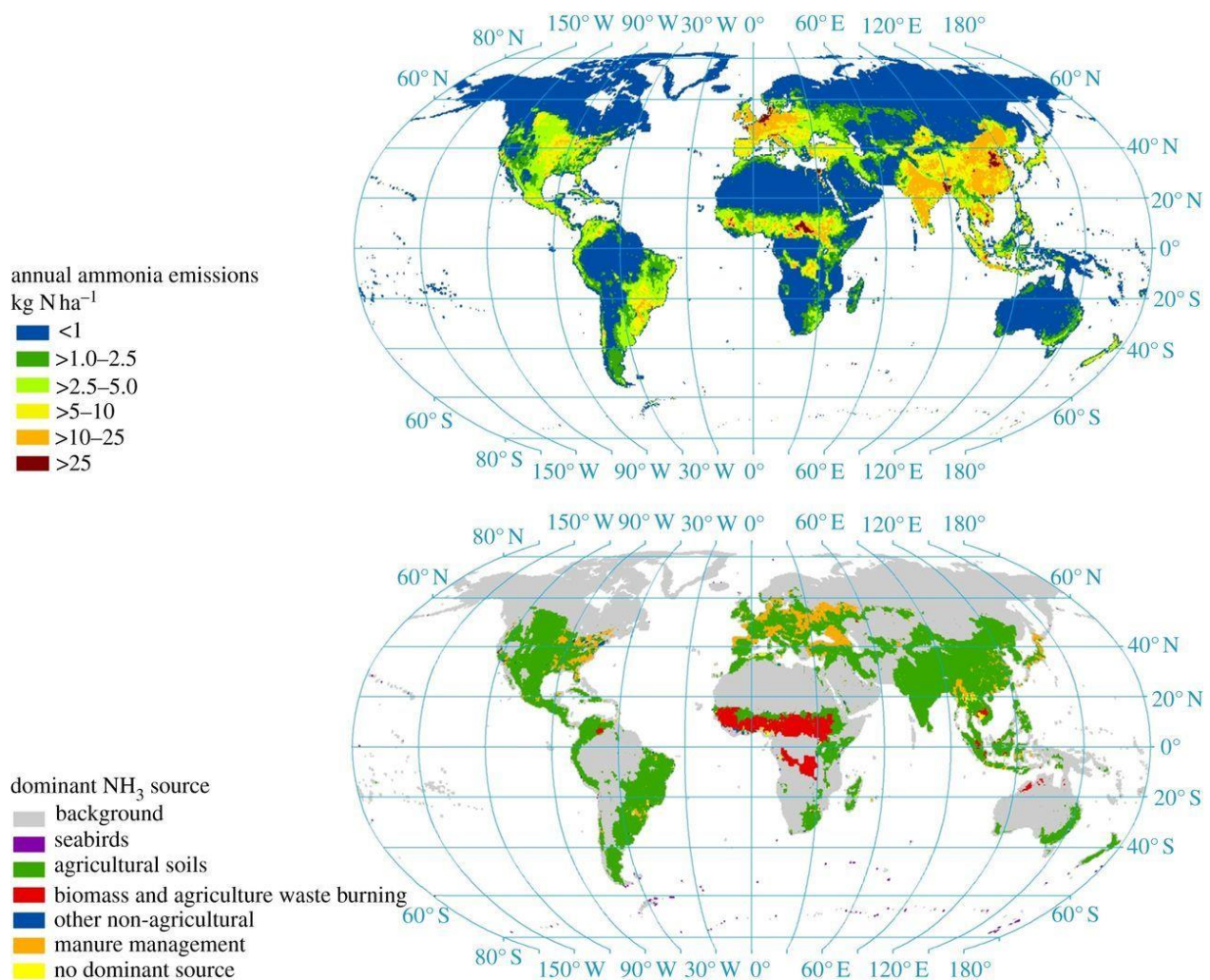


**Figure 1.3. Global ammonia emissions showing the contribution of natural and anthropogenic sources. The Figure is from Sutton et al. (2013).**

## 1.3 $\text{NH}_3$ in the atmosphere

### 1.3.1 Historical evolution

The first ever recorded atmospheric ammonia pollution dates back to year 1800, specifically in spontaneous combustion caves of deposited coal in central Asia (Sutton et al., 2008; Sutton and Howard, 2018). These naturally occurring fire caves can burn for centuries, and will eventually emit, in addition to ammonia, acidic molecules such as hydrochloric acid (HCl), sulfuric acid ( $\text{H}_2\text{SO}_4$ ), and  $\text{HNO}_3$ . Ammonia reacts with these acids to form ammonium salts (Belakovski, 1990), these will later be collected by locals and traded as luxury products (Sutton et al., 2020). Such salts are: ammonium chloride ( $\text{NH}_4\text{Cl}$ ), sulfate ( $\text{NH}_4\text{SO}_4$ ), and nitrate ( $\text{NH}_4\text{NO}_3$ ). The most important and abundant salt of these is sal ammoniac ( $\text{NH}_4\text{Cl}$ ), and can be found in several regions today such as in Tajikistan, and ancient Egypt (now Libya) (Belakovski, 2003).

Ammonium salts were used in medicine, metallurgy, and food (Sutton et al., 2008). The most traded salt among the mentioned beforehand, is sal ammoniac, due to its abundance and stability as compared to ammonium nitrate and sulfate (Sutton et al., 2020). As documented by Ibn-Hauqal in his book *The Oriental Geography*, locals used to collect sal ammoniac from around the cooled edges of the burning caves, trying to protect themselves from the flames by applying clay to their bodies (Ouseley, 1800). The price of nitrogen (sal ammoniac) was equivalent (slightly higher) than spice in 640 AD in places as Egypt and Sicily, it eventually evolved and increased with time up until 1140 AD (Sutton et al., 2020).

In agricultural chemistry, the first scientist to suggest the use of mineral (synthetic) fertilizers is Baron Justus von Liebig (1803 – 1873), he argued that ammonia and nitrates are direct nutrients to plants and their presence in soils is vital to a better yield (Jacobson, 2002). At that time, humans did not know how to fix large amounts of nitrogen yet. However, an earlier attempt took place in 1787 by William Austin and later in 1823 by Johan Wolfgang (Galloway et al., 2013). In 1910, the Haber-Bosch process allowed mass production of ammonia (N-fertilizers production), by adapting the  $\text{NH}_3$  process created by Fritz Haber to an industrial scale production by Carl Bosch (Smil, 2000). As a result, the value of 20<sup>th</sup> century nitrogen is three orders of magnitude lower than that of the tenth century (Erisman et al., 2008).

### 1.3.2 Measuring $\text{NH}_3$

The Nitrogen cycle is one of the most complex and studied cycles among scientific peers (Gruber and Galloway, 2008). Not only is it by itself complex, but the reactivity of nitrogen with the carbon cycle makes it even harder to predict and understand the mechanisms in the N cycle (Takai, 2019). During the 19<sup>th</sup> century, scientists started to recognize atmospheric ammonia, but only to study its function as a fertilizer ingredient (Lawes, 1847). Figure 1.4 shows the mechanisms involved in the nitrogen and carbon cycles, the interactions between both cycles, in three large arenas: the human drivers, the atmospheric drivers, and the biogeochemical cycles (Gruber and Galloway, 2008). The question marks on the figure denote unknown areas, or poorly understood processes. We can see how the interaction between atmospheric nitrogen (e.g. ammonia) and climate warming is not well understood in Figure 1.4.

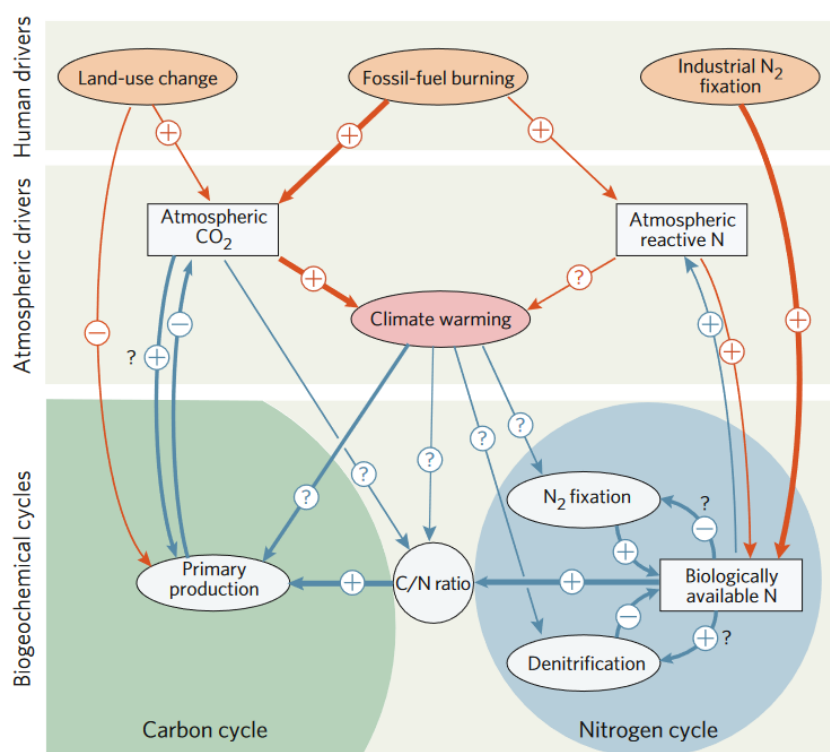


**Figure 1.4.** The main drivers of the interactions between the nitrogen and the carbon cycles during the twenty-first century. The plus signs (+) indicate that the interaction increases the amount of the factor shown (e.g. land-use change increases  $\text{CO}_2$  emissions); the minus (−) signs indicate a decrease; question marks (?) indicate an unknown impact (or, when next to a plus or minus sign, they indicate a high degree of uncertainty). Orange arrows denote the direct anthropogenic impacts, and blue arrows denote natural interactions, many of which could also be anthropogenically modified. Arrow thickness denotes strength of interaction. Figure from Gruber and Galloway (2008).

The understanding of the N cycle only started to increase recently, namely not before the 20<sup>th</sup> century. For instance, during the 1980's period, some measurement techniques allowed the discovery that ammonia can be both emitted and absorbed by plants (Farquhar et al., 1983). However, measuring ammonia was and is still difficult due to its high reactivity with the materials used in the manufacturing of the instruments, as well as its sticky nature and fast conversion to  $\text{NH}_4^+$  (Harper, 2015). It was therefore challenging to obtain accurate measurements. As a result, its role in spring pollution and other contributions to air quality deterioration was far from being understood. By the late 20<sup>th</sup> century, the impacts of nitrogen pollution from agricultural practices started to be well recognized (Novotny, 1999). One of the methods used to measure ammonia was open-path Fourier transform infrared spectrometers (OP-FTIR), where the study focused on measuring ammonia emissions from lagoon during summer (Todd et al., 2001). By that time, FTIR instruments were loaded onto satellites for the sake of studying the meteorology and improving weather forecast. Unintentionally, opening the gate to a new way of probing ammonia from space. The first detection of ammonia from a satellite instrument was around 2008 – 2009 (Beer et al., 2008; Clarisse et al., 2009; Coheur et al., 2009). This discovery allowed us to understand the temporal and spatial variability of atmospheric ammonia. In Chapter 2, I discuss the different satellite instruments that can detect ammonia from space, with an emphasis on the instrument I used in this thesis work.

### 1.3.3 $\text{NH}_3$ trends and mitigation measures

The mass production of nitrogen-based fertilizers did not come without a cost. Several studies showed that the overall trend in ammonia budget is positive globally, Liu (2022) and McDuffie et al. (2020) found an increase of 81 % (between 1970 and 2017), and 78 % (from 1980 to 2018) of ammonia emissions respectively. The global trend in satellite derived ammonia total columns is seen to be mostly driven by the increases observed in East Asia, Western and Central Africa, North America, and Western and Southern Europe (Van Damme et al., 2021). The largest increase on a regional scale is seen in East Asia with an increase of  $75.7 \pm 6.3$  % on a decadal range [2008 – 2018] (Figure 1.5), mostly driven by a rise in emissions in the North China Plain and Chengdu regions (Van Damme et al., 2021). In addition to that, the number of reported coastal dead zones increased dramatically from 9 during the 1960's, to 540 in 2011 (Selman et al., 2008).

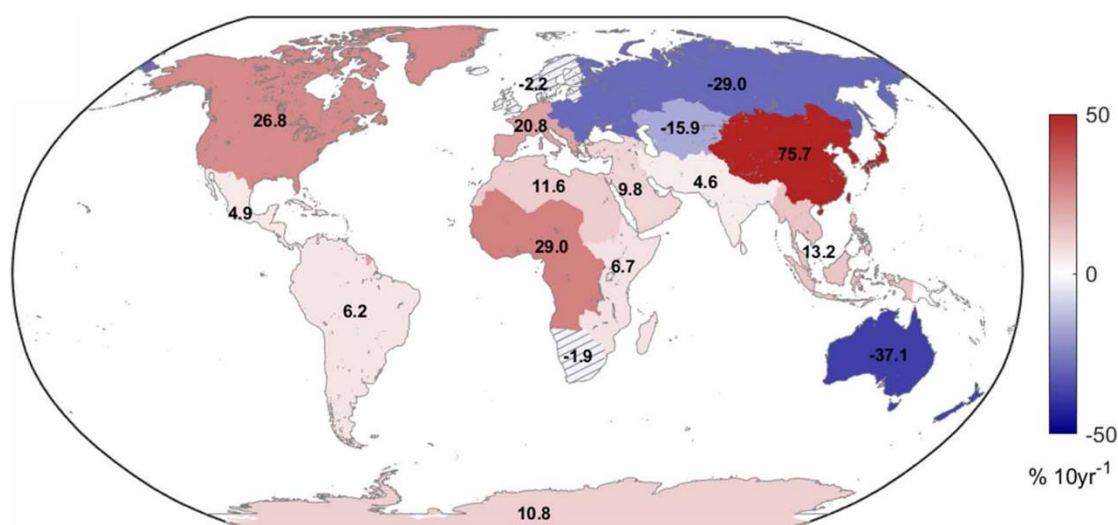


**Figure 1.5.** Regional trends of ammonia total columns [% 10yr<sup>-1</sup>] using satellite data for the period [2008 – 2018]. The Figure is from Van Damme et al. (2021).



In Europe, adopting the Gothenburg Protocol<sup>9</sup> resulted in major reductions of four air pollutants emissions: non-methane volatile organic compounds (NMVOCs), fine particulate matter (PM<sub>2.5</sub>), nitrogen oxides (NO<sub>x</sub>), and sulphur oxides (SO<sub>x</sub>) (Figure 1.6), but not in NH<sub>3</sub> where we see rather a positive trend in Europe overall accounting to +20.8 % 10yr<sup>-1</sup> (Van Damme et al., 2021), Figure 1.5). NO<sub>x</sub> and SO<sub>x</sub> emissions, for instance, decreased by 42 % and 76 % respectively (EEA, 2021) as Figure 1.6 shows. While NH<sub>3</sub>, equally addressed in the Gothenburg Protocol, reduced by only 8 % overall (in all EU-27 member states) from 2005 to 2019 (EEA, 2021). The low reduction in ammonia emissions, reported by EEA (2021), did not guarantee negative trends of ammonia total columns (Van Damme et al., 2021), this means that the meteorological fluctuations play equally a crucial role in NH<sub>3</sub> atmospheric budget and should be tackled to improve the estimation and modelling of atmospheric ammonia (Sutton et al., 2013). The relationship of atmospheric ammonia with meteorological parameters is discussed in detail in Chapter 3.

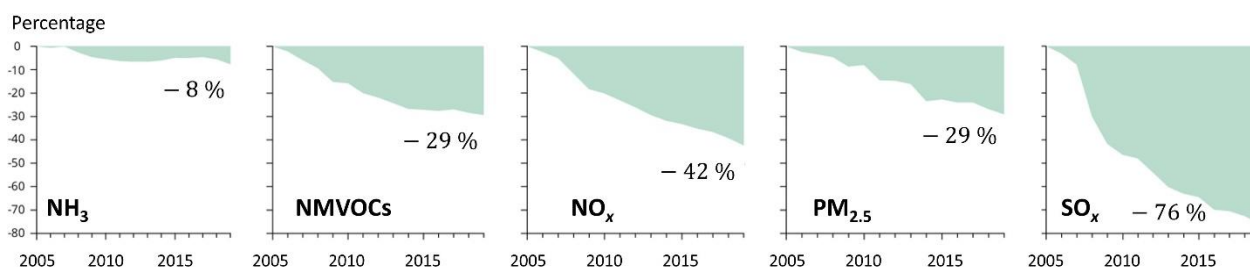


**Figure 1.6. Percentage emission reductions of main air pollutants in 2019 for EU-27 member states, as compared to 2005, following the adoption of the Gothenburg Protocol. The Figure is adapted from the European Environment Agency (EEA, 2021): <https://www.eea.europa.eu/ims/emissions-of-the-main-air>.**

EU countries in which ammonia emissions increased over the whole period [2005 – 2019] are: Austria (+6 %), Estonia (+ 5%), Ireland (+5 %), and Latvia (+22 %) (EEA, 2021). In Van Damme et al. (2021) we can see that among these countries only Austria (+10 % per decade) and Ireland (+4 %) show a positive trend of atmospheric ammonia columns. In parts, the positive trends in ammonia columns could be in part related to the reduction of the acidic content/capacity of the atmosphere. For instance, the reduction of SO<sub>x</sub> and NO<sub>x</sub> emissions in China, caused the life time

<sup>9</sup> The 1999 Gothenburg Protocol to Abate Acidification, Eutrophication and Ground-level Ozone (Gothenburg Protocol), is a protocol that was established in order to address air pollutants such as: Sulphur oxides (SO<sub>x</sub>), nitrogen oxides (NO<sub>x</sub>), ammonia (NH<sub>3</sub>) and non-methane volatile organic compounds (NMVOCs). In 2012, the protocol was amended to include fine particulate matter PM<sub>2.5</sub> and new set of commitments to address in 2020, more details can be found through the following link: <https://unece.org/environment-policy/air/protocol-abate-acidification-eutrophication-and-ground-level-ozone>.



duration of ammonia to increase. In the presence of atmospheric acids, ammonia molecules neutralize the latter to produce ammonium salts ( $\text{PM}_{2.5}$ ). This is considered an important loss mechanism (sink) of ammonia (Abeed et al., 2022; Lachatre et al., 2019). While the numbers shown in Figure 1.6 are only for EU member states, the global budget of ammonia is also increasing (van Damme et al., 2021). Another reason to why the global mitigation of global ammonia budget is not efficient, is the lack of action in China. Being a major contributor to the global atmospheric ammonia ( $>25 \text{ kg N ha}^{-1}$ ) (Sutton et al., 2013), in 2016 China started tackling ammonia emissions (Liu et al., 2019).

### *1.3.4 Future projections*

Since the emissions of ammonia are mainly driven by agricultural practices, and affected by meteorology), climate change and higher temperatures will increase the volatilization of ammonia from the surface (Abeed et al., 2022; Shen et al., 2020). In Ireland for instance, providing the applied amount of fertilizers is kept as is, ammonia concentrations will increase by ~20 % under a relatively moderate climate scenario (SSP2-4.5), and by up to ~40 % under a less likely scenario (SSP5-8.5), also referred to as business as usual, (Abeed et al., (2022), and Chapter 4). A study that focuses on agricultural lands in the U.S. found an increase of volatilized ammonia by 81 % in 2100, as compared to 2010 under the RCP8.5<sup>10</sup> climate scenario (Shen et al., 2020). These projections are shown in Figure 1.7.

Future projections of the world population are not easy to predict (Adam, 2021), however, the most recent United Nations report expected the global population to fall within 8.9 and 12.4 billion in 2100 (UN, 2022). An increase in population count will indeed increase the demand in food production, and therefore increases the cropland area (cropland expansion) (Potapov et al., 2022). Climate change is expected to increase the volatilized ammonia from agricultural lands, as well as biomass burning. In a world with an ever-rising population count (until year 2100 at least), and expanding croplands areas for food production, it is crucial to understand the interaction of ammonia with the biosphere in order to mitigate the  $\text{N}_r$  excess consequences on the planet in the future.

---

<sup>10</sup> RCP8.5 is the “business as usual” climate scenario in which intense warming is predicted, and no mitigation measures are adopted.

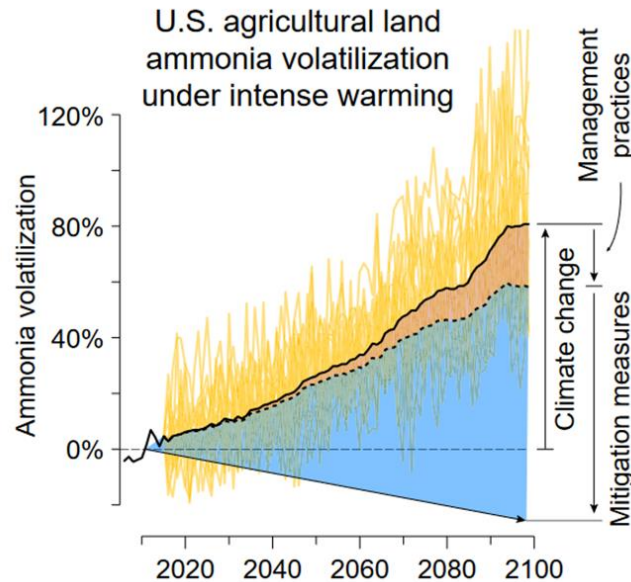


**Figure 1.7. Future Trends of volatilized ammonia in response to future climate warming under RCP8.5. We are looking at individual projections (yellow), the 5-year running mean (black line), the mean with management practices adaptive to climate change (dashed line), and the mean with fixed temperature at the 2006–2015 average level. Figure is from Shen et al. (2020).**

## 1.4 Thesis objectives

In this introduction, I showed how atmospheric ammonia played a vital role in human history, increasing agricultural yields and as such feeding billions of people around the world. This however came at cost of a deteriorating part of the ecosystem by perturbing the nitrogen cycle. This thesis aims at understanding the biosphere-atmosphere interactions, by shedding the light on agriculture-emitted ammonia. To answer this broad question, I choose to focus on three main axes:

1. The effect of meteorological fluctuations on atmospheric ammonia concentrations from agricultural practices.
2. The soil-atmosphere bi-directional exchange of ammonia in soils (forest, cropland, and grassland), with an emphasis on agricultural soils in Europe, and during the growing season.

3. The effect of land-use/cover change on atmospheric ammonia during the Syrian civil war as a case study.

Following this introduction, in Chapter 2, I present the data used during the course of this thesis with an emphasis on the Infrared Atmospheric Sounding Interferometer (IASI) aboard the Metop satellites. Chapter 3 provides an overview of the atmospheric chemistry of ammonia, and its volatilization from manure and soil. Results are presented in Chapters 3, 4, and 5. In Chapter 3, I discuss the effect of meteorology on atmospheric ammonia concentrations. I compare IASI- $\text{NH}_3$  to meteorological data from the European Organisation for the Exploitation of METeorological SATellites (ECMWF) reanalysis (ERA5), during the period [2008 – 2018]. Several regions around the globe are considered, while the main focus is on agricultural ammonia, I also include some industrial regions/hotspot (mainly to compare both source types). In Chapter 4, I explain the soil-atmosphere bi-directional exchange of ammonia, by focusing on Europe during the start of the growing season in 2011. I use for this study, satellite, re-analysis, and model simulation data. Chapter 5 examines the effect of war-induced land-use/cover change, and political disturbances on atmospheric ammonia [2008 – 2019] in two regions in Syria. The first is an agricultural region in the northeast of Syria that was seized by ISIS during the 2013 – 2015 period, and the second is a government-owned fertilizers industry whose activities were highly affected by the events of the war. In Chapter 6 I conclude the work of this thesis, and discuss its limitations and perspectives.



## Chapter 2

### *2 Data and methods*

In this thesis, I use data from the IASI instrument (Infrared Atmospheric Sounding Interferometer), onboard the Metop satellites. I discuss here in details the IASI mission, and the orbit characteristics. I then present other instruments that can detect atmospheric ammonia from space. Finally, I introduce the other datasets used in my thesis to support the satellite observation, such as meteorological and land-related data variables.

#### *2.1 IASI on Metop*

In my studies I use data from the IASI instrument (Infrared Atmospheric Sounding Interferometer), onboard the Metop satellites. In this chapter I discuss in details the IASI mission, and the orbit characteristics. I then introduce the detection of ammonia from space, using different instrumentation. Finally, I present the other datasets used in my thesis, such as meteorological and land-related data.

The IASI instrument is a hyperspectral sounder aboard the Metop (Meteorological Operational satellite) platforms (Clerbaux et al., 2009; Hilton et al., 2012). IASI is considered the most innovative instrument onboard the polar-orbiting Metop satellites (Klaes, 2018).

### 2.1.1 The Metop satellite

Three Metop satellites (Metop-A, B, and C) are the basis of the EUMETSAT (European Organisation for the Exploitation of METeorological SATellites) Polar System (EPS). Metop-A was launched in October 2006, and de-orbited starting October 2021 (Lentze, 2021), after serving for ~15 years, while it was designed to last only 5 years (Clerbaux et al., 2009). The second and third Metop satellites (B and C), are the only currently functional of the Metop series, were launched in September 2012, and November 2018 respectively. Metop-A, and B were launched on a Soyuz-2-1a Fregat vehicle, whereas Metop-C on a Soyuz-ST-B Fregat-M vehicle. In this thesis, the data used are from IASI-A (to cover the period [2008 – 2018]), unless stated otherwise. I show the Metop-A satellite, as an artist view, in Figure 2.1.

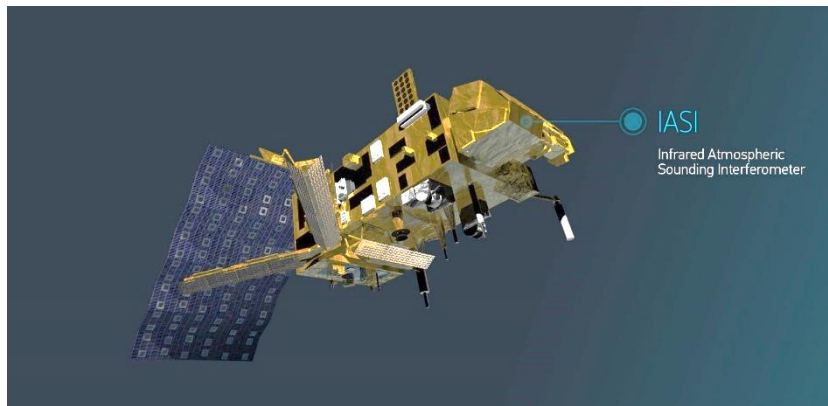


**Figure 2.1 Artist rendering of Metop-A. Figure from EUMETSAT.**

In addition to IASI, each Metop satellite carries a set of 11 instruments. Two of which are dedicated for data collection: the Argos Advanced Data Collection System (A-DCS) that collects data from ocean sensors and distribute it back to operational centres, and the Search and Rescue Satellite (SARSAT) that collects information from the emergency beacons<sup>11</sup> in order to help users in distress. A third non-scientific instrument is the Space Environmental Monitor (SEM), that monitors the space environment (weather) and solar activity, it is necessary to make sure the instrument withstands space weather. The rest of the instruments (8) aim at monitoring meteorology and atmospheric composition of the surface of the Earth, the oceans, and the

---

<sup>11</sup> An emergency beacon is a radio transmitter that is portable and battery powered (radio beacon). It is often used by users in distress in cases of emergencies (e.g. plane crash) such as airplanes, vessels, and individuals in need of rescue.

atmosphere. They achieve this goal by viewing the Earth through different windows of the electromagnetic spectrum:

- Radio: The Global Navigation Satellite System Receiver for Atmospheric Sounding (GRAS) radio receptor.
- Microwave:
  - The Advanced Microwave Sounding Unit-A (AMSU-A) sounder,
  - the Microwave Humidity Sounder (MHS) radiometer,
  - and the Advanced Scatterometer (ASCAT) radar.
- IR (infrared): The High-resolution Infrared Radiation Sounder (HIRS) radiometer.
- Visible-IR: The Advanced Very High Resolution Radiometer (AVHRR) imager.
- UV-Vis (Ultraviolet-visible): The Global Ozone Monitoring Experiment (GOME-2) spectrometer.

The first of the future generation of the Metop satellites, Metop-SG (Second Generation) series, is planned for launch in 2025. It will carry onboard the IASI-NG (IASI New Generation), in addition to other instruments. In addition to the Metop series, the EUMETSAT and the European Space Agency (ESA) will jointly launch two geostationary satellites, named MTG-S1 and S2 (Meteosat Third Generation-Sounder) in 2025. The MTG will carry the infrared sounder IRS (of which IASI is the predecessor). Figure 2.2 shows the timeline of the Metop series (A to C), the Metop-SG (1 and 2), and the MTG (S1 and S2).

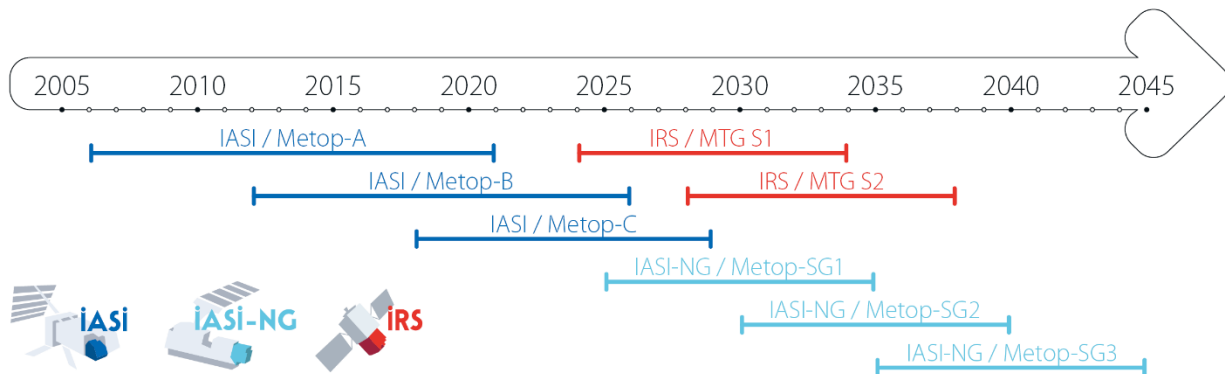


**Figure 2.2.** Timeline of the Metop series, carrying IASI (Metop-A, B, and C), IASI-NG (Metop-SG1, SG2, and SG-3), and the IRS instrument onboard the MTG S1 and S2. Figure by Gaëlle Katchourine (LATMOS).

### 2.1.2 Metop Orbit Characteristics

The Metop satellites are in Low Earth Orbit<sup>12</sup> (LEO), at ~817 km altitude from the Earth surface. The inclination  $i$  of the satellite is at approximately  $98.8^\circ$ , and it is measured relative to the equator. In Figure 2.3 I plot the inclination and altitude of Metop-A prior to the beginning of its de-orbiting process, using the tool IXION (<https://climserv.ipsl.polytechnique.fr/ixion/>). Both parameters vary with time due to friction of the atmosphere (Figure 2.3).

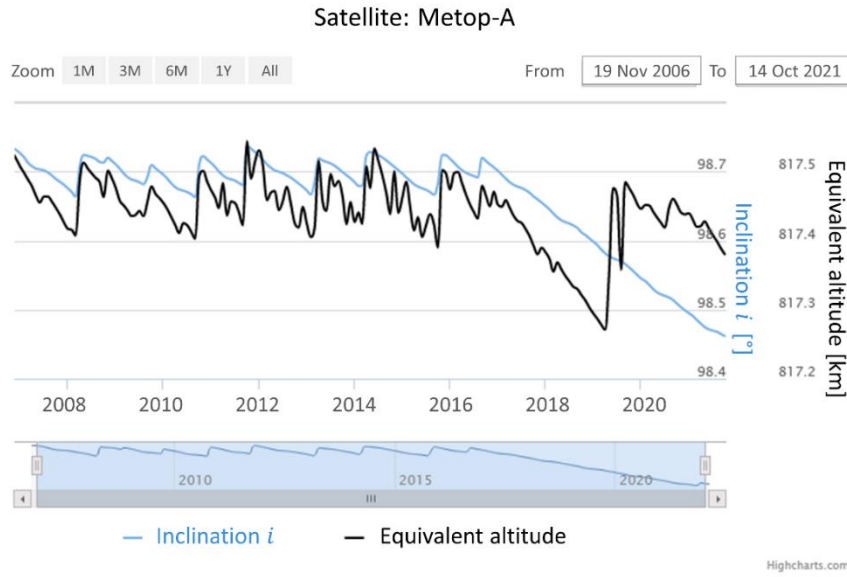


**Figure 2.3.** Metop-A satellite inclination  $i$  in blue [degrees], and altitude in black [km] prior to its de-orbiting that started in 15 October 2021. Figure is generated from IXION: <https://climserv.ipsl.polytechnique.fr/ixion/>.

The Metop satellite can rotate the Earth completely in around ~101 minutes, which means that during one day, it finishes 14 complete orbits (Clerbaux et al., 2009). It also crosses Earth twice a day (approximately at 9:30, and 21:30 local time). The crossing time is expressed in Mean Solar Time (MST), that is equivalent to local time. MST can be expressed as a function of Universal Time<sup>13</sup> ( $UT$ ) and *Longitude*, it is calculated through the following equation:  $MST = UT + Longitude/15$ . The satellite is in a sun-synchronous orbit, as such it follows the movement of the sun.

<sup>12</sup> Satellites at a height lower than 1500 km from the Earth surface are known to be in Low Earth Orbit (LEO).

<sup>13</sup> Formerly known as the Greenwich Mean Time, Universal Time ( $UT$ ) is the mean solar time of the Greenwich meridian (at longitude =  $0^\circ$ ).



In order to fully grasp the crossing time of a satellite, one must understand what we call the crossing nodes. These are the intersection points between the satellite orbit and the Earth equatorial plane. Two nodes exist, the ascending node (when the satellite moves from the south pole towards the north pole), and the descending node (north pole to south pole). The MST at the ascending node of Metop-A is seen to be at a ~21:30 until late 2018 (Figure 2.4). Metop B and C behave the same as Metop-A prior to 2018.

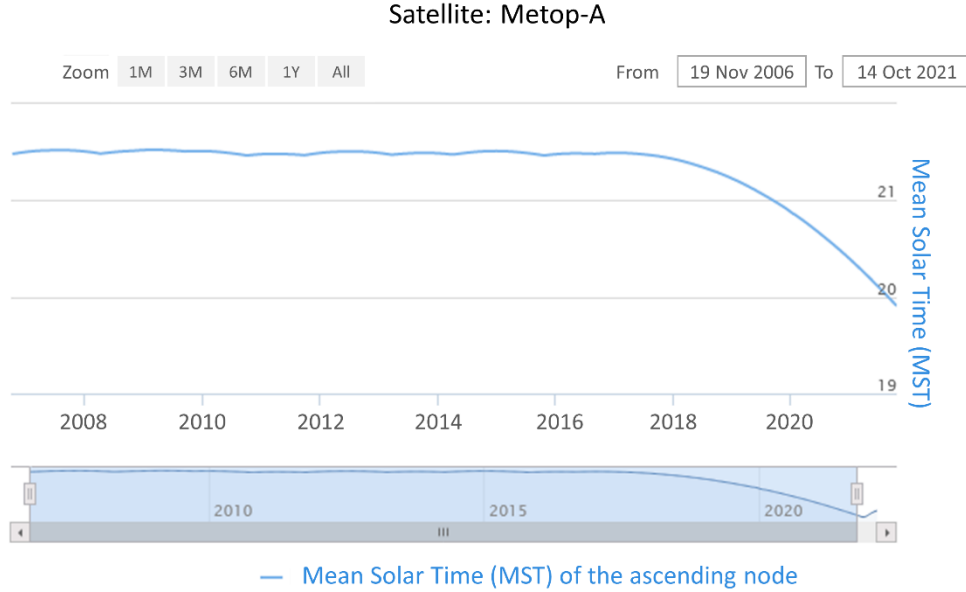


**Figure 2.4.** Mean Solar Time (MST) of the ascending node of Metop-A which is around 21:30, prior to its de-orbiting that started in 15 October 2021. Figure is generated from IXION: <https://climserv.ipsl.polytechnique.fr/ixion/>.

Ammonia concentrations in the atmosphere vary with the time of the day (Van Damme et al., 2022), as it depends, out of many factors, on its emissions and meteorological fluctuations (Viatte et al., 2022). It is important, when comparing different years of IASI data, to be sure that the crossing/detection time of the satellite is the same. In this thesis, and since Metop-A drifted in its orbit/inclination (Figure 2.4), which affected its crossing time, I use data from Metop-A until 2018, and complete the time series with data from Metop-B.

### 2.1.3 The IASI instrument

IASI is a Fourier-transform spectrometer that probes the Earth's atmosphere in the thermal infrared. The instrument is developed by the French space agency, Centre National d'Etudes

Spatiales (CNES), and EUMETSAT. Each instrument weighs around 236 kg, has the size of 1.7 m<sup>3</sup> (Clerbaux et al., 2009).

IASI is a nadir-looking instrument, with a viewing angle of  $\sim 48^\circ$  (Field Of View, FOV). To monitor the Earth, IASI has a moving sensor with an orthogonal (perpendicular to the direction of satellite movement) mode of sweeping. This sensor captures the incoming light reflected by the Earth surface, (in the thermal infrared spectral range between 645 and 2760 cm<sup>-1</sup>). The total width of the IASI swath is  $\sim 2200$  km, with 15 views on each side of the swath. Each view, consists of four footprints (pixels) of 12 km in diameter each, all packed in one grid (50 km  $\times$  50 km). The observing mode of IASI is shown in Figure 2.5.

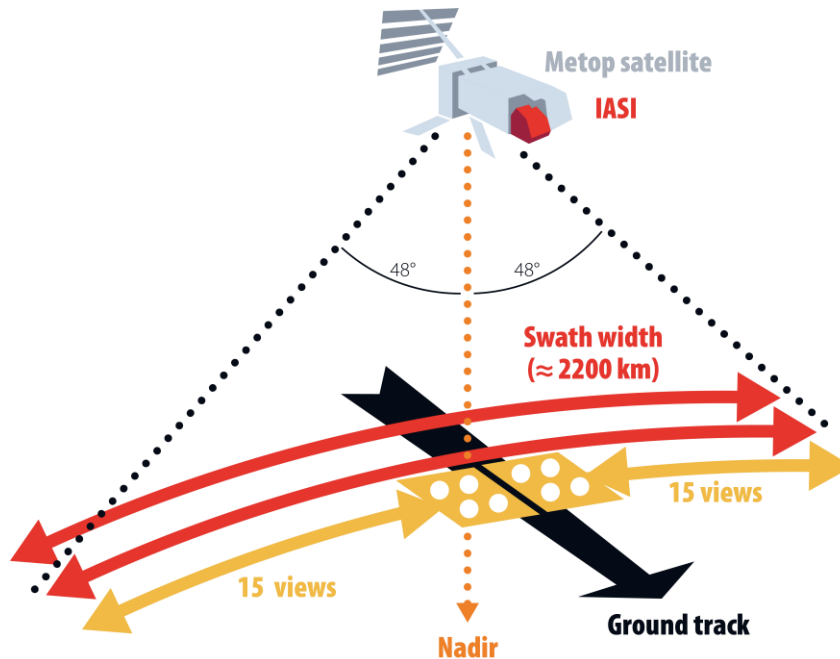


**Figure 2.5. IASI instrument observing mode. Figure by Gaëlle Katchourine (LATMOS).**

IASI receives a total of 1.3 million spectra on a daily basis, this is the size of 3.3 GB of data approximately. Each IASI spectrum contains a total of 8461 radiance channels, with a sampling at each 0.25 cm<sup>-1</sup>. The raw spectral resolution varies between 0.35 and 0.5 cm<sup>-1</sup>, and is wavenumber-dependent. In order to obtain a homogeneous resolution of 0.5 cm<sup>-1</sup>, the radiances are multiplied by an apodization function (Gaussian function) (Clerbaux et al., 2009). IASI can measure the vertical profiles of temperature and relative humidity, with a resolution of 1 K and 10 % respectively (Clerbaux et al., 2009). The main objective of IASI was to improve weather forecast, but it is also able to detect up to 33 atmospheric species (Clerbaux et al., 2015).

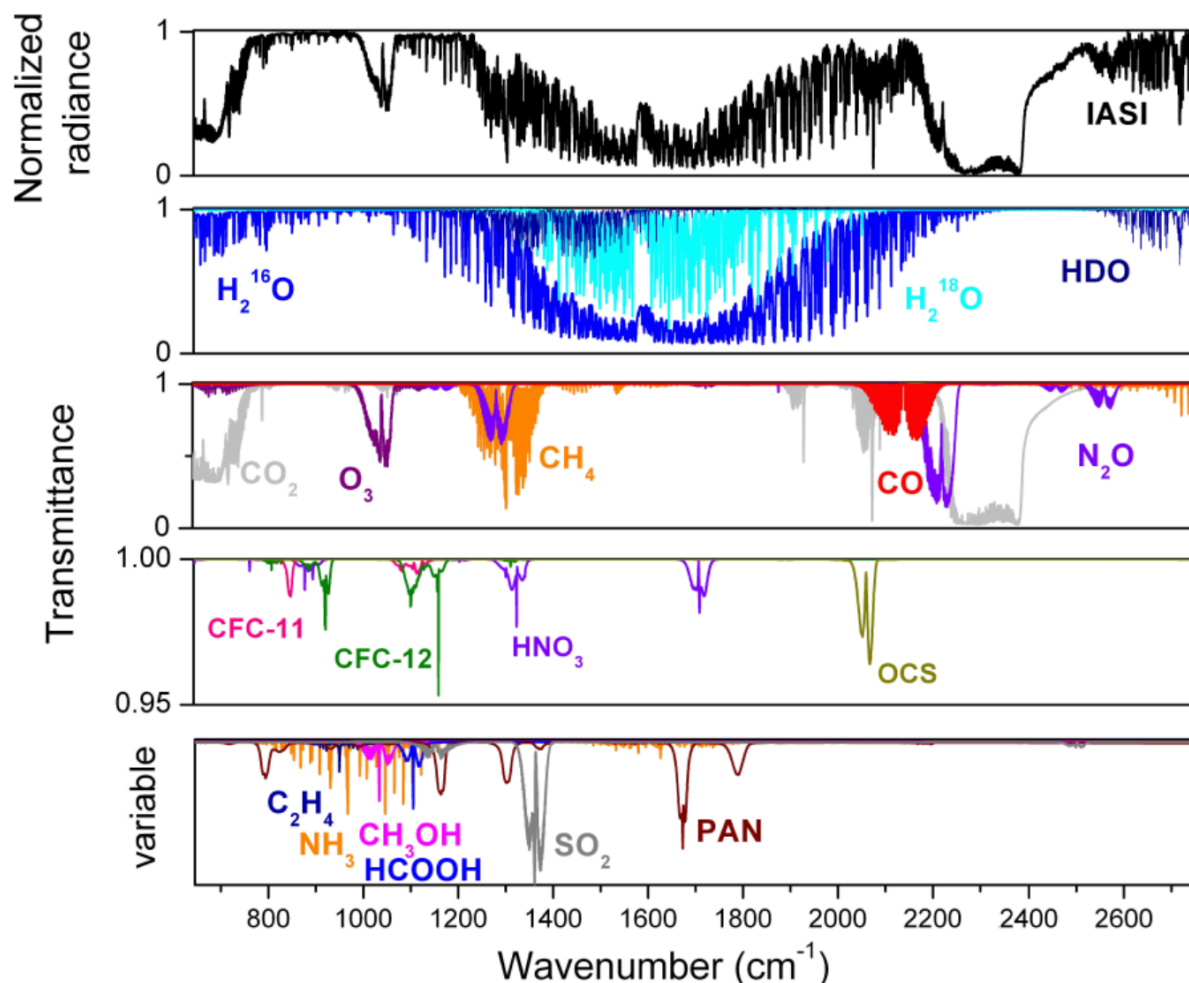


**Figure 2.6.** Top panel: radiance measured by IASI (normalized units) in the spectral range 645 – 2760  $\text{cm}^{-1}$ . Middle panels: simulated radiances of the strong-absorbing species, and the weak-absorbing gases are shown in the lower panel (variable y-axis). Figure from Clerbaux et al. (2009).

Figure 2.6 shows the full spectrum detected by IASI (top panel), and the simulated absorption spectra for different species, in the same spectral range of IASI (middle and lower panels). We can clearly see from Figure 2.6 that the dominant absorbing species is water vapor in its multiple forms (hydrogen and oxygen isotopes), and these are  $\text{H}_2\text{O}^{16}$ , HDO, and  $\text{H}_2\text{O}^{18}$  (Herbin et al., 2009). Among the strong absorbers are: (1) long lived species (more than ten years), such as carbon dioxide ( $\text{CO}_2$ ) (Crevoisier et al., 2009a), methane ( $\text{CH}_4$ ) (Crevoisier et al., 2009b) and nitrous oxide ( $\text{N}_2\text{O}$ ) (Ricaud et al., 2009), and (2) Medium-lived species, such as ozone ( $\text{O}_3$ ) (Eremenko et al., 2008), and carbon monoxide ( $\text{CO}$ ) (George et al., 2015). Despite their low signal, trace gases of lower residence time (lifetime), e.g.  $\text{NH}_3$ , can be equally detected with IASI (weakly-absorbing species shown in Figure 2.6 lower panel). In total, 33 different species can be

identified in IASI spectra (Clarisse et al., 2011; Franco et al., 2019, 2018). These detections are done in three detection bands to cover the full spectral range of IASI, 645 to 2760  $\text{cm}^{-1}$  (15.5 – 3.62  $\mu\text{m}$ ):

- Band 1: 645 – 1210  $\text{cm}^{-1}$
- Band 2: 1210 – 2000  $\text{cm}^{-1}$
- Band 3: 2000 – 2760  $\text{cm}^{-1}$

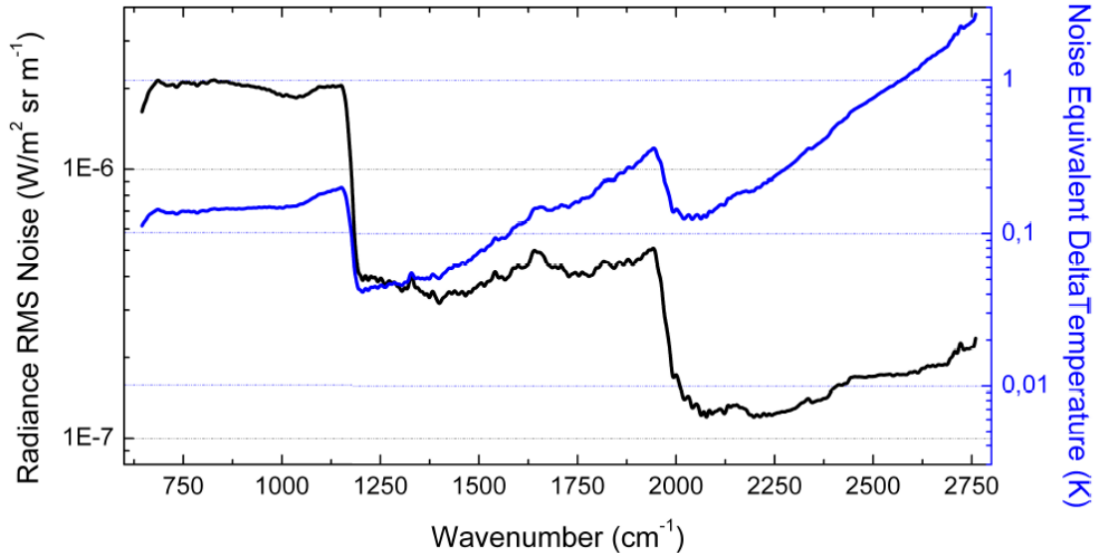


**Figure 2.7.** The radiometric noise of IASI, expressed in  $[\text{W}/\text{m}^2 \text{sr m}^{-1}]$  (left axis, black line), and the noise equivalent temperature difference expressed in Kelvin  $[\text{K}]$  (right axis, blue line). The reference temperature is 280 K. Figure from Clerbaux et al. (2009).

The signal to noise ratio (SNR) is an important measure of the performance of the instrument. The SNR can be expressed either in radiance units ( $\text{W}/\text{m}^2 \text{sr m}^{-1}$ )<sup>14</sup> as we can see on the left axis of Figure 2.7, and in Kelvin (right axis). IASI has an excellent SNR that does not exceed 0.2 K (noise equivalent temperature difference) for wavenumbers lower than 2200  $\text{cm}^{-1}$  (Figure 2.7). Only after 2500  $\text{cm}^{-1}$ , the noise starts to increase due to less thermal infrared emissions (Clerbaux et al., 2009).

<sup>14</sup> Watt per steradian per square meter.

## 2.2 Remote sensing of ammonia from space

In the previous section, I showed that the absorption signal of  $\text{NH}_3$  is weak when compared to other strong and medium-absorbing species, e.g.  $\text{O}_3$  (Figure 2.6). Scientists were able to detect atmospheric ammonia concentrations for the first time in in 2008/2009 from different satellite missions (Beer et al., 2008; Clarisse et al., 2009; Coheur et al., 2009). In 2009, the first detection of ammonia concentrations from IASI was performed in a large and local fire plume (Coheur et al., 2009). Later, a global map of ammonia concentrations was constructed from IASI measurements by Clarisse et al. (2009) (Figure 2.8). The monitoring of ammonia from space did not end with IASI. Ammonia concentrations were equally detected by the Tropospheric Emission Spectrometer (TES) onboard the Aura satellite in 2008 locally over China (Beijing) and North America (San Diego) (Beer et al., 2008), and globally exposing ammonia source regions (Shephard et al., 2011). Only later, scientists were equally able to detect ammonia using the instrument Atmospheric InfraRed Sounder (AIRS) onboard the Aqua satellite launched by NASA in 2002 (Warner et al., 2016),  $\text{NH}_3$  data from AIRS are therefore available since 2002 (published in 2016).

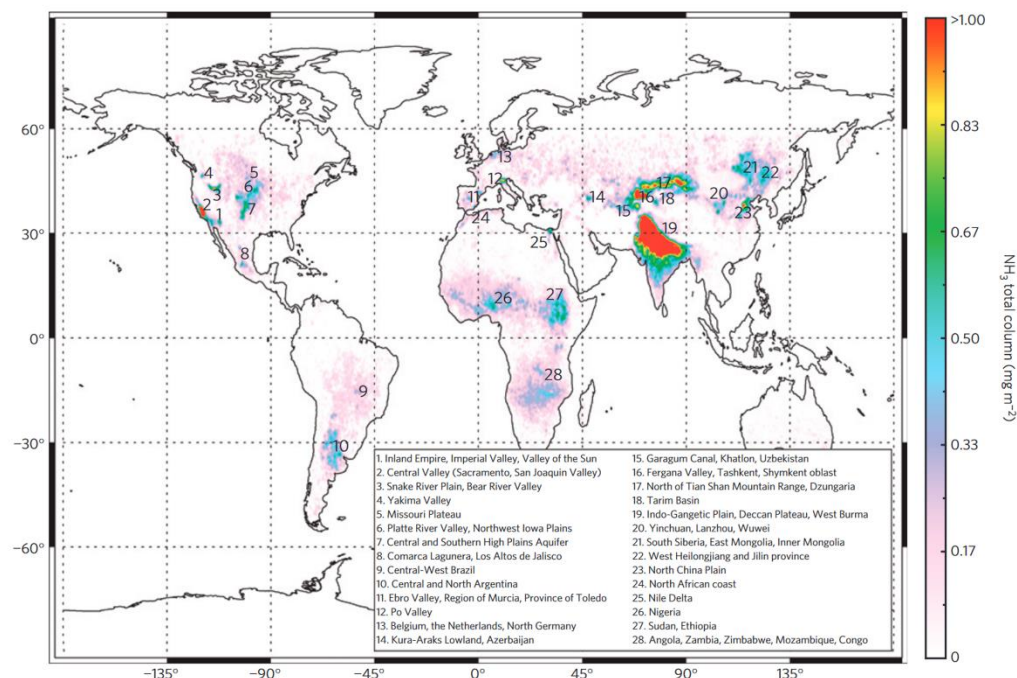


**Figure 2.8. Global distribution of  $\text{NH}_3$  from IASI during the year 2008 [ $\text{mg m}^{-2}$ ]. Figure is from Clarisse et al. (2009).**

In 2011, the National American Space Agency (NASA) launched Cross-track Infrared Sounder (CrIS) onboard the NOAA Suomi-NPP platform (Goldberg et al., 2013). Similar to IASI, CrIS is a Fourier transform spectrometer with a swath width of  $\sim 2200$  km. The ascending node of the former is in the afternoon (13:30), while that for the latter in the morning (9:30) as shown in Section 2.1.2, and Table 1. When compared to TES, IASI can observe the Earth with a better horizontal resolution, even though the spectral resolution of the former ( $0.1 \text{ cm}^{-1}$ ) is finer than that of IASI ( $0.5 \text{ cm}^{-1}$  apodized). Horizontally, TES has a viewing pixel of  $0.53 \times 5.3$  km, while for IASI it is an ellipse of 12km diameter (at nadir). I show in Table 1 the satellite instruments that can detect  $\text{NH}_3$ , the platforms on which they orbit the Earth and the years during which ammonia data are made available. The crossing time and the references are equally shown in Table 1. Among all the instruments shown in Table 1, CrIS has the highest vertical sensitivity to  $\text{NH}_3$ , since its radiometric noise is the lowest (Zavyalov et al., 2013).

**Table 1. Satellite instruments that can detect  $\text{NH}_3$ . The year in which the satellite was launched, the instrument onboard, the platform (satellite), the crossing time and the references relevant to  $\text{NH}_3$  detection.**

Launch year	Instrument	Platform	Crossing time (Local Time or MST)	Reference for $\text{NH}_3$ detection
2002	AIRS	Aqua	13:30, 01:30	(Warner et al., 2016)
2004	TES	Aura	13:30, 01:30	(Shephard et al., 2011)
2008	IASI	Metop	09:30, 21:30	(Clarisse et al., 2009; Coheur et al., 2009; Van Damme et al., 2018; Whitburn et al., 2016)
2011	CrIS	NPP Suomi	13:30, 01:30	(Shephard and Cady-Pereira, 2015)

## 2.3 Ammonia from IASI

### 2.3.1 $\text{NH}_3$ retrieval methods

The retrieval of ammonia from IASI spectra evolved through time since the first detection (Clarisse et al., 2009; Coheur et al., 2009). Clarisse et al. (2009) constructed the first global map of ammonia using IASI data, in their study they calculated brightness temperature differences between an  $\text{NH}_3$ -sensitive channel (at  $867.75 \text{ cm}^{-1}$ ) and two other channels at 861.25 and 873.50

$\text{cm}^{-1}$  (non-sensitive to  $\text{NH}_3$ ). The resulted differences were later multiplied by a factor to be converted into total columns. Although this method is fast, it loses all the information outside of the three channels used in the calculations, making it not very sensitive to  $\text{NH}_3$ . One year later, a second approach was used in Clarisse et al. (2010), in order to detect ammonia in the San Joaquin valley in the U.S.. This method is called the Optimal Estimation Method (OEM), and it was successfully applied by other scientists to retrieve ammonia from TES, CrIS and AIRS (Shephard et al., 2011; Shephard and Cady-Pereira, 2015; Warner et al., 2016). Nevertheless, it was not possible to use this method with IASI spectra on a global scale, since it requires huge computational resources. The OEM method is beneficial to retrieve a vertical column of trace gas, it is therefore used to process  $\text{NH}_3$  data from the CrIS instrument.

### 2.3.2 The Hyperspectral Index (HRI)

The two retrieval methods, mentioned in the previous section, were either lacking sensitivity or required a lot of time and resources to process the millions of IASI spectra. The need for a new method to retrieve ammonia was therefore important. The OEM and the brightness temperature difference methods used part of the spectral information provided by IASI and TES, while other spectral features are available for exploitation.

Figure 2.9 shows an example spectrum of IASI (black line), with lines denoting the channels (vertical) or spectral ranges (horizontal) used in different studies for  $\text{NH}_3$  retrieval. In order to retrieve  $\text{NH}_3$  from TES, Shephard et al. (2011) used the OEM method, exploiting only a set of microwindows between 960 and 970  $\text{cm}^{-1}$  (pink line in Figure 2.9). And the first global map from IASI was calculated based on a single  $\text{NH}_3$  feature at 867.75  $\text{cm}^{-1}$  (orange lines in Figure 2.9) (Clarisse et al., 2009).  $\text{NH}_3$  from IASI was also retrieved using the Fast Optimal Retrieval on Layers for IASI (FORLI), this method is used to retrieve carbon monoxide CO, ozone  $\text{O}_3$   $\text{HNO}_3$  profiles in Hurtmans et al. (2012). The IASI-FORLI method only considers daytime ammonia, which results in high daily averages due to a limited number of measurements per day. This retrieval scheme only exploits a spectral range from 950 to 979  $\text{cm}^{-1}$  (green line in Figure 2.9). Walker et al. (2011) introduced a new reliable method to detect trace gases, such as  $\text{NH}_3$ , using IASI measurements. The HRI method was found to be the best known method to retrieve trace gases (Walker et al., 2011). Not only it is faster than previous methods, but also highly sensitive to  $\text{NH}_3$  since it considers a larger portion of the spectral range (red line in Figure 2.9), relative to



the other methods stated earlier. Later, Van Damme et al. (2014) applied the HRI method on a wider spectral range than in Walker et al. (2011), therefore including more information and enhancing the detectability of  $\text{NH}_3$ . The range for the HRI method shows up as a blue line in Figure 2.9 (Van Damme et al., 2014). Instead of the  $800\text{--}1000\text{ cm}^{-1}$  range (red line in Figure 2.9) used in Walker et al. (2011), Van Damme et al. (2014) uses the range  $800\text{--}1200\text{ cm}^{-1}$  (blue line in Figure 2.9). The second improvement is related to the effect of thermal contrast, that was acknowledged in Clarisse et al. (2010). The thermal contrast TC is the difference between the temperature of the first layer of the atmosphere and the surface.

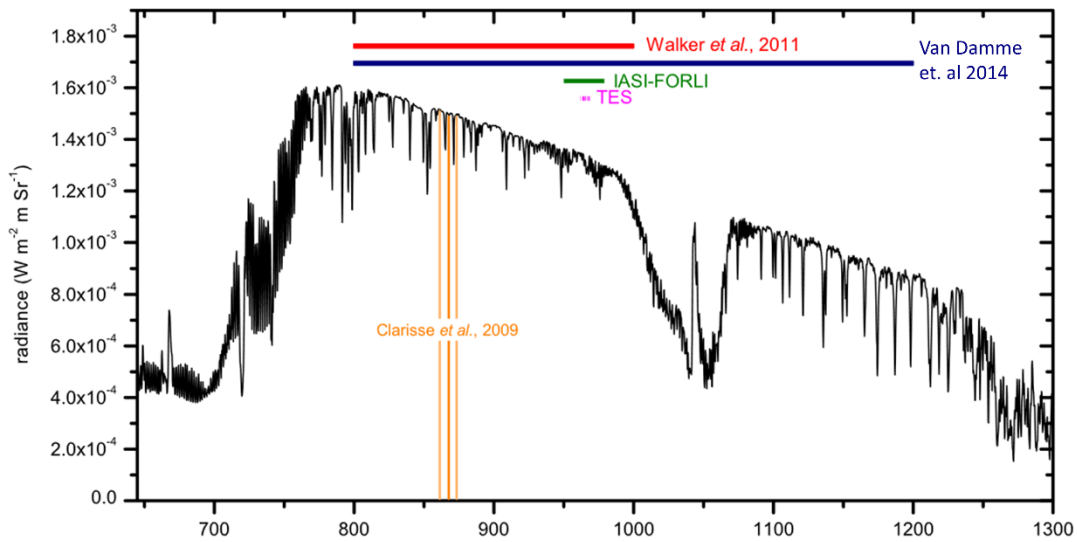


**Figure 2.9.** In black is a measured spectrum of IASI on 30 August 2011 in the California San Joaquin Valley (USA) (black). In orange are the channels used by Clarisse et al. (2009) to construct a global map of  $\text{NH}_3$ . In pink are the windows used by Shephard et al. (2011) to retrieve  $\text{NH}_3$  from TES, and the green line represents the spectral range used by FORLI (Fast Optimal Retrieval on Layers for IASI) on IASI spectra, where the OEM method is employed (Hurtmans et al. 2012). The red and blue lines are the spectral ranges employed using the HRI method on IASI spectra (Van Damme et al. 2014, Walker et al., 2011). Figure is from Van Damme et al. (2014).

To retrieve  $\text{NH}_3$ : Firstly, from each IASI observation, an Hyperspectral Range Index (HRI) is calculated. Secondly, and using theoretical look-up tables (LUTs), the HRI is converted to total columns of  $\text{NH}_3$  (Van Damme et al., 2014). To calculate HRI, a mean background spectrum  $\bar{y}$  is constructed first, in addition to the associated variance-covariance matrix  $S_y^{obs}$  from spectra having no detectable  $\text{NH}_3$ .



The HRI is then defined as:

$$HRI = G(y - \bar{y}) \quad 2-1$$

Where  $y$  is the spectrum that is measured by IASI, and  $G$  the measurement contribution function defined as:

$$G = \left( K^T S_y^{obs-1} K \right) K^T S_y^{obs-1} \quad 2-2$$

Where  $K$  is a difference between two simulated spectra, the first with a small amount of  $NH_3$  and the second is without. The spectra are simulated using the *Atmosphit* model (Coheur et al., 2005). The resulted HRI is a dimensionless parameter, and its sign depends on the sign of  $K$ , which can be negative in the case of an emission<sup>15</sup> spectrum, and positive in the case of an absorption<sup>16</sup> spectrum. HRI is a normalized parameter, as such when  $HRI = 0$ , the spectrum does not contain a detectable amount of  $NH_3$ . Only when  $HRI = 3$  or  $4$ , the signal is considered having a detectable amount of  $NH_3$ .

### 2.3.3 Artificial neural networks for $NH_3$ retrieval

The HRI method was applied later followed by the use of an artificial neural network NN named ANNI- $NH_3$  to retrieve ammonia from IASI spectra (Whitburn et al., 2016). The HRI parameter was calculated as in Van Damme et al. (2014), and then ANNI- $NH_3$  was used to convert the HRI to  $NH_3$  columns. Using the NN to retrieve  $NH_3$  from IASI was an extension to the work of Van Damme et al. (2014), that provided new improvements, among them is the reduction of positive biases of the LUT retrieval, and a complete characterization of uncertainty (Whitburn et al., 2016). However, the first version of the neural network, ANNI- $NH_3$ -v1 (Whitburn et al., 2016), did not properly represent the issue of high TC in the training dataset, which caused it to behave poorly when TC exceeds 10 Kelvin. For instance, the mean error on  $NH_3$  retrieval reached up to 35 % when TC is higher than 10 Kelvin over the land (Van Damme et al., 2017). A second

---

<sup>15</sup> The emission spectrum of a chemical element or chemical compound is the spectrum of frequencies of electromagnetic radiation emitted due to an electron making a transition from a high energy state to a lower energy state.

<sup>16</sup> A material's absorption spectrum is the fraction of incident radiation absorbed by the material over a range of frequencies of Electromagnetic Radiation.

version of the neural network was developed later, and it was referred to as the ANNI-NH<sub>3</sub>-v2.1 (Van Damme et al., 2017). The second version of the NN included multiple changes to the first version (ANNI-NH<sub>3</sub>-v1), among these are: (1) change in the output parameter which avoided resulting infinity values when NH<sub>3</sub> is undetectable, (2) doubling the simulations used in the NN from 250000 to 450000, (3) separating land and sea training networks since the TC is more variable over the land than sea, and (4) reducing the number of input parameters to further simplify the computation (Van Damme et al., 2017).

Version 2 of the NN was further modified and updated to version 3 (ANNI-NH<sub>3</sub>-v3). In v3, several changes to the network architecture and training were applied, as well as changes to the input and post-filtering (Van Damme et al., 2021). Ammonia products from IASI are equally available as re-analysed data, since they employ re-analysed temperature data from the European Centre for Medium-Range Weather Forecasts (ECMWF). At first, the ERA-Interim re-analysis were used in ANNI-NH<sub>3</sub>-v2R, and later the ERA5 reanalysis for the ANNI-NH<sub>3</sub>-v3R. Note that v2 and v3 used the IASI L2<sup>17</sup> meteorological data as input parameters, rather than re-analysed data from the ECMWF. The need to use a homogeneous set of meteorological data arose when noticeable changes were observed when using different versions of IASI L2 data for NH<sub>3</sub> retrieval (Van Damme et al., 2017). For instance, the biases between the ANNI-NH<sub>3</sub>-v2R (using ERA-Interim) and the ANNI-NH<sub>3</sub>-v2.1 (using IASI L2) were increasing as the IASI L2 version changes. This showed clear inconsistency in the NH<sub>3</sub> dataset as the IASI L2 data are updated. While showing a 5-day moving mean of NH<sub>3</sub> over the northern hemisphere, Van Damme et al. (2014) noticed that the ANNI-NH<sub>3</sub>-v2.1 averages are lower than those of ANNI-NH<sub>3</sub>-v2R, once the IASI L2 data was switched to v5.3.1. To highlight the difference between using re-analysed meteorological data and the IASI L2 data for retrieval, Figure 2.10 shows a ten-year average of total columns calculated using different versions of IASI NH<sub>3</sub> products. We can see that the re-analysed versions (v2.2R and v3R) show larger total columns than the v2.2 and v3 products.

Thanks to the improvements of the IASI NH<sub>3</sub> retrieval methods and NN, we can better understand the temporal variability of ammonia (Van Damme et al., 2022), as well as identify,

---

<sup>17</sup> IASI L2 data are derived by a Level 2 processing of the IASI spectra, in the artificial neural network ANNI-NH<sub>3</sub>-v3, humidity and temperature profiles, surface pressure and temperature, and cloud coverage fractions are used as input parameters.

categorize and quantify local hotspots of ammonia (Van Damme et al., 2018). Numerous sources of ammonia have been observed from IASI over the years (Clarisse et al., 2019a; Van Damme et al., 2021), being from agricultural practices and manure management, to industrial activities, in particular fertilizers industries (Dammers et al., 2019; Van Damme et al., 2018), fires (Chang et al., 2021; Coheur et al., 2009; Whitburn et al., 2015) and other natural sources (Clarisse et al., 2019b).

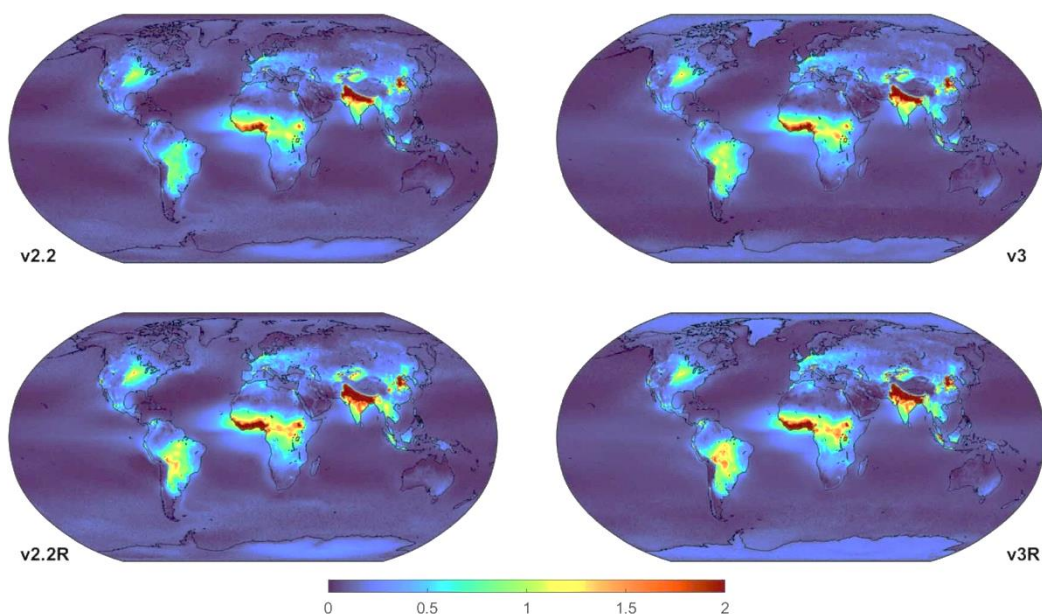


**Figure 2.10.** Global 10-year averages [2008 – 2017] of ammonia total columns expressed in  $\text{mol cm}^{-2}$  using IASI/Metop-A. Here we show ANNI-NH<sub>3</sub>-v2.2 (top left), v2.2R-Interim (bottom left), v3 (top right), and v3R-ERA5 (bottom right) on a  $0.25^\circ \times 0.25^\circ$  grid. Figure is from Van Damme et al. (2021).

NH<sub>3</sub> data from IASI compare well with other satellite instruments, bottom-up and in-situ measurements (Dammers et al., 2019; Marais et al., 2021; Viatte et al., 2020; Whitburn et al., 2015). For instance, satellite-derived emissions of NH<sub>3</sub> from IASI and CrIS show a similar bias when compared to bottom-up emissions in the UK (Marais et al., 2021). The relative error on the bottom-up emissions accounts to 11 – 36 % and 9 – 27 % when compared with IASI- and CrIS-derived emissions respectively. IASI NH<sub>3</sub> data were equally compared to several in-situ platforms in Colorado in the US during summer 2014, the results show a good correlation (0.58) (Guo et al., 2021).

### *2.3.4 IASI NH<sub>3</sub> products used in this thesis*

In this thesis work I use the ANNI-NH<sub>3</sub>-v3R (Van Damme et al., 2021) to examine the NH<sub>3</sub>-biosphere interactions (Chapter 3, and 4), and ANNI-NH<sub>3</sub>-v2.1R (Van Damme et al., 2017) to study the variability of ammonia in Syria (Chapter 5), since the ANNI-NH<sub>3</sub>-v3R data were not available for use at the time of the study. The re-analysed data are suitable when looking at the evolution of trends and/or other long-term processes, due to the homogeneity of the dataset when comparing to IASI L2 data. I considered only daytime ammonia measurements from IASI, since fewer errors on the retrieval were observed during the day and over land (Van Damme et al., 2017). It is also more relevant to look at ammonia concentrations during the day in agricultural regions, as this is when the spreading of fertilizers usually takes place. The IASI-NH<sub>3</sub> are retrieved from the Aeris data infrastructure, for the reanalysed data (<https://iasi.aeris-data.fr/nh3r-era5/>), and the IASI L2 data (<https://iasi.aeris-data.fr/nh3/>).

## *2.4 Meteorological data*

In this thesis, I use several meteorological data from the ECMWF reanalysis (ERA5) (Hersbach et al., 2020). I introduce each parameter used briefly in this section. Data from ERA5 are hourly available from 1959 to the present day, and gridded at a resolution of  $0.25 \times 0.25^\circ$  (native horizontal resolution of ERA5 is approximately 31 km). I interpolate ERA5 data temporally to the IASI morning overpass (~9:30 LST), and spatially to the coincident longitude and latitude of Metop-A. The ERA5 re-analysis data are well explained in the documentation section of Copernicus Data Store (CDS) dataset (Bell et al., 2021; Hersbach et al., 2020). The data are available through the following link: <https://cds.climate.copernicus.eu/cdsapp#!/dataset/reanalysis-era5-single-levels?tab=overview>.

### *2.4.1 Skin temperature*

The skin temperature, namely T<sub>skin</sub> (or land surface temperature), is defined as the temperature of the uppermost surface layer when radiative equilibrium is reached, this includes ocean and land surface temperature. It also represents the theoretical temperature required in order to reach the surface energy balance (ECMWF, 2016).

### 2.4.2 Air surface temperature

The air surface temperature parameter is the temperature of air at 2m height above the surface of land, ocean and other water bodies. This parameter is calculated following an interpolation method between the lowest model level and the surface of the Earth, while considering atmospheric conditions. Both temperature parameters are expressed in Kelvin (K), but I convert them to degrees Celsius on multiple occasions by subtracting 273.15.

### 2.4.3 Total precipitation

The total precipitation parameter is the liquid (and ice) accumulated on the Earth surface (including rain and snow). It consists of both large-scale and convective precipitation. The ECMWF Integrated Forecasting System (IFS) generates the large-scale and the convective precipitation, via its cloud scheme and convection scheme respectively. The cloud scheme considers the cloud's formation and dissipation as a response to changes in atmospheric pressure, temperature and humidity. The total precipitation are calculated for a period of one hour, as the data used here are hourly. The water quantity is expressed in meters (in depth), as if the water spread all over the grid box.

### 2.4.4 Wind speed

I calculate the wind speed from the u and v wind components at 10 m distance using Equation 2-3. The u and v wind components are the wind speed eastward (horizontal wind speed heading toward the east) and northward respectively, at a 10 m height from the Earth surface. They are equally predicted by the IFS of ECMWF. Therefore, the wind speed calculated is the speed at a 10 m height, in a grid box.

$$\text{Wind speed} = \sqrt{u^2 + v^2} \quad 2-3$$

### 2.4.5 Relative humidity

Relative humidity is calculated from the air and dew temperature at 2m height from the Earth surface, using Equation 2-4.  $T_{air}$  is the air temperature at 2m height, previously discussed in Section 2.4.2.  $T_{dew}$  is the dewpoint temperature, and it is an interpolated value between the lowest level of the model and the Earth surface, while considering atmospheric conditions. This parameter is the temperature at which the air should cool down, in order for saturation to occur.

$$RH = 100 \times \frac{\exp(\frac{17.67 \times T_{dew}}{243.5 + T_{dew}})}{\exp(\frac{17.67 \times T_{air}}{243.5 + T_{air}})} \quad 2-4$$

## 2.5 Land data

In addition to atmospheric parameters, in my thesis work I make use of land data such as: land cover type, and fire data (burned area). For example, in Chapter 4, the land type is used to determine the speed of exchange between the soil and the atmosphere, which will later serve in calculating emission potential of ammonia from the soil. In Chapter 5, the land cover type is used as an indicator of cropland expansion or shrinkage when studying the land-use change in Syria, during the civil war. And since ammonia can be emitted from fires, I looked at burned area data in order to see the contribution of fires to the ammonia concentrations in Syria.

### 2.5.1 MODIS Land Cover type

MODIS instruments are orbiting the Earth onboard the Aqua and Terra satellites. The Aqua/Terra MODIS Land Cover product (MCD12Q1 version 6) provides yearly maps of land cover with a 500 m spatial resolution for the period that extends from 2001 until 2019 (Sulla-Menashe and Friedl, 2018). The MOD12Q1 product employs 17 categories of land cover classification (Belward et al., 1999). In Chapter 4, I consider on croplands, forests, shrublands, and grasslands. I do not include barelands, snow cover, and urban areas in the analysis. I am not interested in studying these surfaces, since I focus on ammonia volatilization from the soil in areas amended with fertilizers. I show the emission potential in forests and grasslands/shrublands for comparison with values in the literature. In Chapter 5, I extract the croplands, shrub, and bare lands from these datasets to examine the effect of war and human displacement. The classification

used to represent croplands is defined as lands comprising of at least 60% cultivated area; A shrubland is defined as an area dominated by woody perennials (plants); bare lands (also called *Barren* in the MCD12Q1 product) are defined as lands with an at least 60% non-vegetated area (Sulla-Menashe and Friedl, 2018). In an attempt to estimate the expansion/abandonment of croplands, we use the classes provided by the MODIS product. The yearly grid of 2011 is chosen as the base year; we compare the other years to it. This product agrees 73.6% with the Food and Agriculture Organization (FAO)-Land Cover Classification System (Sulla-Menashe et al., 2019). In addition to that, the percentage of pixels switching back and forth from a class to another (due to spectral similarity) was reduced from the previous version of the product to the current one (<30% for version 6 and 55% for version 5; (Sulla-Menashe et al., 2019)). Data are available here: <https://lpdaac.usgs.gov/products/mcd12q1v006/>.

### 2.5.2 MODIS burned area

I use the Aqua/Terra MODIS burned area product (MCD64A1) (Giglio et al., 2018) to look for fire events in Syria for the study presented in Chapter 5. This product provides the approximate date of burn and the extent of burned area with a 500-m resolution. Data are downloadable here: <https://lpdaac.usgs.gov/products/mcd64a1v061/>. The MCD64A1 MODIS product is not well suited to map small burns ( $\lesssim 100$  ha), this can cause an underestimation of croplands fires that can be significant ( $\sim 10\times$  underestimate). Therefore, only fires greater than 100 ha are well estimated. A patch of land in Syria is  $\sim 20$  ha, therefore one cropland's fire will not be apparent, but rather larger fires of several patches of croplands. In Chapter 5, I use yearly measurements of burned surface area, and then the anomalies of burned surfaces are presented. The use of this product is justified, since the aim of the study was to observe anomalies between years during the spring season, which can be observed using MODIS.





## Chapter 3

### 3 *Ammonia – biosphere interactions*

In Chapter 1, I discussed briefly the pathways of ammonia in the environment following its emission. Here, I identify the main pathways governing the volatilization of ammonia in agricultural fields, starting from fertilizers type and application and ending with the fate of the lost nitrogen. I then present some of the results that I obtained when looking at several agricultural regions, around megacities as well as in different parts of the world. I discuss the effect of several meteorological parameters on the volatilization of ammonia from agricultural soils.

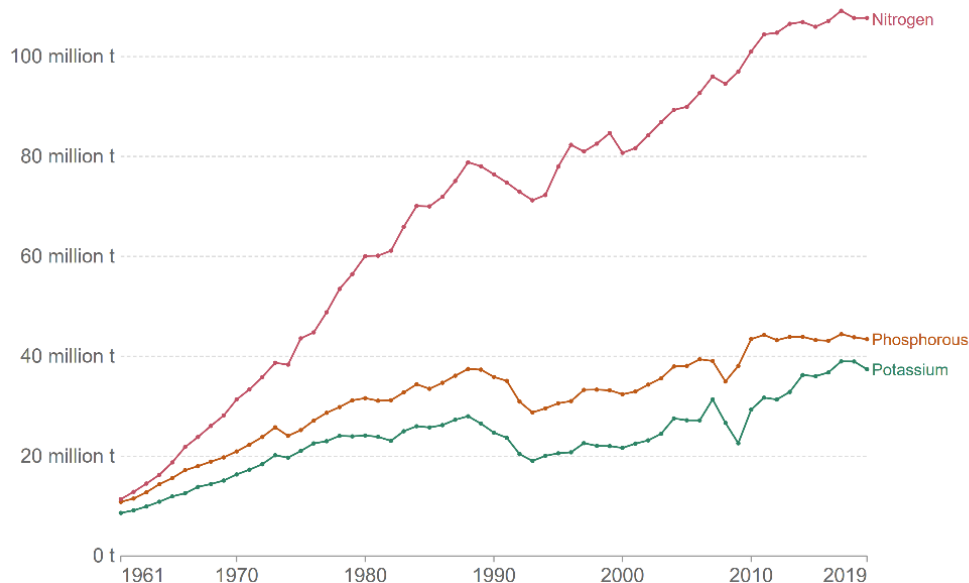


**Figure 3.1. Fertilizer use in agriculture by nutrient, from 1961 to 2019. The fertilizer use in the agricultural sector includes use for crops, livestock, forestry, fisheries, and aquaculture. The figure is retrieved from <https://ourworldindata.org/fertilizers>, and the data is from the Food and Agricultural Organization of the United Nations (FAO).**

Generally, the major nutrients required by a plant are: nitrogen (N), phosphorous (P), potassium (K), sulphur (S), magnesium (Mg), calcium (Ca) and sodium (Na) (Finch et al., 2002). Although all these nutrients are necessary for a plant's growth, nitrogen plays the most important role in increasing the yield in agriculture by speeding up the plants growth and improving the

product's quality (Finch et al., 2002; Leghari et al., 2016). For this reason, it is preferred to use fertilizers containing high percentage of N. For instance, in 2020, ~113 million tonnes (MT) of N were used worldwide, compared to ~48 MT of P, and ~39 MT of K (FAOSTAT, 2020). These numbers were eventually increasing since 2002 when the N used in agriculture accounted to 84 MT. In Figure 3.1, I show the fertilizers use by nutrient type from 1961 until 2019. We can clearly see how the use of N in fertilization increased from year 1961 to 2019, as compared to the other nutrients, phosphorous P and potassium K. In 1961, the yearly global use of P, K and N was estimated to be around 10 million tonnes per year, in 2019 the use of P and K increased to reach around 40 million tonnes, when that of N reached 100 million tonnes.

### 3.1 $\text{NH}_3$ chemistry and transport

In Figure 3.2 I draw the main processes that I will discuss here, numbered from 1 to 6. The N-fertilizer represented in Figure 3.2 is urea since it dominates the global N-fertilizers use (Heffer and Prud'homme, 2016).

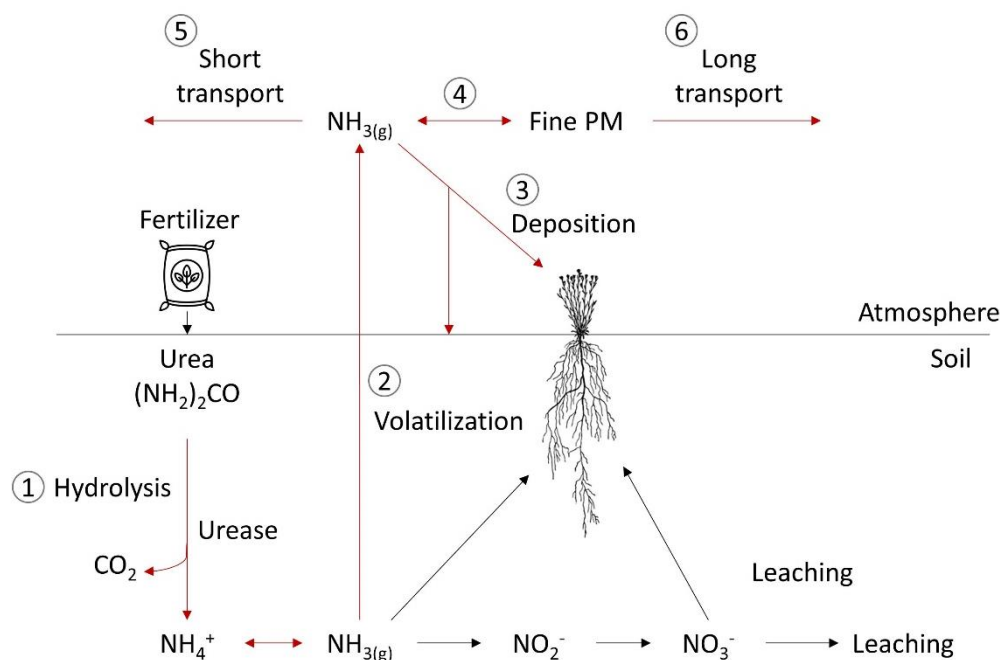


**Figure 3.2. Ammonia pathways following the application of fertilizers. The numbers refer to steps that are affected by soil and meteorological parameters, these are addressed in this Chapter.**

Urea should be spread deep into the soil (~15 cm depth) in order to avoid ammonia volatilization on the soil surface (Adjetei et al., 1999). Once introduced into the soil, urea is dissolved in the soil water (hydrolysis) and as a result  $\text{NH}_4^+$  and  $\text{CO}_2$  are released (process (1) in Figure 3.2). This process requires the presence of the urease enzyme (discussed in the following section). If not assimilated directly by plants, the  $\text{NH}_4^+$  loses one proton ( $\text{H}^+$ ) and becomes  $\text{NH}_3$  gas that can be volatilized (process (2)). The volatilization of ammonia from the soil to the atmosphere depends on multiple conditions within the soil that will be discussed in details in Section 3.1.3.  $\text{NH}_4^+$  can undergo nitrification (see Section 1.1), where the resulted  $\text{NO}_3^-$  can be also assimilated by plants, but also risks leaching in the soil water and eventually leaking to underground soil, and other water bodies in the ecosystem (e.g. rivers, lakes). Once in the atmosphere,  $\text{NH}_3$  can be deposited back on the soil or plant surfaces through wet (precipitation) or dry depositions (process (3)), or

can react with available acids to form ammonium salts on PM (process (4)), or transported to nearby fields as gas (process (5)), and to further regions as PM (process (6)) where the latter can be deposited and re-volatilized as  $\text{NH}_3$ .

### *3.1.1 Fertilizer types and use*

We saw in Chapter 1 that  $\text{N}_r$  can be generated from natural processes, but the naturally available  $\text{N}_r$  is not enough to increase the agricultural yield. Therefore, most of the N uptaken by crops is provided by fertilizers. The rest of the nutrients can be provided by the decomposition of soil organic matter by bacteria and fungi, acid rain (provides sulphur), as well as additives present in fertilizers or added directly to the soil depending on its conditions and type (e.g. sandy soil can be treated by lime with magnesium limestone to enrich the soil with magnesium Mg (Finch et al., 2002)). Along with  $\text{NO}_3^-$ , ammonia is one of the forms of nitrogen that crops can absorb, as  $\text{NH}_3$  gas through leaves stomata (Loubet et al., 2012), or  $\text{NH}_4^+$  in soil water via the roots (von Wirén et al., 2001). Therefore, it is widely used in most synthetic N-fertilizers, or is a result of their dissolution in the soil water (e.g. urea). Several type of nitrogen fertilizers exist, these are:

1. Ammonium nitrate  $\text{NH}_4\text{NO}_3$  (33.5 – 34.5 % N),
2. Ammonium nitrate and lime (21 – 26 % N),
3. Sulphate of ammonia (21 % N, and 60 %  $\text{SO}_3$ ),
4. Sodium nitrate  $\text{NaNO}_3$  (16 % N),
5. Calcium nitrate  $\text{CaNO}_3$  (15.5 % N),
6. Anhydrous ammonia (82 % N),
7. Aqueous ammonia  $\text{NH}_{3(\text{aq})}$  (12 % N),
8. Aqueous nitrogen solution, usually ammonium nitrate mixed with urea (26 – 32 % N) also known as UAN,
9. And urea  $(\text{NH}_2)_2\text{CO}$  (46 % N).

Not all of these fertilizers are used to the same extent. For instance, among all fertilizers, urea dominates the global market, consisting of half of the global use in agriculture (57%) (Heffer and Prud'homme, 2016), and ammonium nitrate dominates the fertilizer use in Europe (45 %) (Fertilizers Europe, 2016). Urea is dominant worldwide due to having the highest N content among other fertilizers (46 % N content) (Finch et al., 2002), and being able to easily decompose into ammonium and incorporate into any type of soil because of its solid form (ACS, 2021). In

Europe, however, ammonium nitrate use is dominant because it is considered more suitable to the soil and climate conditions than urea (Fertilizers Europe, 2016). The only other fertilizer that contains a higher amount of nitrogen is anhydrous ammonia (82 % N content) (Finch et al., 2002). The latter consists of  $\text{NH}_3$  in the liquid form due to compression at high pressure without water, hence the term anhydrous. It is found to be highly more efficient in terms of yield, when compared to using urea fertilization, however its use is not common in developing countries and is dangerous if not handled properly (Naeem et al., 2022). Anhydrous ammonia is widely used in agricultural lands of the United States, where previous accidents due to leakage resulted in dozens of injured individuals, among these, some reported respiratory failures due to exposure to dry  $\text{NH}_3$  (Rispen et al., 2020).

In Figure 3.3, I show the percentage use of N-fertilizers use in Europe (2015/2016), and in the rest of the world (2013). Fertilizer types in Figure 3.3 are classified into 5 main categories: nitrate fertilizers (any fertilizer containing  $\text{NO}_3^-$ ), urea, UAN, all other N fertilizers, and finally NPK<sup>18</sup> fertilizers. We can see how the most widely used fertilizers are urea and ammonium nitrate, where the application of both can eventually lead to the loss of nitrogen to ammonia volatilization.

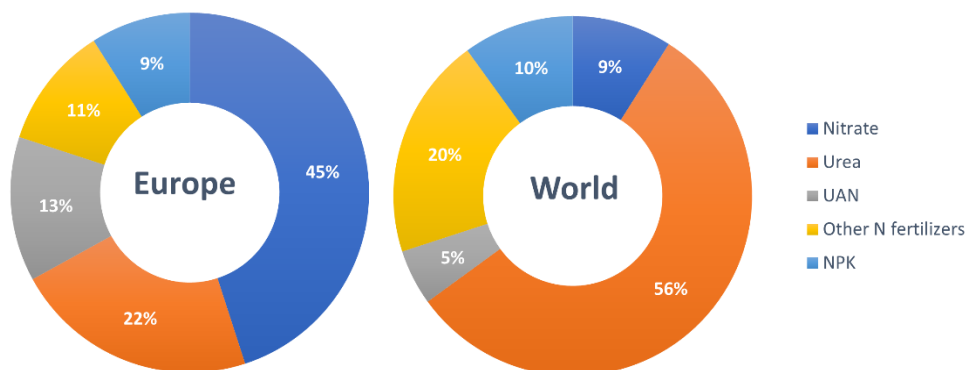


**Figure 3.3. Nitrogen fertilizers consumption in Europe (2015/2016) and in the world (2013). Nitrate fertilizers are those containing  $\text{NO}_3^-$ , UAN is urea mixed with ammonium nitrate (Aqueous nitrogen solution), and NPK are what we call compound fertilizers, these are fertilizers containing several nutrients: N, P, and K in different or similar proportions. Figure is adapted from *Fertilizers Europe* (2016). Report accessible here: <https://www.fertilizerseurope.com/wp-content/uploads/2019/09/Fertilizer-Types-Infinite-Fertilizers.pdf>.**

<sup>18</sup> NPK fertilizers contain nitrogen, phosphorus, and potassium and they are usually characterized by NPK numbers. For example, a 15:15:15 NPK fertilizer contains 15 % N, 15 % P as phosphorus pentoxide ( $\text{P}_2\text{O}_5$ ), and 15 % K as potassium oxide ( $\text{K}_2\text{O}$ ).

### 3.1.2 Urea hydrolysis in the soil

The hydrolysis of urea is the reaction that breaks it down into ammonium  $\text{NH}_4^+$  and bicarbonate  $\text{HCO}_3^-$ , both of which are ions dissolved in water and are easily diffused into the soil relative to urea.  $\text{HCO}_3^-$  is later volatilized as carbon dioxide gas ( $\text{CO}_2$ ). Figure 3.4 shows the hydrolysis reaction, and the fate of  $\text{HCO}_3^-$  (Kissel and Cabrera, 2005).

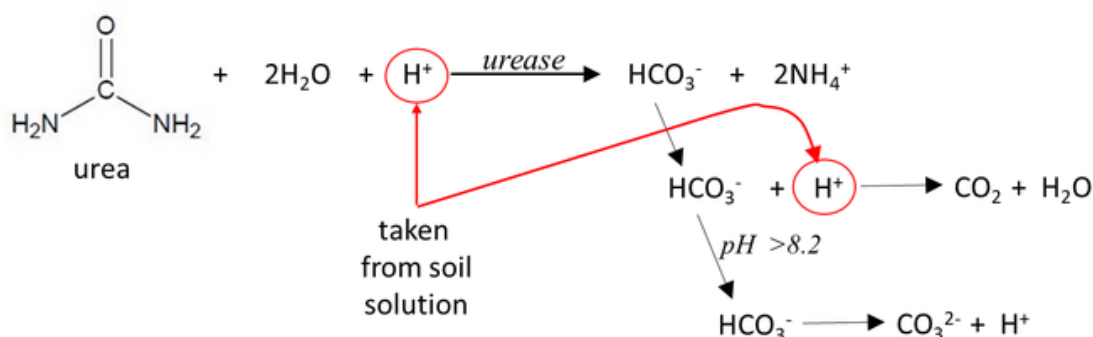


**Figure 3.4. The urea hydrolysis process (Kissel and Cabrera, 2005).**

Urea hydrolysis depends broadly on: (1) water content, (2) acidity (pH) of the soil, and (3) the enzyme urease<sup>19</sup> activity. The latter is highly affected by temperature, for instance, higher temperatures increase the activity of urease and therefore the rate of hydrolysis. Farmers use urease inhibitors in order to slow down the hydrolysis process of urea or UAN<sup>20</sup>, and as a result reduce the loss of nitrogen as volatilized  $\text{NH}_3$ . One of the common inhibitors is NBPT (N-(n-Butyl)thiophosphoric triamide), this molecule locks onto the binding sites of the urease enzyme to prevent it from reacting with urea (Manunza et al., 1999). Ammonia volatilization losses from urea decreased from 35.9 % to 2.7 % of N applied when using NBPT with urea compared to urea alone for a period of 7 days after application (Franzen, 2017). Lower temperatures can also reduce the conversion of urea to  $\text{NH}_4^+$  (slow down the hydrolysis rate). More importantly, this conversion increases exponentially with increasing temperatures (Sahu et al., 2008). Urea hydrolysis is also affected by moisture, as it needs to capture the water from its surroundings in order to dissolve.

<sup>19</sup> Urease is an enzyme that acts as a catalyst in the hydrolysis reaction of urea.

<sup>20</sup> UAN consists of urea and ammonium nitrate dissolved in water and often used as a fertilizer.

A soil water level<sup>21</sup> of 4 % (w/w<sup>22</sup>) is seen to be inferior to the quantity needed for the whole fraction of urea granules to be dissolved, even at a high temperature (30°C), and relative humidity (70 %) (Ni and Pacholski, 2022). The reactivity of urease, however, increases with higher soil moisture, and temperature (Sahrawat, 1948). When the soil water level was at 8 %, and combined with a temperature of 20°C, the hydrolysis of granules increased remarkably up to a 100 % fraction of the added granules to the sample (Ni and Pacholski, 2022).

### 3.1.3 *NH<sub>3</sub> volatilization to the near surface air*

As seen in the previous section, the conditions of the soil (moisture and temperature), and the urease activity play a crucial role in the content of  $\text{NH}_4^+$  resulting from urea hydrolysis. If the hydrolysis rate is high, more ammonia will be ready in the soil quickly. This high rate of  $\text{NH}_3$  availability is not met with a high uptake from the plants roots, since the latter highly depends on the plant's growth stage and type, as well as the competition with the available  $\text{NO}_3^-$  (Cui et al., 2017). Following the hydrolysis of urea,  $\text{NH}_4^+$  and  $\text{NH}_3$  are in equilibrium in the soil, this equilibrium is governed by the dissociation constant of  $\text{NH}_4^+$  (see Section 4.2 in Chapter 4). This reaction is reversible, where acidic medium ( $\text{pH} < 7$ ) favours the formation of  $\text{NH}_4^+$  from  $\text{NH}_3$ , and a basic medium ( $\text{pH} > 7$ ) will favour the formation of  $\text{NH}_3$  gas, making it available for volatilization.  $\text{NH}_3$  however, can either exist in the soil water ( $\text{NH}_{3(\text{aq})}$ ) or in the soil air ( $\text{NH}_{3(\text{gas})}$ ), and the equilibrium between both states of  $\text{NH}_3$  is governed by the Henry's law (see Section 4.2 in Chapter 4). Both of the equilibria mentioned beforehand are affected by soil temperature, where higher temperatures are seen to increase the availability of  $\text{NH}_3$ , e.g. by increasing the value of the Henry's constant that is proportional to  $\text{NH}_{3(\text{gas})}$  concentration (Liehr et al., 2006). In addition to that, temperature reduces the solubility of  $\text{NH}_3$  in soil water, therefore increasing the concentration of ammonia in soil air (gas phase), and resulting in higher volatilization from the soil. For instance, simulated volatilized  $\text{NH}_3$  showed higher correlation with surface air

---

<sup>21</sup> The gravimetric water content is defined as the ratio of the mass lost, attributed to water initially present in the sample, to total mass of the fully dried soil. It is calculated using the following equation: Gravimetric water content (%) =  $100 \times (M_{\text{swc}} - M_{\text{sc}}) / (M_{\text{sc}} - M_{\text{c}})$ .  $M_{\text{swc}}$  is the mass of the wet (moist) soil and container,  $M_{\text{sc}}$  is the mass of the dry soil and container, and  $M_{\text{c}}$  is the mass of the empty container (Topp et al., 2008).

<sup>22</sup> w/w is the weight of the water divided by the weight of the soil.

temperature (at 2m height) in warmer climates ( $r = 0.76$ ) than in colder ones in the United States (Shen et al., 2020) (Figure 3.5).

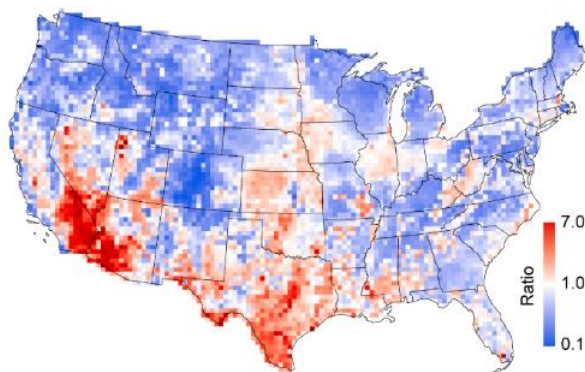


**Figure 3.5 Spatial distribution of a ratio that represents the correlation between ammonia volatilization and air temperature (2m height). Figure from Shen et al. (2020).**

The same study by Shen et al. (2020) examined the effect of total precipitation and wind speed,  $\text{NH}_3$  volatilization was found to be negatively correlated with increased rainfall due to wet deposition ( $r = -0.21$ ), and positively correlated with wind speed (10m) due to short-range transport ( $r = 0.05$ ). The transport and deposition of the volatilized  $\text{NH}_3$  will be discussed in the next section.

### 3.1.4 Transport and deposition

Ammonia has a short lifetime that usually ranges between a few hours to a few days (Behera et al., 2013). It can be transported either on a short range (e.g. 1 km from the source of  $\text{NH}_3$ , Fowler et al., (1998)), or a long range (as deposited ammonium salts that can release  $\text{NH}_3$ ). Once transported,  $\text{NH}_3$  in the gas phase or  $\text{NH}_4^+$  attached to particles will be deposited on land, vegetative and marine surfaces (Wichink Kruit, 2010). Wind speed and direction plays an important role in this transport, as well as temperature and humidity (Olesen and Sommer, 1993), since they govern the equilibria that generate  $\text{NH}_3$  and  $\text{NH}_4^+$  as seen in the previous sections.

Globally, the total budget of the deposited nitrogen accounts to  $56.7 \text{ Tg N yr}^{-1}$ , with the majority being deposited on lands (68 %) rather than oceans (32 %) Figure 3.6 shows the trends in  $\text{NH}_3$  dry deposition from 2008 to 2016, as calculated with IASI data in (Wang et al., 2020). These trends are generally seen in source regions of ammonia, implicating a short-range transport. We can also see how the highest deposition trends  $> 0.2 \text{ kg N ha}^{-1}$  are observed in China, a region



with extensive agricultural practices, and industrial activities that emit  $\text{NH}_3$  (e.g. fertilizers and coke industries). Estimates of dry deposition from IASI from a different study also showed a positive trend of dry deposition that are mainly driven by Chinese agriculture (Liu et al., 2020). These trends are correlated to warmer and more humid periods (Wang et al., 2020).

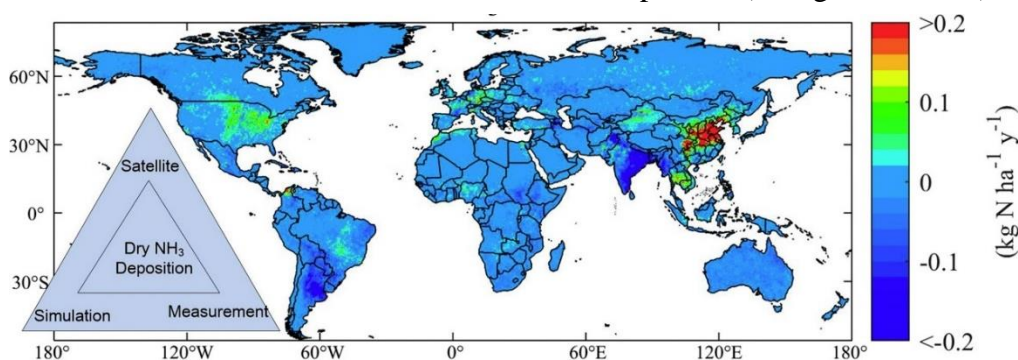


**Figure 3.6. Trend in dry  $\text{NH}_3$  deposition [2008 – 2016]. Figure from Liu et al, (2020).**

The problem with ammonia's deposition is that this “sink” can transform into a source of  $\text{NH}_3$ . For instance, deposition of ammonium salts enriches the land and vegetative surfaces with  $\text{NH}_4^+$ , therefore, enhancing the potential of  $\text{NH}_3$  formation and release based on the conditions of the medium where  $\text{NH}_4^+$  is deposited. Ammonia dissolves in the water film of plants leaves, and will eventually evaporates when the temperature rises. And just like the soil, plants can emit  $\text{NH}_3$  when the atmospheric concentration is higher than the compensation point of canopy (Behera et al., 2013), e.g. the concentration at which the net flux from the canopy is zero (more details in Chapter 4). The compensation point is temperature dependent, and is affected by soil pH,  $\text{NH}_3$  deposition on leaves, and the ammonium concentration inside the canopy (Schjoerring et al., 1998).

### 3.1.5 Formation of fine PM

Being the dominant alkaline (basic) gas in the atmosphere, ammonia is able to neutralize acidic gases, such as: hydrochloric acid ( $\text{HCl}$ ), nitric acid ( $\text{HNO}_3$ ), and sulfuric acid ( $\text{H}_2\text{SO}_4$ ). This process results in the formation of ammonium salts on PM.  $\text{HCl}$  is emitted mainly from waste burning (38 %), biomass fires (19 %), energy production (19 %), and the residential sector (13 %) (Zhang et al., 2022). While at least 41 % of the nitric acid is formed through the oxidation of  $\text{NO}_2$  gas by the hydroxyl radical (Alexander et al., 2020). The emissions of  $\text{H}_2\text{SO}_4$  are dominated by the coal industry and traffic (Lin et al., 2022). The reactions of ammonia with the beforementioned acids are shown in the equations below.



The first two reactions (3-5, 3-6) are reversible due to the high partial pressure of  $NH_4Cl$  and  $NH_4NO_3$ . In other words, they are more easily to breakdown into  $NH_3$  and the corresponding acid ( $HCl$  or  $HNO_3$ ) (Sutton et al., 1998). These two reactions are temperature-dependent, and are also affected by air and surface humidity (Faisal et al., 2022), for instance high temperatures experienced during a dry period will likely reverse reaction 3-6 to result in the volatilization of ammonia from  $NH_4NO_3$ -bearing PM. This is because high temperatures are found to inhibit the formation of  $NH_4NO_3$ , as well as  $NH_4Cl$  (Bassett and Seinfeld, 1984). Ammonium sulphate, however, has a low volatility and is therefore considered as a stable salt (Bassett and Seinfeld, 1984). It was found that, even in the case when less sulfuric acid is present in the atmosphere  $H_2SO_4$ , nitrate can compensate this decline and therefore ammonium nitrate salts PM will form. This is mostly apparent in cold areas such as England (Erisman and Schaap, 2004).  $NH_4^+$ -bearing PM are likely to travel for longer distances with winds, and then get deposited in ecosystems (e.g. forests), and later transform back to  $NH_3$ . Therefore, increasing the nutritional content of the soil, which leads to more greening of plants. This increase in plants growth interferes with the carbon cycle. The exceptional growth of vegetation will lead to a higher capacity in absorbing carbon dioxide ( $CO_2$ ) from the atmosphere. Thus, increasing the global carbon sink (annual carbon gain) by up to  $0.72 \text{ Pg}^{23} \text{ C yr}^{-1}$  (Gurmesa et al., 2022). In urban regions, several studies showed the correlation between PM pollution episodes and fertilizers spreading in neighboring fields (Viatte et al., 2020; Wang et al., 2015; Wu et al., 2016). In the next section, I show some of the results of atmospheric ammonia from IASI in and around large cities in three different domains.

---

<sup>23</sup> Pentagram =  $10^{15}$  grams = 1 billion metric tonnes carbon.

### 3.2 Ammonia concentrations in Europe, Canada, and Mexico

One of the implications of atmospheric ammonia emissions in and around urban regions, is the formation of particulate matter (PM). Megacities, as in cities with 10 million inhabitants or more, are prone to experience PM pollution episodes due to transported ammonia from neighboring rural areas, in addition to industrial-emitted  $\text{NH}_3$  from some types of industries (Yamanouchi et al., 2021).

Europe [41–59° N; –11.25–16.25° E]	North America [35–53° N; 93.75–63.75° W]	Southern North America [9–29° N; 113.75–86.25° W]
A North European plain <sup>c,d</sup>	A Granby (Canada)	A Obregon (Mexico) <sup>c</sup>
B Saxe Anhalt plain (Germany)	B Elmira–Kitchener–Guelph (Canada)	B Torreon (Mexico) <sup>c,d</sup>
C Munich–Mangfall (Germany)	C Brillion area (USA)	C Garcia (Mexico) <sup>b,c</sup>
D Champagne–Ardenne (France)	D New York State (USA)	D Culiacancito (Mexico) <sup>c,d</sup>
E Brittany–Pays de la Loire (France) <sup>d</sup>	E Lancaster County (USA)	E Nayarit (Mexico)
F Pô Valley (Italy) <sup>c,d</sup>	F Wayne County (USA)	F Jalostotitlan–San Juan de Los Lagos (Mexico) <sup>c,d</sup>
G Valley of Piedmont (Italy) <sup>c,d</sup>	G Celina–Coldwater (USA) <sup>c</sup>	G Salamanca–Villagran (Mexico) <sup>a,c</sup>
H Landes area (France)	H Shenandoah Valley–Bridgewater (USA) <sup>c</sup>	H Ezequiel Montes (Mexico) <sup>c,d</sup>
I Vic–Manlleu (Spain) <sup>c,d</sup>	I Lenoir County (USA)	I Tapaon, Loma Alta (Mexico) <sup>c</sup>
J Ebro River basin (Spain) <sup>c,d</sup>		J Tecoman (Mexico)
		K Coyuca de Catalan (Mexico)
		L Morelos (Mexico)
		M Tochtepec–Tehuacan (Mexico) <sup>c</sup>
		N South of Veracruz (Mexico)
		O Cosolaecaque (Mexico) <sup>a,c</sup>
		P Tabasco (Mexico)
		Q Guerrero (Mexico)
		R Chiseac (Guatemala)
		S Texcuaco (Guatemala)

<sup>a</sup> Fertilizer industry; <sup>b</sup> soda ash industry; <sup>c</sup> Van Damme et al. (2018), Clarisse et al. (2019); <sup>d</sup> Dammers et al. (2019).

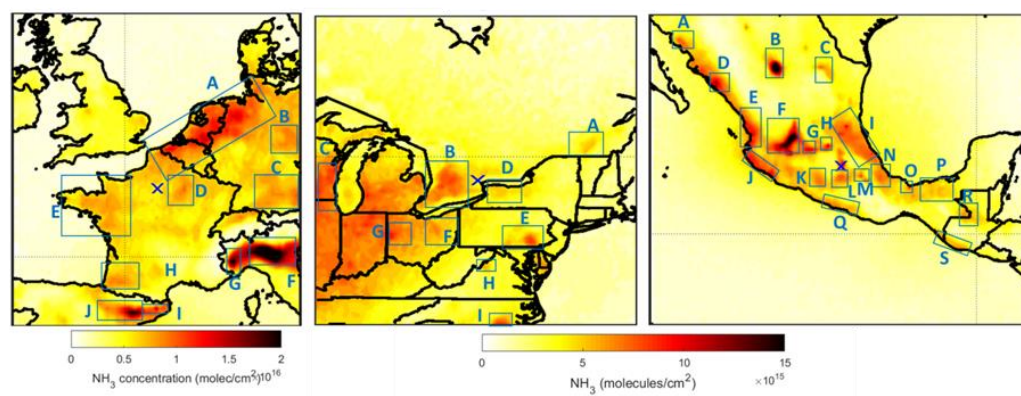


**Figure 3.7.** Source regions of  $\text{NH}_3$  derived from 10 years average of IASI total columns [molecules/cm<sup>2</sup>] from 2008 to 2017. The crosses indicate Paris, Toronto, and Mexico locations (left to right). The three main domains considered are: “Europe” (left), “North America” (middle), and “southern North America” (right). Figure from Viatte et al. (2022).

We investigate air pollution in three large domains, Europe, North America and southern North America in which three major megacities exists: Paris, Mexico, and Toronto respectively. Figure 3.7 shows the three main domains we consider in this study: “Europe (EU)” (left), “North America (NA)” (middle), and “southern North America sNA” (right). In each domain, several sub-regions are considered and are index with alphabetical letters (Figure 3.7). Each of these domains have distinct emission sources, agricultural regulations, and topography. Ten years of measurements from IASI are used to assess the  $\text{NH}_3$  variability over and around the three cities.

For the rest of this chapter, I list the results from a study by Viatte et al. (2022) that I participated to as a second author. Unless stated in the Figure’s caption, I have generated all Figures in this chapter.

### *3.2.1 The effect of skin temperature on $\text{NH}_3$ columns*

We saw in the previous sections of this Chapter how temperature can increase the volatilization of  $\text{NH}_3$  by interfering in all the pathways of  $\text{NH}_3$  from fertilizers application to the deposition of  $\text{NH}_4^+$ -bearing PM. In order to assess the effect of temperature on  $\text{NH}_3$  concentrations from space, I show in Figure 3.8 and Figure 3.9 IASI  $\text{NH}_3$  total columns averaged per bins of ERA5 T skin, for a period of ten years [2008 – 2018]. To calculate these averages, I classify individual temperature measurements (check IASI overpass, Section 2.1.2) into several bins. The first margins of the first bin are the lowest temperature value ( $T_{min}$ ) ever recorded in the region of focus, to  $T_{min} + 1^\circ\text{C}$ . All T skin values within this range are averaged in this bin. These are the values represented in the x axis in Figure 3.8. The  $\text{NH}_3$  concentrations that we see on the y axis in Figure 3.8, are values that fall within the temperature bin. I choose to show the sub regions of Europe first, since they are all agricultural source regions (see Figure 3.7).

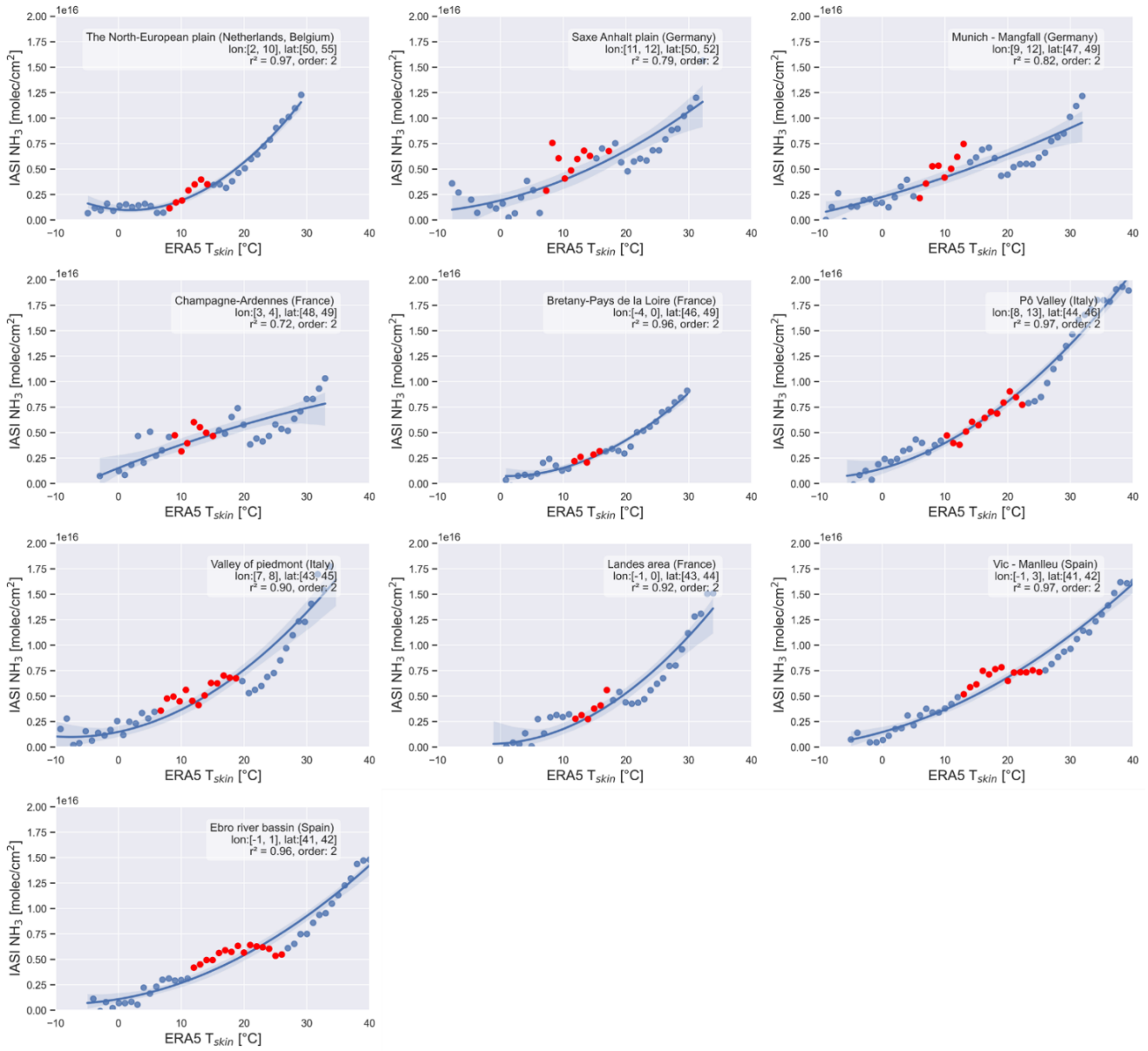


**Figure 3.8.** Yearly IASI  $\text{NH}_3$  total columns (molecules/cm<sup>2</sup>) averaged per bins of ERA5 skin temperatures [°C], with an interval of 1°C between each consecutive bin. The red dots denote the growing seasons, at least 60% of the  $\text{NH}_3$  are detected during March-May and Sept-Nov periods. The regions considered here are the regions presented in Figure 3.7, in the Europe domain.

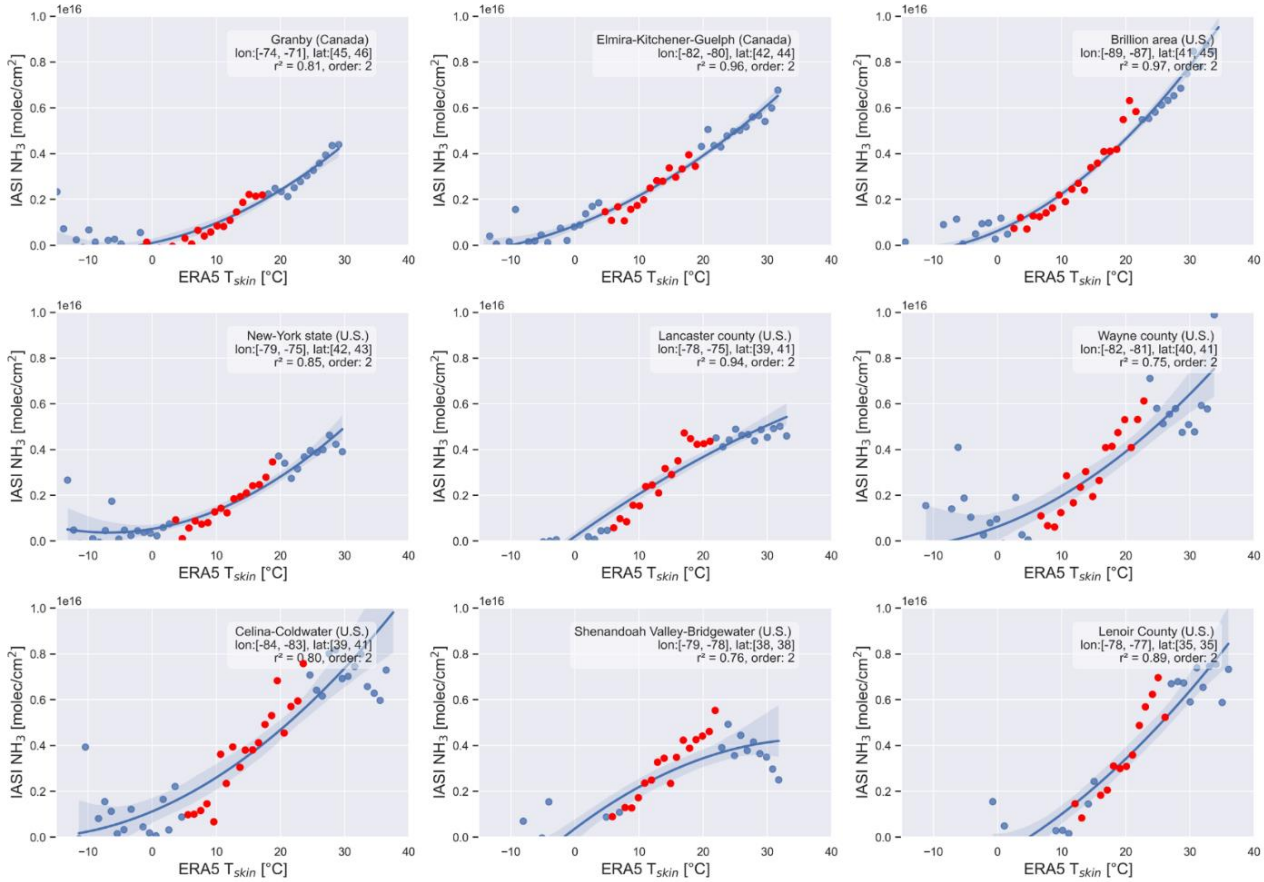


**Figure 3.9.** Same as Figure 3.8 but for regions in North America.

While looking at these plots we notice a “bump” in the curve between 10 and 25 °C of temperature bin approximately. The  $\text{NH}_3$  detected in this range, and indicated as red dots, are found to be mostly measured during the fall and spring growing seasons (up to 80 % of the total measurements per bin). Therefore, they can indicate the fertilizer application period seen from space. For instance, over the Po Valley in Italy (Figure 3.7), 36 % of these measurements (detected in the bins 10–25°C) correspond to the spring season (March–April–May) whereas 35 % correspond to the fall season. This bump was detected to a lower extent in agricultural regions in NA (Figure 3.9). Over the agricultural regions in the southern North America (Mexico City) domain, the bumps are clear in the regions A to D (Figure 3.10). When the seasonal temperatures do not fluctuate during the fertilizer application, any increase in atmospheric  $\text{NH}_3$  is due to the sudden addition of nitrogen fertilizers in the soil. In Mexico, the regions E to M show that the highest  $\text{NH}_3$  concentrations were observed as the temperature increased during the growing



seasons (Figure 3.10 and Figure 3.11). A possible explanation to the resemblance among the regions A to D, is that they share similar climate properties (Steppe<sup>24</sup> and Desert) unlike the rest of the sub-regions in the same domain (tropical/subtropical). Since the temperatures in EU and sNA domains are higher (Figure 3, right panels in Viatte et al., (2022)) in spring and fall seasons (fertilizer application period) than those in NA, this bump is clearer in the latter. In Europe, we can clearly see the bumps too (Figure 3.8) as they are clearer than those of sNA, possibly related to the fact that in autumn in EU precipitation is lower than those in sNA, leading to lower NH<sub>3</sub> loss through wet deposition. In some regions in sNA (e.g. N, O, P and R), high temperatures are seen during the growing seasons (Figure 3.11). Although region O, namely Cosoleacaque, contains a fertilizer industry, the latter is surrounded by agricultural lands.

---

<sup>24</sup> Steppe climates are known to be dry (semi-arid or arid), they receive an average of 25 cm of rainfall per year.

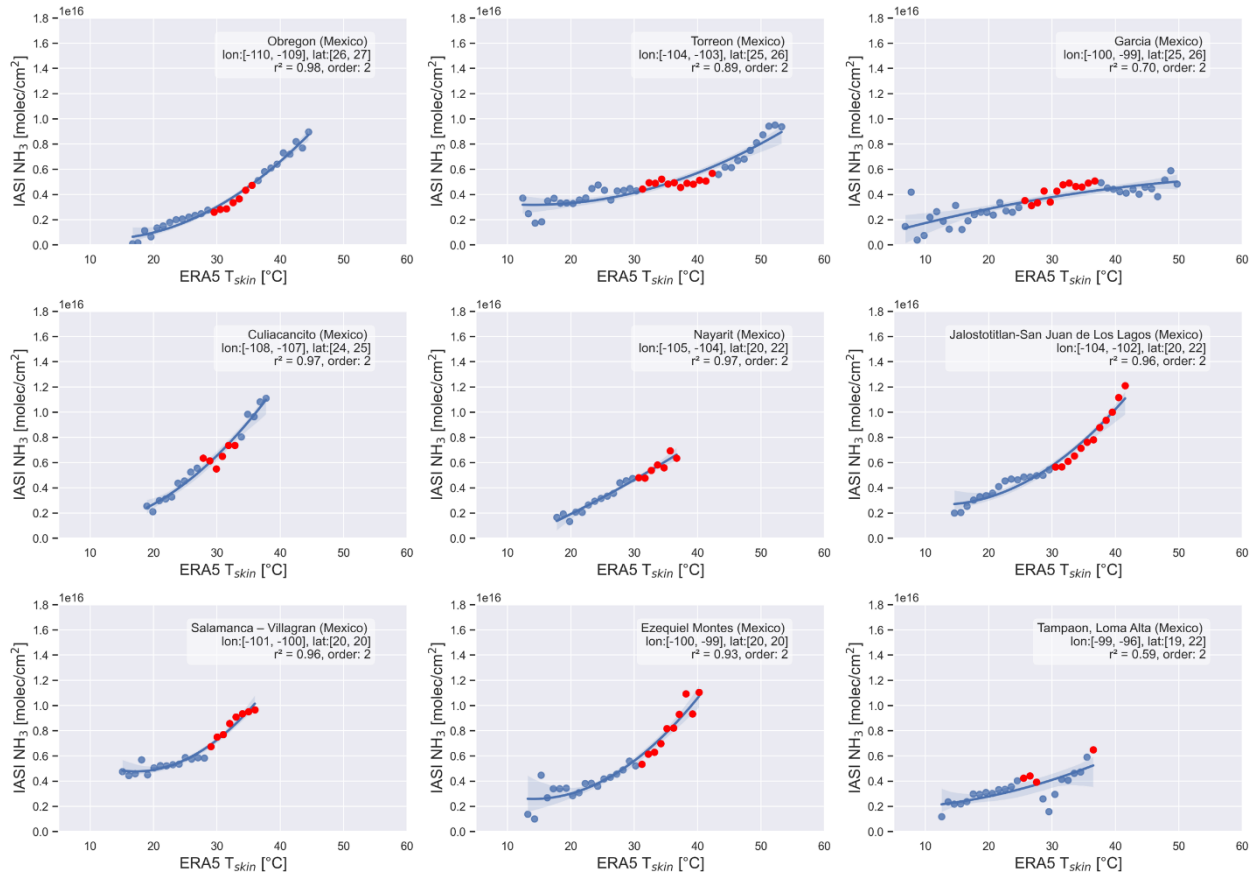


**Figure 3.10.** Same as Figure 3.8 but for regions A to I (left to right, top to bottom) in the southern North America domain.



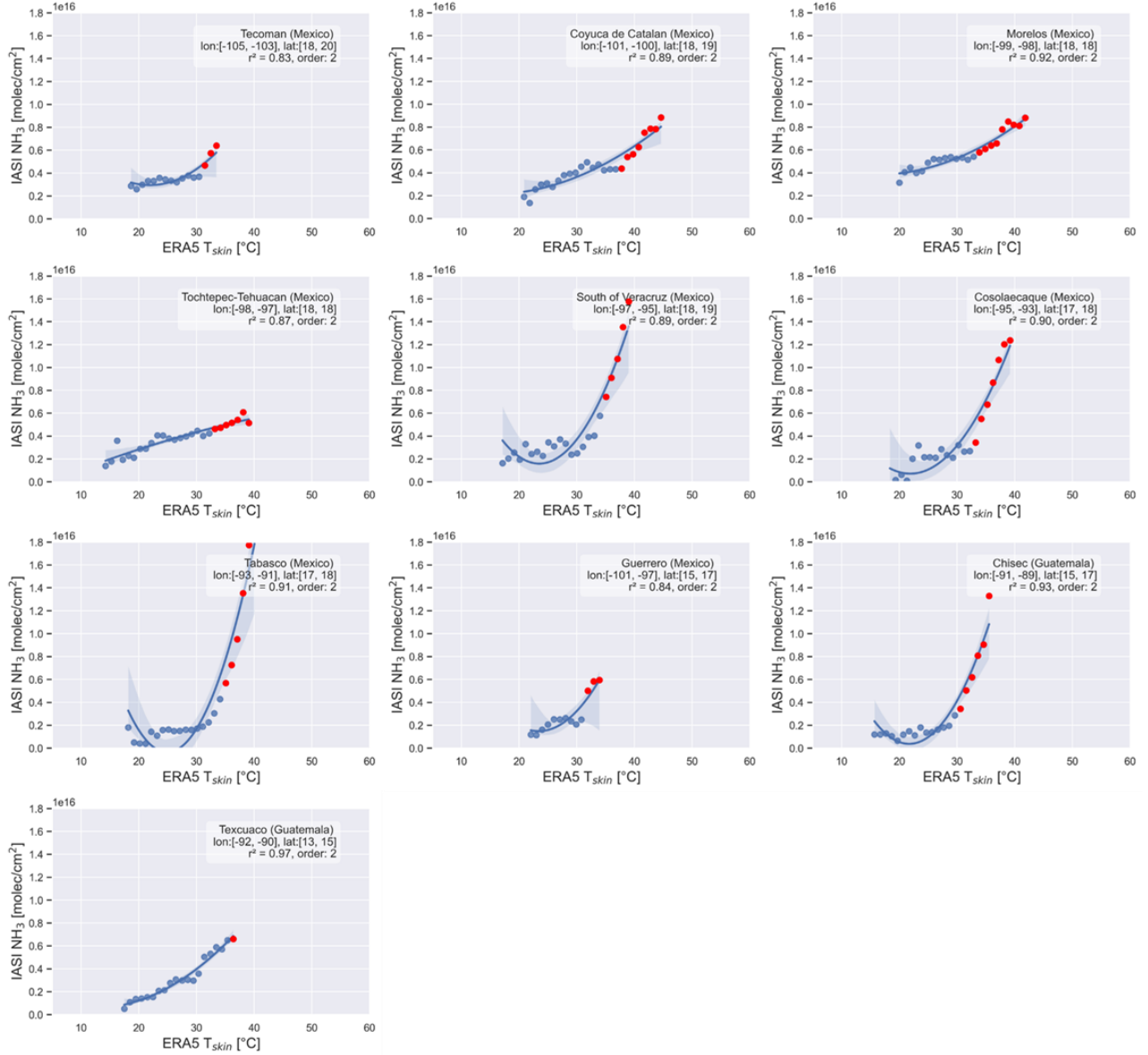


**Figure 3.11.** Same as Figure 3.8 but for regions J to S (left to right, top to bottom) in the southern North America domain.

In order to see the change in atmospheric ammonia in each domain separately, I plot in Figure 3.12  $\text{NH}_3$  total columns averaged per bins of temperature for all the regions in Europe (left panel), North America (middle panel), and southern North America (right panel). We notice that, overall, in Europe we observe the highest correlation between  $T_{\text{skin}}$  and ammonia columns with an  $r^2 = 85\%$ . North America follows right away with an  $r^2 = 80\%$ , and only southern North

America shows a low correlation of  $r^2 = 45\%$ . In sNA, the climate is relatively warm all year long, this can explain the lower correlation observed as compared to the two other domains.

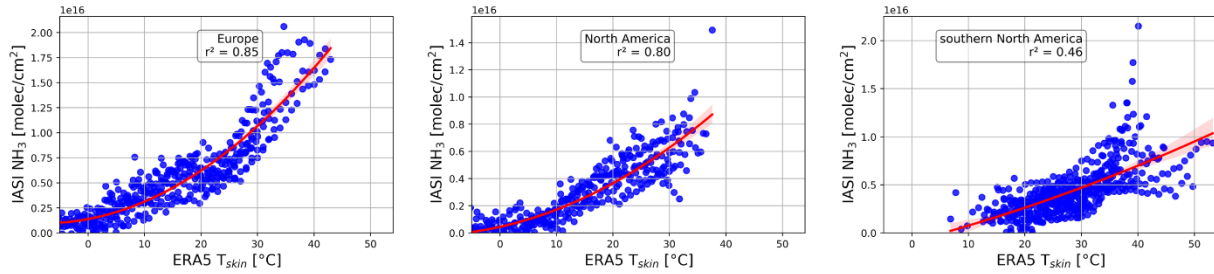


**Figure 3.12.** Evolution of NH<sub>3</sub> with respect to T skin from ERA5 in the three study domains. The figure is done by averaging IASI NH<sub>3</sub> total columns per bins of T skin with an interval of 1°C. Blue dots: yearly IASI NH<sub>3</sub> total columns (molecules/cm<sup>2</sup>) averaged per bins of T skin [°C]. The regions considered here are the regions presented in Figure 4.1 in Europe (left panel), North America (middle panel), and southern North America (right panel). The red line is a polynomial fit of second order, and the relevant  $r^2$  are shown on each panel. Note that I do not consider bins that contain less than 5% of the maximum number of measurements per bin; hence, the averages with (relatively) not enough measurements per bins are excluded.

### 3.2.2 The effect of air temperature on NH<sub>3</sub> total columns

Air and surface temperature rise simultaneously, however the land surface (T skin) heats up faster (and more) than the atmosphere. Land use also affects T skin, for instance in agricultural lands, T skin reduces due to irrigation (Safieddine et al., 2022). In Figure 3.13 I show the correlation between ammonia columns and skin (left) and air (right) temperature changes, in the European domain discussed previously (Section 3.2.1). The colored dots are considered bins containing a relatively high (reliable) number of measurements (at least 150,000 for the whole region), therefore the  $r^2$  calculated only considers these measurements. The empty dots are bins containing less than 150,000 NH<sub>3</sub> measurements per bin. While NH<sub>3</sub> looks like it is increasing exponentially, the first part of the curve (with the high-count bins) is rather increasing linearly, with a coefficient of determination  $R^2 = 87\%$  and  $94\%$  for T skin and air temperature respectively. Both  $R^2$  are very close, and the relationship is considered the same. The only difference can be due to the effect of irrigation in reducing T skin, as compared to T air.

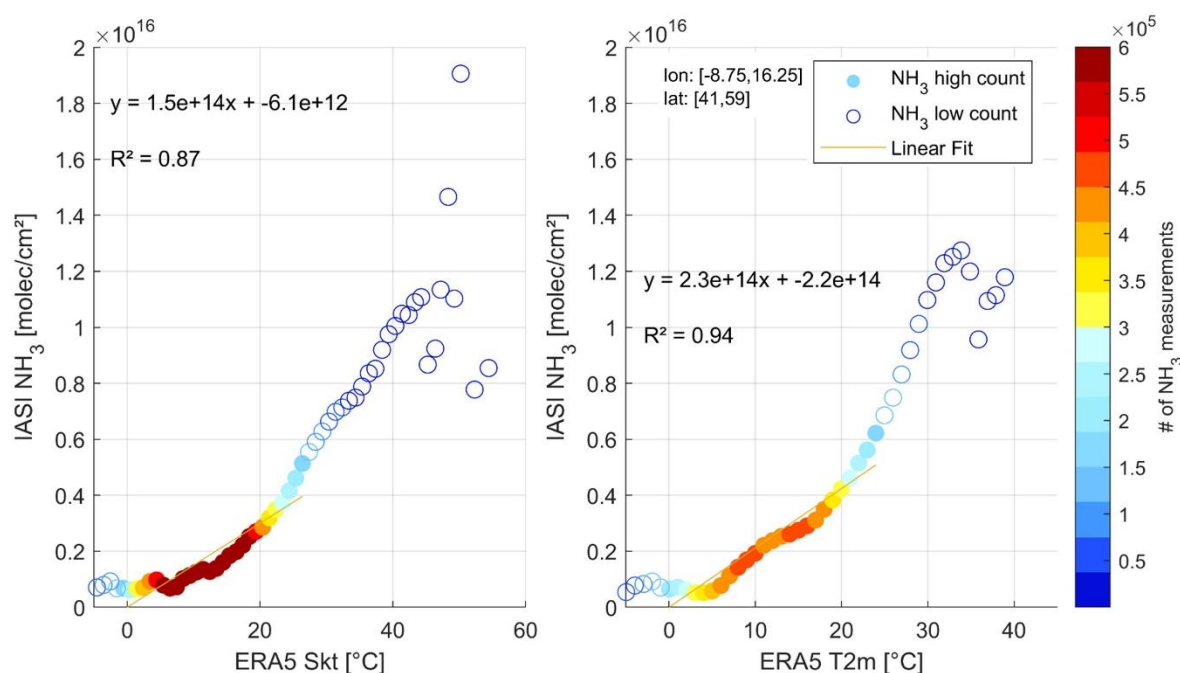


**Figure 3.13.** IASI  $\text{NH}_3$  total columns averaged per bins of skin temperature (left), and air temperature at 2m height (right), with a  $1^\circ\text{C}$  interval between each two consecutive bins. The region considered is Europe (lon:  $[-8.75, 16.25]$ , lat:  $[41, 59]$ ), and the period is  $[2008 - 2018]$ .

### 3.2.3 The effect of relative humidity on $\text{NH}_3$ total columns

The effect of relative humidity on  $\text{NH}_3$  concentrations in each of the study domains is shown in Figure 3.14. The highest coefficient of determination we observe is in Europe, and it accounts to  $r^2 = 0.82$  (negative correlation). A study by Reynolds & Wolf (1987) concluded that the relative humidity of the air does not play a major role in  $\text{NH}_3$  volatilization unless the soil is dry. Other studies showed the same (Van Hove et al., 1989, 1988). We saw in Section 3.1.4 that a RH of 70 % was not enough to compensate for the dryness of the soil. In addition to this, increasing RH eventually increases the deposition of  $\text{NH}_3$  gas to land and vegetative surfaces as we saw in Section 3.1.4. In fact, the soil is drier in most Europe than both of the other domains, with North America being the most humid area. This can explain why we see a good correlation in Europe and lower one in North America. In southern North America, however, throughout the year we observe high temperatures and high humidity, which can explain the low correlation factor  $r^2 = 0.30$  (Figure 3.14).

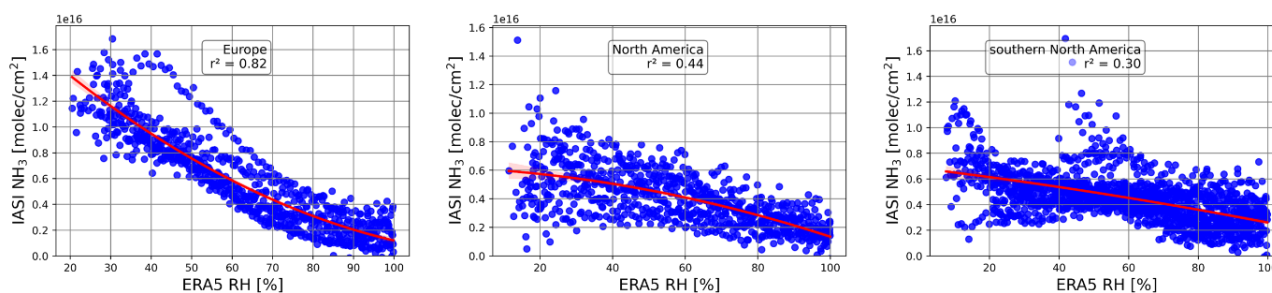


**Figure 3.14.** Same as Figure 4.7 but for NH<sub>3</sub> by averaging IASI NH<sub>3</sub> total columns per bins of RH with an interval of 1%.

Despite the differences in the correlation values, we can still see a decline in ammonia as the relative humidity of the air increases. The high values of NH<sub>3</sub> seen at low RH are dependent of the season. We looked at the times during which the NH<sub>3</sub> concentrations were detected, and we summarize them below:

- **Low RH = 0 – 40%:** Most of the NH<sub>3</sub> detected in all regions are during the spring season, which explains the high values obtained. The high values of NH<sub>3</sub> are highly correlated to fertilizers application. Less deposition will occur when the RH is low, hence increasing the residence time<sup>25</sup> of NH<sub>3</sub> in the atmosphere.
- **Medium RH = 40 – 60%:** The NH<sub>3</sub> detected are during summer and spring. In summer, the emissions of ammonia due to fertilizer application are lower, however, the elevated temperatures will increase NH<sub>3</sub> volatilization from soil and crops. The decline in NH<sub>3</sub> concentrations is steeper ( $R^2 = 0.80$ ) in Europe (left), than in NA (middle) and sNA (right). This can be due to drier soil in parts of Europe, compared with the two other domains considered here.
- **Medium – high RH = 60 – 85%:** The NH<sub>3</sub> is decreasing as RH increases and as the time approaches winter (when RH is highest and the wet deposition of NH<sub>3</sub> increases). In sNA, however, these ammonia measurements correspond to the spring season mostly.
- **High RH = 85 – 100%:** Most of NH<sub>3</sub> detected are during winter in sNA and Europe, and evenly distributed throughout the year in North America, so even if there are NH<sub>3</sub> from fertilizers application, these are deposited quickly due to high RH. The low NH<sub>3</sub> observed

<sup>25</sup> Residence time is the lifetime of a species in the atmosphere before it is lost to deposition or chemical transformation.

in EU and NA are a combination of two main reasons: (1) Less intense growing season (or outside the growing season), and (2) rainy weather (higher precipitations) and RH, therefore more deposition.

### 3.3 Other regions and climate zones around the world

While agriculture is the main source of ammonia (Chapter 1), some industrial facilities release  $\text{NH}_3$  during the production process of some mineral products such as coking industry, and soda ash (Van Damme et al., 2018). While in the previous section I analyze 3 large source regions for the sake of the work done by Viatte et al. (2022), I show here an extension of this work to other regions in the world corresponding to different sources shown on Figure 3.16.

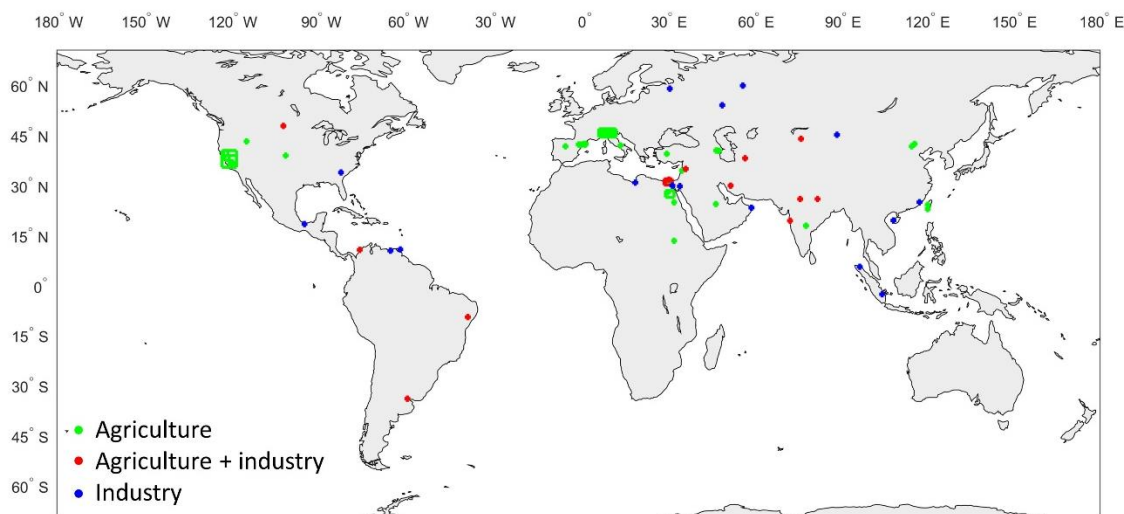


**Figure 3.15.**  $\text{NH}_3$  Source regions around the world. In green are agricultural regions, in red are industries surrounded by agricultural areas, and in blue are industrial hotspots of ammonia.

To choose source regions I refer to the IASI *Overlay* website (<https://squares.ulb.be/NH3-IASI.html>) where  $\text{NH}_3$  hotspots of different source types are displayed. Indeed, not all the regions I consider are identified by Van Damme et al. (2018) as hotspots, but are rather agricultural lands (isolated for instance), and are therefore interesting to study. In Appendix A I summarize in a table the regions names, their coordinates (longitudes and latitudes limits), the dominating climate, the country and main source of  $\text{NH}_3$ . To assign a climate zone, I refer to the *Köppen climate zones* (Beck et al., 2018). Despite the differences in climate, in all the agricultural regions I consider and show in Figure 3.15, the main growing season is during spring (MAM), except for

regions in Lebanon (Baalbeck), Saudi Arabia (Al Kharj), Azerbaijan, and Sudan. For these countries the growing season starts in winter (USDA, 2022b).

In this section I look into different climate zones. These are:

- Steppe climate zone: typical of cold arid regions (e.g. Azerbaijan).
- Humid continental climate: characterized by a hot summer and they lack a dry season (e.g. the agricultural region Erdao Canal Zhangbei in China).
- Desert climates, like in Egypt.
- The Mediterranean climate: dry in general, characterized by hot summers like in Spain and Southern Italy, and warm summers in Portugal.
- Marine west coast climates which are characterized by two main seasons, summer and winter. They do not witness temperature extremes.
- Savana/Monsoon climates have hot or warm summers, with a dry winter.
- Tropical rainforest which are characterized by heavy precipitation throughout the year and warm climates, they are known to receive the most rain among all other biomes.

### 3.3.1 Precipitation and climate zones

In Figure 3.16, I show the relationship between the  $\text{NH}_3$  volatilization from superficial urea application, with the rain volume (mm) 5 days after the fertilization. This study showed that the greatest  $\text{NH}_3$  losses occurred during dry years [2004 – 2007] with a loss that reached up to 25.4 % of the total N applied. The N losses volatilization decreased exponentially as the amount of rainfall increased right after the fertilization (Fontoura and Bayer, 2010).

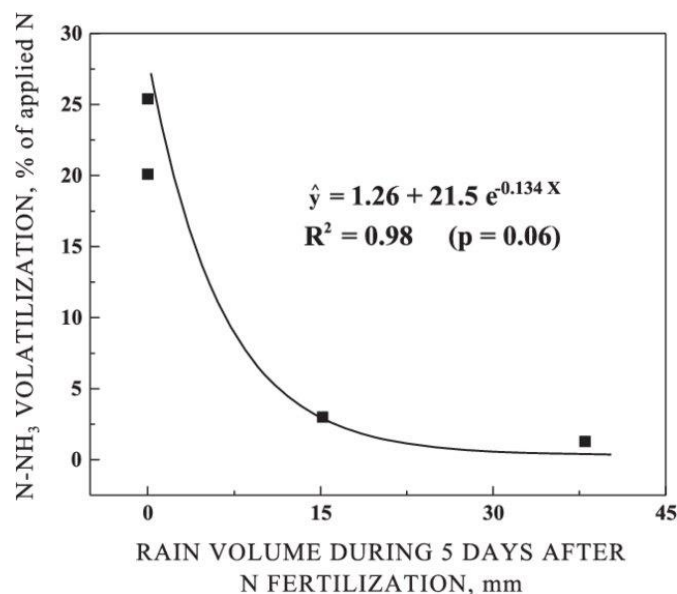


**Figure 3.16.** The relationship between the rainfall volume during the five days following urea application on the soil surface and the cumulative ammonia volatilization in the 20-day period after N application ( $150 \text{ kg ha}^{-1}$ ) in a no-till corn. Each data point refers to a harvest year. Figure from Fontoura and Bayer (2010).

Figure 3.17 shows the yearly  $\text{NH}_3$  total columns (orange line), and the cumulative rainfall during the corresponding year (blue bars), in four different regions, all characterized by a Mediterranean climate. The dashed lines are the linear fit for the  $\text{NH}_3$  total columns (orange dashed line), and the total rainfall (blue dashed line). All regions of Figure 3.17 show a positive trend of  $\text{NH}_3$  except for Canello e Arnone in Italy, it is in fact where we observe positive trends in rainfall during the whole time period [2008 – 2018]. The Mediterranean climate is relatively humid where the rainfall can reach up to  $600 \text{ mm yr}^{-1}$  such as in Italy (Figure 3.17, first panel). In humid conditions, the rainfall and the high RH increase the deposition of  $\text{NH}_3$  to the surface. If we look at the inter-annual variability, we notice that the lowest  $\text{NH}_3$  concentrations are observed during years of relatively high rainfall (Figure 3.17). For instance, in Valladolid in Spain, 2010 to

2014  $\text{NH}_3$  concentration are close to  $3.5 \times 10^{15}$  molecules  $\text{cm}^{-2}$ , the increase observed after 2015 is mostly due to the increase in T skin (next Section). In Bekaa Valley in Lebanon, the lowest  $\text{NH}_3$  concentration is seen during 2011 when the amount of rainfall was the highest recorded during the period of study ( $\sim 28 \text{ mm yr}^{-1}$ ). In Turkey, the positive increase of  $\text{NH}_3$  is most apparent than the rest of the regions, this can also be related to temperature increase.

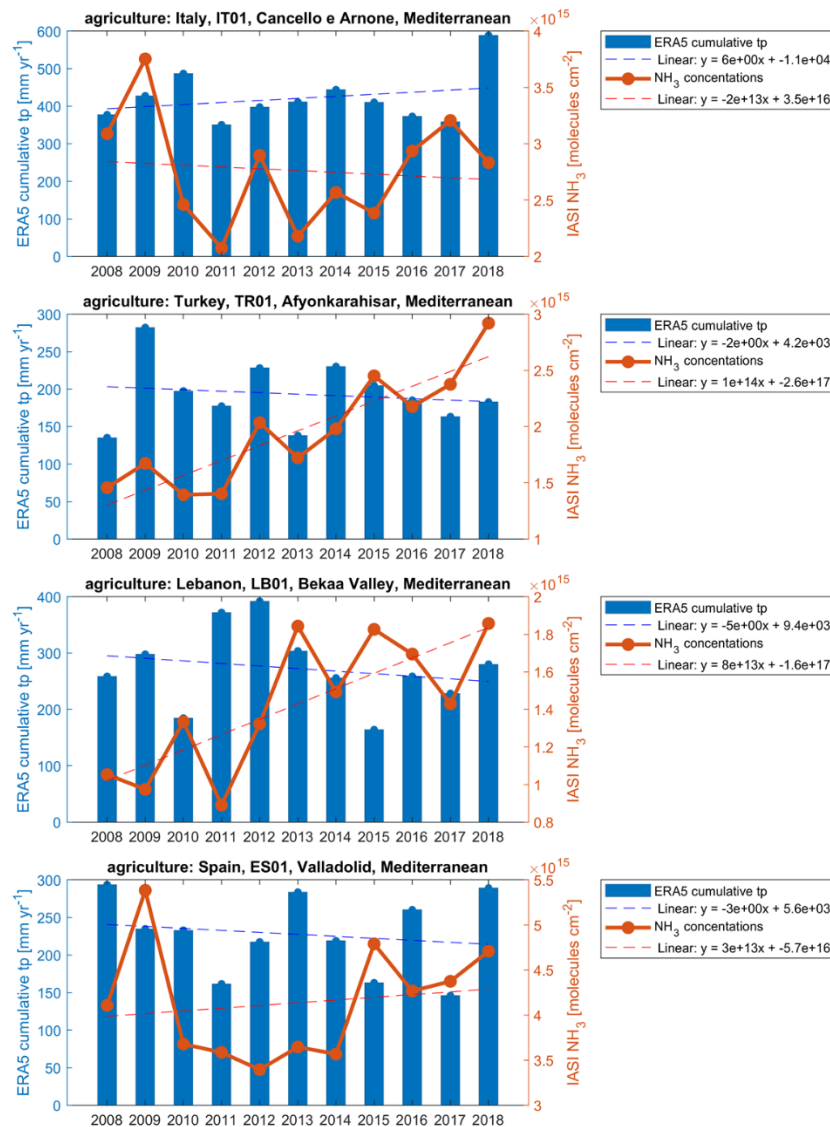


**Figure 3.17.** Yearly  $\text{NH}_3$  and precipitation for the period [2008 – 2018] for four agricultural regions in a Mediterranean climate. The total columns of ammonia (orange line), and the cumulative rainfall during the corresponding year (blue bars), in four different agricultural regions, all characterized by a Mediterranean climate. The dashed lines are the linear fit for the  $\text{NH}_3$  total columns (orange dashed line), and the total rainfall (blue dashed line). The legend contains the linear fit equation, where we can see whether the slope is positive or negative.



In extreme dry climates, such as in Egypt for example, there is very little rainfall (1 – 30 mm yr<sup>-1</sup>). Both the NH<sub>3</sub> and precipitation trends are seen to be positive during the whole period (Figure 3.18). In the Nile Basin, for instance, there seems to be no correlation, since the amount of rainfall is very scarce and will not contribute vastly to the NH<sub>3</sub> deposition. In the Nile Delta (upper panel, Figure 3.18), higher rainfall is seen to reduce atmospheric NH<sub>3</sub>. Finally, what's common among all regions is that interannually, enough rainfall per year can reduce the NH<sub>3</sub> concentration. However, since rainfall is not the only factor playing a role here in NH<sub>3</sub> volatilization, it is recommended to look at temperature changes interannually as well. I do this in the next section. In regions where it is extremely humid all year long (up to 1500 mm yr<sup>-1</sup>), the NH<sub>3</sub> concentrations are seen to be weakly correlated to the amount of yearly rainfall like in Taiwan (Figure 3.19). Figures for the rest of the agricultural regions, like Figure 3.17 and Figure 3.18, are added in Appendix B.

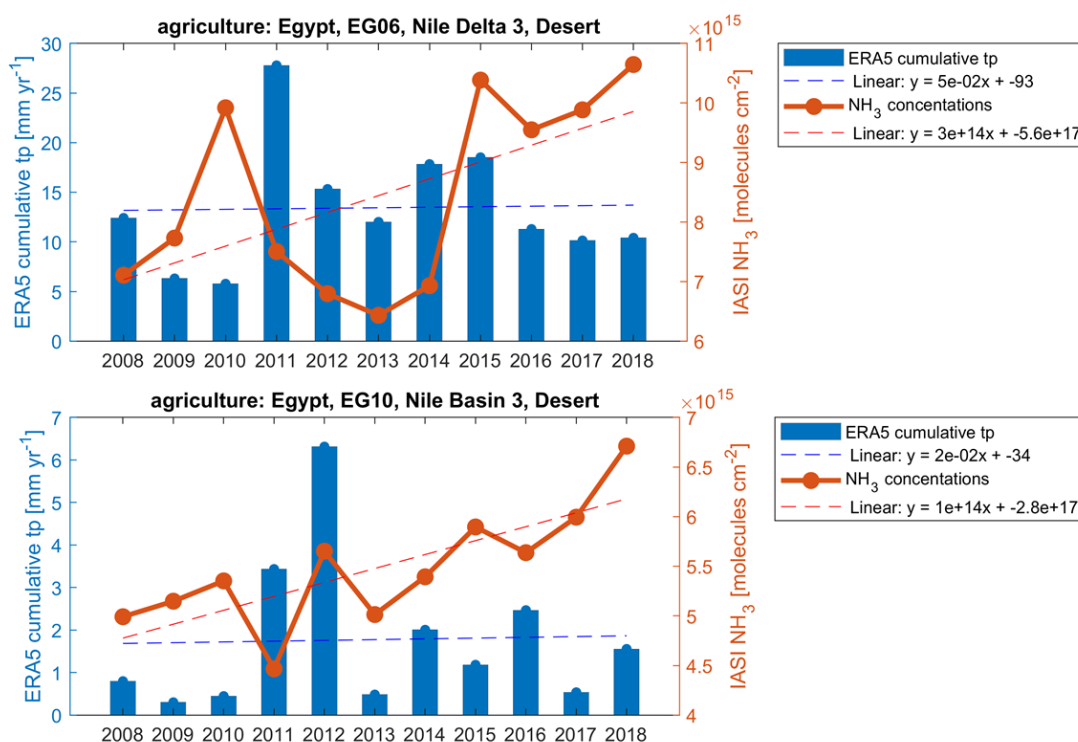


**Figure 3.18.** Same as Figure 3.17 for two agricultural regions in a dry climate (desert), the Nile Delta (upper panel), and the Nile Basin (lower panel).

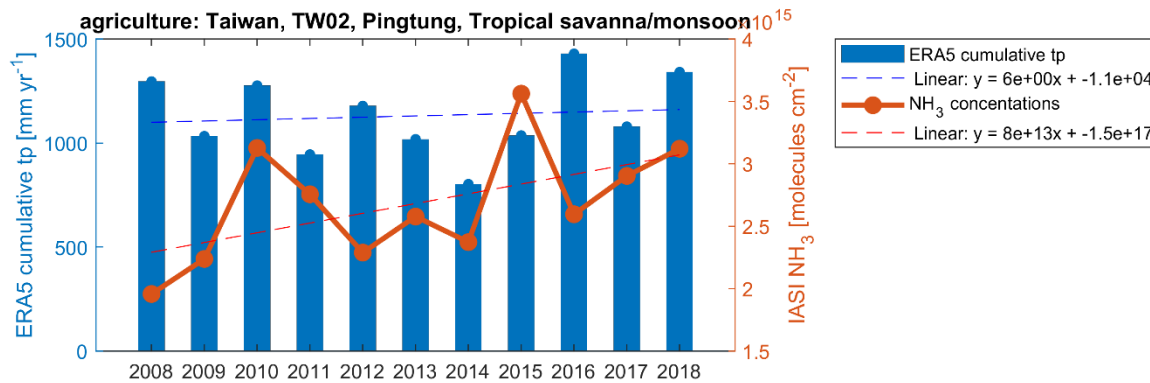


**Figure 3.19.** Same as Figure 3.17 and Figure 3.18 but for an agricultural region in a humid climate (tropical savanna/monsoon), in Taiwan.

### 3.3.2 *T skin and climate zones*

In Figure 3.20 I show below the coefficient of determination ( $R^2$ ) of  $\text{NH}_3$  with  $T_{\text{skin}}$  (from ERA5). The study period is [2008 – 2018], and the regions are agricultural (Appendix A). The  $R^2$  values are calculated from the linear fitting of  $\text{NH}_3$  averaged per bins of total precipitation throughout the whole year (all seasons), with  $1^\circ\text{C}$  interval between consecutive bins.

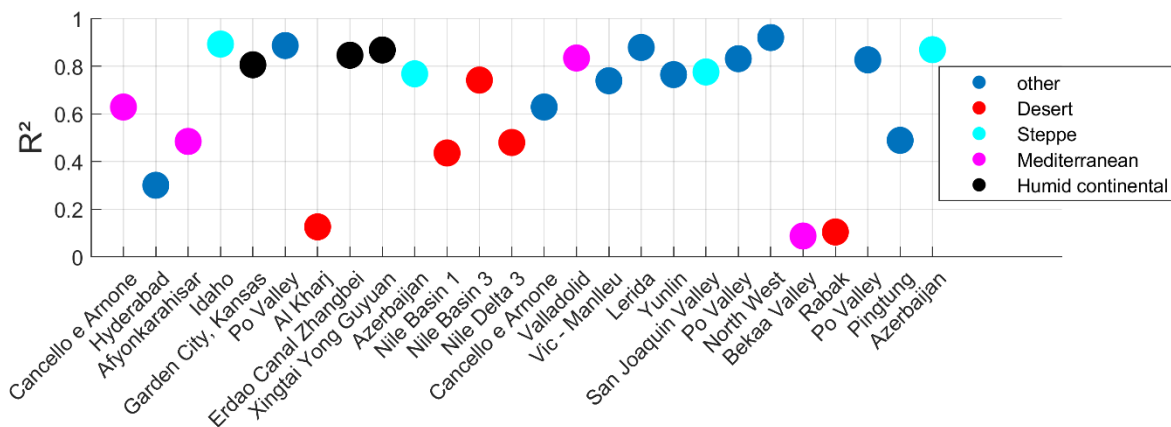


**Figure 3.20.** The coefficient of determination ( $R^2$ ) extracted from a linear regression of IASI- $\text{NH}_3$  and ERA5  $T_{\text{skin}}$ .  $\text{NH}_3$  total columns are averaged per bins of total precipitation with an interval of  $1^\circ\text{C}$  between consecutive bins. These plots are shown in Appendix B.

Regardless of the climate zone to which the region belongs, higher temperatures will always increase the volatilization of  $\text{NH}_3$ . To a lesser extent in warm climate zones (Mediterranean, and desert) with  $R^2$  falling within 0.4 and 0.6 approximately.

While for the other climate zones, we see a high correlation of  $R^2$  above 0.6 and can reach 0.92 (North West Italy). The only regions that show no correlation to T skin are: Al Kharj (Saudi Arabia), Bekaa Valley (Lebanon), and Rabak (Sudan). This lack of correlation is explained by the following factors: high temperatures all-year-long (Saudi Arabia), and absence of growing season during spring and summer when the temperatures are high.

It is clear that the positive correlation between T skin and  $\text{NH}_3$  total columns. In Figure 3.21 I show this example along with others in Appendix C. We can see how positive T skin anomalies increasing by up to  $+5^\circ\text{C}$  in 2015, caused an increase by  $\sim 5 \times 10^{15}$  molecules  $\text{cm}^{-2}$  in monthly ammonia concentrations. This same pattern is observed in all agricultural regions, with the T skin increasing starting year 2015.

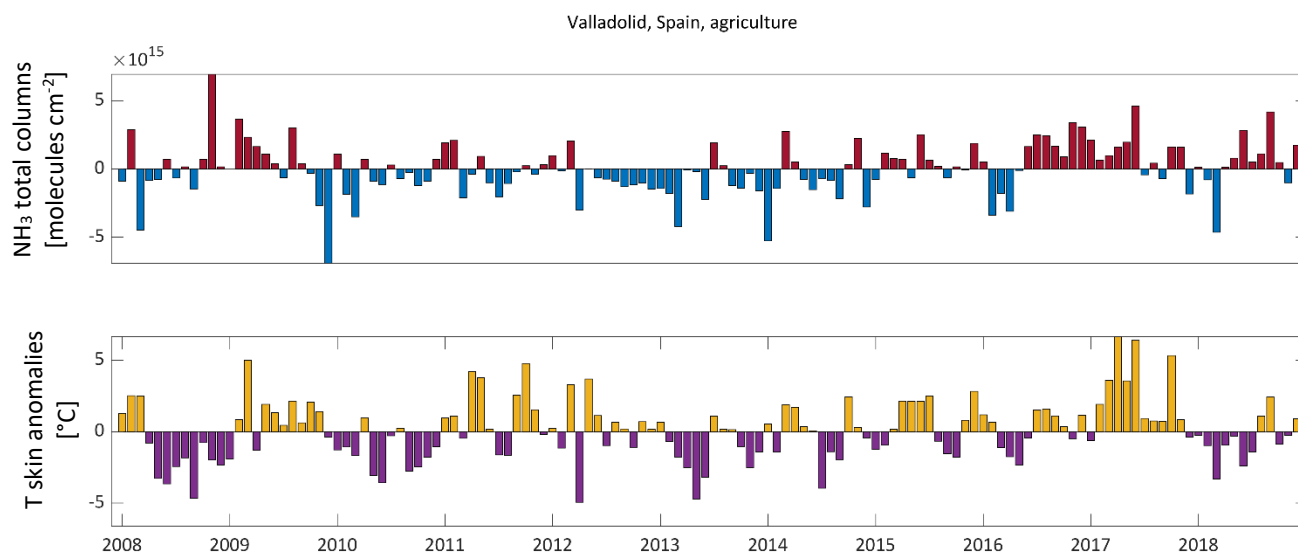


**Figure 3.21. Monthly anomalies of ammonia total columns (top) and T skin (bottom), as compared to the [2008 – 2018] average. The corresponding units are molecules  $\text{cm}^{-2}$  for ammonia, and  $^\circ\text{C}$  for T skin. The regions is Valladolid, an agricultural region in Spain (refer to Appendix A for coordinates).**

In industrial regions, however, positive T skin anomalies do not necessarily induce an increase in atmospheric ammonia. Take as an example the Beech Island region in the U.S., where an  $\text{NH}_3$ -emitting industry resides (Figure 3.22). By the end of year 2009, and beginning 2010, T skin shows negative anomalies in Beech Island, these were rather met with positive anomalies of ammonia. It is unclear why exactly we see this negative correlation, in early 2010 and 2018. The concentrations of ammonia in an industrial region are highly correlated to the industrial activity (Chapter 5, and (Abeed et al., 2021)) as well as the deposition of ammonium salts around the facility. In short, for

a ten-year period of study [2008 – 2018], T skin increase induced more volatilization of soil ammonia from soils (and ammonium salts on PM), indicating more N-loss and therefore less efficient fertilizer use in agricultural lands.

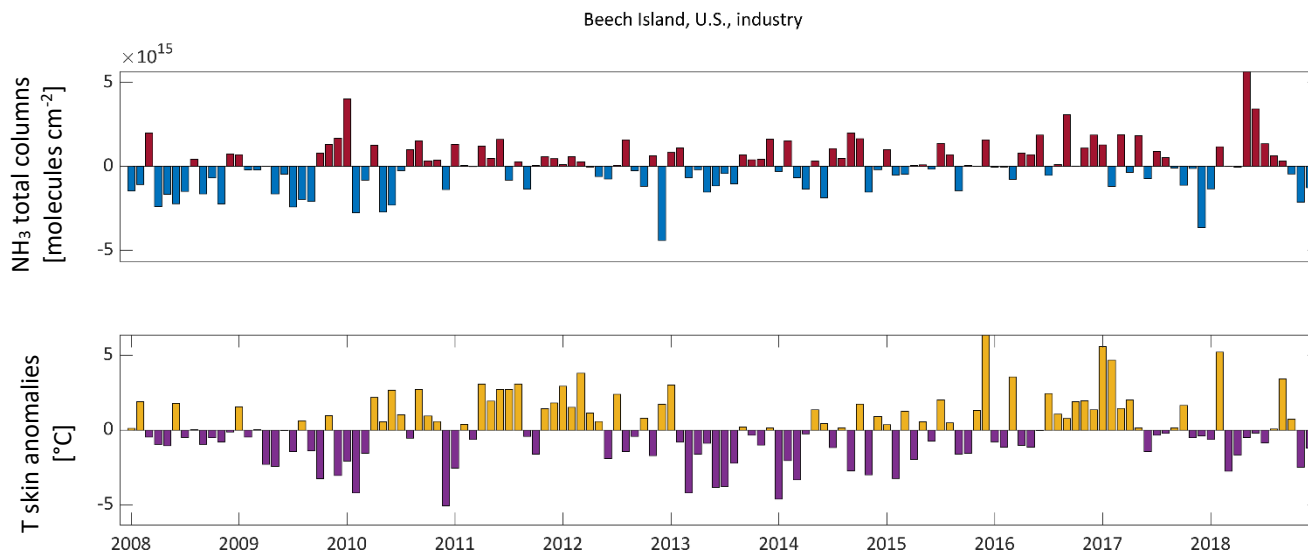


**Figure 3.22.** Same as Figure 4.10, but for an industrial region in the U.S. (Beech Island).

### 3.3.3 Wind speed

Transport by air masses is one of the sinks of atmospheric ammonia. Higher wind speed is expected to transport  $\text{NH}_3$  away from the fields, either as gas ( $\text{NH}_3$ ) or on PM ( $\text{NH}_4^+$ ). In Figure 3.23, I plot the  $\text{NH}_3$  total columns averaged per bins of wind speed, in  $1 \text{ m s}^{-1}$  spaced wind bins. The region I show here is an agricultural land in China, a region previously defined as an ammonia point-source in Clarisse et al. (2019a). We notice that atmospheric ammonia starts to increase once the wind speed exceeds  $10 \text{ m s}^{-1}$ . This can be associated with transport from neighboring sites.

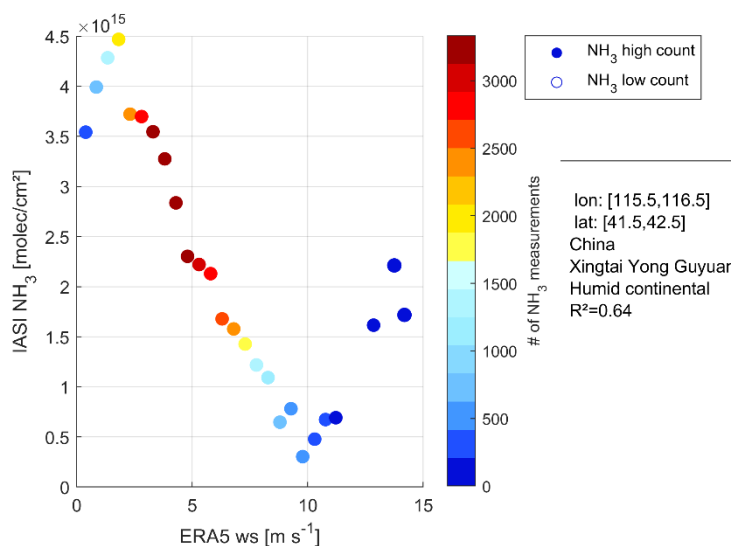


**Figure 3.23.** IASI  $\text{NH}_3$  total columns averaged per bins of wind speed calculated from  $u$  and  $v$  wind components at 10m distance (ERA5), with a  $1 \text{ m s}^{-1}$  interval between each two consecutive bins. The region considered is a Chinese agricultural land (lon: [115.5, 116.5], lat: [41.5, 59.5]), and the period is [2008 – 2018].

### 3.4 Conclusion

In this chapter I showed that it is possible to detect the fertilizers application period by looking the ammonia –  $T_{\text{skin}}$  relationship. This can be used as a proxy for measuring the ammonia volatilization from fertilizers application.  $T_{\text{skin}}$  and air temperature do increase the amount of atmospheric ammonia, with the correlation parameter  $R^2$  slightly higher (0.94) than the one obtained from the relationship of  $\text{NH}_3$  with  $T_{\text{skin}}$  (0.87). No matter the climate zone,  $T_{\text{skin}}$  is always highly correlated to atmospheric  $\text{NH}_3$  ( $R^2 > 0.6$ ), except in regions with all-year-long warm climates and the winter cultivation as the main growing season (e.g. Saudi Arabia). The effect of RH is not homogeneous, in dry conditions atmospheric  $\text{NH}_3$  reduces as RH decreases (0–40%). Higher correlations are observed in Europe ( $r^2 = 0.82$ ), as compared to North America ( $r^2 = 0.44$ ) and southern North America ( $r^2 = 0.33$ ), due to a drier climate in general. Rainfall is seen to be inversely proportional to the concentration of atmospheric ammonia, in regions with medium rainfall, such as Mediterranean climates like regions in Italy, Spain and Lebanon. Humid climates are not directly correlated to rainfall, since the rain occurs all year long, such as regions with  $1500 \text{ mm yr}^{-1}$  cumulative rainfall. In dry climates, such as the Nile region, rainfall is rather observed to increase the volatilization of  $\text{NH}_3$ . This can be a concern if due to climate change rain patterns

change in desert climates. Finally, lower wind speeds are associated with higher  $\text{NH}_3$  concentrations, with a strong correlation over agricultural areas (e.g.  $r^2 = 0.64$  in Xingtai Yong Guyuan in China). However, ammonia starts to increase once the wind speed exceeds  $10 \text{ m s}^{-1}$ , likely indicating transport from neighboring sites.

## Chapter 4

### *4 Ammonia volatilization from agricultural soils in Europe*

Ammonia volatilization is enhanced by higher temperatures, and the fluctuations of other meteorological parameters (Chapter 3). I use simulation data for the month of March during 2011, because Europe witnessed isolated and connected ammonia and particulate matter (PM<sub>2.5</sub>) pollution episodes (Viatte et al., 2022). The second reason is that the fertilizers spreading activities start in March in Europe, as shown by the FAO NDVI (e.g. start of the growing season in Ireland (FAO Earth Observation, 2022)). Combined with the increase in air and land temperatures and decreased of precipitations, ammonia concentrations are expected to increase during March. In this chapter, I study more in details the surface – atmosphere ammonia exchange using IASI satellite data, ERA5 reanalysis, and simulation data from the chemistry transport model GEOS-Chem. By applying a simplified bi-directional exchange model, I plot the first map of ammonia emission potential  $\Gamma_{soil}$ , a powerful parameter that can help us understand the exchange between the surface and the atmosphere, and that is usually calculated from direct field measurements. To have a look at the future projections of ammonia, using the simplified model presented in this study, I estimate the ammonia columns by the end of the century [2075 – 2099], using T skin data from the climate model EC-Earth, under two possible future socioeconomic scenarios (SSP2-4.5 and SSP5-8.5).

Part of the results of this chapter are included in a pre-print publication (Abeed et al., 2022) that is currently under review in *Atmospheric Chemistry and Physics Discussions* (ACPD), and added as Section 4.5 in this chapter. I note the reference Abeed et al., 2022 in the legend of the figures included in the publication.

## 4.1 Introduction

Ammonia columns in Europe are associated with agricultural activities, manure and synthetic fertilizers spreading, notably in the Western, Southern, and the Southwestern parts of the continent. With IASI we can see two peaks of ammonia during the year, referring to the two growing seasons in Europe (spring and fall). The summer season starts in spring (March) and can extend till June in some European countries (USDA, 2022b). Figure 4.1 shows the monthly means of ammonia from IASI in Europe, from January till December 2011. It is clear that the ammonia columns start to increase in March, they then peak in April and return to lower levels in May and June. These ammonia emissions were previously identified to induce  $PM_{2.5}$  pollution episodes in spring (Viatte et al., 2022).

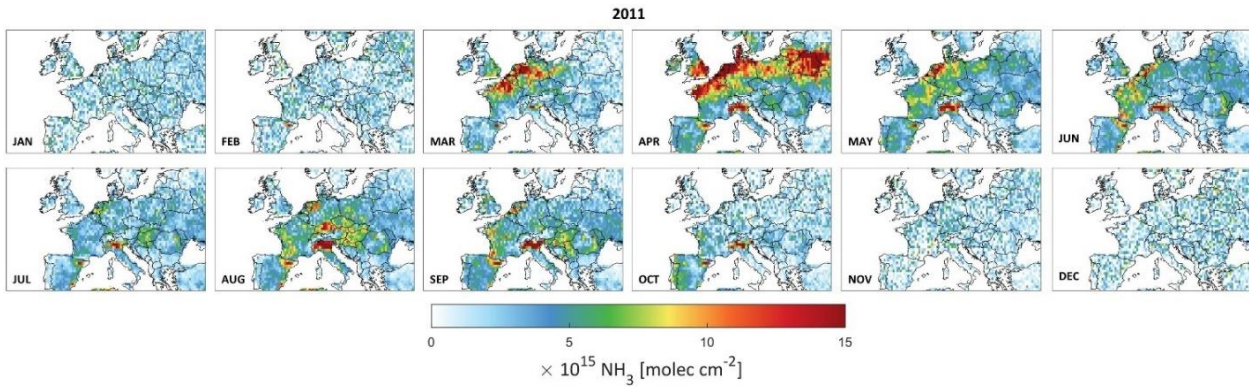


**Figure 4.1. Monthly averages of ammonia in Europe during the year 2011 using IASI NH3-v3R-ERA5 data, on a  $0.5^\circ \times 0.5^\circ$  grid.**

The increase in the application of synthetic fertilizers, and intensification of agricultural practices is believed to be the dominant factor of the global increase in ammonia emissions over the past century (Behera et al., 2013; McDuffie et al., 2020). During the period [2008 – 2018] alone, the increase in ammonia columns in Western and Southern Europe accounted to  $+20.8 \% \text{ yr}^{-1}$  ( $\pm 4.3 \%$ ) (Van Damme et al., 2021). In the Po valley in Northern Italy, for instance, the concentrations of atmospheric ammonia increased continuously from 2015 till 2018 (Figure 4.2).

The top panel in Figure 4.2 shows the monthly anomalies of ammonia for the period [2008 – 2018], calculated relative to the average of the a 10-year average of [2008 – 2018], and the bottom panel shows the corresponding anomalies for T skin. There is a clear correlation between the increase in temperatures and the increase in atmospheric ammonia levels. This relationship was



investigated in Chapter 3. In 2018 for example, higher temperatures and drier weather favored the positive correlations in Western and Southern Europe (Van Damme et al., 2021).

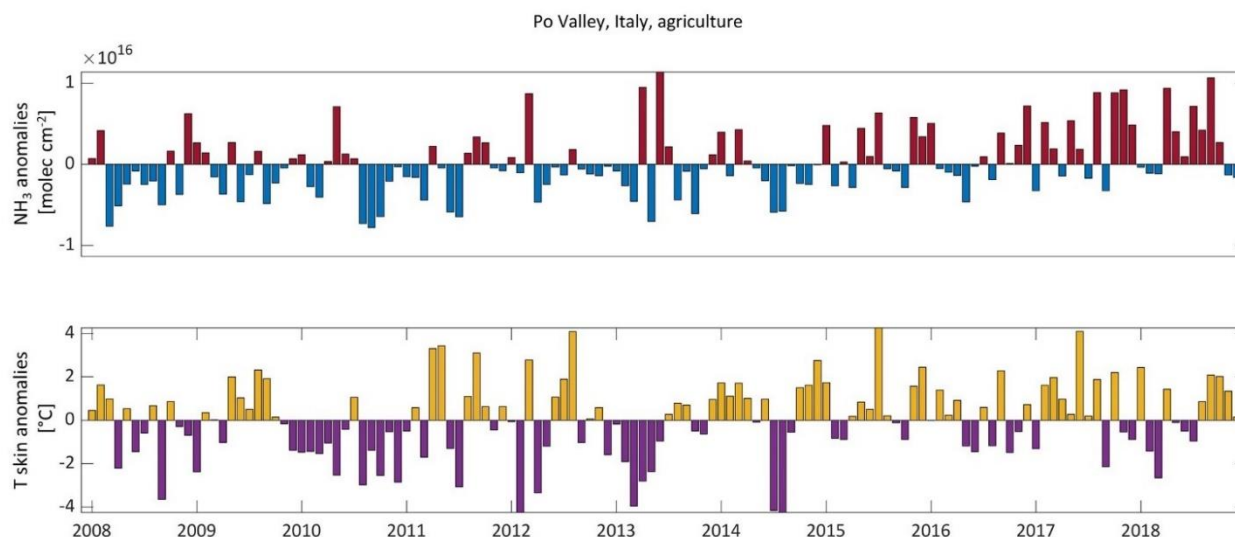


**Figure 4.2. Monthly anomalies of IASI ammonia (top) and ERA5 T skin (bottom), relative to the [2008 – 2018] average, in the Po Valley in Italy [44.7 – 45.7° N; 9 – 11° E].**

In order to meet the needs for a growing population, agricultural practices have intensified during the period [2003 – 2019] (more fertilizer use per surface area), resulting in an increase in the net primary production (NPP) per capita (Potapov et al., 2022), subsequently increasing volatilized ammonia (increase in nitrogen soil content, and cultivated lands). In Europe alone, the area of croplands increased by +9 % from 2003 to 2019, and most of the expansion took place on lands that were abandoned for more than 4 years (Potapov et al., 2022). Between the year 2008 and 2018, the increase in atmospheric ammonia columns accounted to +20.8 % ( $\pm 4.3$  %) in Western and Southern Europe (Van Damme et al., 2021). Therefore, with the increase in croplands area and agricultural activities, climate change will have a significant effect on agricultural practices, with warmer climates enhancing the volatilization of ammonia from soils, especially in intensely fertilized lands (Shen et al., 2020).

## 4.2 *Methods and datasets*

### 4.2.1 *Ammonia emission potential*

The soil emission potential ( $\Gamma_{soil}$ ) has been thoroughly investigated in field and controlled laboratory environments (e.g. David et al., 2009; Flechard et al., 2013; Massad et al., 2010; Mattsson et al., 2008; Nemitz et al., 2000; Wentworth et al., 2014, among others).  $\Gamma_{soil}$  is dimensionless and it can range from 20 (non-fertilized soil in a forest) to the order of  $10^6$  (mixture of slurry in a cropland). It is found to peak right after fertilizers application, due to the increase in ammonium content in the soil (a product of urea hydrolysis), reaching pre-fertilization levels 10 days following the application (Flechard et al., 2010; Massad et al., 2010). Little information exists on regional or global scales to assess the large-scale spatial variability of ammonia emission potentials.

In field studies,  $\Gamma_{soil}$  is calculated by measuring the concentration of ammonium ( $\text{NH}_4^+$ ) and  $\text{H}^+$  ( $10^{-\text{pH}}$ ) in the soil; the ratio between both of these concentrations is  $\Gamma_{soil}$ . In this study, we use IASI satellite data to calculate the ammonia emission potential  $\Gamma_{soil}$ , and to have a regional coverage over Europe. With these, we cannot monitor soil content of ammonium nor its pH. This renders the remote  $\Gamma_{soil}$  calculation challenging, and less straight forward. The full derivation of the equation used to calculate the emission potential is explained in Section 4.2.2. In short, upon its dissolution in the soil water, ammonia follows Henry's law. In steady state conditions between the soil and the near surface, the amount of the ammonia emitted and lost is considered equal. Based on this assumption, the soil emission potential (dimensionless) is calculated through Eq. 4-22 in Section 4.2.2.

$k$  is the soil – atmosphere exchange coefficient or deposition velocity ( $\text{cm s}^{-1}$ ), also known as the mass transfer coefficient (this nomenclature will be used in this study). It is found to be affected by the roughness length of the surface, wind speed, the boundary layer height (Olesen and Sommer, 1993; Van Der Molen et al., 1990), and pH (Lee et al., 2020). It can be explained by a resistance model often used to explain the exchange between the surface and the atmosphere (Wentworth et al., 2014). Different studies provide look up tables values of  $k$  for different land cover types and different seasons based on this resistance model (Aneja et al., 1986; Erisman et al., 1994; Phillips et al., 2004; Roelle and Aneja, 2005; Svensson and Ferm, 1993; Wesely, 1989).

In general, the mass transfer coefficient  $k$  is in the order of  $10^{-3}$  to  $10^{-2}$  m s<sup>-1</sup> in a mixture of soil and manure, and  $10^{-6}$  to  $10^{-5}$  m s<sup>-1</sup> in a mixture of manure alone (Roelle and Aneja, 2005). I discuss and provide more information on  $k$  in Section 4.3.3, and additional details on this calculation in general are provided in the next Section (4.2.2).

#### 4.2.2 Calculation of emission potential $\Gamma_{soil}$

The soil – atmosphere exchange of ammonia is bi-directional, in other words, the soil might either be a source (emission) or a sink (deposition) for ammonia. In the context of agricultural activities, one needs to acknowledge the processes taking place following the application of manure or synthetic fertilizers in order to understand this dynamic. The most vastly used fertilizer types release ammonia and its dissolved form ammonium ( $\text{NH}_4^+$ ) into the soil. Ammonium is a reactive form of nitrogen ( $\text{N}_r$ ), and can be directly uptaken by plants, or transformed into nitrate ( $\text{NO}_3^-$ ) that is equally absorbed through the plants roots (Krupa, 2003).

Prior to its volatilization, ammonia in the soil exists either in the gas phase ( $\text{NH}_3(g)$ ) or in the aqueous/liquid phase ( $\text{NH}_3(aq)$ ), and the equilibrium between both states of ammonia is governed by Henry's law (Eq. 4-8) (Wentworth et al., 2014). I show the computation of the Henry's constant ( $H_{\text{NH}_3}$ ) in Eq. 4-9 (Wichink Kruit, 2010).



$$H_{\text{NH}_3} = \frac{[\text{NH}_3(aq)]}{[\text{NH}_3(g)]} = 5.527 \cdot 10^{-4} \cdot \exp \left[ 4092 \left( \frac{1}{T} - \frac{1}{298.15} \right) \right] \quad 4-9$$

Temperature plays an important role in the equilibrium between the dissolved ( $\text{NH}_3(aq)$ ) and volatilized ammonia ( $\text{NH}_3(g)$ ) in Eq. 4-9. Likewise, the dissolution of ammonia into ammonium in soil water is affected mainly by temperature, but also by soil acidity (pH) (Roelle and Aneja, 2005), this equilibrium is explained by the dissociation constant  $K_{\text{NH}_4^+}$  (Eq. 4-10 to 4-13).



$$K_{NH_4^+} = \frac{[NH_3(aq)][H^+]}{[NH_4^+(aq)]} \quad 4-12$$

$$K_{NH_4^+} = 5.67 \cdot 10^{-10} \exp \left[ -6286 \left( \frac{1}{T} - \frac{1}{298.15} \right) \right] \quad 4-13$$

Once released to the atmosphere, ammonia near the surface exists in the gas phase, hence Henry's law describes the equilibrium between ammonia in the soil (liquid phase), and near the surface (gas phase). This bi-directional exchange between the soil and the atmosphere will continue until the equilibrium is reached, and this occurs when atmospheric ammonia concentration reaches what we call the compensation point  $\chi_{NH_3}$  (the concentration of ammonia at equilibrium).  $\chi_{NH_3}$  is defined as the concentration at which the net  $NH_3$  flux towards the soil is zero (Farquhar et al., 1980), and is expressed in mass per volume ( $kg\ m^{-3}$ ). I can draw a link between the mass density  $\chi_{NH_3}$  and the partial pressure ( $P_{NH_3}$ ) of ammonia near the surface ( $NH_{3(g)}$ ) by applying the ideal gas law ( $PV = nRT$ ), I obtain Eq. 4-14.

$$\chi_{NH_3} = \frac{P_{NH_3} \cdot M_{NH_3}}{R T} \quad 4-14$$

Where  $P_{NH_3}$  is the partial pressure of ammonia near the surface as explained earlier (atm),  $M_{NH_3}$  is the molar mass of ammonia ( $kg\ mol^{-1}$ ),  $R$  is the gas constant ( $0.082\ atm\ L\ mol^{-1}\ K^{-1}$ ), and  $T$  is the temperature in Kelvin.

The partial pressure of ammonia can be equally expressed as a function of the Henry's constant  $H_{NH_3}$  (Eq. 4-9) and the dissociation constant  $K_{NH_4^+}$  (Eq. 4-13) (Wichink Kruit, 2010):

$$P_{NH_3} = \frac{K_{NH_4^+} [NH_4^+]}{H_{NH_3} [H^+]} = \frac{5.67 \cdot 10^{-10} \cdot \exp\left[-6286 \left(\frac{1}{T} - \frac{1}{298.15}\right)\right]}{5.527 \cdot 10^{-4} \cdot \exp\left[4092 \left(\frac{1}{T} - \frac{1}{298.15}\right)\right]} \times \frac{[NH_4^+]}{[H^+]} \quad 4-15$$

From Eq. 4-14 one can see that  $\chi_{NH_3}$  is a function of the partial pressure of ammonia, which in turn is a function of temperature ( $T_{skin}$ ), and the ammonium – pH ratio  $\frac{[NH_4^+]}{[H^+]}$  (also known as the emission potential of ammonia  $\Gamma_{soil}$ ) (Eq. 4-15). If I substitute Eq. 4-15 in 4-14 I get:

$$\chi_{NH_3} = \frac{2.75 \cdot 10^9 \left(\frac{gK}{m^3}\right)}{T_{soil}} \exp\left[\frac{-1.04 \cdot 10^4}{T_{soil}}\right] \Gamma_{NH_3} \quad 4-16$$

$\chi_{NH_3}$  plays an important role in regulating the flux between the surface and the atmosphere. For instance, the flux of ammonia from the soil to the atmosphere (emission) occurs when the concentration of atmospheric ammonia is less than the compensation point  $\chi_{NH_3}$ , while ammonia deposition (atmosphere to surface) occurs when the concentration of ammonia is equal to or greater than  $\chi_{NH_3}$  (Flechar et al., 2011; Wichink Kruit, 2010). It is then crucial to quantify the compensation point in order to understand this exchange. From Eq. 4-16 I conclude that the main variables needed to calculate  $\chi_{NH_3}$  are soil temperature ( $T_{skin}$ ) and  $\Gamma_{soil}$ , the latter is a dimensionless ratio between ammonium and pH ( $NH_4^{+}_{(aq)}$  and  $H^{+}_{(aq)}$  concentrations, respectively, in the soil). In my study, I use  $T_{skin}$  from ERA5. IASI only measures the total columns of ammonia, and is not able to see the dissolved ammonium  $[NH_4^+]$  in the soil. In this case, to calculate the  $\Gamma_{soil}$  I need to look at the fluxes of ammonia and their relation to the dissolved ammonium. The bi-directional exchange of  $NH_3$  between the surface and the atmosphere can be expressed by the flux (assuming a flux independent of time) (Roelle and Aneja, 2005; Zhang et al., 2010):

$$Flux_{NH_3} = k ([NH_3]^{soil} - [NH_3]^{atm}) \quad 4-17$$

Where  $Flux_{NH_3}$  is the bi-directional flux between the soil and the atmosphere ( $\text{molecules (m}^2 \text{ s)}^{-1}$ ),  $k$  is the soil – atmosphere exchange velocity ( $\text{m s}^{-1}$ ), also known as the mass transfer coefficient;

$[NH_3]^{soil}$  is the concentration of  $NH_{3(g)}$  in the soil, and  $[NH_3]^{atm}$  is the concentration of  $NH_{3(g)}$  in the atmosphere (molecules  $m^{-3}$ ). Assuming a first order dissociation of  $NH_3$ , we can express the change in the  $[NH_3]^{col}$  total columns as follows:

$$\frac{d [NH_3]^{col}}{dt} = Flux_{NH_3} - k' [NH_3]^{col} \quad 4-18$$

Where  $k'$  is the rate of dissociation of first order  $k' = 1/\tau$  ( $m\ s^{-1}$ ), with  $\tau$  the lifetime of  $NH_3$  in the atmosphere. Assuming steady state, and considering the  $[NH_3]^{atm}$  as the  $[NH_3]^{col}$ , and  $[NH_3]^{soil}$  as  $\chi_{NH_3}$ , Eq. 4-18 can be written as follows:

$$k \left( \frac{N_a \cdot \chi_{NH_3}}{M_{NH_3}} - \frac{1}{c} [NH_3]^{col} \right) = \frac{[NH_3]^{col}}{\tau} \quad 4-19$$

Where  $c$  is the column height and is equal to 6 km. It is important to note that we neglect the effect of transport by wind since we only look at large regions. Finally, the total column of ammonia  $[NH_3]^{col}$  can be written as:

$$[NH_3]^{col} = \frac{N_a \cdot \chi_{NH_3}}{M_{NH_3} \cdot (c + \frac{1}{k\tau})} \quad 4-20$$

The column height is not considered anymore because it is negligible compared to  $1/k\tau$ , using Eq. 4-16 to 4-20 we get:

$$[NH_3]^{col} = \frac{9.72 \cdot 10^{25}}{T_{soil}} \exp \left[ \frac{-1.04 \cdot 10^4}{T_{soil}} \right] \Gamma_{NH_3} \cdot k\tau \quad \left( \frac{molecules}{cm^2} \right) \quad 4-21$$

Note that  $9.72 \cdot 10^{25} = \frac{a \cdot N_a \cdot c'}{M_{NH_3}} \left( \frac{K\ molecules}{s\ cm^2} \right)$ , where  $a = 2.75 \cdot 10^3$  ( $g\ K\ cm^{-3}$ ),  $N_a$  is Avogadro's number ( $N_a = 6.0221409 \times 10^{23}$   $molecules\ mol^{-1}$ ),  $c' = 100$  is a factor used to convert  $k$  from  $m\ s^{-1}$  to  $cm\ s^{-1}$  (since  $[NH_3]^{col}$  is in  $molecules\ cm^{-2}$ ), and  $M_{NH_3}$  is the molar mass of ammonia gas ( $M = 17.031\ g\ mol^{-1}$ ). The emission potential of  $NH_3$  from the soil can be written as:

$$\Gamma_{soil} = \frac{[NH_3]^{col} \cdot T_{soil}}{\exp(\frac{-b}{T_{soil}})} \cdot \frac{M_{NH_3}}{a \cdot N_a \cdot c'} \cdot \frac{1}{k\tau} \quad 4-22$$

Where  $[NH_3]^{col}$  is the total column concentration of ammonia (molecules  $\text{cm}^{-2}$ ), measured by satellite remote sensors, in this case, IASI.  $T_{soil}$  is the soil temperature at the surface, which can be expressed as the skin temperature,  $T_{skin}$  (Kelvin), extracted from ERA5 (Chapter 2, section 2.4.1),  $\tau$  is the lifetime of ammonia (seconds), and  $b$  is a constant ( $b = 1.04 \times 10^4 \text{ K}$ ).

### 4.2.3 MODIS Land Cover Type

In order to assign a mass transfer coefficient  $k$  to each land type, I use MODIS land cover (refer to Chapter 2, Section 2.5.1). From the land use categories included in the MOD12Q1 product (Belward et al., 1999) I focus on croplands, forests, shrublands, and grasslands. I do not include barelands, snow cover, and urban areas in our analysis; I am not interested in studying these surfaces, since I focus on ammonia volatilization from the soil in areas amended with fertilizers. I show the emission potential in Forests and grasslands/shrublands for comparison with values in the literature. In an attempt to calculate an emission potential (Eq. 4-22) that is relevant to the land cover/use, I therefore assign a mass transfer coefficient  $k$  to each land type based on literature values (Aneja et al., 1986; Erisman et al., 1994; Roelle and Aneja, 2005; Svensson and Ferm, 1993; Wesely, 1989) and I discuss it in Section 4.3.2.

### 4.2.4 GEOS-Chem chemistry transport model

In this study I use version 12.7.2 of the GEOS-Chem chemical transport model (Bey et al., 2001). The model is driven by the Modern-Era Retrospective Analysis for Research and Applications version 2 (MERRA-2) reanalysis product, including nested domains over Europe at a  $0.5^\circ \times 0.625^\circ$  horizontal resolution. MERRA-2 is the second version of the MERRA atmospheric reanalysis product by NASA's Global Modeling Assimilation Office (NASA/GMAO) (Gelaro et al., 2017). Boundary conditions for the nested domains are created using a global simulation for the same months at  $2^\circ \times 2.5^\circ$  resolution. I generate model output for March of 2011, preceded by a one month of discarded model spin-up time for the nested run, and two months for the global simulation. March corresponds well to the month of fertilizer

application in Europe, and as such to the beginning of the growing season (FAO, 2022; USDA, 2022b).

Output includes the monthly mean for selected diagnostics. Anthropogenic emissions are taken primarily from the global Community Emissions Data System (CEDS) inventory (Hoesly et al., 2018). Biogenic non-agricultural ammonia, as well as ocean ammonia sources, are taken from the Global Emission Inventories Activities database (GEIA, Bouwman et al., (1997)). Open fire emissions are generated using the GFED 4.1s inventory (Randerson et al., 2015). I use the Harmonized Emissions Component module (HEMCO) to obtain the ammonia emissions over Europe (Keller et al., 2014).

#### *4.2.5 EC-Earth climate model*

To analyze how future climate will affect ammonia concentration and emission potential, I use the ECMWF climate model the European Earth Consortium climate model (EC-Earth, <http://www.ec-earth.org/>). While other climate models exist, we choose this one because IASI's ammonia product uses ERA5 for the retrievals and we calculate the emission potential from the T skin product of ERA5. The reanalysis uses the ECMWF's Integrated Forecasting System for the atmosphere–land component (IFS). IFS is also used in EC-Earth and is complemented with other model components to simulate the full range of Earth system interactions that are relevant to climate (Döscher et al., 2022). I note that the versions of the IFS models used in ERA5 and in EC-Earth are not identical as the climate model product is not assimilated and is not initialized with observations several times a day like ERA5. The EC-Earth simulations are included in the Climate model intercomparison project, phase 6 (Eyring et al., 2016), part of the Intergovernmental Panel on Climate Change (IPCC) report of 2021 (Masson-Delmotte, et al., 2021). I use the so-called Scenario Model Intercomparison Project (ScenarioMIP), covering the period [2015 – 2100] for future projections under different shared socio-economic pathways (SSP) (Riahi et al., 2017). I analyze two scenarios, the SSP2-4.5 corresponding to “middle of the road” socio-economic family with a nominal  $4.5\text{W/m}^2$  radiative forcing level by 2100 - approximately corresponding to the RCP-4.5 scenario, and the SSP5-8.5 marks the upper edge of the SSP scenario spectrum with a high reference scenario in a high fossil-fuel development world throughout the 21st century.



## 4.3 Results

### 4.3.1 GEOS-Chem vs. IASI

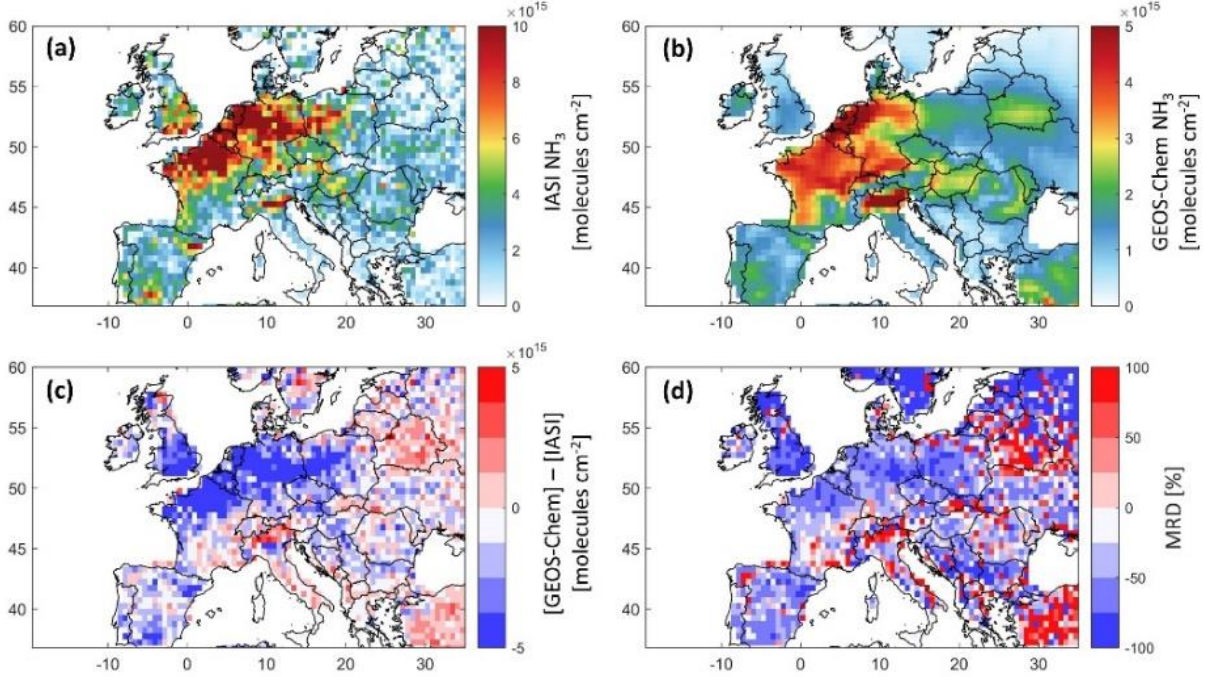


**Figure 4.3.** Ammonia total column concentrations from IASI (panel a), and GEOS-Chem (panel b), the difference between both datasets (panel c) in molecules  $\text{cm}^{-2}$ , and the Mean Relative Difference (MRD) in % (panel d); all data are a monthly average of March 2011, and over Europe at a  $0.5^\circ \times 0.625^\circ$  grid resolution. Note that the colour bar limits are different between panels (a) and (b).

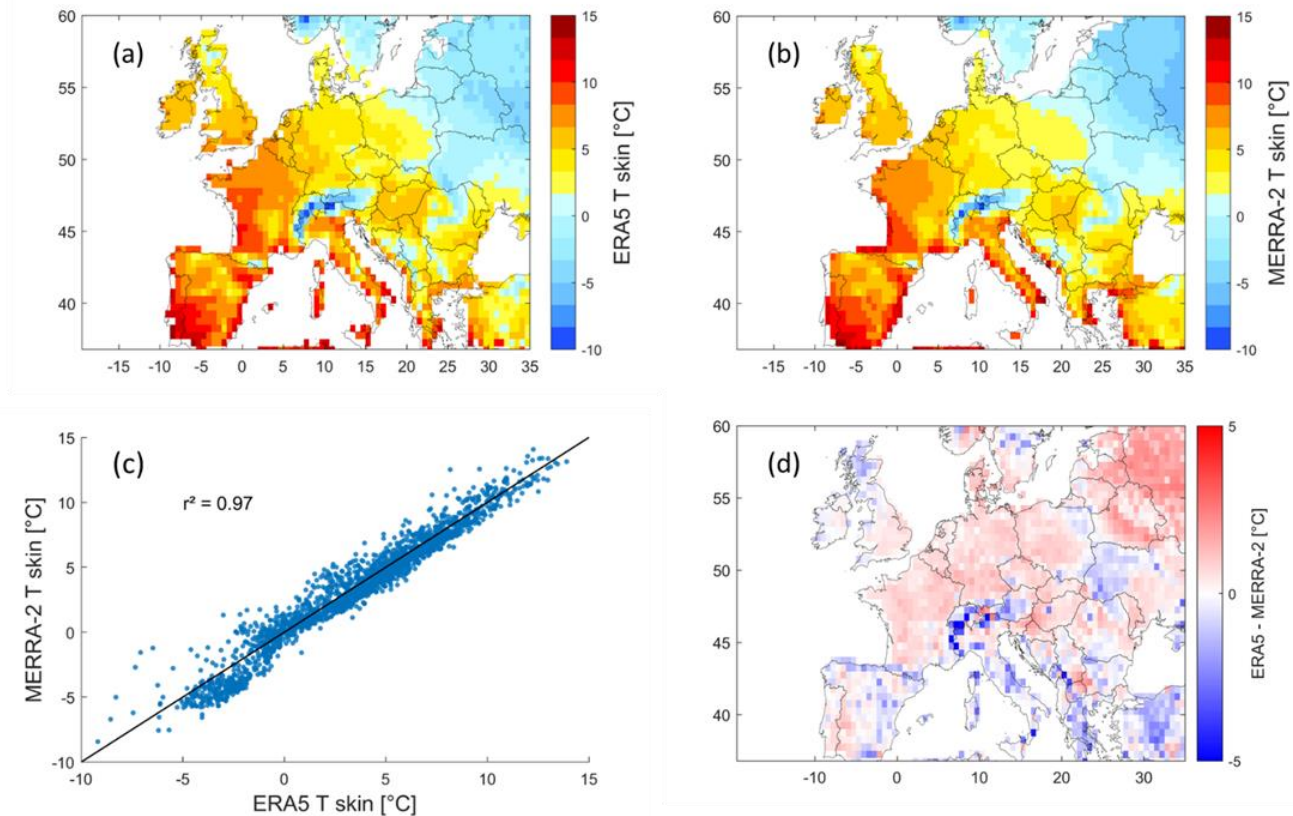
Ammonia lifetime  $\tau$  is a crucial parameter to calculate the emission potential  $I_{\text{soil}}$ . I use the GEOS-Chem model to calculate the lifetimes of ammonia during March 2011. In order to analyse how well the model simulates atmospheric ammonia, I compare the output of GEOS-Chem to the IASI total columns of ammonia gridded on the same horizontal resolution ( $0.5^\circ \times 0.625^\circ$ ) and during the same time period.

Figure 4.3 shows the IASI  $\text{NH}_3$  distribution (panel a), and that from GEOS-Chem (panel b), the bias between the two (panel c), and the percentage mean relative difference MRD (panel d), all during March 2011. I calculate MRD following the equation  $\frac{(\text{GeosChem } \text{NH}_3 - \text{IASI } \text{NH}_3) \times 100}{\text{IASI } \text{NH}_3}$  at each grid point.

Generally, both GEOS-Chem and IASI show coincident sources of ammonia, reflecting the good ability of the model to reproduce ammonia columns over major agricultural source regions in Europe. The bias between IASI and GEOS-Chem and the MRD are shown in Figure 4.3c and d. Ammonia columns from GEOS-Chem are underestimated by up to  $2 \times 10^{16}$  molecules/cm<sup>2</sup> in some source regions/over hotspots, especially in England, North Eastern France, the North European Plain (Netherlands, Belgium, and Germany), and Spain (around Barcelona). Whitburn et al. (2016) found similar results, in which they show that GEOS-Chem underestimates ammonia columns by up to  $1 \times 10^{16}$  molecules/cm<sup>2</sup> in Europe on a yearly average in 2009, notably in the North European Plain. It is important to note that, in our study, I compare only one month of data (March, 2011) that marks the start of the growing season in the majority of the countries of interest (FAO, 2022; USDA, 2022b). The differences are mainly because of the time coincidence, and the fact that only cloud-free data are used to retrieve ammonia. IASI observes ammonia during the satellite overpass (~9:30 AM local time), whereas the GEOS-Chem simulation is averaged over the whole month including all hours of the day. In Western and Northern Europe, the MRD is mostly less than -50 %, for instance, in the North European Plain (-49 %). If I look at the average MRD in regions of focus, I see that the Po Valley in Italy exhibits the highest MRD value (+110 %), whereas the best represented region is New Aquitaine in the southwest of France (-20 %). The rest of the regions have mean MRDs that fluctuate between -64 % and -42 %. A summary of the results of this study, including the MRD over some source regions is listed in Table 2. Although the bias and MRD can be considered high, the spatial distribution is consistent between IASI and GEOS-Chem. Therefore, according to the steady state approximation, the meteorological and soil parameters affecting one dataset (e.g. IASI NH<sub>3</sub>) are applicable to the other (e.g. model simulation). It is worth noting that although I do not use the latest version of GEOS-Chem, the results I obtain reflects our current understanding of the regional chemistry at this horizontal and temporal resolution.

The ammonia data I use in this study are a product of an artificial neural network (Chapter 2), and skin temperatures from re-analysed data ERA5. GEOS-Chem, on the other hand, uses the MERRA-2 skin temperatures. It is therefore crucial to compare both datasets. In panels (a) and (b) from Figure 4.4, I plot the T skin from ERA5 and MERRA-2, respectively, for the month of March 2011. Panel (c) is a scatter plot of both datasets over the whole domain, and panel (d) is the bias between both datasets ( $[ERA5] - [MERRA-2]$ ). The coefficient of determination  $r^2$  shows

that ERA5 and MERRA-2 agree to a great extent with a value of 97 % (Figure 4.4c). The bias shows minor differences (up to 5°C in absolute value), these differences are only remarkable in the Alps region where one can see that ERA5 underestimates T skin relative to MERRA-2 (Figure 5.7.5d). MERRA-2 overestimates T skin in Eastern, Central, Western, and parts of Southern Europe by less than 3°C. For the calculation of the emission potential, T skin is needed. Here I will study it for both ERA5 and MERRA-2 later in this chapter. The results are summarized in Table 2 below.



**Figure 4.4.** A comparison between T skin from ERA5 and MERRA-2: (a) T skin monthly average from ERA5, and (b) MERRA-2; (c) scatter plot of T skin from MERRA-2 (y axis) and ERA5 (x axis); and (d) the difference between the two datasets [°C].

**Table 2. Summary of ammonia average lifetime, emission potential, concentrations and the T skin in selected regions in Europe.**

Region	Country	$\tau_{NH_3}$ [hours]	T skin [°C]			$\Gamma_{soil} \times 10^4$ [dimensionless]				NH <sub>3</sub> concentrations [molecules $\times 10^{15}$ cm <sup>-2</sup> ]		
			ERA5 IASI Overpass	ERA5	MERRA-2	Case 1	Case 2	Case 3	Case 4	IASI	GEOS- Chem	Mean MRD [%]
Ireland	Ireland	3.34	8.74	5.78	6.23	0.73	0.72	0.94	0.26	2.5	1.5	− 46
England	England	3.15	8.54	5.87	5.73	0.82	0.78	2.06	0.58	4.8	1.2	− 64
North European Plains	Belgium, Netherlands	5.16	7.46	4.46	4.57	1.86	1.71	2.51	1.00	7.7	3.9	− 49
Brittany	France	6.93	10.48	8.13	8.16	1.19	1.09	1.48	0.70	5.8	3.7	− 60
New Aquitaine	France	8.05	11.25	7.72	7.47	0.59	0.57	0.49	0.30	4.0	2.9	− 20
Po Valley	Italy	7.10	8.95	4.93	5.46	1.50	1.63	0.89	0.40	3.8	4.0	+ 110
Valladolid	Spain	4.53	11.64	6.87	6.93	0.55	0.55	0.62	0.20	2.5	1.3	− 42
Barcelona	Spain	4.94	12.61	7.05	9.44	0.43	0.46	0.65	0.28	3.2	1.5	− 49

#### 4.3.2 Ammonia emissions, losses and lifetime in Europe

Most of the ammonia emissions in Europe are due to agricultural activities. Figure 4.5 shows the repartitions of the emission sources in Europe in March 2011. The anthropogenic sources (i.e. mainly manure management, and fertilizers application) contribute to 83 % of the total ammonia emissions. Then, the emissions from natural sources follow (i.e. soil of natural vegetation, oceans, and wild animals) representing 16 % of the total ammonia, whereas the remaining 1 % correspond to emissions from biomass burning and ships.

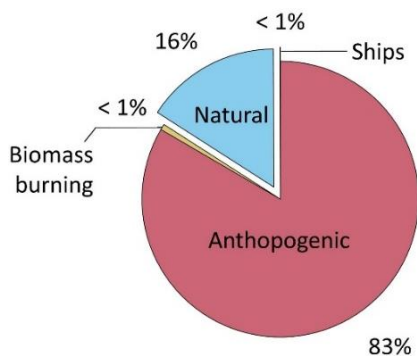


**Figure 4.5. Repartitions of ammonia emissions from anthropogenic, natural sources, biomass burning and ships. The data are from the Harmonized Emissions Component module (HEMCO) that is used in GEOS-Chem, and the period covered is March 2011, in the European domain. Anthropogenic sources are mainly agricultural activities that include manure management and fertilizers application. Natural sources include emissions from natural vegetations, oceans and wild animals.**

Figure 4.6 shows the total emissions (panel (a)), and losses (panel (b)), total burden (panel (c)), and the lifetime of ammonia, from GEOS-Chem in March 2011. I identify 8 source regions, shown as rectangles A to H in panel (a), which I investigate thoroughly in this study. In the calculation of the total loss of ammonia (Figure 4.6b), I considered dry deposition, chemistry, transport, and wet deposition (including loss to convection) from the GEOS-Chem model simulation, which are all possible loss pathways for ammonia (David et al., 2009). Figure 4.6b shows that the largest losses occur logically where I have the highest sources detected (see Figure 4.6a).

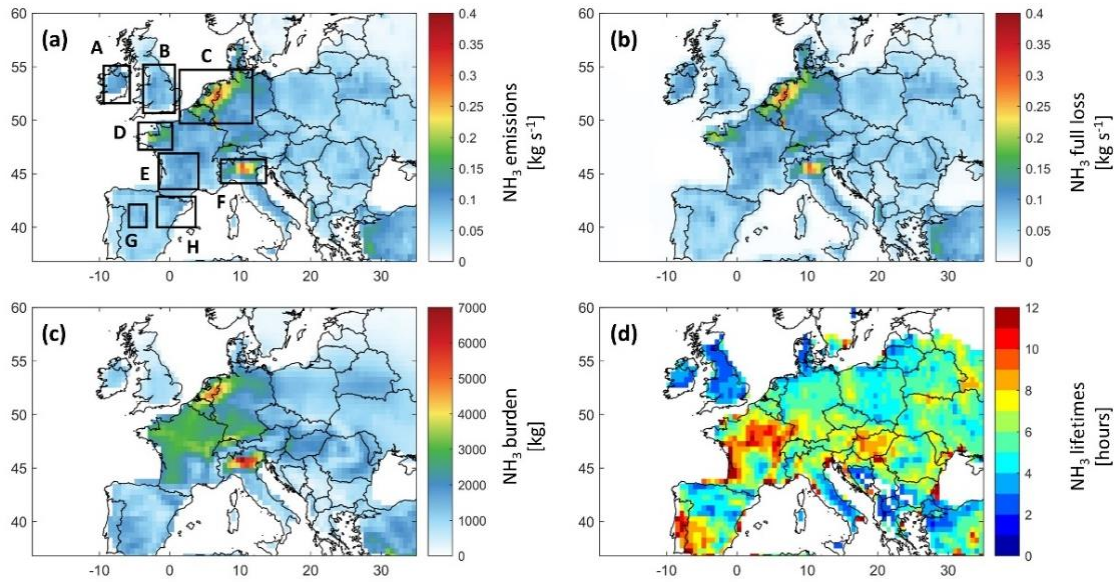


**Figure 4.6. Ammonia budget in Europe from GEOS-Chem: (a) Ammonia emissions from the Harmonized Emissions Component module (HEMCO) in  $\text{kg s}^{-1}$  with our regions of interest shown in rectangles, (b) ammonia full loss in  $\text{kg s}^{-1}$ , (c) ammonia total burden in kg, and (d) ammonia lifetime in hours. All plots refer to March 2011 and are presented at a  $0.5^\circ \times 0.625^\circ$  grid resolution.**

The total ammonia burden (Figure 4.6c) is calculated as the integrated sum of ammonia along the atmospheric column in the model grid box. One can clearly detect ammonia hotspots over Europe, in particular the North European Plain (region C), Brittany (region D) and the Po Valley (region F). All of these regions are characterized by intense agricultural activities, as the total emissions and loss show (Figure 4.6a, and b). The total burden is generally the highest over France, Belgium, The Netherlands, and parts of Germany and Italy (Figure 4.6c). I show in panel (d) the lifetime  $\tau_{ss}$  of ammonia calculated from the total burden and losses. In the case of a gas



with a short lifetime, such as ammonia, the emissions are relatively well-balanced spatially by eventual sinks/losses (steady-state approximation). Therefore, one can calculate a steady-state lifetime ( $\tau_{ss}$ ) as the ratio between the total burden  $B$  (Figure 4.6c) and the total emissions  $E$  or losses  $L$  (sum of all emitted / lost molecules of ammonia, Figure 4.6a or b) using the following equation:  $\tau_{ss} = B/L$  (Plumb and Stolarski, 2013).

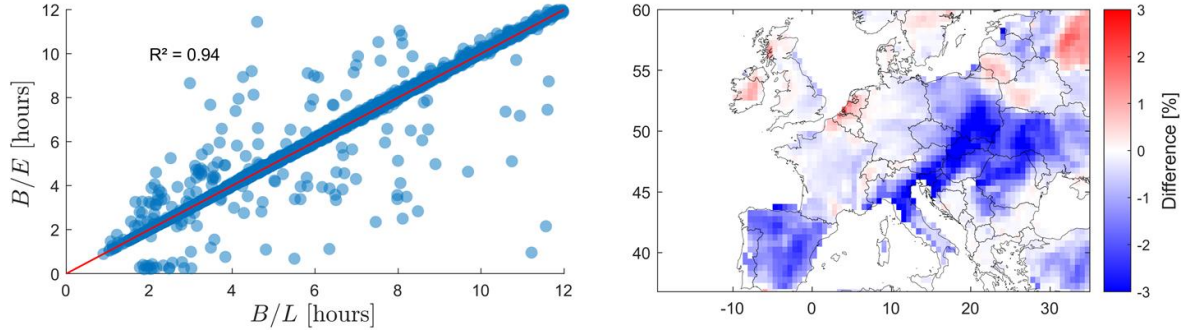


**Figure 4.7.** Left panel: A regression plot of ammonia lifetimes calculated using emissions (y axis) and losses (x axis), with a coefficient of determination  $R^2 = 0.94$ . Right panel: the difference between both datasets displayed on the left, difference =  $\frac{B/E - B/L}{B/L} \times 100$ .

Note that the  $\tau_{ss}$  is more or less the same whether I calculate it using the losses or the emissions. For instance, in selected source regions (rectangles in Figure 4.6a) the total emissions and losses are very close with minor biases that are less than 2%. In Figure 4.7 I show the difference between calculating ammonia lifetime using the emissions and losses. The left panel shows a regression plot of both methods (with a coefficient of determination  $R^2 = 0.94$ ), and the right panel shows the percentage difference between both lifetimes (Figure 4.7).

On a monthly average,  $\tau_{ss}$  can go up to 12 hours, and it can reach 1 day (24 hours) in coastal regions such as in New Aquitaine in France (region E). The latter can be related to the high probability of air stagnation in that area in comparison to Northern Europe (Garrido-Perez et al., 2018), since higher  $PM_{2.5}$  pollution episodes were found under stagnant meteorological conditions (AQEG, 2012). Ammonium molecules carried on these  $PM_{2.5}$  can transform back into ammonia. Our results agree with the literature suggesting a lifetime between a few hours to a few days (Behera et al., 2013; Pinder et al., 2008), and with those calculated by Evangeliou et al. (2021) over Europe, showing a monthly average of ammonia lifetime that ranges from 10 to 13 hours,

despite that they do not consider ammonia emissions to natural sources that consist of 16% of the total ammonia (Figure 4.5). Shorter lifetimes from industrial sources of ammonia were reported in Dammers et al. (2019), with a mean lifetime of ammonia that is equal to 2.35 hours ( $\pm 1.16$ ). A recent study found lifetimes of ammonia that vary between 5 and 25 hours, roughly, in Europe (Luo et al., 2022); these values are higher since, in addition to ammonia loss, Luo et al. (2022) included the loss of ammonium, and thus considering the loss of ammonia only terminal when the ammonium is also lost/deposited. This approach is not considered here nor in Evangeliou et al. (2021).

Notably, ammonia lifetime and burden (Figure 4.6c, and d) each have different spatial distribution compared to the other 2 panels (Figure 4.6a, and b). The ammonia residence time in the atmosphere varies depending on the sources and more importantly on the locally dominant loss mechanisms. For this reason, in Figure 4.8, we show the relative contribution of the ammonia loss mechanisms, presented as pie charts, for the agricultural source regions shown in black boxes in Figure 4.6a.

The fastest loss mechanisms are either chemical (i.e. in the vast majority transformation to particulate matter) or through wet and dry deposition (Tournadre et al., 2020). Figure 4.8 shows that more than 50 % of the ammonia molecules in the atmosphere are lost to chemical reactions in most of the regions (A, B, C, H, and F). The shortest residence time of ammonia is observed in England, where the chemical removal was significantly higher than other sinks and represented up to 73 % of the total ammonia loss pathways, suggesting a rapid transformation into inorganic particulate matter ( $PM_{2.5}$ ). In the regions D, G and E the chemical loss makes up 50 %, 49 %, and 42 %, respectively. In fact, in March 2011, PM was found to be mostly composed of inorganic nitrate (41 %), and ammonium (20 %) (Viatte et al., 2022) over Europe, both of which are products of atmospheric ammonia. Nitrate-bearing  $PM_{2.5}$  are formed when nitric acid ( $HNO_3$ ) reacts with ammonia (Yang et al., 2022), and ammonium is a direct product of the hydrolysis of ammonia. 41% of the nitric acid formed in the atmosphere is produced from the reaction between nitrogen dioxide ( $NO_2$ ) and the hydroxyl radical (OH) (Alexander et al., 2020). These chemical pathways help explain the large chemical losses in most of the regions studied in Figure 4.8.

Ammonia loss to transport is the highest in regions neighbouring the Atlantic Ocean, accounting for 30 %, 27 %, 32 %, and 34 % of total sinks in regions A, D, E, and G respectively.

These regions are exposed to the North Atlantic Drift, also known as the Gulf Stream, that is associated with high wind speed and cyclonic activity (Barnes et al., 2022). In other regions, 14 % to 22 % of the total ammonia is lost to transport mechanisms, and in all regions, 11 to 22 % is lost to dry deposition (Figure 4.8). During March, precipitation is relatively lower as compared to winter (December, January, February) in Europe. Furthermore, 2011 was a particular dry year compared to the 1981 – 2010 average (Met Office, 2016). Drought was reported to be severe in areas such as France, Belgium and the Netherlands, and moderate in England and Ireland (EDO, 2011). This can help explain the low percentage of wet deposition during March 2011 (1 to 5 % out of the total loss of ammonia).

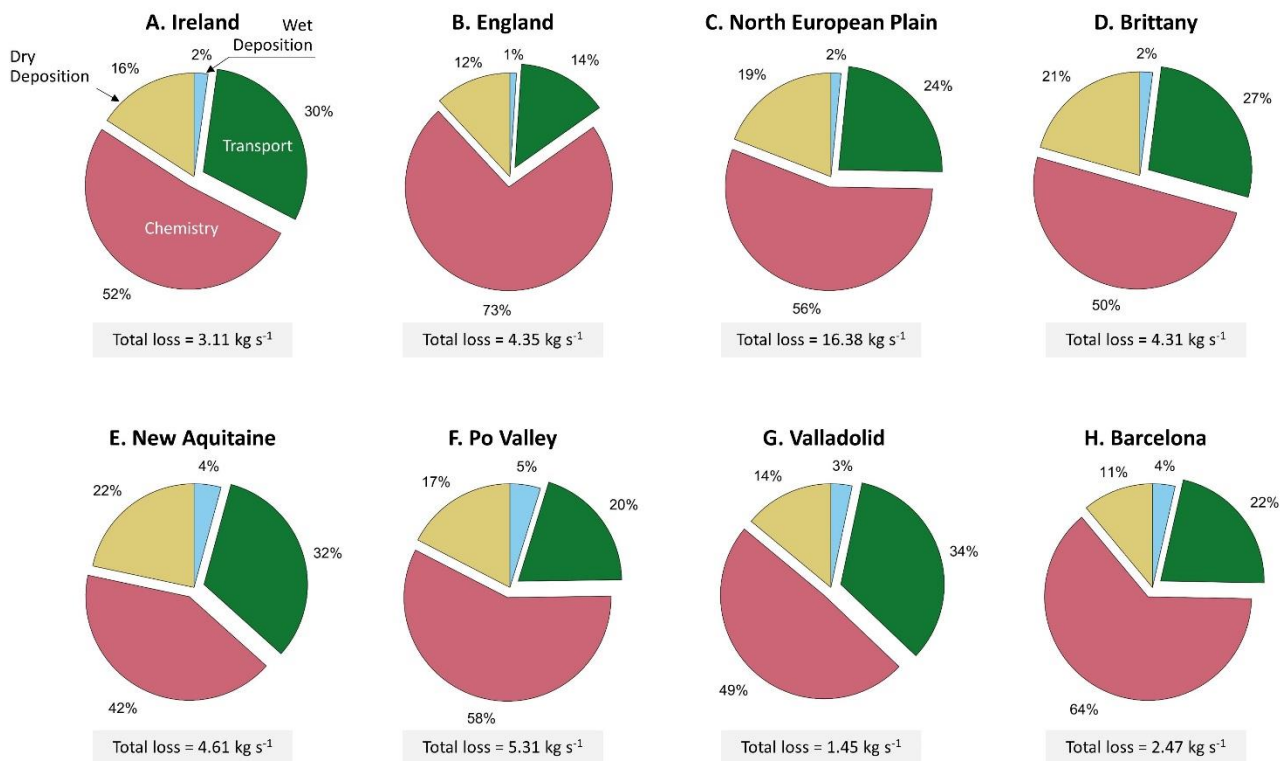


**Figure 4.8.** Repartition of the ammonia loss mechanisms for major agricultural areas in Europe, during March 2011, as retrieved from GEOS-Chem, with the total ammonia loss shown in a grey box under each pie chart ( $\text{kg s}^{-1}$ ). The regions are shown in black boxes in Figure 2a.



### 4.3.3 Mass transfer coefficient estimation

To calculate emission potential, a calculation of the mass transfer coefficient  $k$ , which relates to the land type, is necessary. Figure 4.9 shows the land cover type from MODIS in Europe (left panel), and the corresponding assigned mass transfer coefficient  $k$  (right panel) needed to calculate the emission potential Eq.4-22). In order to choose a mass transfer coefficient that is convenient for the different land types relevant to this study, we searched for  $k$  values in the literature. Not all land types have been studied for ammonia transfer coefficient.

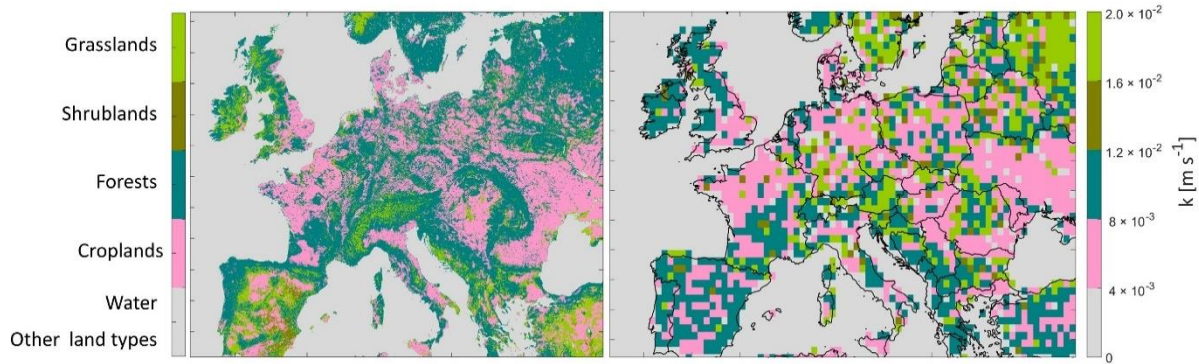


**Figure 4.9.** MODIS Land Cover Type, at a  $500 \text{ m} \times 500 \text{ m}$  grid box (left panel), and interpolated mass transfer coefficient  $k$  on a horizontal resolution of  $0.5^\circ \times 0.625^\circ$  grid box (right panel).

For water bodies and other land types that are not considered here (see Section 4.2.3), the mass transfer values  $k$  were set to zero and represented in grey colour in Figure 4.9. In a laboratory experiment, Svensson et al. (1993) reported  $k = 4.3 \times 10^{-3} \text{ m s}^{-1}$  for a mixture of soil and swine manure, as therefore, we assign this value to croplands. Due to the lack of  $k$  values for non-fertilized forests, shrublands and grasslands in the literature, we used values originally assigned for  $\text{SO}_2$ , bearing in mind that these are approximate values and they reflect mostly the conditions of the soil cover type (short, medium or tall grass). To assign a  $k$  value for forests, we used values reported in Aneja (1986) ( $k = 2 \times 10^{-2} \text{ m s}^{-1}$ ), which originally represent deposition velocity (mass transfer) of  $\text{SO}_2$  in a forest (high crops). For shrublands and grasslands (the two land types have the same  $k$ ), we used the value  $k = 8 \times 10^{-3} \text{ m s}^{-1}$  that has been reported in Aneja et al. (1986) as the deposition velocity (mass transfer) of  $\text{SO}_2$  in a grassland (medium crops). These values are the best attempt to test the validity of using MODIS and lookup tables of  $k$  values to calculate a realistic soil emission potential. As a result, Figure 4.9 (left panel) includes 5 land

types, while  $k$  values are reported for 4 land types (other land type/water, croplands, forests, and shrublands/grasslands). After choosing the  $k$  values, we assigned them for each land type on the (500 m  $\times$  500 m) grid. We then extrapolate the array with the  $k$  values from 500 m  $\times$  500 m to the resolution of GEOS-Chem (0.5°  $\times$  0.625° grid box). This leads to averaging different fine pixels with different land cover types into a coarser grid. The result is shown on the right panel of Figure 4.9.

Uncertainties of this methodological approach can be summarized as follows:

- (1) The  $k$  value assigned for croplands is approximate and therefore not the same in every cropland over Europe.
- (2) The  $k$  value assigned for forests represents the SO<sub>2</sub> exchange in high croplands, and ammonia might change especially when the latter is highly affected by humidity; it can easily dissolve in the water film on leaves in high humid conditions.
- (3) The extrapolation of a fine array (500 m  $\times$  500 m) will merge several grids together and average them in order to construct the coarser grid box (0.5°  $\times$  0.625°); the result is therefore an average that might mix croplands with neighbouring forests/barelands/grasslands. This leads to a range of different  $k$  values that are shown on Figure 4.9.

Using the land-type specific  $k$  value is necessary in order to reflect realistic emissions potential, as ammonia exchange in a forest is different from that of croplands or unfertilized grasslands, due to different barriers (long, medium or short crop / grass), and ammonium soil content in each land type.

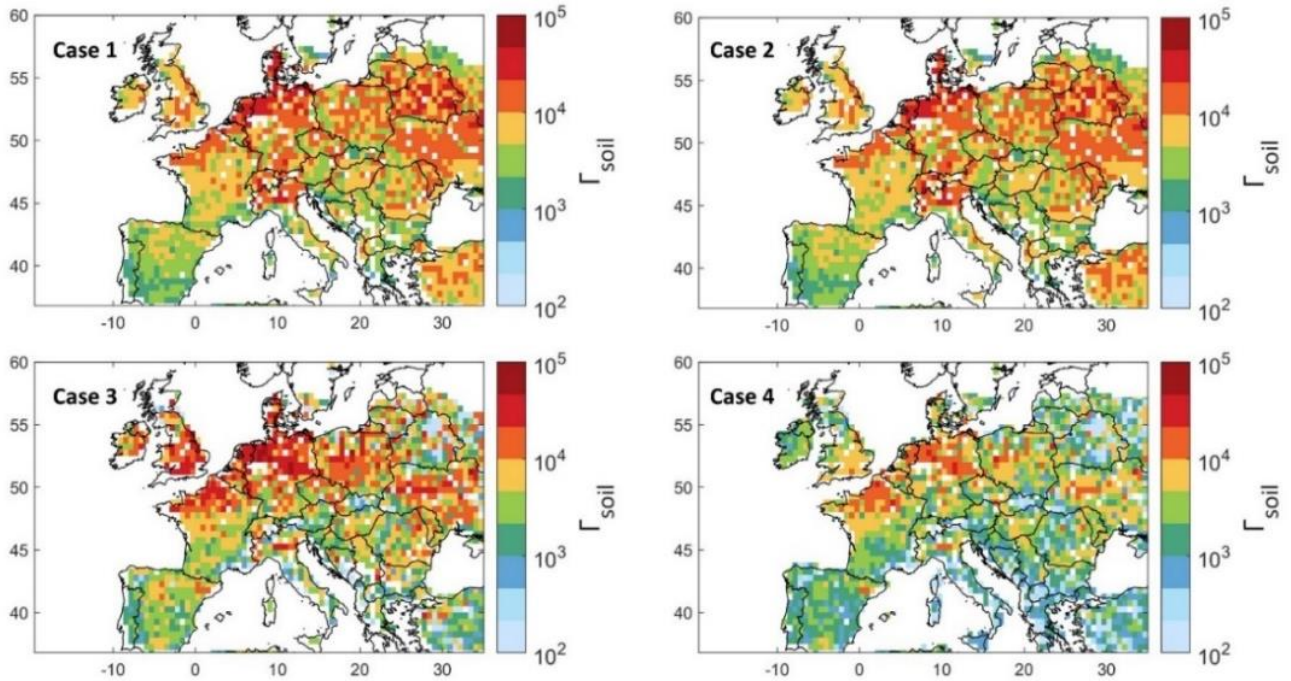
#### *4.3.4 Emission potential in Europe*

Figure 4.10 illustrates the ammonia soil emission potential  $\Gamma_{soil}$  calculated using Eq. 4-22 and  $k$  values presented in Figure 4.9. After assigning the variable mass transfer coefficient, the remaining variables needed to calculate  $\Gamma_{soil}$  in Eq. 4-22 are ammonia concentration and lifetime, as well as the skin temperature. For this reason, the emission potential  $\Gamma_{soil}$  shown in Figure 4.10 are calculated using different configurations:

- Case 1: GEOS-Chem ammonia and lifetime with MERRA-2 T skin, i.e. simulated  $\Gamma_{soil}$ ,

- Case 2: GEOS-Chem ammonia and lifetime and ERA5 Tskin, to check the effect of using ERA5 vs MERRA-2 for skin temperature,
- Case 3: IASI's  $\text{NH}_3$ , ERA5 T skin and GEOS-Chem ammonia lifetime,
- Case 4: IASI's  $\text{NH}_3$ , ERA5 T skin and ammonia lifetime from Evangeliou et al. (2021), that were calculated using LMDz-OR-INCA chemistry transport model. The latter couples three models: the general circulation model GCM (LMDz) (Hourdin et al., 2006), the Interaction with Chemistry and Aerosols (INCA) (Folberth et al., 2006), and the land surface dynamical vegetation model (ORCHIDEE) (Krinner et al., 2005).

Based upon the four cases, I calculate a range of emission potentials, and filtered data points with ammonia total column concentration less than  $5 \times 10^{14}$  molecules  $\text{cm}^{-2}$ . The latter are mostly grid boxes concentrated above  $56^\circ$  North that we consider as noise (shown in white pixels on Figure 4.10).



**Figure 4.10.** Ammonia soil emission potential ( $\Gamma_{soil}$ ) on a log10 scale from model simulation, observation and reanalysis for 4 different cases (see text for details).

T skin from ERA5 and MERRA-2 agree very well, with a coefficient of determination  $r^2 = 0.97$  (Figure 4.4). This explains the excellent spatial correlation between cases 1 and 2, where the correlation coefficient between  $\Gamma_{soil}$  from cases 1 and 2 is  $r^2 = 0.97$ . Since IASI- $\text{NH}_3$  retrievals

use ERA5 T skin, this also suggests that using MERRA-2 or ERA5 does not affect our  $\Gamma_{soil}$  calculation. In case 3, the emission potential agrees spatially and in value with that of GEOS-Chem. However, we observe higher  $\Gamma_{soil}$  in regions such as Ireland, England, North France, Northeastern Spain, and Poland. This is due to the underestimation of ammonia from GEOS-Chem as compared to IASI observations (Figure 4.3a). For instance,  $\Gamma_{soil}$  from IASI and ERA5 (case 3) differs with that from GEOS-chem and ERA5 (case 2) by up to -70 % in the Po Valley (Italy) and +60 % in England. Looking at Table 2, this difference can be explained by the corresponding MRD for each of the regions, in which it is -64 % for England and +110 % for the Po Valley. Similarly, the differences between case 3 and 4 reach up to +66 % in England, and this is mostly due to the 10-hours difference between ammonia lifetime from GEOS-Chem and Evangeliou et al. (2021). The lowest  $\Gamma_{soil}$  were obtained in case 4, due to the higher lifetimes than those calculated from GEOS-Chem. Note that  $\Gamma_{soil}$  is inversely proportional to ammonia lifetime (Eq. 4-22). In fact, the longer ammonia stays in the atmosphere (longer lifetime), the less the flux will be directed from the soil to the atmosphere (less ammonia emission).

Figure 4.11 shows the emission potential (similarly to what I show in Figure 4.10) but from a fixed and averaged  $k$  value for all land types. This Figure highlights the importance of using a variable  $k$  that is adjusted to each land type. The fixed  $k$  used is calculated assuming 14 days of fertilization ( $k = 10^{-3} \text{ m s}^{-1}$ ), 7 days when  $k$  value reduces ( $k = 10^{-5} \text{ m s}^{-1}$ ), and 10 days when  $k$  is low ( $k = 10^{-6} \text{ m s}^{-1}$ ) resulting in average of  $k = 4.5 \times 10^{-4} \text{ m s}^{-1}$ .

In the four cases presented in Figure 4.10, one can see similar spatial distribution of ammonia emission potential ranging from  $12 \times 10^{-1}$  in a forest to  $9.5 \times 10^4$  in a cropland (monthly average considering all the cases). In agricultural lands, our results show that  $\Gamma_{soil}$  ranges from  $2 \times 10^3$  to  $9.5 \times 10^4$ . Our values for croplands start at around  $10^3$ . In fact, most of the studies summarized in Zhang et al. (2010) reported  $\Gamma_{soil}$  that range mostly from  $10^3$  to  $10^4$  in fertilized croplands/grasslands; the minimum  $\Gamma_{soil}$  reported is in the order of  $10^2$  and the maximum is of the order of  $10^5$ . Therefore, our values fit within the range of  $\Gamma_{soil}$  calculated in the literature and summarized in Zhang et al. (2010) and the references within. Personne et al. (2015) focused on Grignon, an agricultural region near Paris, France ( $48^\circ 51'N$ ,  $1^\circ 58'E$ ). They obtained  $\Gamma_{soil}$  values between  $1.1 \times 10^4$  to  $5.8 \times 10^6$ . In the present study, the emission potential over this region is between  $5 \times 10^3$  (case 4) to  $2 \times 10^4$  (case 2). In this study, it is expected to obtain lower values

than the ones measured over specific field. Therefore, we consider our results to be in good agreement with the obtained values in Personne et al. (2015), since ours reflect an average of a coarse patch of land of the size  $55 \times 70 \text{ km}^2$  approximately, with a 31-day mean.

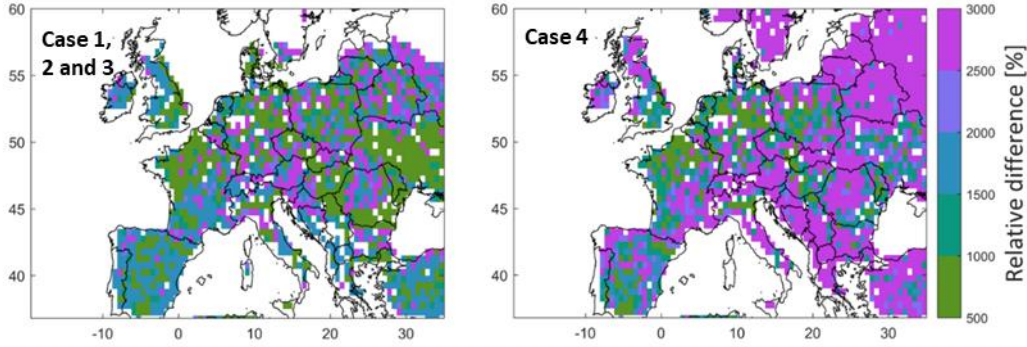


**Figure 4.11.** Relative difference (%) of  $\Gamma_{soil}$  between a fixed and a variable  $k$  value:  $\frac{\Gamma_{fixed k} - \Gamma_{variable k}}{\Gamma_{variable k}} \times 100$ . Cases 1, 2 and 3 are identical due to the use of  $\text{NH}_3$  lifetime from GEOS-Chem; case 4 is different due to the use of  $\text{NH}_3$  lifetime from Evangeliou et al. (2021).

In Figure 4.11 I show the difference in the emission potential between fixed and spatially variable  $k$ , where one can see that a fixed  $k$  might overestimate  $\Gamma_{soil}$  by 10 to  $10^3$  on a log10 scale (500 – 3000 %), in agricultural areas. In cases 1, 2, and 3 the high differences (greater than +2500 %) are spread out such as noise, whereas in case 4 those differences are clearly outside the agricultural areas. The distinction between ammonia from croplands and regions with no ammonia is clear in case 4 (Figure 4.10). This is due to the homogeneity of the ammonia lifetimes calculated by Evangeliou et al. (2021) (Figure 4.13, left panel). The difference between the lifetimes calculated by GEOS-Chem and those from Evangeliou et al. (2021) are shown on the right panel of Figure 4.13. Higher biases are seen in non-agricultural areas. Both lifetime grids are calculated with different simulation models, but another possible explanation of the bias in the non-agricultural areas can be due to the absence of the emissions from natural sources in Evangeliou et al. (2021) calculations. These emissions consist only 16% of the total ammonia from GEOS-Chem (Figure 4.5).



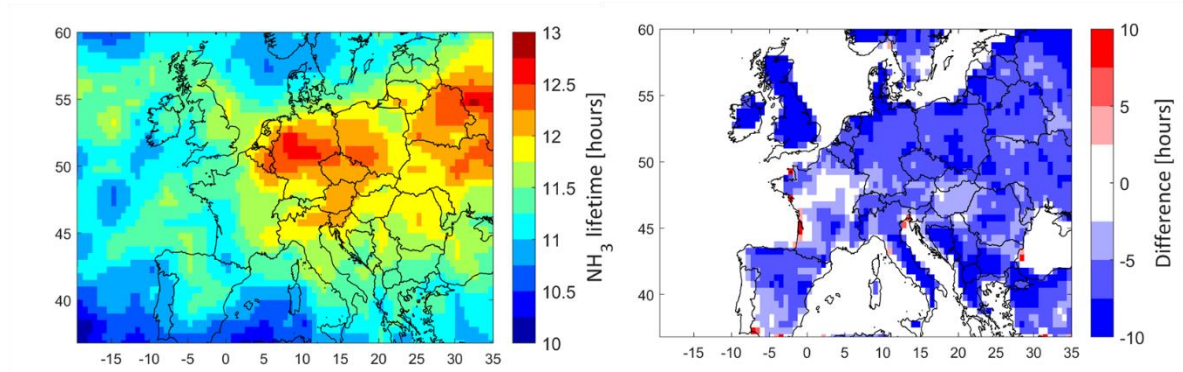


**Figure 4.13.** Left: Ammonia lifetimes calculated by Evangeliou et al. (2021) during March 2011. Right: the difference between the lifetimes calculated from GEOS-Chem in this study and those calculated by Evangeliou et al. (2021) ( $\tau_{\text{GEOS-Chem}} - \tau_{\text{Evangeliou et al.}}$ ).

The mean emission potentials per ammonia source region in Europe (shown in rectangles in Figure 4.6) and per case are shown in Figure 4.12, and listed in Table 2. Table 2 shows the average lifetime from GEOS-Chem (hours), the average T skin from the three datasets that we used ( $^{\circ}\text{C}$ ), the average ammonia emission potential in all the cases examined (dimensionless), and the average ammonia columns from IASI and GEOS-Chem ( $\text{molecules cm}^{-2}$ ). The four cases show a similar pattern with the North European Plain exhibiting the highest emission potential. This has been shown in Figure 4.3, Figure 4.6, and Figure 4.10, as well as in Table 2, where  $\Gamma_{\text{soil}}$  is higher in regions with high ammonia columns. This is expected in fertilized lands (croplands), since  $\Gamma_{\text{soil}}$  is proportional to the concentration of ammonia near the surface. The latter increases when the soil content in ammonium ( $\text{NH}_4^+$ ) increases following the application of nitrogen-based fertilizers.

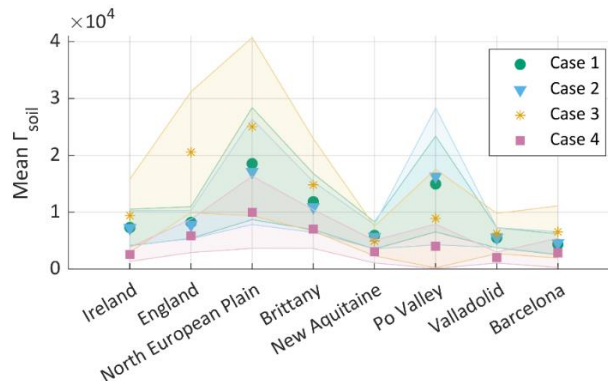


**Figure 4.12.** Mean ammonia emission potential  $\Gamma_{\text{soil}}$  per region and per case, with the error margin on the mean as the shaded area (95<sup>th</sup> percentile) for cases 1 to 4. The cases are explained in Figure 4.10 and its discussion.

Figure 4.12 also shows that for cases 1 and 2 (GEOS-Chem) the emission potential in the Po Valley is higher as compared to case 3 (IASI), although it stays within the margin of error. This is due to the effect of temperature. Table 2 shows that at the time of the IASI overpass,  $T_{skin}$  from ERA5 in the Po Valley is almost twice as large (8.95 °C) as the monthly averaged temperature (4.46 °C). The effect of skin temperature through Eq. 4-22 makes the emission potential highly dependent. In fact,  $\Gamma_{soil}$  is both directly and inversely proportional to  $T_{skin}$ , however, the exponential in the denominator has ~10 times more effect on the value of  $\Gamma_{soil}$  than the  $T_{skin}$  in the numerator. Therefore, through Eq. 4-22, we conclude that an increase in temperature by 1°C will reduce  $\Gamma_{soil}$  by around -8%.

The standard deviation (shaded area) is found to be the highest in the North European Plain, which is also the largest region (hence higher variability is expected), especially when considering case 3 with IASI. IASI distinguishes different source sub-regions, leading to higher spatial variability of ammonia, and therefore  $\Gamma_{soil}$ . As Figure 4.12 has shown, case 4 has the lowest  $\Gamma_{soil}$ , with a factor of two lower than cases 1 to 3. This is due to the longer lifetimes calculated by Evangeliou et al. (2021). However, we note that all the regions exhibit the same inter-variability between each of the case, regardless of the lifetimes used.

### 4.3.5 Case study: ammonia increase with temperature under future scenarios

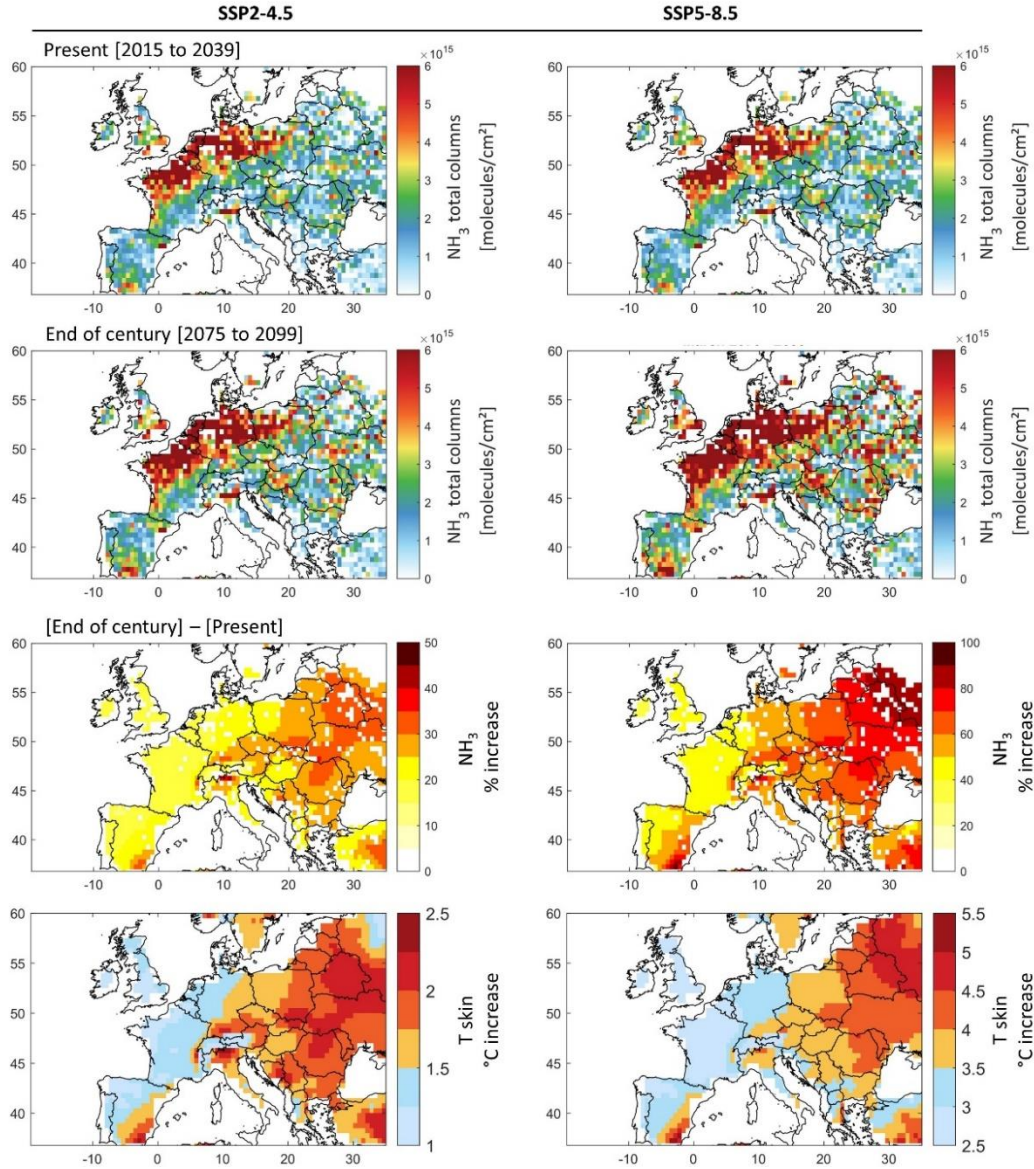


**Figure 4.14.** First and second rows: Ammonia total column concentrations during March (monthly averages) under the present climate [2015 to 2039] (first row), and in the end of century climate [2075 to 2099] (second row), under the socioeconomic scenarios SSP2-4.5 (left) and SSP5-8.5 (right). Third and fourth rows: The percentage increase in ammonia concentration (third row), and the change in  $T_{\text{skin}}$  in °C (fourth row) by the end of the century [2075 to 2099] with respect to present climate [2015 to 2039] under SSP2-4.5 (left) and SSP5-8.5 (right). Ammonia columns were calculated using ammonia emission potential  $\Gamma_{\text{soil}}$  derived from IASI and ERA5 for March 2011 (case 3), and EC-Earth  $T_{\text{skin}}$  simulations for SSP2-4.5 and SSP5-8.5 extending from 2015 till 2099.

As seen in Eq. 4-22, higher skin temperatures favor volatilization of ammonia from the soil. In an attempt to understand how our simplified emission potential model behaves under changing



climate, as well as under future scenarios, we adopt the future T skin simulations from EC-Earth climate model, into Eq. 4-22. The two climate socioeconomic scenarios that we consider are SSP2-4.5 (“middle of the road” scenario where trends broadly follow their historical patterns), and SSP5-8.5 (a world of rapid and unconstrained growth in economic output and energy use) (Riahi et al., 2017).

I calculate current and future ammonia columns assuming that the emission potential  $\Gamma_{soil}$  remains unchanged. In other words, we assume that the same amount of fertilizers and manure is used until 2100 in the agricultural fields and farms (unchanged ammonium soil content). The future columns of ammonia are calculated using Eq. 4-21, while using  $\Gamma_{soil}$  calculated previously for March 2011, and  $T_{soil}$  from EC-Earth for the corresponding time range.

Figure 4.14 shows ammonia columns during the 25-year [2015 – 2039] representing the present climate (upper panels), and the end of the century [2075 – 2099] (middle panels). The ammonia columns in the 25-year average climate of the end of century with respect to present day climate (lower panels) are also shown.

Spatially, the present climate ammonia columns calculated from the T skin of the climate model and our emission potential from IASI (case 3 in Figure 4.10), agree very well with those shown in Figure 4.3. I do not aim at validating or directly comparing the two, as we are only interested in the climate response on ammonia concentration, i.e. by the difference due to skin temperature increase (lower panels).

From Figure 4.14 (lower panels) it can be seen that the increase in ammonia columns by the end of the century is more severe on the east side of Europe. Under the most likely scenario (SSP2-4.5), ammonia columns vary between +15 % in France, to around +20 % in the North European Plain (Figure 4.14). The largest increase is detected in Eastern Europe, where ammonia columns show an increase of up to a +50 % (Figure 5.14, lower left panels), creating new potential hotspots/sources of ammonia in Belarus, Ukraine, Hungary, Moldova, parts of Romania and Switzerland. Under the SSP5-8.5 scenario, the results show an increase in ammonia columns of up to +100 % in Eastern Europe (Figure 5.14, right lower panel). This is directly related to the higher projected increase in skin temperature over these regions. Other studies have equally reported Eastern Europe to be more affected by climate change under future scenarios, as

compared to Western Europe (European Environment Agency, 2022; Jacob et al., 2018). Spatially, the increase in ammonia coincides with the increase in T skin.

Figure 4.15 depicts the change in ammonia columns under the SSP2-4.5 and SSP5-8.5 scenarios, for our source regions (shown as rectangles in Figure 4.6). Ammonia columns increase is foreseen to be the highest in the Po Valley (Italy) with +26 % and +59 % under SSP2-4.5 and SSP5-8.5 respectively. It is then followed by the agricultural areas around Barcelona (Spain), and the North European Plain (Belgium, the Netherlands) with an increase of +21 % (+49 %) and +20 % (+53 %) respectively, under the SSP2-4.5 (SSP5-8.5) scenario. Under the SSP5-8.5, the increase in ammonia columns in percentage is more than twice the change under SSP2-4.5 (+127 % in the case of the Po Valley for instance). The Po Valley is adjacent to the Alps mountains, and due to global warming, this region is expected to experience increased evapotranspiration (Donnelly et al., 2017), which is a major factor that leads to the volatilization of ammonia.

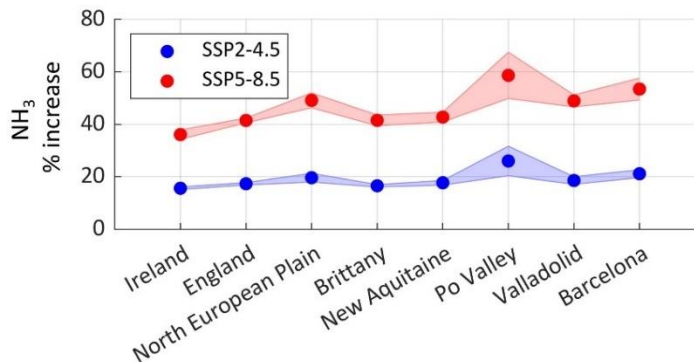


**Figure 4.15.** The percentage increase in ammonia concentration by the end of the century [2075 to 2099] with respect to the present climate [2015 to 2039] under the two climate scenarios SSP2-4.5 (blue) and SSP5-8.5 (red), in the source regions investigated in this study. The shades around each line represent the standard deviation from the mean.

The local and regional effect of volatilization of ammonia under different climate scenarios remains difficult to be properly assessed. Even under the “middle of the road” scenario 2-4.5, and without climate extremes (Husted & Schjoerring, 1996) (e.g. heatwaves), Europe might be facing big challenges in air or downwind agricultural regions, since chemistry and atmospheric transport (Figure 4.8) drive the loss of ammonia during the growing season in this part of the world.

An increase in ammonia concentration poses a significant and yet poorly understood effect on local and regional air quality through the increase in  $PM_{2.5}$  concentration. We note, however, that ammonia columns in the soil are governed by a threshold. Higher temperatures will increase the rate of volatilization of ammonia from the soil, but only up to a certain point where no dissolved ammonium is left. Plants, however, can also be a source of ammonia when exposed to stressful conditions. For example, under heat stress and in instances where there is no ammonia in the air, increase in air temperature results in exponential increase in ammonia emission from plants' leaves (Husted and Schjoerring, 1996).

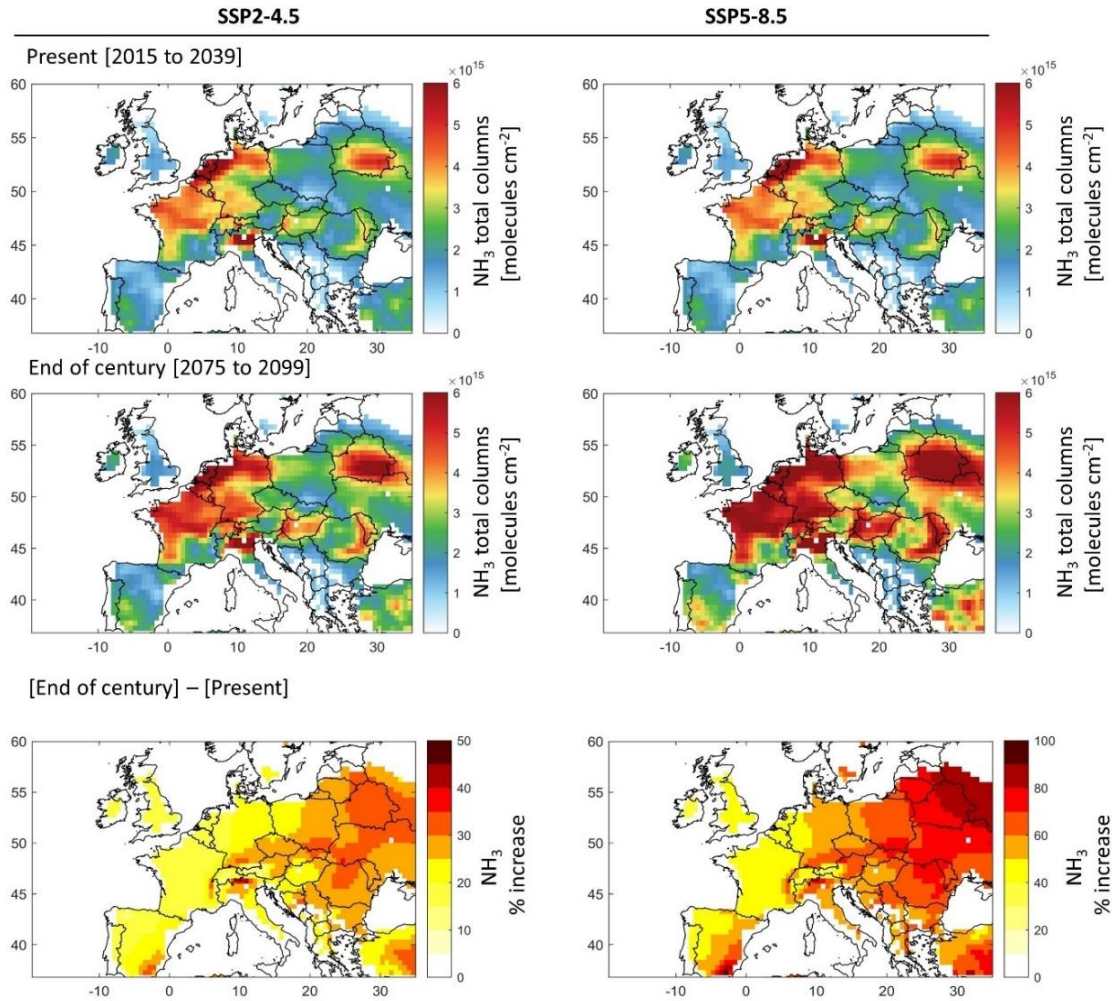


**Figure 4.16.** Same as Figure 4.14, but using emission potential  $\Gamma_{soil}$  derived from GEOS-Chem and MERRA-2.

Figure 4.16 shows future levels of ammonia using only simulation data (GEOS-Chem and EC-Earth). It is the same as Figure 4.14, but with  $\Gamma_{soil}$  from GEOS-Chem and MERRA-2 (case

1). One can see clearly the new hotspots in Eastern Europe (concentrated on Belarus), as compared to the ammonia concentrations from IASI. This can be due to the lower concentrations of ammonia in this region (March 2011), that can be below the detection limits of IASI. The increase in ammonia under both scenarios and from both IASI and GEOS-Chem agree greatly in Western and Southern Europe, the regions where we see high ammonia concentrations from both simulation and observation.

#### *4.4 Discussion and conclusions*

Agriculture worldwide has fed the human race for thousands of years, and will continue to do so, as mankind highly relies on it. Emissions from agricultural activities will inevitably increase, in order to meet the expected yield. In this chapter, I use a variety of state-of-the-art datasets (satellite, reanalysis and model simulation) to calculate the first regional map of ammonia emission potential during the start of the growing season in Europe. The emission potential can be used as a proxy to calculate ammonia columns in the atmosphere, and as such to assess its deposition, atmospheric transport, and contribution to PM formation. Here, we show that the GEOS-Chem chemistry transport model is able to reproduce key spatio-temporal patterns of ammonia levels over Europe. The ammonia budget is governed by the emissions over source regions (North European Plain, Brittany and the Po valley), as well as by key loss processes. We find that chemical loss pathway is responsible of 50 % or more of the total ammonia loss over Europe. From the GEOS-Chem simulation, we calculate the average ammonia lifetime in the atmosphere which ranges between 4 and 12 hours in agricultural source regions of Europe. From this, and using the mass transfer coefficient for different land cover types, we calculate a range of emission potentials  $\Gamma_{soil}$  from IASI and GEOS-Chem. We find that  $\Gamma_{soil}$  ranges between from  $2 \times 10^3$  to  $9.5 \times 10^4$  in fertilized lands (croplands). Choosing a variable  $k$  from the literature, and based on different land cover types from MODIS, we calculate  $\Gamma_{soil}$  values that are consistent with those found in the literature. The increase in T skin is expected to have an effect on the emission of ammonia from the soil. Using T skin from the EC-Earth climate model, we estimate ammonia columns by the end of the century [2075 – 2099], and compare it to columns of the present climate [2015 – 2039]. Our results show that ammonia columns will double under the SSP5-8.5 scenario, and will increase by up to 50 % under the most likely SSP2-4.5 scenario. The eastern part of Europe is the most affected by the change in temperatures, and it is where we find the highest

ammonia columns increase. Among the regions of focus, Italy, Spain, Belgium and the Netherlands are the most affected, as compared to France, England and Ireland. The highest increase in ammonia columns is observed in the Po Valley in Italy (+59 % under the SSP5-8.5).

In this chapter, I also calculate ammonia concentration under future climate and during the start of the growing season (March) in Europe. However, in order to grasp the yearly budget of ammonia, it is crucial to apply this method to all seasons of the year; especially in regions with extensive agricultural activities, such as the United States, India, and China. In addition to this, more field measurements of ammonia emission potential ( $\Gamma_{soil}$ ) in different land use / cover types are required, this can help us perform better comparison with emission potentials calculated from model and satellite data. Finally, having ammonia columns at different times of the day, from field observations or satellite measurements will allow quantification of daily emission potentials, that will in turn help us understand its diurnal variability. This will be ensured with the launch of the Infrared Sounder (IRS) on the Meteosat Third Generation (MTG) geostationary satellites scheduled in 2025.

## 4.5 Published article

<https://doi.org/10.5194/egusphere-2022-1046>  
Preprint. Discussion started: 3 November 2022  
© Author(s) 2022. CC BY 4.0 License.



### 1 **Estimating agricultural ammonia volatilization over Europe** 2 **using satellite observations and simulation data**

3 Rimal Abeed<sup>1</sup>, Camille Viatte<sup>1</sup>, William C. Porter<sup>2</sup>, Nikolaos Evangeliou<sup>3</sup>, Cathy Clerbaux<sup>1,4</sup>,  
4 Lieven Clarisse<sup>4</sup>, Martin Van Damme<sup>4,5</sup>, Pierre-François Coheur<sup>4</sup>, and Sarah Safieddine<sup>1</sup>

5  
6 <sup>1</sup>LATMOS/IPSL, Sorbonne Université, UVSQ, CNRS, Paris, France

7 <sup>2</sup>Department of Environmental Sciences, University of California, Riverside, CA 92521, USA

8 <sup>3</sup>Norwegian Institute for Air Research (NILU), Department of Atmospheric and Climate Research (ATMOS),  
9 Kjeller, Norway

10 <sup>4</sup>Université libre de Bruxelles (ULB), Spectroscopy, Quantum Chemistry and Atmospheric Remote Sensing  
11 (SQUARES), Brussels, Belgium

12 <sup>5</sup>Belgian Institute for Space Aeronomy (BIRA-IASB), Brussels 1180, Belgium

13  
14 Correspondence to: Rimal Abeed [rimal.abeed@latmos.ipsl.fr](mailto:rimal.abeed@latmos.ipsl.fr)

#### 15 16 **Abstract**

17 Ammonia (NH<sub>3</sub>) is one of the most important gases emitted from agricultural practices. It affects air  
18 quality and the overall climate, and in turn influenced by long term climate trends as well as by short term  
19 fluctuations in local and regional meteorology. Previous studies have established the capability of the Infrared  
20 Atmospheric Sounding Interferometer (IASI) series of instruments aboard the Metop satellites to measure  
21 ammonia from space since 2007. In this study, we explore the interactions between atmospheric ammonia, land  
22 and meteorological variability, and long-term climate trends in Europe. We investigate the emission potential  
23 ( $\Gamma_{soil}$ ) of ammonia from the soil, which describes the soil – atmosphere ammonia exchange.  $\Gamma_{soil}$  is generally  
24 calculated in-field or in laboratory experiments; here, and for the first time, we investigate a method which assesses  
25 it remotely using satellite data, reanalysis data products, and model simulations.

26 We focus on ammonia emission potential during March 2011, which marks the start of growing season  
27 in Europe. Our results show that  $\Gamma_{soil}$  ranges from  $2 \times 10^3$  to  $9.5 \times 10^4$  (dimensionless) in a fertilized cropland,  
28 such as in the North European Plain, and is of the order of  $10 - 10^2$  in a non-fertilized soil (e.g. forest and grassland).  
29 These results agree with in-field measurements from the literature, suggesting that our method can be used in other  
30 seasons and regions in the world. However, some improvements are needed in the determination of mass transfer  
31 coefficient  $k$  (m s<sup>-1</sup>), which is a crucial parameter to derive  $\Gamma_{soil}$ .

32 Using a climate model, we estimate the expected increase in ammonia columns by the end of the century  
33 based on the increase in skin temperature (T<sub>skin</sub>), under two different climate scenarios. Ammonia columns are  
34 projected to increase by up to 50 %, particularly in Eastern Europe, under the SSP2-4.5 scenario, and might even  
35 double (increase of 100 %) under the SSP5-8.5 scenario. The increase in skin temperature is responsible for a  
36 formation of new hotspots of ammonia in Belarus, Ukraine, Hungary, Moldova, parts of Romania, and  
37 Switzerland.  
38



<https://doi.org/10.5194/egusphere-2022-1046>

Preprint. Discussion started: 3 November 2022

© Author(s) 2022. CC BY 4.0 License.



## 39 1. Introduction

40 Ammonia ( $\text{NH}_3$ ) emissions have been increasing in a continuous manner from 1970 to 2017 (McDuffie et al.,  
41 2020). During the period 2008 – 2018 alone, the increase in ammonia columns in Western and Southern Europe  
42 accounted to  $20.8 \text{ \% yr}^{-1}$  ( $\pm 4.3 \text{ \%}$ ), and to  $12.8$  ( $\pm 1.3 \text{ \%}$ ) globally (Van Damme et al., 2021). Although ammonia  
43 alone is stable against heat and light, it is considered a very reactive base, whereas it constitutes the largest portion  
44 of the reactive nitrogen ( $\text{N}_r$ ) on Earth. The vast majority of atmospheric ammonia not deposited is transformed into  
45 fine particulate matter ( $\text{PM}_{2.5}$ ) composed of ammonium ( $\text{NH}_4^+$ ), through acid – base chemical reactions with  
46 available acids in the environment, namely sulfuric acid ( $\text{H}_2\text{SO}_4$ ), hydrochloric acid ( $\text{HCl}$ ), and nitric acid ( $\text{HNO}_3$ )  
47 (Yu et al., 2018), while only 10 % of the total ammonia gas are believed to be oxidized by hydroxyl radicals ( $\text{OH}^\cdot$ )  
48 (Roelle and Aneja, 2005).  $\text{PM}_{2.5}$  has degrading effects on human health, especially respiratory diseases (Bauer et  
49 al., 2016). In addition to agriculture, ammonia can be emitted from industrial processes, biomass burning (Van  
50 Damme et al., 2018), and natural activities such as from seal colonies (Theobald et al., 2006).

51  
52 Soils are known to be a source of atmospheric ammonia, especially in areas of intensive agricultural practices  
53 (Schlesinger and Hartley, 1992), and this is due to enriching the soil with the reactive nitrogen present in fertilizers.  
54 The increase in the application of synthetic fertilizers, and intensification of agricultural practices is believed to be  
55 the dominant factor of the global increase in ammonia emissions over the past century (Behera et al., 2013;  
56 McDuffie et al., 2020).

57  
58 Following the application of fertilizers, ammonium and ammonia are released in the soil. Prior to its volatilization,  
59 ammonia in the soil exists either in the gas phase ( $\text{NH}_{3(g)}$ ) or in the aqueous/liquid phase ( $\text{NH}_{3(aq)}$ ), the equilibrium  
60 between both states of ammonia is governed by Henry's law (Wentworth et al., 2014), as shown in A. The  
61 dissociation of ammonia in soil water is affected by soil acidity (pH) and temperature (Roelle and Aneja, 2005)  
62 (Eq. (A-1) and (A-2) in Appendix A); it is explained by the dissociation constant  $K_{\text{NH}_4^+}$ . Once released to the  
63 atmosphere, ammonia near the surface exists in the gas phase, hence Henry's law describes the equilibrium  
64 between ammonia in the soil (liquid phase), and near the surface (gas phase). This bi-directional exchange between  
65 the soil and the atmosphere will continue until the equilibrium is reached, and this occurs when ammonia  
66 concentration is equal to the compensation point  $\chi_{\text{NH}_3}$  (the concentration of ammonia at equilibrium). The flux of  
67 ammonia from the soil to the atmosphere (emission) occurs when the concentration of atmospheric ammonia is  
68 less than the compensation point  $\chi_{\text{NH}_3}$ , while ammonia deposition occurs when the concentration of ammonia is  
69 equal to or greater than  $\chi_{\text{NH}_3}$  (Flechar et al., 2011; Wichink Kruit, 2010). It is then crucial to quantify the  
70 compensation point in order to understand this bi-directional exchange. The main variables needed to calculate  
71  $\chi_{\text{NH}_3}$  are soil temperature ( $T_{\text{skin}}$ ) and  $I_{\text{soil}}$ , which is a dimensionless ratio between ammonium and pH ( $\text{NH}_4^+(\text{aq})$   
72 and  $\text{H}^+(\text{aq})$  concentrations, respectively, in the soil). All the equations are described in Appendix A (Eq. (A-1) to  
73 (A-15)).

74  
75 The soil emission potential ( $I_{\text{soil}}$ ) has been thoroughly investigated in field and controlled laboratory environments  
76 (e.g. David et al., 2009; Flechar et al., 2013; Massad et al., 2010; Mattsson et al., 2008; Nemitz et al., 2000;  
77 Wentworth et al., 2014, among others).  $I_{\text{soil}}$  is dimensionless and it can range from 20 (non-fertilized soil in a  
78 forest) to the order of  $10^6$  (mixture of slurry in a cropland). It is found to peak right after fertilizers application,  
79 due to the increase in ammonium content in the soil (a product of urea hydrolysis), reaching pre-fertilization levels  
80 10 days following the application (Flechar et al., 2010; Massad et al., 2010). Little information exists on regional  
81 or global scales to assess the large-scale spatial variability of ammonia emission potentials.

82  
83 In order to meet the needs for a growing population, agricultural practices have intensified during the period 2003  
84 – 2019 (more fertilizer use per surface area), resulting in an increase in the net primary production (NPP) per capita

<https://doi.org/10.5194/egusphere-2022-1046>  
 Preprint. Discussion started: 3 November 2022  
 © Author(s) 2022. CC BY 4.0 License.



(Potapov et al., 2022), subsequently increasing volatilized ammonia (increase in nitrogen soil content, and cultivated lands). In Europe alone, the area of croplands increased by 9 % from 2003 to 2019, and most of the expansion took place on lands that were abandoned for more than 4 years (Potapov et al., 2022). Between the year 2008 and 2018, the increase in atmospheric ammonia columns accounted to 20.8 % ( $\pm 4.3$  %) in Western and Southern Europe (Van Damme et al., 2021). With the increase in croplands area and agricultural activities, climate change will have a significant effect on agricultural practices, with warmer climates enhancing the volatilization of ammonia from soils, especially in intensely fertilized lands (Shen et al., 2020).

This study aims at exploring ammonia emission potential/volatilization in Europe, using infrared satellite data of ammonia columns, reanalysis temperature data, and chemical transport model simulations to provide information on chemical sources and sinks. We specifically study the relationship between satellite-derived ammonia concentration at the start of the growing season, soil emission potentials and their spatial variability over Europe during March of 2011. Section 2 provides the methods/datasets used. Simulation results are described in Sect. 3, and regional emission potentials are shown and discussed in Sect. 4. Using a climate model, future projections of ammonia columns are investigated under different climate scenarios in Sect. 5. Discussion and conclusions are listed in Sect. 6.

## 2. Methodology

### 2.1. Calculation of the emission potential

In this study, we use IASI satellite data to calculate the ammonia emission potential  $\Gamma_{soil}$  instead of field soil measurements. In field studies,  $\Gamma_{soil}$  is calculated by measuring the concentration of ammonium ( $\text{NH}_4^+$ ) and  $\text{H}^+$  ( $10^{\text{pH}}$ ) in the soil; the ratio between both of these concentrations is  $\Gamma_{soil}$ . In this study, we use infrared satellite ammonia to have a regional coverage over Europe. With these, we cannot monitor soil content of ammonium nor its pH. This renders the remote  $\Gamma_{soil}$  calculation challenging, and less straight forward. The full derivation of the equation used to calculate the emission potential is explained in Appendix A, and was briefly described in the introduction. In short, upon its dissolution in the soil water, ammonia follows Henry's law. In steady state conditions between the soil and the near surface, the amount of the ammonia emitted and lost is considered equal. Based on this assumption, the soil emission potential (dimensionless) is calculated as follows Eq. (2-1) or Eq. (A-15) in Appendix A:

$$\Gamma_{soil} = \frac{[\text{NH}_3]^{col} \cdot T_{soil}}{\exp\left(\frac{-b}{T_{soil}}\right)} \cdot \frac{M_{\text{NH}_3}}{a \cdot N_a \cdot c'} \cdot \frac{1}{k\tau} \quad (2-1)$$

Where  $[\text{NH}_3]^{col}$  is the total column concentration of ammonia (molecules  $\text{cm}^{-2}$ ), measured by satellite remote sensors,  $T_{soil}$  is the soil temperature at the surface, which can be expressed as the skin temperature,  $T_{skin}$  (Kelvin),  $a$  and  $b$  are constants ( $a = 2.75 \times 10^3 \text{ g K cm}^{-3}$ ,  $b = 1.04 \times 10^4 \text{ K}$ ),  $M_{\text{NH}_3}$  is the molar mass of ammonia gas ( $M = 17.031 \text{ g mol}^{-1}$ ), and  $N_a$  is Avogadro's number ( $N_a = 6.0221409 \times 10^{23} \text{ molecules mol}^{-1}$ ),  $c'$  is equals to 100 and is added to convert  $k$  from  $\text{m s}^{-1}$  to  $\text{cm s}^{-1}$  (since  $[\text{NH}_3]^{col}$  is in molecules  $\text{cm}^{-2}$ ), and  $\tau$  the lifetime of ammonia (seconds).  $k$  is the soil – atmosphere exchange coefficient or deposition velocity ( $\text{cm s}^{-1}$ ), also known as the mass transfer coefficient (this nomenclature will be used in this study). It is found to be affected by the roughness length of the surface, wind speed, the boundary layer height (Olesen and Sommer, 1993; Van Der Molen et al., 1990), and pH



<https://doi.org/10.5194/egusphere-2022-1046>  
 Preprint. Discussion started: 3 November 2022  
 © Author(s) 2022. CC BY 4.0 License.



(Lee et al., 2020). It can be explained by a resistance model often used to explain the exchange between the surface and the atmosphere (Wentworth et al., 2014). Different studies provide look up tables values of  $k$  for different land cover types and different seasons based on this resistance model (Aneja et al., 1986; Erisman et al., 1994; Phillips et al., 2004; Roelle and Aneja, 2005; Svensson and Ferm, 1993; Wesely, 1989). In general, the mass transfer coefficient  $k$  is in the order of  $10^{-3}$  to  $10^{-2}$   $\text{m s}^{-1}$  in a mixture of soil and manure, and  $10^{-6}$  to  $10^{-5}$   $\text{m s}^{-1}$  in a mixture of manure alone (Roelle and Aneja, 2005). We discuss and provide more information on  $k$  in Sect. 4, and additional details on this calculation in general are provided in Appendix A.

## 2.2. IASI ammonia, ERA5 T skin, and MODIS Land cover

The Infrared Atmospheric Sounding Interferometer (IASI) is considered advanced the most innovative instrument onboard the polar-orbiting Metop satellites (Klaes, 2018). Three IASI instruments are onboard Metop-A, B and C, the series of satellites launched by the EUMETSAT (European Organization for the Exploitation of Meteorological Satellites) in 2006, 2012, and 2018, respectively. The Metop-A satellite was de-orbited in October 2021 (Lentze, 2021), and as a result only two instruments (IASI-B and C onboard Metop-B and C) are operating today. The observations from IASI cover any location on Earth at 9:30 in the morning (AM) and in the evening (PM), local solar time. It can detect a variety of atmospheric species including trace gases (Clerbaux et al., 2009). The IASI Fourier-transform spectrometer monitors the atmosphere in the spectral range between 645 and 2760  $\text{cm}^{-1}$  (thermal infrared), and is nadir-looking. IASI has a swath width that measures 2200 km, with a pixel size of  $\sim 12$  km.

Ammonia was first detected with IASI using the  $\nu_2$  vibrational band of ammonia ( $\sim 950$   $\text{cm}^{-1}$ ) (Clerbaux et al., 2009; Coheur et al., 2009). The ammonia total columns used in this study are the product of an Artificial Neural Network and re-analyzed temperature data from the European Centre for Medium-Range Weather Forecasts (ECMWF) product ERA5 ANNI-NH<sub>3</sub>-v3R-ERA5 (Van Damme et al., 2021). Several studies used ammonia data from IASI to study hotspots of ammonia of different source types including both natural and anthropogenic sources (Clarisse, Van Damme, Clerbaux, et al., 2019; Clarisse, Van Damme, Gardner, et al., 2019; Dammers et al., 2019; Van Damme et al., 2018, 2021; Viatte et al., 2021). Recently, IASI observations were used to study the effect of war and conflict on agricultural practices in Syria (Abeed et al., 2021).

Fewer errors on the retrieval were observed during the day and over land (Van Damme et al., 2017), hence, we use only daytime ammonia measurements from IASI. Comparisons with ammonia measured using a ground-based instrument showed a good correlation of  $R=0.75$  (Viatte et al., 2021). Satellite ammonia data from CrIS (Crosstrack Infrared Sounder) (Shephard and Cady-Pereira, 2015) were compared with those from IASI, and were equally found to give similar results when looking at concentrations from a wildfire (Adams et al., 2019), showing consistency when studying seasonal and inter-annual variability (Viatte et al., 2020).

In addition to ammonia, we look at skin temperature ( $T_{\text{skin}}$  or land surface temperature LST) data from the ECMWF reanalysis (ERA5) at a grid resolution of  $0.25 \times 0.25^\circ$  (Hersbach et al., 2020). ERA5 Temperatures are interpolated temporally and spatially to the IASI morning overpass ( $\sim 9:30$  A.M. local time), since we only consider daytime ammonia. ERA5 temperature data are also used in the retrieval process of the ammonia data we used in this study NH<sub>3</sub>-v3R-ERA5 (Van Damme et al., 2021).  $T_{\text{skin}}$  is defined as the temperature of the uppermost surface layer when radiative equilibrium is reached. It also represents the theoretical temperature required in order to reach the surface energy balance (ECMWF, 2016).

https://doi.org/10.5194/egusphere-2022-1046  
 Preprint. Discussion started: 3 November 2022  
 © Author(s) 2022. CC BY 4.0 License.



In order to assign a mass transfer coefficient  $k$  to each land type, the moderate resolution imaging spectroradiometer (MODIS), a series of instruments orbiting the Earth aboard the Aqua and Terra satellites, is used. The data product MCD12Q1 (version 6) is a combined Aqua/Terra Land cover type product, with a spatial resolution of 500 m. This product provides maps of land cover type from 2001 through 2019 (Sulla-Menashe and Friedl, 2018). From the land use categories included in the MOD12Q1 product (Belward et al., 1999) we focus on croplands, forests, shrublands, and grasslands. We do not include barelands, snow cover, and urban areas in our analysis; we are not interested in studying these surfaces, since we focus on ammonia volatilization from the soil in areas amended with fertilizers. We show the emission potential in Forests and grasslands/shrublands for comparison with values in the literature. In an attempt to calculate an emission potential (Eq. (2-1)) that is relevant to the land cover/use, we therefore assign a mass transfer coefficient  $k$  to each land type based on literature values (Aneja et al., 1986; Erisman et al., 1994; Roelle and Aneja, 2005; Svensson and Ferm, 1993; Wesely, 1989) and we discuss it in Sect. 4.

### 2.3. Model simulations

#### 2.3.1. GEOS-Chem Chemistry Transport Model

In this study we use version 12.7.2 of the GEOS-Chem chemical transport model (Bey et al., 2001). The model is driven by the Modern-Era Retrospective Analysis for Research and Applications version 2 (MERRA-2) reanalysis product, including nested domains over Europe at a  $0.5^\circ \times 0.625^\circ$  horizontal resolution. MERRA-2 is the second version of the MERRA atmospheric reanalysis product by NASA Global Modulation Assimilation Office (NASA/GMAO) (Gelaro et al., 2017). Boundary conditions for the nested domains are created using a global simulation for the same months at  $2^\circ \times 2.5^\circ$  resolution. We generate model output for March of 2011, preceded by a one month of discarded model spin-up time for the nested run, and two months for the global simulation. March corresponds well to the month of fertilizer application in Europe, and as such to the beginning of the growing season (FAO, 2022; USDA, 2022).

Output includes the monthly mean for selected diagnostics. Anthropogenic emissions are taken primarily from the global Community Emissions Data System (CEDS) inventory (Hoesly et al., 2018). Biogenic non-agricultural ammonia, as well as ocean ammonia sources, are taken from the Global Emission Inventories Activities database (GEIA, (Bouwman et al., 1997)). Open fire emissions are generated using the GFED 4.1s inventory (Randerson et al., 2015). We used the Harmonized Emissions Component module (HEMCO) to obtain the ammonia emissions over Europe (Keller et al., 2014).

#### 2.3.2. EC-Earth Climate model

To analyze how future climate will affect ammonia concentration and emission potential, we use the ECMWF climate model the European Earth Consortium climate model (EC-Earth, <http://www.ec-earth.org/>). While other climate models exist, we choose this one because the ammonia product from IASI uses ERA5 for the retrievals and we calculate the emission potential from the T skin product of ERA5. The reanalysis uses the ECMWF Integrated Forecasting System for the atmosphere-land component (IFS). IFS is also used in EC-Earth and is complemented with other model components to simulate the full range of Earth system interactions that are relevant to climate (Döscher et al., 2021). We note that the versions of the IFS models used in ERA5 and in EC-Earth are not identical as the climate model product is not assimilated and is not initialized with observations

<https://doi.org/10.5194/egusphere-2022-1046>

Preprint. Discussion started: 3 November 2022

© Author(s) 2022. CC BY 4.0 License.



several times a day like ERA5. The EC-Earth simulations are included in the Climate model intercomparison project, phase 6 (Eyring et al., 2016), part of the Intergovernmental Panel on Climate Change (IPCC) report of 2021 (Masson-Delmotte, et al., 2021). We use the so-called Scenario Model Intercomparison Project (ScenarioMIP), covering the period [2015 – 2100] for future projections under different shared socio-economic pathways (SSP) (Riahi et al., 2017). We analyze two scenarios, the SSP2-4.5 corresponding to “middle of the road” socio-economic family with a nominal  $4.5\text{W/m}^2$  radiative forcing level by 2100 - approximately corresponding to the RCP-4.5 scenario, and the SSP5-8.5 marks the upper edge of the SSP scenario spectrum with a high reference scenario in a high fossil-fuel development world throughout the 21st century.

### 3. GEOS-Chem model simulation: validation and analysis

#### 3.1. GEOS-Chem validation with IASI

In order to analyse how well the model simulates atmospheric ammonia, we use the simulated GEOS-Chem monthly averaged (March 2011) ammonia total columns output (Sect. 2.3.1). We compare those to the IASI total columns of ammonia gridded on the same horizontal resolution ( $0.5^\circ \times 0.625^\circ$ ) and over the same month.

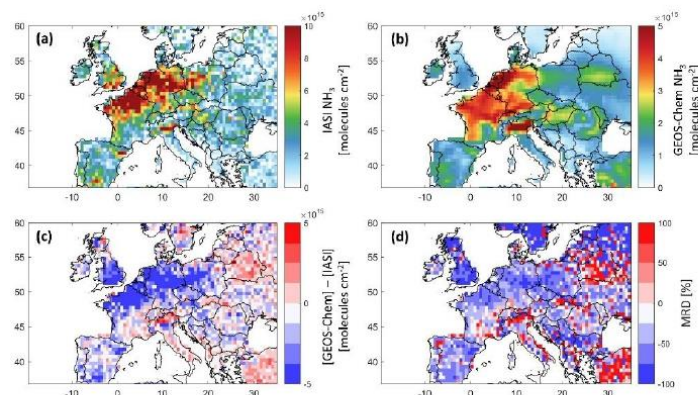


**Figure 1.** Ammonia total column concentrations from IASI (panel a), and GEOS-Chem (panel b), the difference between both datasets (panel c) in molecules  $\text{cm}^{-2}$ , and the Mean Relative Difference (MRD) in % (panel d); all data are a monthly average of March 2011, and over Europe at a  $0.5^\circ \times 0.625^\circ$  grid resolution. Note that the colour bar limits are different between panels (a) and (b).

Figure 1 shows the IASI  $\text{NH}_3$  distribution (Figure 1a), and that from GEOS-Chem (Figure 1b), the bias between the two (Figure 1c), and the mean relative difference MRD (Figure 1d), all during March 2011. MRD is calculated as the mean of the ratio  $\frac{(\text{GeosChem } \text{NH}_3 - \text{IASI } \text{NH}_3) \times 100}{\text{IASI } \text{NH}_3}$  at each grid point.



<https://doi.org/10.5194/egusphere-2022-1046>

Preprint. Discussion started: 3 November 2022

© Author(s) 2022. CC BY 4.0 License.



231 Generally, both GEOS-Chem and IASI show coincident sources of ammonia, reflecting the good ability of the  
232 model to reproduce ammonia columns over major agricultural source regions in Europe. The bias between IASI  
233 and GEOS-Chem and the MRD are shown in Figure 1c and d. Ammonia columns from GEOS-Chem are  
234 underestimated by up to  $2 \times 10^{16}$  molecules/cm<sup>2</sup> in some source regions/over hotspots, especially in England, North  
235 Eastern France, the North European Plain (Netherlands, Belgium), and Spain (around Barcelona). Similar results  
236 were found in the study of Whitburn et al. (2016), in which they show that GEOS-Chem underestimates ammonia  
237 columns by up to  $1 \times 10^{16}$  molecules/cm<sup>2</sup> in Europe on a yearly average in 2009, notably in the North European  
238 Plain. It is important to note that, in our study, we compare only one month of data (March, 2011) that marks the  
239 start of the growing season in the majority of the countries of interest (FAO, 2022; USDA, 2022). The differences  
240 are mainly because of the time coincidence, and the fact that only cloud-free data are used to retrieve ammonia;  
241 IASI observes ammonia during the satellite overpass (~9:30 AM local time), whereas the GEOS-Chem simulation  
242 is averaged over the whole month including all hours of the day. In Western and Northern Europe, the MRD is  
243 mostly less than -50 %, for instance, in the North European Plain (-49 %). If we look at the average MRD in  
244 regions of focus, we see that the Po Valley in Italy has the highest MRD value (+110 %), whereas the best  
245 represented region is New Aquitaine in the southwest of France (-20 %). The rest of the regions have mean MRDs  
246 that fluctuate between -64 % and -42 %. A summary of the results of this study, including the MRD over some  
247 source regions is listed in Table 1. Although the bias and MRD can be considered high, the spatial distribution is  
248 consistent between IASI and GEOS-Chem. Therefore, according to the steady state approximation, the  
249 meteorological and soil parameters affecting one dataset (e.g. IASI NH<sub>3</sub>) are applicable to the other (e.g. model  
250 simulation). It is worth noting that although we do not use the latest version of GEOS-Chem, the results we obtain  
251 reflects our current understanding of the regional chemistry at this horizontal and temporal resolution.

### 252 3.2. Ammonia emissions, losses and lifetime in Europe

253 In order to understand the NH<sub>3</sub> spatial variability in Europe during the application of fertilizers, a detailed analysis  
254 of the output of the GEOS-Chem simulation for the month of March 2011 is shown in Figure 2.  
255 The anthropogenic sources (i.e. mainly agriculture) contribute 83 % of the total ammonia emissions during March  
256 2011 in Europe. The ammonia emissions from natural sources (i.e. soil of natural vegetation, oceans, and wild  
257 animals) follow representing 16 % of the total emissions, whereas the remaining 1 % correspond to the ammonia  
258 emissions from biomass burning and ships (not shown here).  
259 Figure 2a shows ammonia monthly emissions. Most of them are due to agricultural activities (not shown here); we  
260 identify 8 source regions which we investigate thoroughly in this study shown as rectangles A to H. The highest  
261 agricultural sources over Europe include the North European Plain, Brittany, and the Po Valley (regions C, D, and  
262 F).  
263 In the calculation of the total loss of ammonia (Figure 2b), we considered dry deposition, chemistry, transport, and  
264 wet deposition (in which we included ammonia loss to convection) from the GEOS-Chem model simulation, which  
265 are all possible loss processes for ammonia (David et al., 2009). Figure 2b shows that the largest losses occur  
266 logically where we have the highest sources detected (see Figure 2a).

<https://doi.org/10.5194/egusphere-2022-1046>  
 Preprint. Discussion started: 3 November 2022  
 © Author(s) 2022. CC BY 4.0 License.

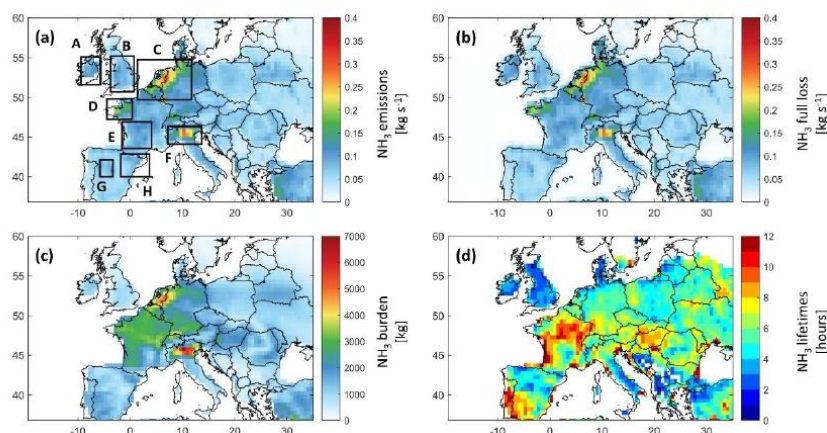


**Figure 2. Ammonia budget in Europe from GEOS-Chem: (a) Ammonia emissions from the Harmonized Emissions Component module (HEMCO) in  $\text{kg s}^{-1}$  with our regions of interest shown in rectangles, (b) ammonia full loss in  $\text{kg s}^{-1}$ , (c) ammonia total burden in kg, and (d) ammonia lifetime in hours. All plots refer to March 2011 and are presented at a  $0.5^\circ \times 0.625^\circ$  grid resolution.**

269 The total ammonia burden (Figure 2c) is calculated as the integrated sum of all ammonia columns in the model  
 270 grid box. We can clearly detect ammonia hotspots over Europe, in particular the North European Plain, Brittany  
 271 and the Po Valley, all regions characterized by intense agricultural activities, as the total emissions and deposition  
 272 show (Figure 1 and Figure 2). We also see that the burden is generally the highest over France, Belgium, The  
 273 Netherlands, and parts of Germany and Italy.

274  
 275 We finally get the lifetime  $\tau_{ss}$  of ammonia (Figure 2d). In the case of a gas with a short lifetime, such as ammonia,  
 276 the emissions are relatively well-balanced spatially by eventual sinks/losses (steady-state approximation).  
 277 Therefore, we can calculate a steady-state lifetime as the ratio between the total burden  $B$  (Figure 2c) and the total  
 278 emissions  $E$  or losses  $L$  (sum of all emitted / lost molecules, Figure 2a or b) using the following equation:  $\tau_{ss} =$   
 279  $B/L$  (Plumb and Stolarski, 2013).

280  
 281 We note that the  $\tau_{ss}$  is more or less the same whether we calculate it using the losses or the emissions. For instance,  
 282 in selected source regions (rectangles in Figure 2a) the total emissions and losses are very close with very low  
 283 biases that are less than 2% (not shown here). Our results show that  $\tau_{ss}$ , on a monthly average, can go up to 12  
 284 hours, and it can reach 1 day (24 hours) in coastal regions such as region E in New Aquitaine in France. The latter  
 285 can be related to the high probability of air stagnation in that area in comparison to Northern Europe (Garrido-  
 286 Perez et al., 2018), since higher  $\text{PM}_{2.5}$  pollution episodes were found under stagnant meteorological conditions  
 287 (AQEG, 2012); and ammonium molecules carried on these  $\text{PM}_{2.5}$  can transform back into ammonia. Our results  
 288 agree with the literature suggesting a residence time between a few hours to a few days (Behera et al., 2013; Pinder  
 289 et al., 2008), and with those calculated by Evangelizou et al. (2021) over Europe, showing a monthly average of  
 290 ammonia lifetime that ranges from 10 to 13 hours in Europe. The figure adapted from Evangelizou et al. (2021) is

<https://doi.org/10.5194/egusphere-2022-1046>  
 Preprint. Discussion started: 3 November 2022  
 © Author(s) 2022. CC BY 4.0 License.



shown in supplementary material (Figure S1). Shorter lifetimes from industrial sources of ammonia were reported in Dammers et al. (2019), with a mean lifetime of ammonia that is equal to 2.35 hours ( $\pm 1.16$ ). A recent study found lifetimes of ammonia that vary between 5 and 25 hours, roughly, in Europe (Luo et al., 2022); these values are higher since, in addition to ammonia loss, Luo et al. (2022) included the loss of ammonium, and thus considering the loss of ammonia only terminal when the ammonium is also lost/deposited. This approach is not considered here nor in Evangeliou et al. (2021).

Notably, ammonia lifetime and burden (Figure 2c, and d) each have different spatial distribution compared to the other 2 panels (Figure 2a, and b). The ammonia residence time in the atmosphere varies depending on the sources and more importantly on the locally dominant loss mechanisms. For this reason, in Figure 3, we show the relative contribution of the ammonia loss mechanisms, presented as pie charts, for the agricultural source regions shown in black boxes in Figure 2a.

The fastest loss mechanisms are either chemical (i.e. in the vast majority transformation to particulate matter) or through wet and dry deposition (Tournadre et al., 2020). Figure 3 shows that more than 50 % of the ammonia molecules in the atmosphere are lost to chemical reactions in most of the regions (A, B, C, H, and F). The shortest residence time of ammonia is observed in England, where the chemical removal was significantly higher than other sinks and represented up to 73 % of the total ammonia loss pathways, suggesting a rapid transformation into inorganic particulate matter ( $PM_{2.5}$ ). In the regions D, G and E the chemical loss makes up 50 %, 49 %, and 42 %, respectively. In fact, in March 2011, PM was found to be mostly composed of inorganic nitrate (41 %), and ammonium (20 %) (Viatte et al., 2022) over Europe, both of which are products of atmospheric ammonia. Nitrate-bearing  $PM_{2.5}$  are formed when nitric acid ( $HNO_3$ ) reacts with ammonia (Yang et al., 2022), and ammonium is a direct product of the hydrolysis of ammonia. 41% of the nitric acid formed in the atmosphere is produced from the reaction between nitrogen dioxide ( $NO_2$ ) and the hydroxyl radical (OH) (Alexander et al., 2020). These chemical pathways help explain the large chemical losses in most of the regions studied in Figure 3.

Ammonia loss to transport is the highest in regions neighboring the Atlantic Ocean, accounting for 30 %, 27 %, 32 %, and 34 % of total sinks in regions A, D, E, and G respectively. These regions are exposed to the North Atlantic Drift, also known as the Gulf Stream, that is associated with high wind speed and cyclonic activity (Barnes et al., 2022). In other regions, 14 % to 22 % of the total ammonia is lost to transport mechanisms, and in all regions, 11 to 22 % is lost to dry deposition (Figure 3). During March, precipitation is relatively lower as compared to winter (December, January, February) in Europe. Furthermore, 2011 was a particular dry year compared to the 1981 – 2010 average (Met Office, 2016). Drought was reported to be severe in areas such as France, Belgium and the Netherlands, and moderate in England and Ireland (EDO, 2011). This can help explain the low percentage of wet deposition during March 2011 (1 to 5 % out of the total loss of ammonia).



<https://doi.org/10.5194/egusphere-2022-1046>  
 Preprint. Discussion started: 3 November 2022  
 © Author(s) 2022. CC BY 4.0 License.

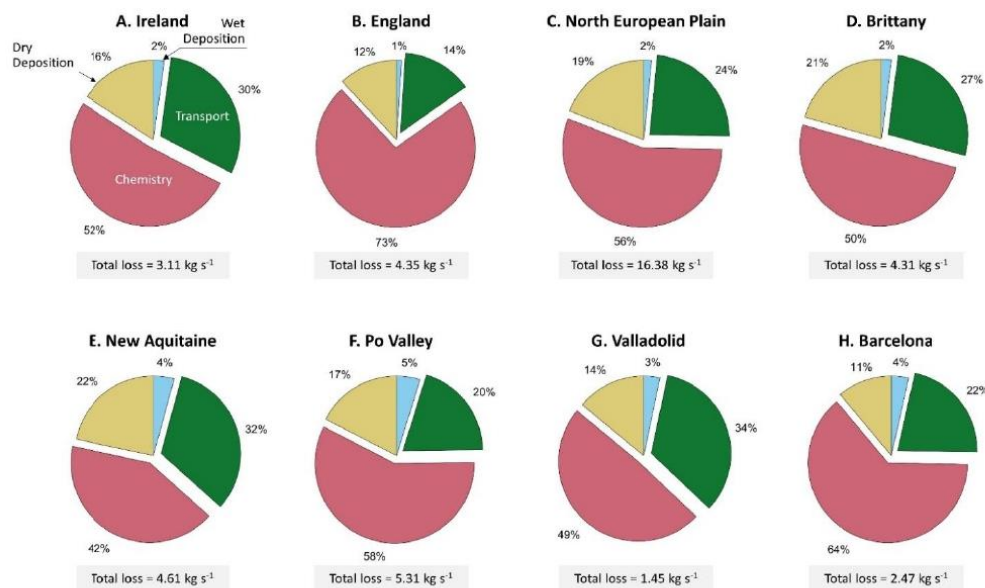


**Figure 3.** Repartition of the ammonia loss mechanisms for major agricultural areas in Europe, during March 2011, as retrieved from GEOS-Chem, with the total ammonia loss shown in a grey box under each pie chart ( $\text{kg s}^{-1}$ ). The regions are shown in black boxes in Figure 2a.

326

#### 327 4. Ammonia emission potential over Europe

328

329 To calculate emission potential, a calculation of the mass transfer coefficient  $k$ , which relates to the land type, is  
 330 necessary. Figure 4 shows the land cover type from MODIS in Europe (left panel), and the corresponding assigned  
 331 mass transfer coefficient  $k$  (right panel) needed to calculate the emission potential (Eq. (2-1)). In order to choose  
 332 a mass transfer coefficient that is convenient for the different land types relevant to this study, we searched for  $k$   
 333 values in the literature. Not all land types have been studied for ammonia transfer coefficient.

334 For water bodies and other land types that are not considered here (see Sect. 2.2), the mass transfer values  $k$  were  
 335 set to zero and represented in grey colour in Figure 4. In a laboratory experiment, Svensson et al. (1993) reported  
 336  $k = 4.3 \times 10^{-3} \text{ m s}^{-1}$  for a mixture of soil and swine manure, as therefore, we assign this value to croplands. Due  
 337 to the lack of  $k$  values for non-fertilized forests, shrublands and grasslands in the literature, we used values  
 338 originally assigned for  $\text{SO}_2$ , bearing in mind that these are approximate values and they reflect mostly the  
 339 conditions of the soil cover type (short, medium or tall grass). To assign a  $k$  value for forests, we used values  
 340 reported in Aneja (1986) ( $k = 2 \times 10^{-2} \text{ m s}^{-1}$ ), which originally represent deposition velocity (mass transfer) of

<https://doi.org/10.5194/egusphere-2022-1046>  
 Preprint. Discussion started: 3 November 2022  
 © Author(s) 2022. CC BY 4.0 License.



SO<sub>2</sub> in a forest (high crops). For shrublands and grasslands (the two land types have the same  $k$ ), we used the value  $k = 8 \times 10^{-3} \text{ m s}^{-1}$  that has been reported in Aneja et al. (1986) as the deposition velocity (mass transfer) of SO<sub>2</sub> in a grassland (medium crops). These values are the best attempt to test the validity of using MODIS and lookup tables of  $k$  values to calculate a realistic soil emission potential. As a result, Figure 4 (left panel) includes 5 land types, while  $k$  values are reported for 4 land types (other land type/water, croplands, forests, and shrublands/grasslands).

After choosing the  $k$  values, we assigned them for each land type on the  $(500 \text{ m} \times 500 \text{ m})$  grid. We then extrapolate the array with the  $k$  values from  $500 \text{ m} \times 500 \text{ m}$  to the resolution of GEOS-Chem ( $0.5^\circ \times 0.625^\circ$  grid box). This leads to averaging different fine pixels with different land cover types into a coarser grid. The result is shown on the right panel of Figure 4.

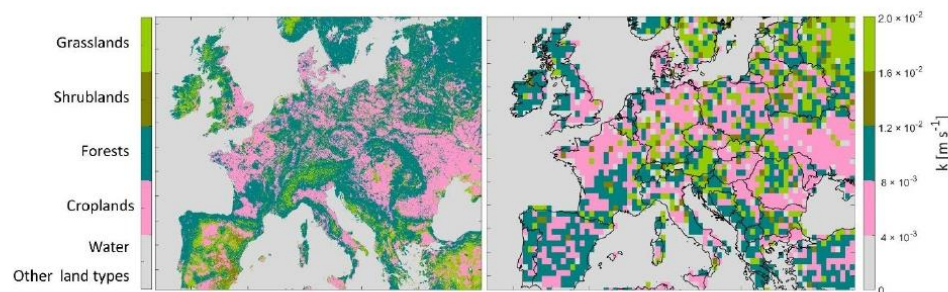


**Figure 4. MODIS Land Cover Type, at a  $500 \text{ m} \times 500 \text{ m}$  grid box (left panel), and interpolated mass transfer coefficient  $k$  on a horizontal resolution of  $0.5^\circ \times 0.625^\circ$  grid box (right panel).**

Uncertainties of this methodological approach can be summarized as follows:

- (1) The  $k$  value assigned for croplands is approximate and therefore not the same in every cropland over Europe.
- (2) The  $k$  value assigned for forests represents the SO<sub>2</sub> exchange in high croplands, and ammonia might change especially when the latter is highly affected by humidity; it can easily dissolve in the water film on leaves in high humid conditions.
- (3) The extrapolation of a fine array ( $500 \text{ m} \times 500 \text{ m}$ ) will merge several grids together and average them in order to construct the coarser grid box ( $0.5^\circ \times 0.625^\circ$ ); the result is therefore an average that might mix croplands with neighboring forests/barelands/grasslands. This leads to a range of different  $k$  values that are shown on Figure 4.

Using the land-type specific  $k$  value is necessary in order to reflect realistic emissions potential, as ammonia exchange in a forest is different from that of croplands or unfertilized grasslands, due to different barriers (long, medium or short crop / grass), and ammonium soil content in each land type.



<https://doi.org/10.5194/egusphere-2022-1046>  
 Preprint. Discussion started: 3 November 2022  
 © Author(s) 2022. CC BY 4.0 License.

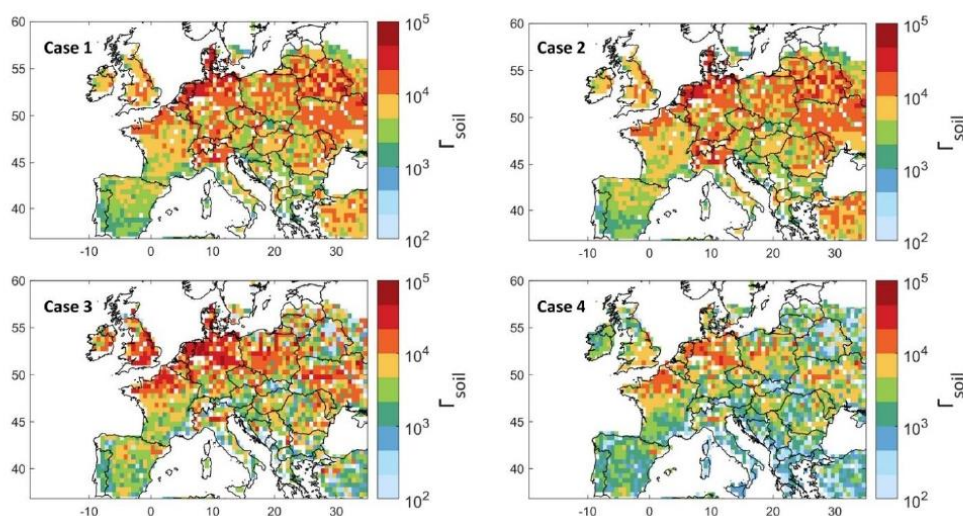


**Figure 5.** Ammonia soil emission potential ( $\Gamma_{soil}$ ) on a log10 scale from model simulation, observation and reanalysis for 4 different cases (see text for details).

We show in supplementary material Figure S2, the emission potential (similarly to what we show in Figure 5) but from a fixed and averaged  $k$  value for all land types. Figure S2 shows the importance of using a variable  $k$  that is adjusted to each land type is depicted in supplementary materials (Figure S2). In Figure S2, the fixed  $k$  used is calculated assuming 14 days of fertilization ( $k = 10^{-3} \text{ m s}^{-1}$ ), 7 days when  $k$  value reduces ( $k = 10^{-5} \text{ m s}^{-1}$ ), and 10 days when  $k$  is low ( $k = 10^{-6} \text{ m s}^{-1}$ ) resulting in average of  $k = 4.5 \times 10^{-4} \text{ m s}^{-1}$ . The difference in the emission potential between fixed and spatially variable  $k$  is shown in supplementary material Figure S3, where we see that a fixed  $k$  might overestimate  $\Gamma_{soil}$  by 10 to  $10^3$  on a log10 scale (500 – 3000 %), in agricultural areas.

Figure 5 illustrates the ammonia soil emission potential  $\Gamma_{soil}$  calculated using Eq. (2-1) and  $k$  values presented in Figure 4. After assigning the variable mass transfer coefficient, the remaining variables needed to calculate  $\Gamma_{soil}$  in Eq. (2-1) are ammonia concentration and lifetime, as well as the skin temperature. For this reason, the emission potential  $\Gamma_{soil}$  shown in Figure 5 is calculated using different configurations.

- Case 1: GEOS-Chem ammonia and lifetime with MERRA-2 T skin, i.e. simulated  $\Gamma_{soil}$ ,
- Case 2: GEOS-Chem ammonia and lifetime and ERA5 Tskin, to check the effect of using ERA5 vs MERRA-2 for skin temperature,
- Case 3: IASI ammonia, ERA5 T skin and GEOS-Chem ammonia lifetime,
- Case 4: IASI ammonia, ERA5 T skin and ammonia lifetime from Evangeliou et al. (2021), that were calculated using LMDz-OR-INCA chemistry transport model. The latter couples three models: The general circulation model GCM (LMDz) (Hourdin et al., 2006), the Interaction with Chemistry and

<https://doi.org/10.5194/egusphere-2022-1046>  
 Preprint. Discussion started: 3 November 2022  
 © Author(s) 2022. CC BY 4.0 License.



Aerosols (INCA) (Folberth et al., 2006), and the land surface dynamical vegetation model (ORCHIDEE) (Krinner et al., 2005).

Based upon the four cases, we calculate a range of emission potentials. When calculating  $\Gamma_{soil}$ , we filtered data points with ammonia total column concentration less than  $5 \times 10^{14}$  molecules  $\text{cm}^{-2}$ . The latter are mostly grid boxes concentrated above  $56^\circ$  North that we consider as noise (shown in white pixels on Figure 5).

T skin from ERA5 and MERRA-2 agree very well, with a coefficient of determination  $r^2 = 0.97$  (Figure S4 in the supplementary material). This explains the excellent spatial correlation between cases 1 and 2. Since IASI-NH<sub>3</sub> retrievals use ERA5 T skin, this also suggests that using MERRA-2 or ERA5 does not affect our  $\Gamma_{soil}$  calculation. In case 3, the emission potential agrees spatially and in value with that of GEOS-Chem. However, we observe higher  $\Gamma_{soil}$  in regions such as Ireland, England, North France, Northeastern Spain, and Poland. This is due to the underestimation/overestimation of ammonia from GEOS-Chem as compared to IASI observations (Figure 1a). For instance,  $\Gamma_{soil}$  from IASI and ERA5 (case 3) differs with that from GEOS-Chem and ERA5 (case 2) by up to -70 % in the Po Valley (Italy) and +60 % in England. Looking at Table 1, this difference can be explained by the corresponding MRD for each of the regions, in which it is -64 % for England and +110 % for the Po Valley. Similarly, the differences between case 3 and 4 reach up to +66 % in England, and this is mostly due to the 10-hours difference between ammonia lifetime from GEOS-Chem and Evangeliou et al. (2021) (Figure S1 in the supplementary material). The lowest  $\Gamma_{soil}$  were obtained in case 4, due to the higher lifetimes than those calculated from GEOS-Chem (Figure S1); note that  $\Gamma_{soil}$  is inversely proportional to ammonia lifetime (Eq. (2-1). In fact, the longer ammonia stays in the atmosphere (longer lifetime), the less the flux will be directed from the soil to the atmosphere (less ammonia emission).

In the four cases presented in Figure 5, we see similar spatial distribution of ammonia emission potential ranging from  $12 \times 10^{-1}$  in a forest to  $9.5 \times 10^4$  in a cropland (monthly average considering all the cases). In agricultural lands, our results show that  $\Gamma_{soil}$  ranges from  $2 \times 10^3$  to  $9.5 \times 10^4$ . Our values for croplands start at around  $10^3$ . In fact, most of the studies summarized in Zhang et al. (2010) reported  $\Gamma_{soil}$  that range mostly from  $10^3$  to  $10^4$  in fertilized croplands/grasslands; the minimum  $\Gamma_{soil}$  reported is in the order of  $10^2$  and the maximum is of the order of  $10^5$ . Therefore, our values fit within the range of  $\Gamma_{soil}$  calculated in the literature and summarized in Zhang et al. (2010) and the references within. Personne et al. (2015) focused on Grignon, an agricultural region near Paris, France ( $48^\circ 51'N$ ,  $1^\circ 58'E$ ). They obtained  $\Gamma_{soil}$  values between  $1.1 \times 10^4$  to  $5.8 \times 10^6$ . In the present study, the emission potential over this region is between  $5 \times 10^3$  (case 4) to  $2 \times 10^4$  (case 2). In this study, it is expected to obtain lower values than the ones measured over specific field. Therefore, we consider our results to be in good agreement with the obtained values in Personne et al. (2015), since ours reflect an average of a coarse patch of land of the size  $55 \times 70 \text{ km}^2$  approximately, with a 31-day mean.

The mean emission potentials per ammonia source region in Europe (shown in rectangles in Figure 2 and Figure 3) and per case are shown in Figure 6, and listed in Table 1. Table 1 shows the average lifetime from GEOS-Chem (hours), the average T skin from the three datasets that we used ( $^\circ\text{C}$ ), the average ammonia emission potential in all the cases examined (dimensionless), and the average ammonia columns from IASI and GEOS-Chem (molecules  $\text{cm}^{-2}$ ). The four cases show a similar pattern with the North European Plain exhibiting the highest emission potential. This has been shown in Figure 1, Figure 2, and Figure 5, as well as in Table 1, where  $\Gamma_{soil}$  is higher in regions with high ammonia columns. This is expected in fertilized lands (croplands), since  $\Gamma_{soil}$  is proportional to the concentration of ammonia near the surface. The latter increases when the soil content in ammonium ( $\text{NH}_4^+$ ) increases following the application of nitrogen-based fertilizers.

<https://doi.org/10.5194/egusphere-2022-1046>  
 Preprint. Discussion started: 3 November 2022  
 © Author(s) 2022. CC BY 4.0 License.



Figure 6 also shows that for cases 1 and 2 (GEOS-Chem) the emission potential in the Po Valley is higher as compared to case 3 (IASI), although it stays within the margin of error. This is due to the effect of temperature. Table 1 shows that at the time of the IASI overpass,  $T_{\text{skin}}$  from ERA5 in the Po Valley is almost twice as large ( $8.95^{\circ}\text{C}$ ) as the monthly averaged temperature ( $4.46^{\circ}\text{C}$ ). The effect of skin temperature through Eq. (2-1) makes the emission potential highly dependent. In fact,  $\Gamma_{\text{soil}}$  is both directly and inversely proportional to  $T_{\text{skin}}$ , however, the exponential in the denominator has  $\sim 10$  times more effect on the value of  $\Gamma_{\text{soil}}$  than the  $T_{\text{skin}}$  in the numerator. Therefore, through Eq. (2-1), we conclude that an increase in temperature by  $1^{\circ}\text{C}$  will reduce  $\Gamma_{\text{soil}}$  by around  $-8\%$ .

The standard deviation (shaded area) is found to be the highest in the North European Plain, which is also the largest region (hence higher variability is expected), especially when considering case 3 with IASI. IASI distinguishes different source sub-regions, leading to higher spatial variability of ammonia, and therefore  $\Gamma_{\text{soil}}$ . As Figure 5 has shown, case 4 has the lowest  $\Gamma_{\text{soil}}$ , with a factor of two lower than cases 1 to 3. This is due to the longer lifetimes calculated by Evangelio et al. (2021). However, we note that all the regions exhibit the same inter-variability between each of the case, regardless of the lifetimes used.

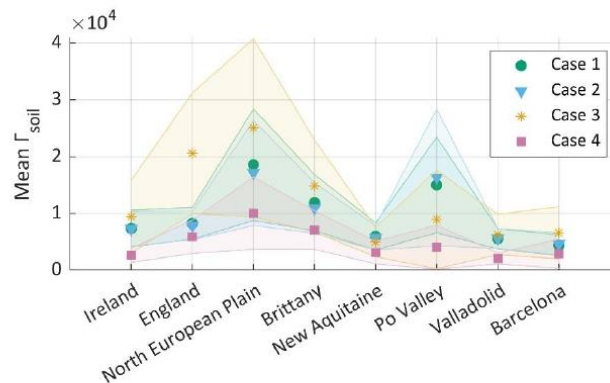


**Figure 6.** Mean ammonia emission potential  $\Gamma_{\text{soil}}$  per region and per case, with the error margin on the mean as the shaded area (95<sup>th</sup> percentile) for cases 1 to 4. The cases are explained in Figure 5 and its discussion.

<https://doi.org/10.5194/egusphere-2022-1046>  
 Preprint. Discussion started: 3 November 2022  
 © Author(s) 2022. CC BY 4.0 License.



**Table 1.** Summary of  $\text{NH}_3$  average lifetime, emission potential, concentrations and the T skin in selected regions in Europe.

Region	Country	$\tau_{\text{NH}_3}$ [hours]	T skin [°C]			$\Gamma_{\text{soil}} \times 10^4$ [dimensionless]				NH <sub>3</sub> concentrations [molecules $\times 10^{15} \text{ cm}^{-2}$ ]		
			ERA5 IASI Overpass	ERA5	MERRA-2	Case 1	Case 2	Case 3	Case 4	IASI	GEOS-Chem	Mean MRD [%]
Ireland	Ireland	3.34	8.74	5.78	6.23	0.73	0.72	0.94	0.26	2.5	1.5	− 46
England	England	3.15	8.54	5.87	5.73	0.82	0.78	2.06	0.58	4.8	1.2	− 64
North European Plains	Belgium, Netherlands	5.16	7.46	4.93	4.57	1.86	1.71	2.51	1.00	7.7	3.9	− 49
Brittany	France	6.93	10.48	8.13	8.16	1.19	1.09	1.48	0.70	5.8	3.7	− 60
New Aquitaine	France	8.05	11.25	7.72	7.47	0.59	0.57	0.49	0.30	4.0	2.9	− 20
Po Valley	Italy	7.10	8.95	4.46	5.46	1.50	1.63	0.89	0.40	3.8	4.0	+ 110
Valladolid	Spain	4.53	11.64	6.87	6.93	0.55	0.55	0.62	0.20	2.5	1.3	− 42
Barcelona	Spain	4.94	12.61	7.05	9.44	0.43	0.46	0.65	0.28	3.2	1.5	− 49



<https://doi.org/10.5194/egusphere-2022-1046>  
 Preprint. Discussion started: 3 November 2022  
 © Author(s) 2022. CC BY 4.0 License.



## 464 5. Ammonia under future scenarios

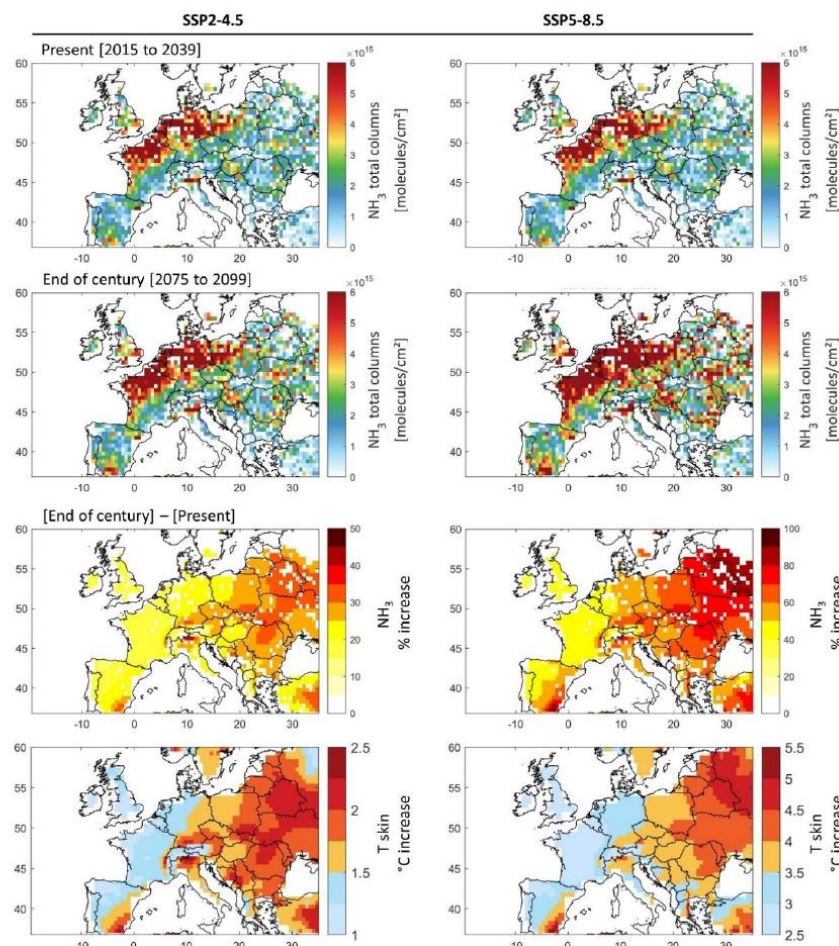


**Figure 7.** First and second rows: Ammonia total column concentrations during March (monthly averages) under the present climate [2015 to 2039] (first row), and in the end of century climate [2075 to 2099] (second row), under the socio-economic scenarios SSP2-4.5 (left) and SSP5-8.5 (right). Third and fourth rows: The percentage increase in ammonia concentration (third row), and the change in T<sub>skin</sub> in °C (fourth row) by the end of the century [2075 to 2099] with respect to present climate [2015 to 2039] under SSP2-4.5 (left) and SSP5-8.5 (right). Ammonia columns were calculated using ammonia emission potential  $I_{soil}$  derived from IASI and ERA5 for March 2011 (case 3), and EC-Earth T<sub>skin</sub> simulations for SSP2-4.5 and SSP5-8.5 extending from 2015 till 2099.

<https://doi.org/10.5194/egusphere-2022-1046>  
 Preprint. Discussion started: 3 November 2022  
 © Author(s) 2022. CC BY 4.0 License.



As seen in Eq. (2-1), higher skin temperatures favour volatilization of ammonia from the soil. In an attempt to understand how our simplified emission potential model behaves under changing climate, as well as under future scenarios, we adopt the future T skin simulations from EC-Earth climate model, into Eq. (2-1). The two climate socio-economic scenarios that we consider are SSP2-4.5 (“middle of the road” scenario where trends broadly follow their historical patterns), and SSP5-8.5 (a world of rapid and unconstrained growth in economic output and energy use) (Riahi et al., 2017). The same Figure constructed using  $\Gamma_{soil}$  from GEOS-Chem (case 1) is shown in the supplementary material as Figure S5.

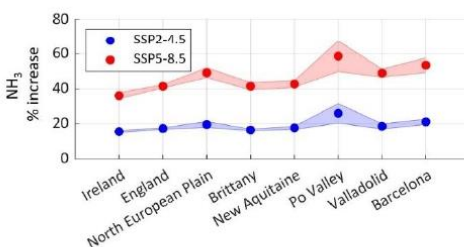
We calculate current and future ammonia columns assuming that the emission potential  $\Gamma_{soil}$  remains unchanged. In other words, we assume that the same amount of fertilizers and manure is used until 2100 in the agricultural fields and farms (unchanged ammonium soil content).

Figure 7 shows ammonia columns during the 25-year [2015 – 2039] representing the present climate (upper panels), and the end of the century [2075 – 2099] (middle panels). The ammonia columns in the 25-year average climate of the end of century with respect to present day climate (lower panels) are also shown.

Spatially, the present climate ammonia columns calculated from the T skin of the climate model and our emission potential from IASI (case 3 in Figure 5), agree very well with those shown in Figure 1. We do not aim at validating or directly comparing the two, as we are only interested in the climate response on ammonia concentration, i.e. by the difference due to skin temperature increase (lower panels).

From Figure 7 (lower panels) it can be seen that the increase in ammonia columns by the end of the century is more severe on the east side of Europe. Under the most likely scenario (SSP2-4.5), ammonia columns vary between +15 % in France, to around +20 % in the North European Plain (Figure 7). The largest increase is detected in Eastern Europe, where ammonia columns show an increase of up to a +50 % (Figure 7, lower left panels), creating new potential hotspots/sources of ammonia in Belarus, Ukraine, Hungary, Moldova, parts of Romania and Switzerland. Under the SSP5-8.5 scenario, the results show an increase in ammonia columns of up to +100 % in Eastern Europe (Figure 7, right lower panel). This is directly related to the higher projected increase in skin temperature over these regions. Other studies have equally reported Eastern Europe to be more affected by climate change under future scenarios, as compared to western Europe (European Environment Agency, 2022; Jacob et al., 2018). Spatially, the increase in ammonia coincides with the increase in T skin.

Figure 8 depicts the change in ammonia columns under the SSP2-4.5 and SSP5-8.5 scenarios, for our source regions (shown as rectangles in Figure 2). Ammonia columns increase is foreseen to be the highest in the Po Valley (Italy) with +26 % and +59 % under SSP2-4.5 and SSP5-8.5 respectively. It is then followed by the agricultural



**Figure 8.** The percentage increase in ammonia concentration by the end of the century [2075 to 2099] with respect to the present climate [2015 to 2039] under the two climate scenarios SSP2-4.5 (blue) and SSP5-8.5 (red), in the source regions investigated in this study. The shades around each line represent the standard deviation from the mean.



<https://doi.org/10.5194/egusphere-2022-1046>  
 Preprint. Discussion started: 3 November 2022  
 © Author(s) 2022. CC BY 4.0 License.



497 areas around Barcelona (Spain), and the North European Plain (Belgium, Netherlands) with an increase of +21 %  
 498 (+49 %) and +20 % (+53 %) respectively, under the SSP2-4.5 (SSP5-8.5) scenario. Under the SSP5-8.5, the  
 499 increase in ammonia columns in percentage is more than twice the change under SSP2-4.5 (+127 % in the case of  
 500 the Po Valley for instance). The Po Valley is adjacent to the Alps mountains, and due to global warming, this  
 501 region is expected to experience increased evapotranspiration (Donnelly et al., 2017), which is a major factor that  
 502 leads to the volatilization of ammonia.

503 The local and regional effect of volatilization of ammonia under different climate scenarios remains difficult to be  
 504 properly assessed. Even under the “middle of the road” scenario 2-4.5, and without climate extremes (e.g.  
 505 heatwaves), Europe might be facing big challenges in air or downwind agricultural regions, since chemistry and  
 506 atmospheric transport (Figure 3) drive the loss of ammonia during the growing season in this part of the world.

507  
 508 An increase in ammonia concentration poses a significant and yet poorly understood effect on local and regional  
 509 air quality through the increase in  $PM_{2.5}$  concentration. We note, however, that ammonia columns in the soil are  
 510 governed by a threshold. Higher temperatures will increase the rate of volatilization of ammonia from the soil, but  
 511 only up to a certain point where no dissolved ammonium is left. Plants, however, can also be a source of ammonia  
 512 when exposed to stressful conditions. For example, under heat stress and in instances where there are no ammonia  
 513 in the air, increase in air temperature results in exponential increase in ammonia emission from plants’ leaves  
 514 (Husted and Schjoerring, 1996).

## 515 6. Discussion and conclusions

516  
 517 Agriculture worldwide has fed the human race for thousands of years, and will continue to do so, as mankind  
 518 highly relies on it. Emissions from agricultural activities will inevitably increase, in order to meet the expected  
 519 yield. In this study, we use a variety of state-of-the-art datasets (satellite, reanalysis and model simulation) to  
 520 calculate the first regional map of ammonia emission potential during the start of the growing season in Europe.  
 521 The emission potential can be used as a proxy to calculate ammonia columns in the atmosphere, and as such to  
 522 assess its deposition, atmospheric transport, and contribution to PM formation. First, we show that the GEOS-  
 523 Chem chemistry transport model is able to reproduce key spatio-temporal patterns of ammonia levels over Europe.  
 524 The ammonia budget is governed by the emissions over source regions (North European Plain, Brittany and the  
 525 Po valley), as well as by key loss processes. We find that chemical loss pathway is responsible of 50 % or more of  
 526 the total ammonia loss over Europe. From the GEOS-Chem simulation, we calculate the average ammonia lifetime  
 527 in the atmosphere which ranges between 4 and 12 hours in agricultural source regions of Europe. From this, and  
 528 using the mass transfer coefficient for different land cover types, we calculate a range of emission potentials  
 529  $\Gamma_{soil}$  from IASI and GEOS-Chem. We find that  $\Gamma_{soil}$  ranges between from  $2 \times 10^3$  to  $9.5 \times 10^4$  in fertilized lands  
 530 (croplands). Choosing a variable  $k$  from the literature, and based on different land cover types from MODIS, we  
 531 calculate  $\Gamma_{soil}$  values that are consistent with those found in the literature. The increase in T skin is expected to  
 532 have an effect on the emission of ammonia from the soil. Using T skin from the EC-Earth climate model, we  
 533 estimate ammonia columns by the end of the century [2075 – 2099], and compare it to columns of the present  
 534 climate [2015 – 2039]. Our results show that ammonia columns will double under the SSP5-8.5 scenario, and will  
 535 increase by up to 50 % under the most likely SSP2-4.5 scenario. The eastern part of Europe is the most affected  
 536 by the change in temperatures, and it is where we find the highest ammonia columns increase. Among the regions  
 537 of focus, Italy, Spain, Belgium and the Netherlands are the most affected, as compared to France, England and  
 538 Ireland. The highest increase in ammonia columns is observed in the Po Valley in Italy (+59 % under the SSP5-  
 539 8.5).

540

<https://doi.org/10.5194/egusphere-2022-1046>  
 Preprint. Discussion started: 3 November 2022  
 © Author(s) 2022. CC BY 4.0 License.



541 We calculate ammonia concentration under future climate and during the start of the growing season (March) in  
 542 Europe. However, in order to grasp the yearly budget of ammonia, it is crucial to apply this method to all seasons  
 543 of the year; especially in regions with extensive agricultural activities, such as the United States, India, and China.  
 544 In addition to this, more field measurements of ammonia emission potential ( $I_{soil}$ ) in different land use / cover  
 545 types are required, this can help us perform better comparison with emission potentials calculated from model and  
 546 satellite data. Finally, having ammonia columns at different times of the day, from field observations or satellite  
 547 measurements will allow quantification of daily emission potentials, that will in turn help us understand its diurnal  
 548 variability. This will be ensured with the launch of the Infrared Sounder (IRS) on the Meteosat Third Generation  
 549 (MTG) geostationary satellites scheduled in 2025.



<https://doi.org/10.5194/egusphere-2022-1046>  
Preprint. Discussion started: 3 November 2022  
© Author(s) 2022. CC BY 4.0 License.



550

551

## A. Appendix A

552

### 1. Ammonia-Ammonium equilibrium

553

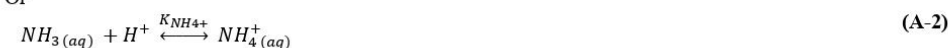
Ammonia ( $\text{NH}_3$ ) is a water-soluble gas, it undergoes protonation with  $\text{H}^+$  from the hydronium ion  $\text{H}_3\text{O}^+$  in an aqueous solution in order to give ammonium ( $\text{NH}_4^+$  cation), the dissociation equation is expressed as follows:

554



555

556 Or



557

558 With  $K_{\text{NH}_4^+}$  as the ammonium-ammonia dissociation equilibrium constant that can be expressed as:

$$K_{\text{NH}_4^+} = \frac{[\text{NH}_3(\text{aq})][\text{H}^+]}{[\text{NH}_4^+(\text{aq})]} \quad (\text{A-3})$$

559

560

561 The solubility of ammonia in water is affected by the temperature and the acidity (pH) of the solvent (water). The equilibrium constant can be expressed as follows:

562

$$K_{\text{NH}_4^+} = 5.67 \cdot 10^{-10} \exp \left[ -6286 \left( \frac{1}{T} - \frac{1}{298.15} \right) \right] \quad (\text{A-4})$$

563

564

### 2. Henry's equilibrium

565

Upon its dissolution in water,  $\text{NH}_3$  obeys the Henry's law. Ammonia gas ( $\text{NH}_3(\text{g})$ ) near the surface of the solvent is in equilibrium with the dissolved ammonia in the aqueous phase  $\text{NH}_3(\text{aq})$  (in water). Henry's equilibrium is expressed as follows:

566



567

568

569 With  $H_{\text{NH}_3}$  as the Henry's constant, it can be expressed as follows (Wichink Kruit, 2010):

$$H_{\text{NH}_3} = \frac{[\text{NH}_3(\text{aq})]}{[\text{NH}_3(\text{g})]} = 5.527 \cdot 10^{-4} \cdot \exp \left[ 4092 \left( \frac{1}{T} - \frac{1}{298.15} \right) \right] \quad (\text{A-6})$$

570

571

The partial pressure of ammonia near the surface of the soil can be calculated using Henry's constant and the dissociation equilibrium (Wichink Kruit, 2010):

572

$$P_{\text{NH}_3} = \frac{K_{\text{NH}_4^+} [\text{NH}_4^+]}{H_{\text{NH}_3} [\text{H}^+]} = \frac{5.67 \cdot 10^{-10} \cdot \exp \left[ -6286 \left( \frac{1}{T} - \frac{1}{298.15} \right) \right]}{5.527 \cdot 10^{-4} \cdot \exp \left[ 4092 \left( \frac{1}{T} - \frac{1}{298.15} \right) \right]} \times \frac{[\text{NH}_4^+]}{[\text{H}^+]} \quad (\text{A-7})$$

573

574

575

If we use the ideal gas law ( $PV=nRT$ ), we can draw the link between the mass density of ammonia ( $\text{NH}_3(\text{g})$ ) and the partial pressure:

<https://doi.org/10.5194/egusphere-2022-1046>  
Preprint. Discussion started: 3 November 2022  
© Author(s) 2022. CC BY 4.0 License.



$$\chi_{NH_3} = \frac{P_{NH_3} \cdot M_{NH_3}}{R \cdot T} \quad (A-8)$$

Where  $\chi_{NH_3}$  is the concentration of  $NH_3$  at the soil surface ( $kg\ m^{-3}$ ),  $P_{NH_3}$  is the partial pressure of  $NH_3$  near the surface (atm),  $M_{NH_3}$  is the molar mass of  $NH_3$  ( $kg\ mol^{-1}$ ),  $R$  is the gas constant ( $0.082\ atm\ L\ mol^{-1}\ K^{-1}$ ), and  $T$  is the temperature in Kelvin.  
Substituting Eq. (A-5) in (A-6) we get:

$$\chi_{NH_3} = \frac{2.75 \cdot 10^9 \left(\frac{gK}{m^3}\right)}{T_{soil}} \exp \left[ \frac{-1.04 \cdot 10^4}{T_{soil}} \right] \Gamma_{soil} \quad (A-9)$$

Where  $\chi_{NH_3}$  is the concentration of ammonia at the soil surface at equilibrium ( $g\ m^{-3}$ ), and is referred to as the compensation point,  $T_{soil}$  is the temperature of the soil (Kelvin),  $\Gamma_{NH_3}$  is the  $NH_3$  emission potential from the soil and is a dimensionless ratio between  $[NH_4^+]$  and  $[H^+]$ .

### 3. Ammonia total columns from IASI

In this study we use the total columns of ammonia from IASI (molecules  $m^{-2}$ ) in order to calculate the emission potential  $\Gamma_{soil}$ , we should draw the link between these columns and this parameter. The bi-directional exchange of  $NH_3$  between the surface and the atmosphere can be expressed by the flux (assuming a flux independent of time) (Roelle and Aneja, 2005; Zhang et al., 2010):

$$Flux_{NH_3} = k ([NH_3]^{soil} - [NH_3]^{atm}) \quad (A-10)$$

Where  $Flux_{NH_3}$  is the bidirectional flux between the soil and the atmosphere (molecules ( $m^2\ s^{-1}$ )),  $k$  is the soil – atmosphere exchange velocity ( $m\ s^{-1}$ ), also known as the mass transfer coefficient;  $[NH_3]^{soil}$  is the concentration of  $NH_3$  in the soil, and  $[NH_3]^{atm}$  is the concentration of  $NH_3$  in the atmosphere (molecules  $m^{-3}$ ).

Assuming a first order dissociation of  $NH_3$ , we can express the change in the  $[NH_3]^{col}$  total columns as follows:

$$\frac{d [NH_3]^{col}}{dt} = Flux_{NH_3} - k' [NH_3]^{col} \quad (A-11)$$

Where  $k'$  is the rate of dissociation of first order  $k' = 1/\tau$  ( $m\ s^{-1}$ ), with  $\tau$  the lifetime of  $NH_3$  in the atmosphere. Assuming steady state, and considering the  $[NH_3]^{atm}$  as the  $[NH_3]^{col}$ , and  $[NH_3]^{soil}$  as  $\chi_{NH_3}$ , Eq. (A-9) can be written as:

$$k \left( \frac{N_a \cdot \chi_{NH_3}}{M_{NH_3}} - \frac{1}{c} [NH_3]^{col} \right) = \frac{[NH_3]^{col}}{\tau} \quad (A-12)$$

Where  $c$  is the column height and is equal to 6 km. It is important to note that we neglect the effect of transport by wind since we only look at large regions. Finally, the total column of ammonia  $[NH_3]^{col}$  can be written as:

$$[NH_3]^{col} = \frac{N_a \cdot \chi_{NH_3}}{M_{NH_3} \cdot (c + \frac{1}{k\tau})} \quad (A-13)$$

The column height is not considered anymore because it is negligible compared to  $1/k\tau$ , using Eq. (A-6) in (A-11) we get:

<https://doi.org/10.5194/egusphere-2022-1046>  
 Preprint. Discussion started: 3 November 2022  
 © Author(s) 2022. CC BY 4.0 License.



$$[NH_3]^{col} = \frac{2.75 \cdot 10^{27} \left( \frac{gK}{cm^3} \right)}{T_{soil}} \exp \left[ \frac{-1.04 \cdot 10^4}{T_{soil}} \right] \Gamma_{NH_3} \cdot k\tau \quad \left( \frac{molecules}{cm^2} \right) \quad (A-14)$$

605  
 606 Note that  $2.75 \cdot 10^{27} = \frac{a \cdot N_a \cdot c_l}{M_{NH_3}} \left( \frac{K \cdot molecules}{cm^3} \right)$ , where  $a = 2.75 \cdot 10^3 (g K cm^{-3})$ ,  $N_a$  Avogadro's number  
 607  $(6.0221409 \times 10^{23} \text{ molecules mol}^{-1})$ ,  $10^{-2}$  is added to convert  $k$  from  $m s^{-1}$  to  $cm s^{-1}$ , and  $M_{NH_3}$  the molar mass of  
 608  $NH_3$  ( $17.031 \text{ g mol}^{-1}$ ). The emission potential of  $NH_3$  from the soil can be written as:

$$\Gamma_{soil} = \frac{[NH_3]^{col} \cdot T_{soil}}{\exp \left( \frac{-b}{T_{soil}} \right)} \frac{M_{NH_3}}{a \cdot N_a \cdot 10^{-2}} \cdot \frac{1}{k\tau} \quad (A-15)$$

609  
 610 Where  $b = 1.04 \times 10^4 K$ .

<https://doi.org/10.5194/egusphere-2022-1046>  
 Preprint. Discussion started: 3 November 2022  
 © Author(s) 2022. CC BY 4.0 License.



#### 611 **Author contribution**

612 RA contributed to the conception and design of the article, developed the code, wrote the manuscript, analysed and  
 613 interpreted of the data, and approved the version for submission; CV, CC, and PFC revised the manuscript; WCP provided  
 614 the GEOS-Chem simulation data, and revised the manuscript; NE provided ammonia lifetime calculation using the LMDz-  
 615 OR-INCA chemistry transport model and commented on the manuscript; MVD and LC contributed to the acquisition of the  
 616 IASI ammonia data (NH<sub>3</sub>-v3R-ERA5), and revised the manuscript; SS contributed to the conception and design of the article,  
 617 provided the EC-Earth temperature data, and revised the manuscript, and approved the version for submission.

#### 618 **Acknowledgments**

619 The IASI mission is a joint mission of Eumetsat and the Centre National d'Etudes Spatiales (CNES, France). The authors  
 620 acknowledge the Aeris data infrastructure for providing the IASI L1C and L2 data.

#### 621 **Funding information**

622 Rimal Abeed is grateful to CNES for financial support. The research in Belgium was funded by the Belgian State Federal  
 623 Office for Scientific, Technical and Cultural Affairs (Prodex HIRS) and the Air Liquide Foundation (TAPIR project). This  
 624 work is also partly supported by the FED-iWIN project ARENBERG ("Assessing the Reactive Nitrogen Budget and Emissions  
 625 at Regional and Global Scales") funded via the Belgian Science Policy Office (BELSPO). L. Clarisse is Research Associate  
 626 supported by the Belgian F.R.S.-FNRS. C. Clerbaux is grateful to CNES for scientific collaboration and financial support. N.  
 627 Evangeliou was funded by Norges Forskningsråd (ROM- FORSK – Program for romforskning of the Research Council of  
 628 Norway (grant no. 275407)).

#### 629 **Competing interests**

630 The authors are aware of no competing interests.

#### 631 **Data accessibility statement**

632 The IASI-NH<sub>3</sub> used in this study are retrieved from the Aeris data infrastructure (<https://iasi.aeris-data.fr/nh3r-era5/>). ERA5  
 633 skin temperature from 1979 to present are available for download in the following DOI: [10.24381/cds.adbb2d47](https://doi.org/10.24381/cds.adbb2d47). The GEOS-  
 634 Chem outputs used in this study are only available upon request. EC-Earth3 model output prepared for CMIP6 ScenarioMIP  
 635 are retrieved here: <https://doi.org/10.22033/ESGF/CMIP6.727>. The MODIS land cover data are available for download in the  
 636 following link: <https://doi.org/10.5067/MODIS/MCD12Q1.006>.

637  
638  
639  
640  
641  
642  
643  
644  
645



<https://doi.org/10.5194/egusphere-2022-1046>  
 Preprint. Discussion started: 3 November 2022  
 © Author(s) 2022. CC BY 4.0 License.



## 646 References

- 647 Abeer, R., Clerbaux, C., Clarisse, L., Van Damme, M., Coheur, P.-F., and Safieddine, S. A space view of agricultural and  
 648 industrial changes during the Syrian civil war. *Elem. Sci. Anthr.* <https://doi.org/10.1525/elementa.2021.000041>  
 649 (2021)
- 650 Adams, C., McLinden, C. A., Shephard, M. W., Dickson, N., Dammers, E., Chen, J., Makar, P., Cady-Pereira, K. E., Tam,  
 651 N., Kharol, S. K., Lamsal, L. N., and Krotkov, N. A. Satellite-derived emissions of carbon monoxide, ammonia, and  
 652 nitrogen dioxide from the 2016 Horse River wildfire in the Fort McMurray area. *Atmospheric Chem. Phys.*  
 653 <https://doi.org/10.5194/acp-19-2577-2019> (2019)
- 654 Alexander, B., Sherwen, T., Holmes, C. D., Fisher, J. A., Chen, Q., Evans, M. J., and Kasibhatla, P. Global inorganic nitrate  
 655 production mechanisms: Comparison of a global model with nitrate isotope observations. *Atmospheric Chem. Phys.*  
 656 <https://doi.org/10.5194/acp-20-3859-2020> (2020)
- 657 Aneja, V. P., Rogers, H. H., and Stahel, E. P. Dry Deposition of Ammonia at Environmental Concentrations on Selected  
 658 Plant Species. *J. Air Pollut. Control Assoc.* <https://doi.org/10.1080/00022470.1986.10466183> (1986)
- 659 AQEG. *Fine particulate matter (PM<sub>2.5</sub>) in the United Kingdom* (p. 203). Air Quality Expert Group (AQEG), prepared for  
 660 the Department for Environment, Food and Rural Affairs (Defra), Scottish Executive, Welsh Government and the  
 661 Department of the Environment in Northern Ireland. [https://uk-](https://uk-air.defra.gov.uk/assets/documents/reports/cat11/1212141150_AQEG_Fine_Part particulate_Matter_in_the_UK.pdf)  
 662 [air.defra.gov.uk/assets/documents/reports/cat11/1212141150\\_AQEG\\_Fine\\_Part particulate\\_Matter\\_in\\_the\\_UK.pdf](https://uk-air.defra.gov.uk/assets/documents/reports/cat11/1212141150_AQEG_Fine_Part particulate_Matter_in_the_UK.pdf)  
 663 (2012)
- 664 Barnes, A. P., Svensson, C., and Kjeldsen, T. R. North Atlantic air pressure and temperature conditions associated with  
 665 heavy rainfall in Great Britain. *Int. J. Climatol.* <https://doi.org/10.1002/joc.7414> (2022)
- 666 Bauer, S. E., Tsigaridis, K., and Miller, R. Significant atmospheric aerosol pollution caused by world food cultivation.  
 667 *Geophys. Res. Lett.* <https://doi.org/10.1002/2016GL068354> (2016)
- 668 Behera, S. N., Sharma, M., Aneja, V. P., and Balasubramanian, R. Ammonia in the atmosphere: A review on emission  
 669 sources, atmospheric chemistry and deposition on terrestrial bodies. *Env. Sci Pollut Res.*  
 670 <https://doi.org/10.1007/s11356-013-2051-9> (2013)
- 671 Belward, A. S., Estes, John E., and Kline, K. D. The IGBP-DIS Global 1-Km Land-Cover Data Set DIS-Cover: A Project  
 672 Overview. *Photogramm. Eng. Remote Sens.* [https://www.asprs.org/wp-](https://www.asprs.org/wp-content/uploads/pers/1999journal/sep/1999_sept_1013-1020.pdf)  
 673 [content/uploads/pers/1999journal/sep/1999\\_sept\\_1013-1020.pdf](https://www.asprs.org/wp-content/uploads/pers/1999journal/sep/1999_sept_1013-1020.pdf) (1999)
- 674 Bey, I., Jacob, D. J., Yantosca, R. M., Logan, J. A., Field, B. D., Fiore, A. M., Li, Q., Liu, H. Y., Mickley, L. J., and Schultz,  
 675 M. G. Global modeling of tropospheric chemistry with assimilated meteorology: Model description and evaluation.  
 676 *J. Geophys. Res. Atmospheres.* <https://doi.org/10.1029/2001JD000807> (2001)
- 677 Bouwman, A. F., Lee, D. S., Asman, W. a. H., Dentener, F. J., Van Der Hoek, K. W., and Olivier, J. G. J. A global high-  
 678 resolution emission inventory for ammonia. *Glob. Biogeochem. Cycles.* <https://doi.org/10.1029/97GB02266> (1997)
- 679 Clarisse, L., Van Damme, M., Clerbaux, C., and Coheur, P.-F. Tracking down global NH<sub>3</sub> point sources with wind-adjusted  
 680 superresolution. *Atmospheric Meas. Tech.* <https://doi.org/10.5194/amt-12-5457-2019> (2019)
- 681 Clarisse, L., Van Damme, M., Gardner, W., Coheur, P.-F., Clerbaux, C., Whitburn, S., Hadji-Lazaro, J., and Hurtmans, D.  
 682 Atmospheric ammonia (NH<sub>3</sub>) emanations from Lake Natron's saline mudflats. *Sci. Rep.*  
 683 <https://doi.org/10.1038/s41598-019-39935-3> (2019)
- 684 Clerbaux, C., Boynard, A., Clarisse, L., George, M., Hadji-Lazaro, J., Herbin, H., Hurtmans, D., Pommier, M., Razavi, A.,  
 685 Turquety, S., and Wespes, C. Monitoring of atmospheric composition using the thermal infrared IASI/MetOp  
 686 sounder. *Atmospheric Chem. Phys.* <https://doi.org/10.5194/acp-9-6041-2009> (2009)
- 687 Coheur, P.-F., Clarisse, L., Turquety, S., Hurtmans, D., and Clerbaux, C. IASI measurements of reactive trace species in  
 688 biomass burning plumes. *Atmospheric Chem. Phys.* <https://doi.org/10.5194/acp-9-5655-2009> (2009)
- 689 Dammers, E., McLinden, C. A., Griffin, D., Shephard, M. W., Van Der Graaf, S., Lutsch, E., Schaap, M., Gainairu-Matz, Y.,  
 690 Fioletov, V., Van Damme, M., Whitburn, S., Clarisse, L., Cady-Pereira, K., Clerbaux, C., Coheur, P. F., and  
 691 Erismann, J. W. NH<sub>3</sub> emissions from large point sources derived from CrIS and IASI satellite observations.  
 692 *Atmospheric Chem. Phys.* <https://doi.org/10.5194/acp-19-12261-2019> (2019)

<https://doi.org/10.5194/egusphere-2022-1046>  
 Preprint. Discussion started: 3 November 2022  
 © Author(s) 2022. CC BY 4.0 License.



- David, M., Loubet, B., Cellier, P., Mattsson, M., Schjoerring, J. K., Nemitz, E., Roche, R., Riedo, M., and Sutton, M. A. Ammonia sources and sinks in an intensively managed grassland canopy. *Biogeosciences*. <https://doi.org/10.5194/bg-6-1903-2009> (2009)
- Donnelly, C., Greuell, W., Andersson, J., Gerten, D., Pisacane, G., Roudier, P., and Ludwig, F. Impacts of climate change on European hydrology at 1.5, 2 and 3 degrees mean global warming above preindustrial level. *Clim. Change*. <https://doi.org/10.1007/s10584-017-1971-7> (2017)
- Döscher, R., Acosta, M., Alessandri, A., Anthoni, P., Arneth, A., Arsouze, T., Bergmann, T., Bernadello, R., Bousetta, S., Caron, L.-P., Carver, G., Castrillo, M., Catalano, F., Cvijanovic, I., Davini, P., Dekker, E., Doblas-Reyes, F. J., Docquier, D., Echevarria, P., ... Zhang, Q. The EC-Earth3 Earth System Model for the Climate Model Intercomparison Project 6. *Geosci. Model Dev. Discuss.* <https://doi.org/10.5194/gmd-2020-446> (2021)
- ECMWF. *IFS Documentation CY43R1*. ECMWF. <https://www.ecmwf.int/sites/default/files/elibrary/2016/17117-part-iv-physical-processes.pdf> (2016)
- EDO, G. D. O. *Drought news in Europe: Situation in April 2011—Short Analysis of data from the European Drought Observatory (EDO)* (p. 2). <https://edo.jrc.ec.europa.eu/documents/news/EDODroughtNews201104.pdf> (2011)
- Erisman, J. W., Van Pul, A., and Wyers, P. Parametrization of surface resistance for the quantification of atmospheric deposition of acidifying pollutants and ozone. *Atmos. Environ.* [https://doi.org/10.1016/1352-2310\(94\)90433-2](https://doi.org/10.1016/1352-2310(94)90433-2) (1994)
- European Environment Agency. *Global and European temperatures*. <https://www.eea.europa.eu/ims/global-and-european-temperatures> (2022)
- Evangelio, N., Balkanski, Y., Eckhardt, S., Cozic, A., Van Damme, M., Coheur, P.-F., Clarisse, L., Shephard, M., Cady-Pereira, K., and Hauglustaine, D. 10-year satellite-constrained fluxes of ammonia improve performance of chemistry transport models. *Atmospheric Chem. Phys.* <https://doi.org/10.5194/acp-21-4431-2021> (2021)
- Eyring, V., Bony, S., Meehl, G. A., Senior, C. A., Stevens, B., Stouffer, R. J., and Taylor, K. E. Overview of the Coupled Model Intercomparison Project Phase 6 (CMIP6) experimental design and organization. *Geosci. Model Dev.* <https://doi.org/10.5194/gmd-9-1937-2016> (2016)
- FAO. *FAO, GIEWS, Earth Observation*. <https://www.fao.org/giews/earthobservation/country/index.jsp?lang=en&code=FRA> (2022)
- Flechard, C. R., Massad, R.-S., Loubet, B., Personne, E., Simpson, D., Bash, J. O., Cooter, E. J., Nemitz, E., and Sutton, M. A. Advances in understanding, models and parameterizations of biosphere-atmosphere ammonia exchange. *Biogeosciences*. <https://doi.org/10.5194/bg-10-5183-2013> (2013)
- Flechard, C. R., Nemitz, E., Smith, R. I., Fowler, D., Vermeulen, A. T., Bleeker, A., Erisman, J. W., Simpson, D., Zhang, L., Tang, Y. S., and Sutton, M. A. Dry deposition of reactive nitrogen to European ecosystems: A comparison of inferential models across the NitroEurope network. *Atmospheric Chem. Phys.* <https://doi.org/10.5194/acp-11-2703-2011> (2011)
- Flechard, C. R., Spirig, C., Neftel, A., and Ammann, C. The annual ammonia budget of fertilised cut grassland – Part 2: Seasonal variations and compensation point modeling. *Biogeosciences*. <https://doi.org/10.5194/bg-7-537-2010> (2010)
- Folberth, G. A., Hauglustaine, D. A., Lathière, J., and Brocheton, F. Interactive chemistry in the Laboratoire de Météorologie Dynamique general circulation model: Model description and impact analysis of biogenic hydrocarbons on tropospheric chemistry. *Atmospheric Chem. Phys.* <https://doi.org/10.5194/acp-6-2273-2006> (2006)
- Garrido-Perez, J. M., Ordóñez, C., García-Herrera, R., and Barriopedro, D. Air stagnation in Europe: Spatiotemporal variability and impact on air quality. *Sci. Total Environ.* <https://doi.org/10.1016/j.scitotenv.2018.07.238> (2018)
- Gelaro, R., McCarty, W., Suárez, M. J., Todling, R., Molod, A., Takacs, L., Randles, C. A., Darmenov, A., Bosilovich, M. G., Reichle, R., Wargan, K., Coy, L., Cullather, R., Draper, C., Akella, S., Buchard, V., Conaty, A., Silva, A. M. da, Gu, W., ... Zhao, B. The Modern-Era Retrospective Analysis for Research and Applications, Version 2 (MERRA-2). *J. Clim.* <https://doi.org/10.1175/JCLI-D-16-0758.1> (2017)
- Hersbach, H., Bell, B., Berrisford, P., Hirahara, S., Horányi, A., Muñoz-Sabater, J., Nicolas, J., Peubey, C., Radu, R., Schepers, D., Simmons, A., Soci, C., Abdalla, S., Abellan, X., Balsamo, G., Bechtold, P., Biavati, G., Bidlot, J., Bonavita, M., ... Thépaut, J.-N. The ERA5 global reanalysis. *Q. J. R. Meteorol. Soc.* <https://doi.org/10.1002/qj.3803> (2020)



<https://doi.org/10.5194/egusphere-2022-1046>  
 Preprint. Discussion started: 3 November 2022  
 © Author(s) 2022. CC BY 4.0 License.



- 743 Hoesly, R. M., Smith, S. J., Feng, L., Klimont, Z., Janssens-Maenhout, G., Pitkanen, T., Seibert, J. J., Vu, L., Andres, R. J.,  
 744 Bolt, R. M., Bond, T. C., Dawidowski, L., Kholod, N., Kurokawa, J., Li, M., Liu, L., Lu, Z., Moura, M. C. P.,  
 745 O'Rourke, P. R., and Zhang, Q. Historical (1750–2014) anthropogenic emissions of reactive gases and aerosols  
 746 from the Community Emissions Data System (CEDS). *Geosci. Model Dev.* [https://doi.org/10.5194/gmd-11-369-](https://doi.org/10.5194/gmd-11-369-2018)  
 747 [2018](https://doi.org/10.5194/gmd-11-369-2018) (2018)
- 748 Hourdin, F., Musat, I., Bony, S., Braconnot, P., Codron, F., Dufresne, J.-L., Fairhead, L., Filiberti, M.-A., Friedlingstein, P.,  
 749 Grandpeix, J.-Y., Krinner, G., LeVan, P., Li, Z.-X., and Lott, F. The LMDZ4 general circulation model: Climate  
 750 performance and sensitivity to parametrized physics with emphasis on tropical convection. *Clim. Dyn.*  
 751 <https://doi.org/10.1007/s00382-006-0158-0> (2006)
- 752 Husted, S., and Schjoerring, J. K. Ammonia Flux between Oilseed Rape Plants and the Atmosphere in Response to Changes  
 753 in Leaf Temperature, Light Intensity, and Air Humidity (Interactions with Leaf Conductance and Apoplastic NH<sub>4</sub><sup>+</sup>  
 754 and H<sup>+</sup> Concentrations). *Plant Physiol.* <https://doi.org/10.1104/pp.112.1.67> (1996)
- 755 Jacob, D., Kotova, L., Teichmann, C., Sobolowski, S. P., Vautard, R., Donnelly, C., Koutroulis, A. G., Grillakis, M. G.,  
 756 Tسانis, I. K., Damm, A., Sakalli, A., and van Vliet, M. T. H. Climate Impacts in Europe Under +1.5°C Global  
 757 Warming. *Earth's Future.* <https://doi.org/10.1002/2017EF000710> (2018)
- 758 Keller, C. A., Long, M. S., Yantosca, R. M., Da Silva, A. M., Pawson, S., and Jacob, D. J. HEMCO v1.0: A versatile,  
 759 ESMF-compliant component for calculating emissions in atmospheric models. *Geosci. Model Dev.*  
 760 <https://doi.org/10.5194/gmd-7-1409-2014> (2014)
- 761 Klaes, K. D. The EUMETSAT Polar System. *Comprehensive Remote Sensing.* Elsevier.  
 762 <https://doi.org/10.1016/B978-0-12-409548-9.10318-5> (2018)
- 763 Krinner, G., Viovy, N., de Noblet-Ducoudré, N., Ogée, J., Polcher, J., Friedlingstein, P., Ciais, P., Sitch, S., and Prentice, I.  
 764 C. A dynamic global vegetation model for studies of the coupled atmosphere-biosphere system. *Glob. Biogeochem.*  
 765 *Cycles.* <https://doi.org/10.1029/2003GB002199> (2005)
- 766 Lee, W., An, S., and Choi, Y. Ammonia harvesting via membrane gas extraction at moderately alkaline pH: A step toward  
 767 net-profitable nitrogen recovery from domestic wastewater. *Chem. Eng. J.*  
 768 <https://doi.org/10.1016/j.cej.2020.126662> (2020)
- 769 Lentze, G. *Metop-A satellite retiring after 15 years of huge benefits to forecasting* [Text]. ECMWF. ECMWF.  
 770 [https://www.ecmwf.int/en/about/media-centre/news/2021/metop-satellite-retiring-after-15-years-huge-benefits-](https://www.ecmwf.int/en/about/media-centre/news/2021/metop-satellite-retiring-after-15-years-huge-benefits-forecasting)  
 771 [forecasting](https://www.ecmwf.int/en/about/media-centre/news/2021/metop-satellite-retiring-after-15-years-huge-benefits-forecasting) (2021, November 12)
- 772 Luo, Z., Zhang, Y., Chen, W., Van Damme, M., Coheur, P.-F., and Clarisse, L. Estimating global ammonia (NH<sub>3</sub>)  
 773 emissions based on IASI observations from 2008 to 2018. *Atmospheric Chem. Phys.* [https://doi.org/10.5194/acp-22-](https://doi.org/10.5194/acp-22-10375-2022)  
 774 [10375-2022](https://doi.org/10.5194/acp-22-10375-2022) (2022)
- 775 Massad, R.-S., Nemitz, E., and Sutton, M. A. Review and parameterisation of bi-directional ammonia exchange between  
 776 vegetation and the atmosphere. *Atmospheric Chem. Phys.* <https://doi.org/10.5194/acp-10-10359-2010> (2010)
- 777 Masson-Delmotte, V., P. Zhai, A. Pirani, S.L., Connors, C. Péan, S. Berger, N. Caud, Y. Chen, L. Goldfarb, M.I. Gomis, M.  
 778 Huang, K. Leitzell, E. Lonnoy, J.B.R., and Matthews, T.K. Maycock, T. Waterfield, O. Yelekçi, R. Yu, and B.  
 779 Zhou. *IPCC, 2021: Climate Change 2021: The Physical Science Basis. Contribution of Working Group I to the*  
 780 *Sixth Assessment Report of the Intergovernmental Panel on Climate Change.* Cambridge University Press. In Press.  
 781 <https://www.ipcc.ch/assessment-report/ar6/> (2021)
- 782 Mattsson, M., B. H., M. D., Loubet, B., M. R., Theobald, M., Sutton, M., Bruhn, D., Neftel, A., and Schjoerring, J. Temporal  
 783 variability in bioassays of ammonia emission potential in relation to plant and soil N parameters in intensively  
 784 managed grassland. *Biogeosciences Discuss.* <https://doi.org/10.5194/bgd-5-2749-2008> (2008)
- 785 McDuffie, E. E., Smith, S. J., O'Rourke, P., Tibrewal, K., Venkataraman, C., Marais, E. A., Zheng, B., Crippa, M., Brauer,  
 786 M., and Martin, R. V. A global anthropogenic emission inventory of atmospheric pollutants from sector- and fuel-  
 787 specific sources (1970–2017): An application of the Community Emissions Data System (CEDS). *Earth Syst. Sci.*  
 788 *Data.* <https://doi.org/10.5194/essd-12-3413-2020> (2020)
- 789 Met Office. *Exceptionally warm and dry Spring 2011.* Met Office.  
 790 [https://www.metoffice.gov.uk/binaries/content/assets/metofficegovuk/pdf/weather/learn-about/uk-past-](https://www.metoffice.gov.uk/binaries/content/assets/metofficegovuk/pdf/weather/learn-about/uk-past-events/interesting/2011/exceptionally-warm-and-dry-spring-2011---met-office.pdf)  
 791 [events/interesting/2011/exceptionally-warm-and-dry-spring-2011---met-office.pdf](https://www.metoffice.gov.uk/binaries/content/assets/metofficegovuk/pdf/weather/learn-about/uk-past-events/interesting/2011/exceptionally-warm-and-dry-spring-2011---met-office.pdf) (2016)

<https://doi.org/10.5194/egusphere-2022-1046>  
 Preprint. Discussion started: 3 November 2022  
 © Author(s) 2022. CC BY 4.0 License.



- 792 Nemitz, E., Sutton, M. A., Schjoerring, J. K., Husted, S., and Paul Wyers, G. Resistance modelling of ammonia exchange  
 793 over oilseed rape. *Agric. For. Meteorol.* [https://doi.org/10.1016/S0168-1923\(00\)00206-9](https://doi.org/10.1016/S0168-1923(00)00206-9) (2000)
- 794 Olesen, J. E., and Sommer, S. G. Modelling effects of wind speed and surface cover on ammonia volatilization from stored  
 795 pig slurry. *Atmospheric Environ. Part Gen. Top.* [https://doi.org/10.1016/0960-1686\(93\)90030-3](https://doi.org/10.1016/0960-1686(93)90030-3) (1993)
- 796 Personne, E., Tardy, F., Générumont, S., Decuq, C., Gueudet, J.-C., Mascher, N., Durand, B., Masson, S., Lauransot, M.,  
 797 Fléchar, C., Burkhardt, J., and Loubet, B. Investigating sources and sinks for ammonia exchanges between the  
 798 atmosphere and a wheat canopy following slurry application with trailing hose. *Agric. For. Meteorol.*  
 799 <https://doi.org/10.1016/j.agrformet.2015.03.002> (2015)
- 800 Phillips, S. B., Arya, S. P., and Aneja, V. P. Ammonia flux and dry deposition velocity from near-surface concentration  
 801 gradient measurements over a grass surface in North Carolina. *Atmos. Environ.*  
 802 <https://doi.org/10.1016/j.atmosenv.2004.02.054> (2004)
- 803 Pinder, R. W., Gilliland, A. B., and Dennis, R. L. Environmental impact of atmospheric NH<sub>3</sub> emissions under present and  
 804 future conditions in the eastern United States. *Geophys. Res. Lett.* <https://doi.org/10.1029/2008GL033732> (2008)
- 805 Plumb, R. A., and Stolarski, R. S. Chapter 2: The Theory of Estimating Lifetimes Using Models and Observations. *SPARC*  
 806 *Lifetimes Rep. 2013 – SPARC Rep. No 6*. [https://pages.jh.edu/rstolar1/other\\_pubs/LifetimeReport\\_Ch2.pdf](https://pages.jh.edu/rstolar1/other_pubs/LifetimeReport_Ch2.pdf) (2013)
- 807 Potapov, P., Turubanova, S., Hansen, M. C., Tyukavina, A., Zalles, V., Khan, A., Song, X.-P., Pickens, A., Shen, Q., and  
 808 Cortez, J. Global maps of cropland extent and change show accelerated cropland expansion in the twenty-first  
 809 century. *Nat. Food*. <https://doi.org/10.1038/s43016-021-00429-z> (2022)
- 810 Randerson, J. T., Van Der Werf, G. R., Giglio, L., Collatz, G. J., and Kasibhatla, P. S. Global Fire Emissions Database,  
 811 Version 4.1 (GFEDv4). *ORNL DAAC*. <https://doi.org/10.3334/ORNLDAA/1293> (2015)
- 812 Riahi, K., van Vuuren, D. P., Kriegler, E., Edmonds, J., O'Neill, B. C., Fujimori, S., Bauer, N., Calvin, K., Dellink, R.,  
 813 Fricko, O., Lutz, W., Popp, A., Cuaserna, J. C., Kc, S., Leimbach, M., Jiang, L., Kram, T., Rao, S., Emmerling, J.,  
 814 ... Tavoni, M. The Shared Socioeconomic Pathways and their energy, land use, and greenhouse gas emissions  
 815 implications: An overview. *Glob. Environ. Change*. <https://doi.org/10.1016/j.gloenvcha.2016.05.009> (2017)
- 816 Roelle, P. A., and Aneja, V. P. Modeling of Ammonia Emissions from Soils. *Environ. Eng. Sci.*  
 817 <https://doi.org/10.1089/ees.2005.22.58> (2005)
- 818 Schlesinger, W. H., and Hartley, A. E. A global budget for atmospheric NH<sub>3</sub>. *Biogeochemistry*.  
 819 <https://doi.org/10.1007/BF00002936> (1992)
- 820 Shen, H., Chen, Y., Hu, Y., Ran, L., Lam, S. K., Pavur, G. K., Zhou, F., Pleim, J. E., and Russell, A. G. Intense Warming  
 821 Will Significantly Increase Cropland Ammonia Volatilization Threatening Food Security and Ecosystem Health.  
 822 *One Earth*. <https://doi.org/10.1016/j.oneear.2020.06.015> (2020)
- 823 Shephard, M. W., and Cady-Pereira, K. E. Cross-track Infrared Sounder (CrIS) satellite observations of tropospheric  
 824 ammonia. *Atmos Meas Tech*. <https://doi.org/10.5194/amt-8-1323-2015> (2015)
- 825 Sulla-Menashe, D., and Friedl, M. A. *User Guide to Collection 6 MODIS Land Cover (MCD12Q1 and MCD12C1) Product*.  
 826 [https://lpdaac.usgs.gov/documents/101/MCD12\\_User\\_Guide\\_V6.pdf](https://lpdaac.usgs.gov/documents/101/MCD12_User_Guide_V6.pdf) (2018)
- 827 Svensson, L., and Ferm, M. Mass Transfer Coefficient and Equilibrium Concentration as Key Factors in a New Approach to  
 828 Estimate Ammonia Emission from Livestock Manure. *J. Agric. Eng. Res.* <https://doi.org/10.1006/jaer.1993.1056>  
 829 (1993)
- 830 Theobald, M. R., Crittenden, P. D., Hunt, A. P., Tang, Y. S., Dragosits, U., and Sutton, M. A. Ammonia emissions from a  
 831 Cape fur seal colony, Cape Cross, Namibia. *Geophys. Res. Lett.* <https://doi.org/10.1029/2005GL024384> (2006)
- 832 Tournadre, B., Chelin, P., Ray, M., Cuesta, J., Kutzner, R. D., Landsheere, X., Fortems-Cheiney, A., Flaud, J.-M., Hase, F.,  
 833 Blumenstock, T., Orphal, J., Viatte, C., and Camy-Peyret, C. Atmospheric ammonia (NH<sub>3</sub>) over the Paris megacity:  
 834 9 years of total column observations from ground-based infrared remote sensing. *Atmospheric Meas. Tech.*  
 835 <https://doi.org/10.5194/amt-13-3923-2020> (2020)
- 836 USDA. *Europe—Crop Calendars*. *Foreign Agric. Serv. US Dep. Agric.* Foreign Agricultural Service, U.S. Department of  
 837 Agriculture. [https://ipad.fas.usda.gov/rssiws/al/crop\\_calendar/europe.aspx](https://ipad.fas.usda.gov/rssiws/al/crop_calendar/europe.aspx) (2022, May 12)
- 838 Van Damme, M., Clarisse, L., Franco, B., Sutton, M. A., Erisman, J. W., Wichink Kruit, R., van Zanten, M., Whitburn, S.,  
 839 Hadji-Lazar, J., Hurtmans, D., Clerbaux, C., and Coheur, P.-F. Global, regional and national trends of atmospheric  
 840 ammonia derived from a decadal (2008–2018) satellite record. *Environ. Res. Lett.* <https://doi.org/10.1088/1748-9326/abd5e0>  
 841 (2021)



<https://doi.org/10.5194/egusphere-2022-1046>  
 Preprint. Discussion started: 3 November 2022  
 © Author(s) 2022. CC BY 4.0 License.



- 842 Van Damme, M., Clarisse, L., Whitburn, S., Hadji-Lazaro, J., Hurtmans, D., Clerbaux, C., and Coheur, P.-F. Industrial and  
 843 agricultural ammonia point sources exposed. *Nature*. <https://doi.org/10.1038/s41586-018-0747-1> (2018)
- 844 Van Damme, M., Whitburn, S., Clarisse, L., Clerbaux, C., Hurtmans, D., and Coheur, P.-F. Version 2 of the IASI NH<sub>3</sub>  
 845 neural network retrieval algorithm; near-real time and reanalysed datasets. *Atmos. Meas. Tech.*, 10, 4905–4914,  
 846 <https://doi.org/10.5194/amt-10-4905-2017> (2017)
- 847 Van Der Molen, J., Beljaars, A. C. M., Chardon, W. J., Jury, W. A., and Faassen, H. G. van. Ammonia volatilization from  
 848 arable land after application of cattle slurry. 2. Derivation of a transfer model. *Neth. J. Agric. Sci.*  
 849 <https://doi.org/10.18174/njas.v38i3A.16586> (1990)
- 850 Viatte, C., Abeed, R., Yamanouchi, S., Porter, W., Safieddine, S., Van Damme, M., Clarisse, L., Herrera, B., Grutter, M.,  
 851 Coheur, P.-F., Strong, K., and Clerbaux, C. NH<sub>3</sub> spatio-temporal variability over Paris, Mexico and Toronto and its  
 852 link to PM<sub>2.5</sub> during pollution events. *EGUsphere*. <https://doi.org/10.5194/egusphere-2022-413> (2022)
- 853 Viatte, C., Petit, J.-E., Yamanouchi, S., Van Damme, M., Doucerain, C., Germain-Piaulenne, E., Gros, V., Favez, O.,  
 854 Clarisse, L., Coheur, P.-F., Strong, K., and Clerbaux, C. Ammonia and PM<sub>2.5</sub> Air Pollution in Paris during the  
 855 2020 COVID Lockdown. *Atmosphere*. <https://doi.org/10.3390/atmos12020160> (2021)
- 856 Viatte, C., Wang, T., Van Damme, M., Dammers, E., Meleux, F., Clarisse, L., Shephard, M. W., Whitburn, S., Coheur, P. F.,  
 857 Cady-Pereira, K. E., and Clerbaux, C. Atmospheric ammonia variability and link with particulate matter formation:  
 858 A case study over the Paris area. *Atmospheric Chem. Phys.* <https://doi.org/10.5194/acp-20-577-2020> (2020)
- 859 Wentworth, G. R., Murphy, J. G., Gregoire, P. K., Cheyne, C. A. L., Tevlin, A. G., and Hems, R. Soil–atmosphere exchange  
 860 of ammonia in a non-fertilized grassland: Measured emission potentials and inferred fluxes. *Biogeosciences*.  
 861 <https://doi.org/10.5194/bg-11-5675-2014> (2014)
- 862 Wesely, M. L. Parameterization of surface resistances to gaseous dry deposition in regional-scale numerical models.  
 863 *Atmospheric Environ.* 1967. [https://doi.org/10.1016/0004-6981\(89\)90153-4](https://doi.org/10.1016/0004-6981(89)90153-4) (1989)
- 864 Whitburn, S., Damme, M. V., Clarisse, L., Bauduin, S., Heald, C. L., Hadji-Lazaro, J., Hurtmans, D., Zondlo, M. A.,  
 865 Clerbaux, C., and Coheur, P.-F. A flexible and robust neural network IASI-NH<sub>3</sub> retrieval algorithm. *J. Geophys.*  
 866 *Res. Atmospheres*. <https://doi.org/10.1002/2016JD024828> (2016)
- 867 Wichink Kruit, R. Surface-atmosphere exchange of ammonia. Ph.D., Wageningen University. Wageningen, Netherlands,  
 868 <https://edepot.wur.nl/137586> (2010)
- 869 Yang, S., Yuan, B., Peng, Y., Huang, S., Chen, W., Hu, W., Pei, C., Zhou, J., Parrish, D. D., Wang, W., He, X., Cheng, C.,  
 870 Li, X.-B., Yang, X., Song, Y., Wang, H., Qi, J., Wang, B., Wang, C., ... Shao, M. The formation and mitigation of  
 871 nitrate pollution: Comparison between urban and suburban environments. *Atmospheric Chem. Phys.*  
 872 <https://doi.org/10.5194/acp-22-4539-2022> (2022)
- 873 Yu, F., Nair, A. A., and Luo, G. Long-Term Trend of Gaseous Ammonia Over the United States: Modeling and Comparison  
 874 with Observations. *J. Geophys. Res. Atmospheres*. <https://doi.org/10.1029/2018JD028412> (2018)
- 875 Zhang, L., Wright, L. P., and Asman, W. a. H. Bi-directional air-surface exchange of atmospheric ammonia: A review of  
 876 measurements and a development of a big-leaf model for applications in regional-scale air-quality models. *J.*  
 877 *Geophys. Res. Atmospheres*. <https://doi.org/10.1029/2009JD013589> (2010)

## Chapter 5

### *5 Industrial and agricultural changes during the Syrian war*

In the previous chapters, I discussed the ammonia exchange between the soil and the atmosphere. I showed the effect of meteorological, and soil parameters on ammonia volatilization from agricultural lands. In order to complete the discussion, I will study in this chapter a case study that explores the effect of land use change, induced by conflict and human displacement, on the levels of ammonia using IASI data. During my PhD years, the war in Syria was one of the most talked about in the world. Here, I investigate two regions in Syria with two different ammonia sources: the first is a fertilizers industry (providing most of the synthetic fertilizers reserve of the country, and managed by the government), and the second is an agricultural region heavily affected by human displacement, and the invasion of the Islamic State in Iraq and Syria (ISIS) along with other political parties. Unlike the politically-stable agricultural regions explored in previous chapters, the north east of Syria witnessed changes that cannot be predicted by simulation models and inventories. The fluctuations of ammonia levels were not mainly driven and predicted by climatology, but rather by the events of the war. I use different datasets to support this analysis, including satellite (IASI Metop A/B, combined Aqua/Terra MODIS, Sentinel-2 imagery), and re-analysis data (ERA5 from ECMWF). This study provides a novel and complete view (before, during, and after) of the effect of the war in Syria on important agricultural sources. It shows how atmospheric chemistry can be used as a powerful tool to study changes in social patterns/activities induced by political events and conflict. In this chapter I first introduce the topic, then discuss some of the results that are not mentioned in the published article. To look at ammonia in both source regions, I use IASI product NH<sub>3</sub>-v3R-ERA5 (Van Damme et al., 2021). To better visualize the industrial activity (in Homs), I look at satellite imagery from Sentinel-2 L1C (Lamquin et al., 2018). In the agricultural region, I look at MODIS land cover type product (MCD12Q1 version 6) to study the changes in land cover such as expansion or abandonment of croplands' area (Sulla-Menashe and Friedl, 2018). Since atmospheric ammonia levels are affected by meteorological parameters, I also consider wind speed, T<sub>skin</sub>, and precipitation from ERA5.

Finally, the possible contribution of fires to atmospheric ammonia in the agricultural region are tested by using MODIS fire mask product MCD64A1 (Giglio et al., 2018).

I introduce the regions considered in Section 5.1, then I discuss briefly the timeline of the war relevant to the study in Section 5.2. The results are presented in sections 5.3 to 5.5. Only Figures Figure 5.2, Figure 5.3, and Figure 5.4 are adapted from Abeed et al. (2021).

## 5.1 Regions of study

The war in Syria is one of the most violent wars the current century has witnessed. Among the country's most vital sectors, agriculture and food production were heavily affected. The conflict started in early 2011, ignited by anti-government protests in Homs, in Central Syria. In spite of the damage, Syria's income from agricultural production still accounted to 26% of the total Gross Domestic Product (GDP, (FAO, 2017)) in 2017. Several studies used remote sensing data to monitor the social, economic and environmental damage and changes in Syria caused by war events (Corbane et al., 2016; Eklund et al., 2017; Jaafar and Woertz, 2016; Lubin and Saleem, 2019; Mohamed et al., 2020).



**Figure 5.1. A map showing Syria (in red) and the locations of the two regions of focus in this work: Homs where the fertilizers industry is located (industrial region marked with a black cross), and the northeast of Syria with croplands (agricultural region in the black box).**

To investigate the effect of the war on the agricultural sector one can consider “source regions”, or regions with remarkably high ammonia concentration. After investigation, I focus on two important regions, the first is an industrial one located in the city of Homs (marked with a

black cross in Figure 5.1), and marked as one of the 200+ ammonia hotspots identified in the world (the hostpost of Homs, <https://squares.ulb.be/NH3-IASI.html>, Van Damme et al., (2018)). In this region resides the General Fertilizer Company (GFC), it was the only fertilizers industry functioning during the period of the war (FAO/WFP, 2017). The second is an agricultural region in the northeast of Syria, the location is shown as a rectangle in Figure 5.1. The northeast of Syria consists of vast croplands that produce most of the country's wheat, in addition to other crops.

## *5.2 The war timeline*

It is important to note that the political situation was not the same everywhere in Syria during the war period. This allowed the recovery of some regions while others were still politically disturbed and unsafe to access. Therefore, the studied regions I focus on do not share the same conflict timeline. In the industrial region, for instance, the perturbations started to affect the activity of the fertilizers plant in 2011, and then they intensified in 2013 and 2014, when the forced military siege around the city of Homs worsened (ISW, 2013). While in the agricultural region, in northeast Syria, one can see changes in ammonia levels starting 2013 up until 2019. This region witnessed the presence of several militia groups and armies. Those who played the most crucial role in the agricultural changes are the Islamic State in Iraq and Syria (ISIS) and the Kurdish forces (also referred to as the Syrian Democratic Forces, SDF). ISIS started to infiltrate in the region during summer 2013 and they continued to expand until they seized a large area of the Syrian and the Iraqi territories in 2015. Starting that year and up until 2019, the power of ISIS was defeated by the SDF. In 2019, the SDF reclaimed the de facto autonomous region known by the name Rojava in northeast Syria, bringing more stability to the region, and as result higher agricultural activity. Relevant and key events are presented in Figure 5.2.



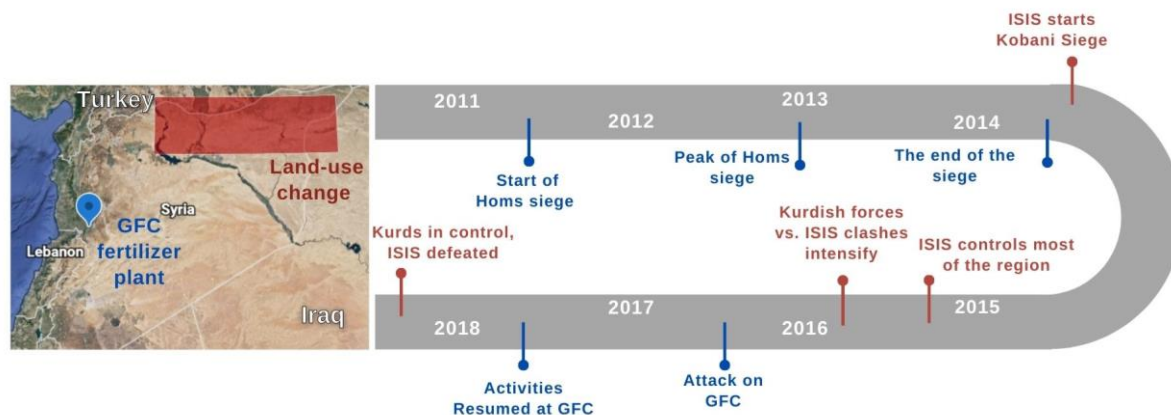


Figure 5.2. Graphical timeline of the Syrian civil war events relevant to this study. In blue are those that affected the General Fertilizers Company (blue pin in left panel and discussed in section 5.3), and in red are those associated to the land-use changes in the agricultural region in Northeast Syria (red box in left panel and discussed in section 5.4). Adapted from Abeed et al. (2021).

### 5.3 The industrial region

#### 5.3.1 Ammonia changes due to the war events

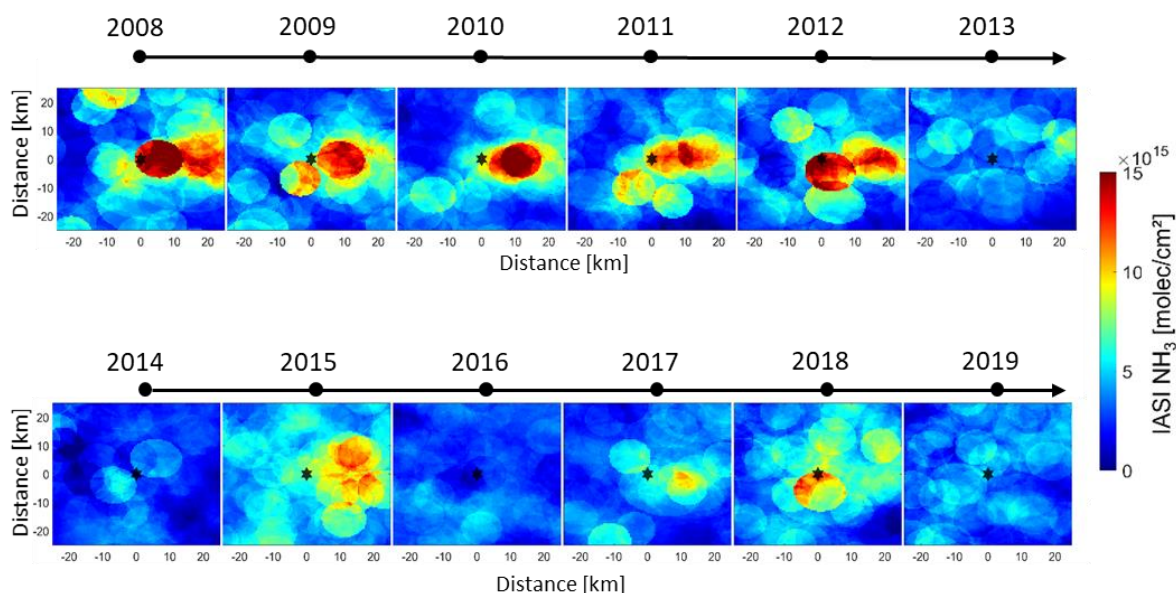
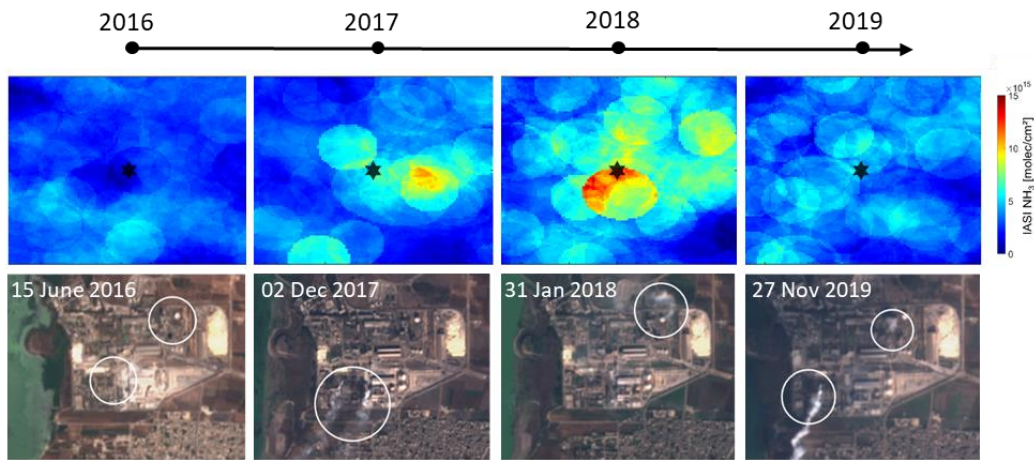


Figure 5.3. Yearly spatial average of IASI  $\text{NH}_3$  total columns ( $\text{molec}/\text{cm}^2$ ) around the fertilizers industry (indicated with a black star in the middle of the plot), from 2008 until 2019. The average is calculated using an oversampling method (Van Damme et al., 2018; Zhu et al., 2014). Adapted from Abeed et al. (2021).

To start, I show in Figure 5.3 the ammonia columns around the GFC plant as yearly averages to see the interannual changes for the period [2008 – 2019], using an oversampling method that

is used in other studies to identify hotspots of trace gases (Van Damme et al., 2018; Zhu et al., 2014). Before the war, [2008 – 2012], the plant activity seems stable. Ammonia concentrations were equally steady before year 2013 (Figure 5.3). One can observe a decrease in the activity of the fertilizers industry that is reflected in less atmospheric ammonia, mostly during 2013 and 2014. The decrease accounted for  $-17\%$  and  $-47\%$ , during 2013 and 2014 respectively, in comparison to pre-war ammonia average [2008 – 2012]. During these two years, the military siege around the city of Homs and the clashes were at their peak (CNN, 2014).



**Figure 5.4.** Upper panel: Yearly spatial average of ammonia total columns ( $\text{molec}/\text{cm}^2$ ) around the fertilizers industry (indicated with a black star in the middle of the plot). Lower panel: Visible satellite images from Sentinel 2 L1C of the fertilizers company on days of suspension of activities (2016), and resume of production (2017, 2018, and 2019). Figure adapted from Abeed et al. (2021).

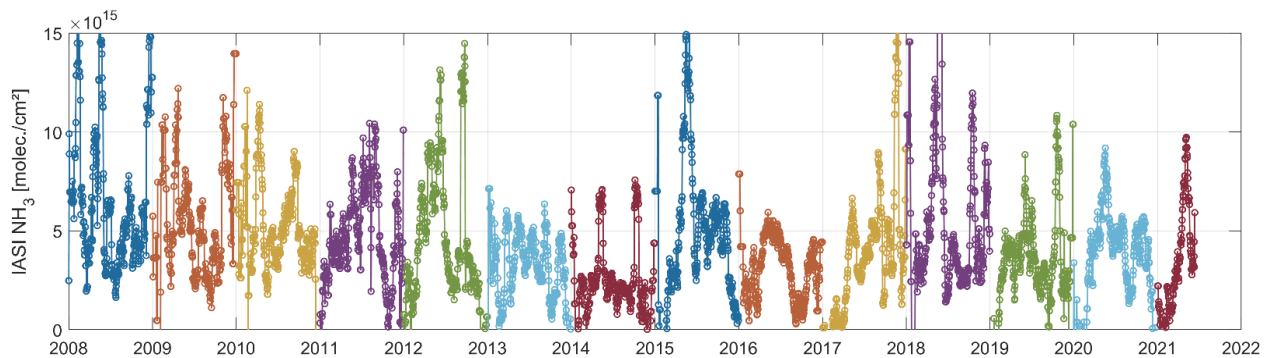


**Figure 5.5.** 20-day running mean of ammonia total columns, for the fertilizer industry, during the period [2008 – 2021] using IASI/Metop A data [2008 – 2019], and IASI/Metop B data to complete the period [2020 – 2021].

In 2016, ammonia decrease accounted to  $-32\%$  in comparison to pre-war average. In Figure 5.4 I show ammonia yearly average around the industry as in Figure 5.3. during the period [2016 – 2019] (upper panel), and satellite images reflecting the activity of the plant during those years (lower panel). The fertilizers plant ceased to function in June 2016 due to an attack on the plant itself (FAO/WFP, 2019). Visible satellite images show that the chimney of the industry was indeed not releasing any smoke during the time of the halt (Figure 5.4). Only in 2017, we see an activity as the satellite images show, together with the ammonia concentrations increase (Figure 5.4).

In my article (Abeed et al., 2021), I do not show the total columns of ammonia after year 2019, since the changes during the pandemic period, [2020 – 2021], are anomalous and including them in the study would obscure the analysis. But in order to see if the activity of the fertilizer industry came back to pre-war normal or not, I plot in Figure 5.5 the 20-day running mean for ammonia total columns, of the same area shown in Figure 5.4, for the period [2008 – 06/2021]. Ammonia concentrations in 2020 and early to mid-2021 are similar to those in 2019. Even before the pandemic outbreak in early 2020, it is important to mention that the ammonia plant is already working less frequently since 2019, due to less workforce after the Russians started to manage the GFC (Enab Baladi, 2019). As a result, the concentrations in 2020 and 2021 are indeed less than the pre-war average.

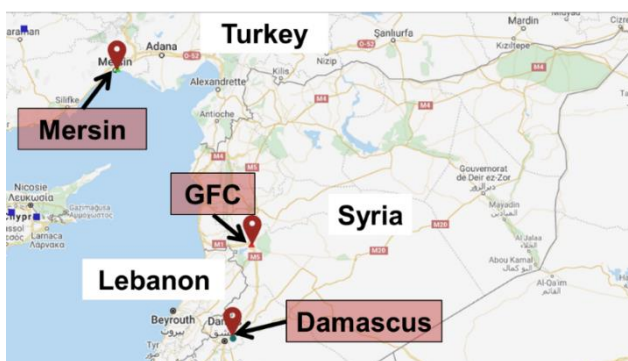


**Figure 5.6.** Map showing the location of three ammonia sources: soda ash industry in Turkey (city of Mersin), Fertilizers industry in Syria (GFC in Homs city), and an industrial region in Damascus (city of Damascus). Source: Google Maps.

Meteorological fluctuations in the whole region might have affected the availability of atmospheric ammonia. In that case, these fluctuations would be captured by emission inventories and there would be no need for an in-depth study of the war events relation to the changes in ammonia levels. In order to answer this concern, I look at two nearby ammonia hotspots/sources from industrial activities. The first is an industrial region in the east of Damascus in Syria, and the second is a soda ash industry in the city of Mersin (Turkey) (locations are shown in Figure 5.6). I plot in the upper panel of Figure 5.5 the ammonia changes in Damascus for the period [2008 – 2019], and since this region is surrounded by agricultural fields I prefer to show a spatial average using the oversampling method I refer to earlier in this chapter. We can see that ammonia levels decrease from 2011 until 2014, also in 2016 and 2017. This pattern is not similar to that observed from the GFC plant, since the decrease in GFC occurs in 2013, 2014 and 2016 (Figure 5.3, and Figure 5.5). The lower panel of Figure 5.7 shows the 20-day running mean of ammonia in Mersin, one can see that ammonia levels seem to increase after 2015 in a constant manner (Figure 5.7). The Damascus source is clearly affected by other war-related events that I do not attempt to explain here. Damascus is the capital of Syria, it is an industrial region, and during the war it was known as a hub for chemical weapons manufacturing (BBC News, 2017).



### 5.3.2 Local air quality in Homs in relation to the industry

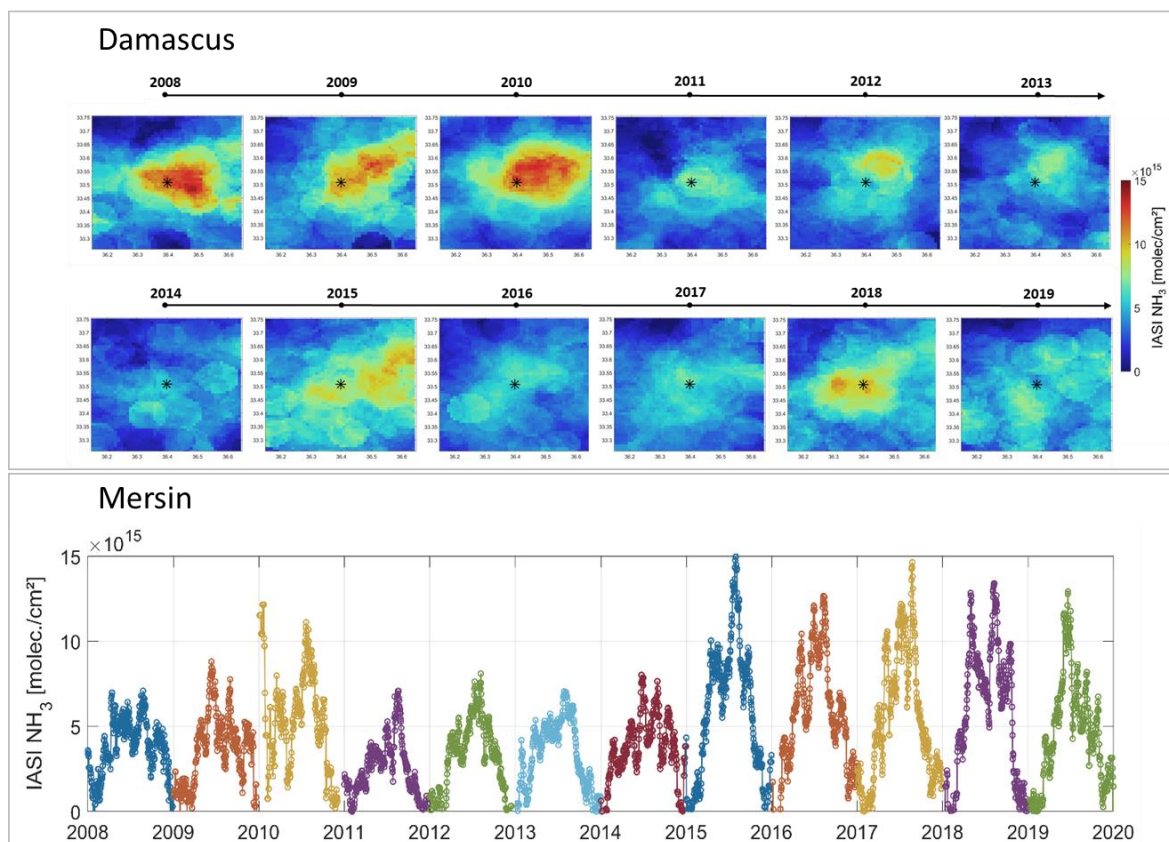


**Figure 5.7.** Upper panel: Oversampled yearly spatial average of ammonia total columns (molec/cm<sup>2</sup>) over an industrial region in the east of Damascus (the centre of the industrial area is indicated with a black star). Lower panel: 20-day running mean of IASI daily total columns of ammonia (molec/cm<sup>2</sup>) averaged over the soda ash industry in Mersin.

Ammonia emitted from the GFC industry affects the nearby air quality and environment in the city of Homs. It is deposited in the nearby lake (Qattinah lake), which results in eutrophication and algal bloom events (Mohamad, 2019). Furthermore, ammonia is a short-lived gas, and it can transform within hours into particulate matter PM as explained in chapters 1 and 3. However, no local observations of air quality exist and analyzing space-derived proxies of PM<sub>2.5</sub> is not recommended (Christopher and Gupta, 2010). It is worth noting that when one looks at remote atmospheric nitrogen dioxide (NO<sub>2</sub>) levels around the GFC industry (Figure 5.8), as a tracer of anthropogenic activities, one can find a net decrease of NO<sub>2</sub> tropospheric column. As in all wars, many anthropogenic activities are slowed down (people are less likely to take their cars, go to work, and resume normal life activities). Looking at nitrogen dioxide, however, the levels seem to decrease starting 2011, until the end of the siege in 2014 (red line in Figure 5.8), and later in

2016. This confirms that the industry was functioning with less activity than before the period war. It is also an expected pattern, as when the siege ended in May 2014 several buses were sent to transport the civilians and rebels out of the city of Homs (Al Arabiya News, 2014; BBC News, 2014). Later in 2016, one can see less  $\text{NO}_2$  concentrations, as the industry was attacked this year as mentioned in Section 5.3.1. Therefore, while there is an improvement in the local air quality due to less atmospheric ammonia and nitrogen dioxide, it would be hard to pin point the contribution of GFC suspended activities to it.

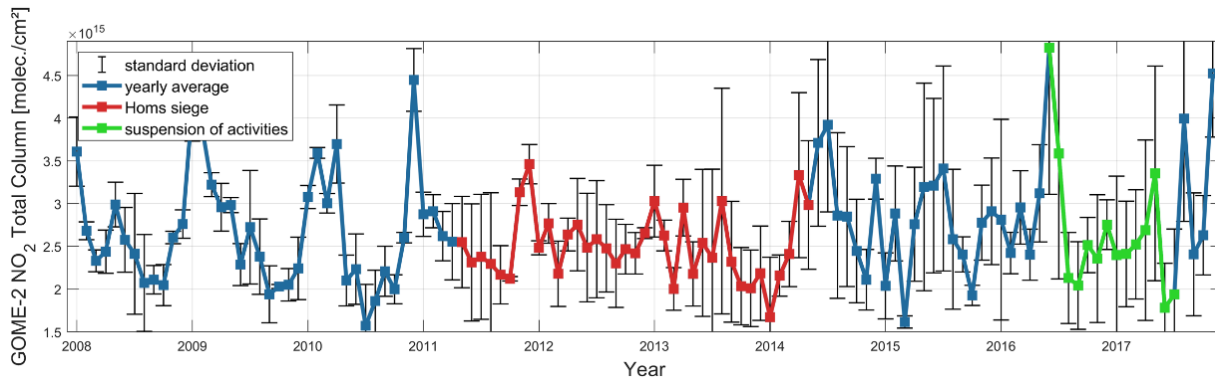


**Figure 5.8. GOME-2 Monthly averages of  $\text{NO}_2$  total columns over the GFC until 2017.**

## 5.4 The agricultural region

Contrary to the industrial region, the analysis of the ammonia levels in the agricultural region shows an increase during the war. The most remarkable periods are when ISIS seized the fields in the northeast of Syria ([2013 – 2015]), then later the SDF controlled them ([2017 – 2019]) (see Figure 5.2). The ammonia levels were even higher during the ruling of SDF [2017 – 2019] than during the occupation of ISIS [2013 – 2015]. In Figure 5.9 I show on the left the change in cultivated area during the year 2015 (panel (a)) and 2019 (panel (b)), as compared to pre-war cultivated area (2011). On the right, I show the spring (March-April-May) anomalies of ammonia (%), and T skin (°C) in the northeast of Syria for the period [2008 – 2019] as compared to pre-war spring average [2008 – 2012] (Figure 5.9c, d). In 2015, the croplands area increases by +10 %, likewise, the anomalies of ammonia during that year show an increase that accounts for more than +55 % (Figure 5.9c).

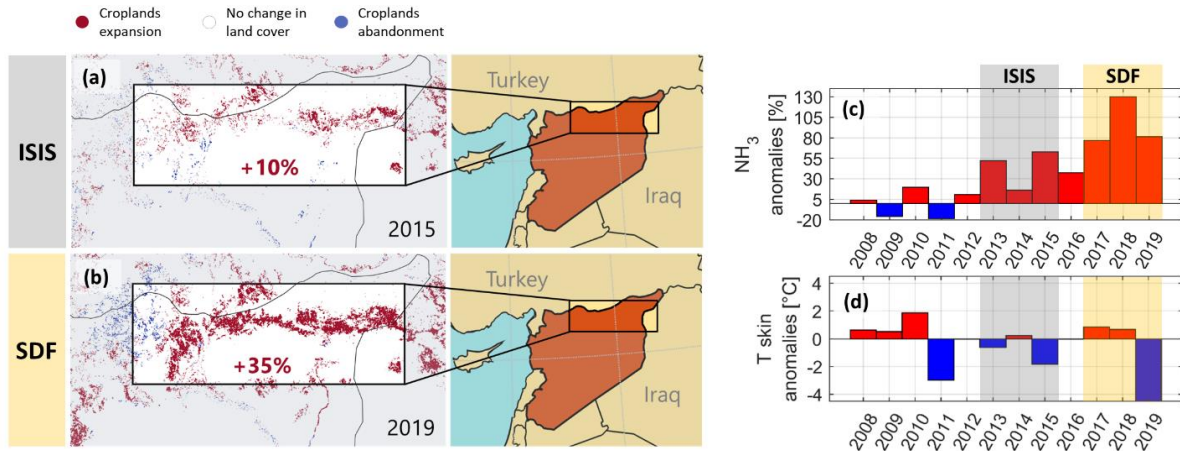


**Figure 5.9.** On the left: the change in cultivated area during 2015 (panel (a)) and 2019 (panel (b)) as compared to the land cover in 2011 in north east Syria, using MODIS Land Cover Type product. The colour red denotes an expansion in croplands (active cultivation), blue denotes an abandonment of the croplands, and white means there was no change in the land cover. On the right: spring March-April-May anomalies of IASI ammonia (panel (c)), and ERA5 T skin in °C (panel (d)) as compared to pre-war spring average [2008 – 2012]. The black (yellow) rectangles in panels (c) and (d) denote the period of occupation of ISIS (SDF).

The territory controlled by ISIS started to shrink in 2015 until they lost the battle to the Kurdish forces (SDF) by July 2019 (BBC News, 2019). The security conditions in 2019 allowed even a larger increase in the cultivated area that accounts for +35 % (Figure 5.9b). In 2019 atmospheric ammonia is +80 % higher than pre-war average, although this year witnessed the highest increase in cultivated area, the ammonia levels are lower than in 2018 due to negative temperature

anomalies in 2019 as compared to 2018 (Figure 5.9d). As we saw in Chapters 3 and 4, higher temperature anomalies induce more volatilization of ammonia in agricultural fields. In this case study, the main driver in the ammonia increase is the political disturbances, and not meteorology. In Figure 5.9d, one can see negative temperature anomalies while ammonia is higher, during the occupation of ISIS for instance [2013 – 2015]. The effect of meteorology is studied in details in Abeed et al. (2021).

### *5.5 Can we draw a link between both regions?*

The GFC industry is a government-owned company, in Syria, the only official source of fertilizers is the Agricultural Cooperative Bank (ACB), a body owned by the Syrian state (FAO, 2003). The ACB calculates each farmer's needs for seeds and fertilizers, and distributes portions at low prices accordingly. Since the GFC was the only functioning plant during the war, one can argue that the decrease in fertilizers production in GFC must have affected the availability of fertilizers in the market and resulted in less fertilizer use in the northeast of Syria. However, even before the war starts, parallel (illegal) markets existed, where fertilizers are indeed sold at higher prices, and such transactions are hard to detect and track (FAO, 2003). Due to the lack of Nitrogen-fertilizers (N-fertilizers) in the market, the gap was met with imported fertilizers (both legally and illegally). Therefore, Syrian farmers relied on imported fertilizers that are sold in the black market.

In Figure 5.10, I show the production, import and export data for the N- and NPK fertilizers<sup>26</sup>, during the years I could find available through the Food and Agriculture Organization (FAO). It is very tricky to know how much N-fertilizers were actually available in the market, as not all of these are documented nor legally sold. Alternatively, one can draw a relationship between NPK fertilizers import quantity (which is observed to increase from 2013 to 2019 in Figure 5.10. and atmospheric ammonia (which also appears to increase from 2013 and onward in Figure 5.9c, and also Article Figure 5).

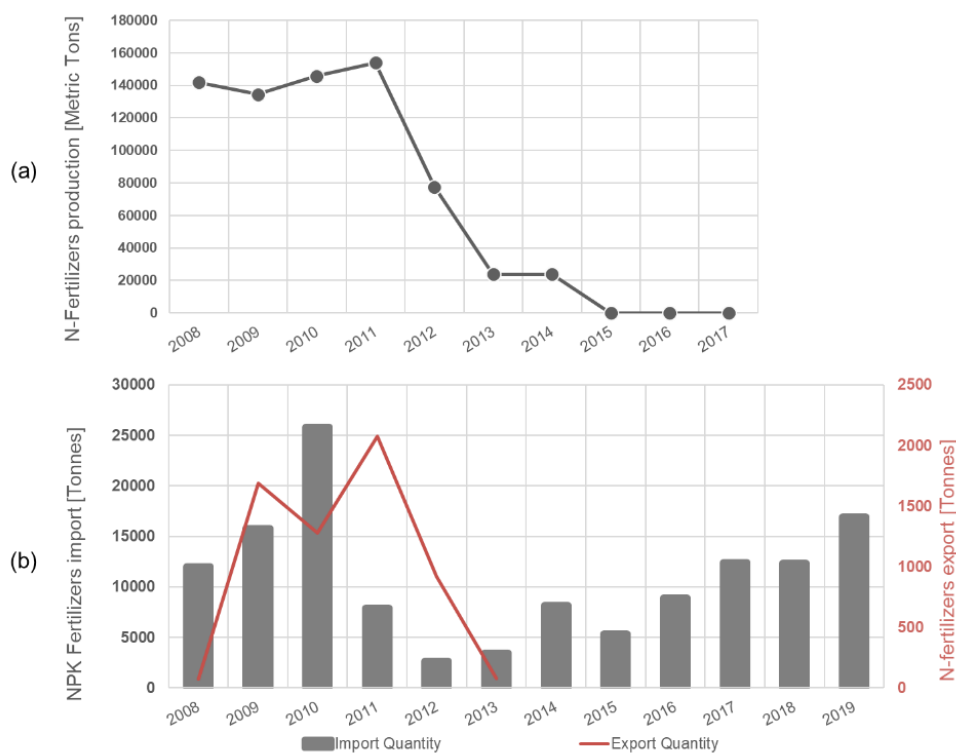


**Figure 5.10. Panel a: N-fertilizers production data [Metric Tonnes] for the years 2008 – 2017. Panel b: NPK fertilizers import quantity for the years [2008 – 2019] (grey bars), and export quantity for the years [2008 – 2013] (red line) [Tonnes], source: FAOSTAT (<https://knoema.com/FAORFBFP/faostat-fertilizers-by-product>).**

## 5.6 Conclusion

As demonstrated with this case study, instruments onboard satellites, such as IASI, are powerful enough to provide atmospheric data from which the impact of geopolitical situations can be documented. This is particularly useful when access to the region of study is restricted owing to political complications. I learned from this study that the relationship ammonia –

<sup>26</sup> N-fertilizers are nitrogen-based fertilizers such as urea they all derive from ammonia. NPK fertilizers contain nitrogen (N), phosphorus (P), and potassium (K), these are considered the primary nutrients necessary to plant growth.

cropland cover is not linear as it depends on other factors. Although the cropland cover expanded in the northeast of Syria during the war (larger agricultural area, induce more fertilizer use), in the context of a conflict, the quantity of atmospheric ammonia depends on the economic situation (whether or not the farmers can buy fertilizers), the political events (human displacement away from or migration to agricultural areas), and meteorology. The fluctuations in atmospheric ammonia in the industrial region (Homs city), are directly affected by the siege around the city, the attack, and later the lack of workforce. Such events are completely controlled by politics.

The current available emissions inventories are likely to underestimate the amount of ammonia emitted (Van Damme et al., 2018). These inventories might not account for the events of war. In northeast Syria, the changes in T skin normally are expected to reduce the volatilization of ammonia, but the results of this study show the opposite, hence why an in-depth investigation of the political events is needed. The same notion applies to the changes in atmospheric ammonia levels in the industrial region that are solely driven by politics.

In addition to studying conflict-related changes, monitoring atmospheric composition can also show the effect of an economic crisis, e.g. the one undergoing in Lebanon. Measurements by Sentinel 5P (Veefkind et al., 2012) show an increase in air pollution by nitrogen dioxide  $\text{NO}_2$  in 2022 due to the excessive use of diesel-fed generators in the absence of electrical supply from the government (LCAT, 2022). Another example of monitoring the changes due to an economic crisis is the study of that showed a decrease (unlike the case of Lebanon) in  $\text{NO}_2$  concentrations in Athens after 2008, associated with the very high prices of gasoline (Vrekoussis et al., 2013). The disruptions due to war and/or a local crisis are not unidirectional, and hence such satellite instruments are crucial in order to remotely monitor these changes. The results briefly presented in this chapter are published in the journal *Elementa – Science of the Anthropocene* (Section 5.7).



## 5.7 Published article



Abeed, R, et al. 2021. A space view of agricultural and industrial changes during the Syrian civil war. *Elem Sci Anth*, 9: 1. DOI: <https://doi.org/10.1525/elementa.2021.000041>

## RESEARCH ARTICLE

## A space view of agricultural and industrial changes during the Syrian civil war

Rimal Abeed<sup>1,\*</sup>, Cathy Clerbaux<sup>1,2</sup>, Lieven Clarisse<sup>2</sup>, Martin Van Damme<sup>2</sup>, Pierre-François Coheur<sup>2</sup>, and Sarah Safieddine<sup>1</sup>

The agricultural sector in Syria was heavily affected by the civil war that started in 2011. We investigate the war's impact on the country's atmospheric ammonia ( $\text{NH}_3$ ) from 2008 to 2019, using measurements from the infrared atmospheric sounding interferometer instrument on board the Metop satellites. We examine the changes in  $\text{NH}_3$  close to a fertilizer industry, whose activities were suspended due to conflict-related events. We also explore the effect of war-induced land use/land cover changes on agriculture-emitted ammonia in north-east Syria that has witnessed battles between different groups. The interpretation of the changes in  $\text{NH}_3$  is supported by different datasets: visible satellite imagery to assess the effect on industrial activity, reanalysis data from the European center for medium-range weather forecasts to look at the effect of meteorology (temperature, wind speed, and precipitation), and land cover and burned area products from the moderate resolution imaging spectroradiometer (MODIS) to examine land use/land cover changes and fire events during the study period. We show that the  $\text{NH}_3$  columns are directly affected by the war. Periods of intense conflict are reflected in lower values over the industry reaching -17%, -47%, and -32% in 2013, 2014, and 2016, respectively, compared to the [2008–2012] average, and a decrease reaching -14% and -15% in the croplands' area in northeast Syria during 2017 and 2018 (compared to 2011), respectively. Toward the end of the control of Islamic State in Iraq and Syria, an increase in atmospheric  $\text{NH}_3$  was accompanied by an increase in croplands' area that reached up to +35% in 2019 as compared to prewar (2011). This study shows the relevance of remote-sensing data of atmospheric composition in studying societal changes at a local and regional scale.

**Keywords:** Ammonia, Agriculture, Syria, Remote sensing, IASI, Satellite

### 1. Introduction

The Syrian civil war started in March 2011 and caused dramatic social, political, economic, and environmental consequences over the whole country. Agriculture suffered massively, which also affected the economy directly since the agricultural sector makes up to 26% of the gross domestic product (FAO, 2017a). Several studies used satellite-retrieved data and/or imagery to examine the changes in the region during the conflict (Corbane et al., 2016; Jaafar and Woertz, 2016; Eklund et al., 2017; Dammers et al., 2019; Mohamed et al., 2020). The crisis caused a massive displacement of refugees, inside Syria and to other countries. A total of 13.2 million individuals were displaced. This includes 6.6 million refugees outside of

Syria and more than 6 million internally displaced (UNHCR, 2019). Naturally, this led to land-use changes, abandonment/expansion of cultivated lands, and a direct effect on industrial activities related to agriculture, such as the fertilizer industries.

One tracer of agricultural activity is atmospheric ammonia ( $\text{NH}_3$ ), the main component of widely used nitrogen fertilizers that are essential for plant growth, such as urea and anhydrous  $\text{NH}_3$  among other products (Finch et al., 2002). It is an alkaline, highly soluble and short-lived gas and the most abundant form of reactive nitrogen (Schlesinger and Hartley, 1992; Anderson et al., 2003). As the only alkaline gas in the atmosphere, it plays an important role in the acidity of cloud water, precipitation, and fine particulate matter ( $\text{PM}_{2.5}$ ), as well as in the formation of the latter (Behera et al., 2013). Agriculture is the main anthropogenic contributor to the global  $\text{NH}_3$  budget. Other sources are some types of industries (fertilizer, coking, soda ash, nickel, geothermal, and explosive), urban, biomass burning, and natural emissions such as seal colonies, seabirds and oceans (Theobald et al., 2006; Paulot et al., 2015; Whitburn et al., 2015; Riddick et al.,

<sup>1</sup> LATMOS/IPSL, Sorbonne Université, UVSQ, CNRS, Paris, France

<sup>2</sup> Université libre de Bruxelles (ULB), Spectroscopy, Quantum Chemistry and Atmospheric Remote Sensing (SQUARES), Brussels, Belgium

\*Corresponding author:  
Email: [rimal.abeed@latmos.ipsl.fr](mailto:rimal.abeed@latmos.ipsl.fr)

2017; Van Damme et al., 2018; Chang et al., 2021). The excess in nitrogen in ecosystems leads to acidification of soil and water bodies and loss in biodiversity (Bobbink et al., 1998; Guthrie et al., 2018).

In this work, we investigate the war's effect on  $\text{NH}_3$  concentrations in Syria. For this analysis, we rely on remote sensing data described in Section 2. In Section 3, we briefly discuss the main historical events that led to major land-use changes and fluctuations in  $\text{NH}_3$  concentrations. In Section 4, we discuss the results of the case study of 1 fertilizer industry and agricultural region/land use change in the northeast part of Syria. In Section 5, we formulate our conclusions.

## 2. Materials and methods

### 2.1. Infrared atmospheric sounding interferometer (IASI) $\text{NH}_3$

IASI satellite instruments were launched onboard the polar-orbiting Metop platforms in October 2006 (IASI-A), September 2012 (IASI-B), and November 2018 (IASI-C). The instruments are nadir-looking Fourier-transform spectrometers that probe the Earth's atmosphere in the thermal infrared spectral range between 645 and 2,760  $\text{cm}^{-1}$ , with a spectral resolution of 0.5  $\text{cm}^{-1}$  (apodized). IASI monitors the atmospheric composition at any location 2 times per day, at around approximately 9:30 AM and PM (local time). Each instrument measures many of the chemical components that play a key role in the climate system and in several aspects of atmospheric pollution (Clerbaux et al., 2009).

The detection of  $\text{NH}_3$  by IASI is done in the thermal infrared using its  $\nu_2$  vibrational band (approximately 950  $\text{cm}^{-1}$ ; Coheur et al., 2009). The  $\text{NH}_3$  total columns exploited here were derived from IASI radiances using an Artificial Neural Network (Whitburn et al., 2016) and reanalyzed ERA-Interim data, ANNI-NH3-v2.1R (Van Damme et al., 2017). In the past, the IASI instrument has been used to identify, categorize, and quantify local hot-spots of  $\text{NH}_3$  (Van Damme et al., 2018). Numerous sources of  $\text{NH}_3$  have been observed from IASI over the years (Clarisse et al., 2019a; Van Damme et al., 2021), being from agricultural practices and manure management, to industrial activities, in particular fertilizers industries (Van Damme et al., 2018; Dammers et al., 2019), fires (Coheur et al., 2009; Whitburn et al., 2015; Chang et al., 2021), and other natural sources (Clarisse et al., 2019b).

Only daytime measurements are considered in this study, as higher relative errors were observed from the nighttime measurements (Van Damme et al., 2017). The uncertainty estimates on the retrieved total columns can range from 5% to 1,000%; the lower uncertainties correspond to measurements during the day, in spring, and where  $\text{NH}_3$  concentrations are high (Van Damme et al., 2017). In order to cover the period before and after the war in Syria with the same instrument, only IASI-A data are used. Comparison of  $\text{NH}_3$  measurements from IASI with other satellite instruments, such as Crosstrack Infrared Sounder (Shephard and Cady-Pereira, 2015), exhibits consistent seasonal and interannual variability (Viatte et al., 2020). In a case study, Viatte et al. (2021) coupled

ground-based measurement of  $\text{NH}_3$  with IASI (on board Metop A, B, and C). The 2 instruments showed high agreement, with a Pearson's correlation coefficient  $R = .75$ . A recent validation of the IASI  $\text{NH}_3$  product using reconstructed in situ columns based on aircraft profile measurements showed very good agreement (Guo et al., 2021).

In order to achieve a higher resolution spatial average, we averaged IASI- $\text{NH}_3$  total columns using an oversampling method, widely used in other studies for different trace gases concentrations using different instruments (Zhu et al., 2014; Van Damme et al., 2018).

### 2.2. Meteorology, land cover, and burned area

Relevant meteorological parameters used in this study are the skin temperature ( $T_{\text{skin}}$  or land surface temperature), total precipitation, and near surface wind speed. The parameters are extracted daily from the European center for medium-range weather forecast's reanalysis (ERA5; Hersbach et al., 2020) and interpolated in time and space to the IASI morning observations. The resolution of ERA5 datasets is at  $0.25 \times 0.25^\circ$  grid (native horizontal resolution of ERA5 is approximately 31 km).  $T_{\text{skin}}$  is defined as the temperature of the surface at radiative equilibrium. It is derived from the surface energy balance within the land model in ERA5. The total precipitation product combines both large-scale and convective precipitations. The wind speed was calculated from the  $u$  and  $v$  wind components at 10 m of height above the surface of the Earth. The  $u$  component is defined as the horizontal wind speed heading toward the east, and the  $v$  component is the horizontal wind speed moving toward the north.

MODIS instruments are orbiting the Earth onboard the Aqua and Terra satellites. The Aqua/Terra MODIS Land Cover product (MCD12Q1 version 6) provides yearly maps of land cover with a 500 m spatial resolution for the period that extends from 2001 until 2019 (Sulla-Menashe and Friedl, 2018). The MOD12Q1 product employs 17 categories of land cover classification (Belward et al., 1999). In this work, we extract the croplands, shrub, and bare lands from these datasets to examine the effect of war and human displacement. The classification used in this study to represent croplands is defined as lands comprising of at least 60% cultivated area; A shrubland is defined as an area dominated by woody perennials (plants); Bare lands (also called *Barren* in the MCD12Q1 product) are defined as lands with an at least 60% non-vegetated area (Sulla-Menashe and Friedl, 2018). In an attempt to estimate the expansion/abandonment of croplands, we use the classes provided by the MODIS product. The yearly grid of 2011 is chosen as the base year; we compare the other years to it. This product agrees 73.6% with the Food and Agriculture Organization (FAO)-Land Cover Classification System (Sulla-Menashe et al., 2019). In addition to that, the percentage of pixels switching back and forth from a class to another (due to spectral similarity) was reduced from the previous version of the product to the current one ( $<30\%$  for version 6 and  $55\%$  for version 5; Sulla-Menashe et al., 2019). Finally, we used the Aqua/Terra MODIS burned area product (MCD64A1) to look for fire events during the study period



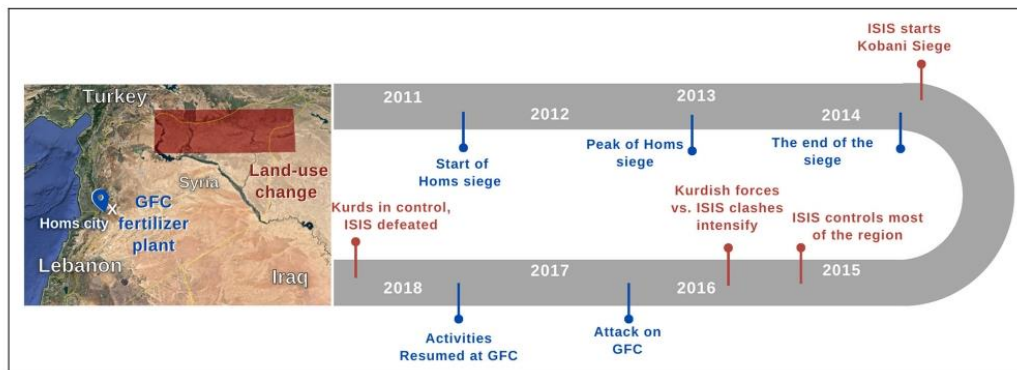


**Figure 1. Graphical time line of the Syrian civil war events relevant to this study.** In blue are those that affected the General Fertilizers Company (GFC) (blue pin in left panel and discussed in Section 4.1), and in red are those associated to the land-use changes in the northeast region of interest (red box in left panel and discussed in Section 4.2). DOI: <https://doi.org/10.1525/elementa.2021.000041.f1>

(Giglio et al., 2018). This product provides the approximate date of burn and the extent of burned area with a 500-m resolution.

### 3. The conflict historical time line and evolution as related to this study

To understand the  $\text{NH}_3$  variability for the 2 case studies discussed hereafter, we have listed the main relevant events and present them as a graphical time line in **Figure 1**. The General Fertilizers Company (GFC), a total of 3 plants, is first investigated in this study. Its location and remarkable events are shown in blue in **Figure 1**. It was affected by the siege of the city/region of Homs that started in May 2011 and peaked in 2013 when an external militia group intervened in the battle (ISW, 2013). The siege later ended in May 2014. Production in GFC between these dates was heavily affected. For example, during 2012, fertilizers production in GFC decreased dramatically due to the lack in fuel and electricity needs, as Islamic State in Iraq and Syria (ISIS) took over the nearby gas fields that were crucial for the production (Aita, 2020). Between 2014 and 2016, production was very low when compared to the prewar period, until an attack occurred on the plant itself during the second half of 2016 and the production stopped completely (FAO/WFP, 2017). The GFC plants resumed production in mid-July 2017 (Enab Baladi, 2019a; Aita, 2020).

On the other hand, in the northeastern part of the country (location and events shown in red in **Figure 1**), the most important series of events with direct effect on land use occurred a few years after the start of the war, in the period that extends from 2013 to 2019. ISIS started to infiltrate in the region during summer 2013 (Wilson Center, 2019). By January 2014, ISIS had already controlled a large part of the region shown in red in **Figure 1** (ISW, 2014). From September to December 2014, massive destruction was reported in regions close to the Turkish borders (included in our region of interest) due to the bombardments and clashes between ISIS

and Kurdish forces (Walsh, 2014). ISIS continued to expand until it had seized a large area of the Syrian and the Iraqi territories in 2015. The croplands area increased during the occupation of ISIS. Later during 2015, the territory controlled by ISIS started to shrink according to studies conducted by IHS Markit (2017) as the Syrian Democratic Forces (commonly referred as Kurdish forces by media) started expelling ISIS from the area, until they eventually took control over most of northeast Syria by July 2019 (Liveuamap, 2019). This occurred after confrontations that included Kurdish forces, Turkish military, and ISIS fighters as well as government and international troops. By 2017, ISIS had lost control of 98% of the territory claimed in 2015 (FOX 32, 2017; BBC, 2018). In 2019, freed from ISIS (BBC, 2019), the security conditions allowed a large increase in the croplands area.

## 4. Results and discussions

### 4.1. Temporal changes of $\text{NH}_3$ columns over a fertilizer factory

The GFC is located in Qattinah, south of Homs city (central Syria). The Homs city location is shown as a white cross in **Figure 1**. The company has been operating since 1972 and is owned by the Syrian government (Zammar et al., 2006). GFC is considered as one of the most important fertilizer production facilities in Syria, providing fertilizers for farmers all around the country. It was the only functioning fertilizers company in 2016 (FAO/WFP, 2017). GFC manufactures various fertilizer components and related products such as  $\text{NH}_3$ , urea, and nitric acid (Zammar et al., 2006). In October 2018, a Russian oil and gas company signed an investment contract with the Syrian government, which allows it to exploit the three main plants of GFC for 40 renewable years (Enab Baladi, 2019a; Al-Allaf and Said, 2021).

We used the IASI  $\text{NH}_3$  daytime measurements to calculate total column daily averages around GFC. **Figure 2** illustrates the war effect on atmospheric  $\text{NH}_3$ . In panel

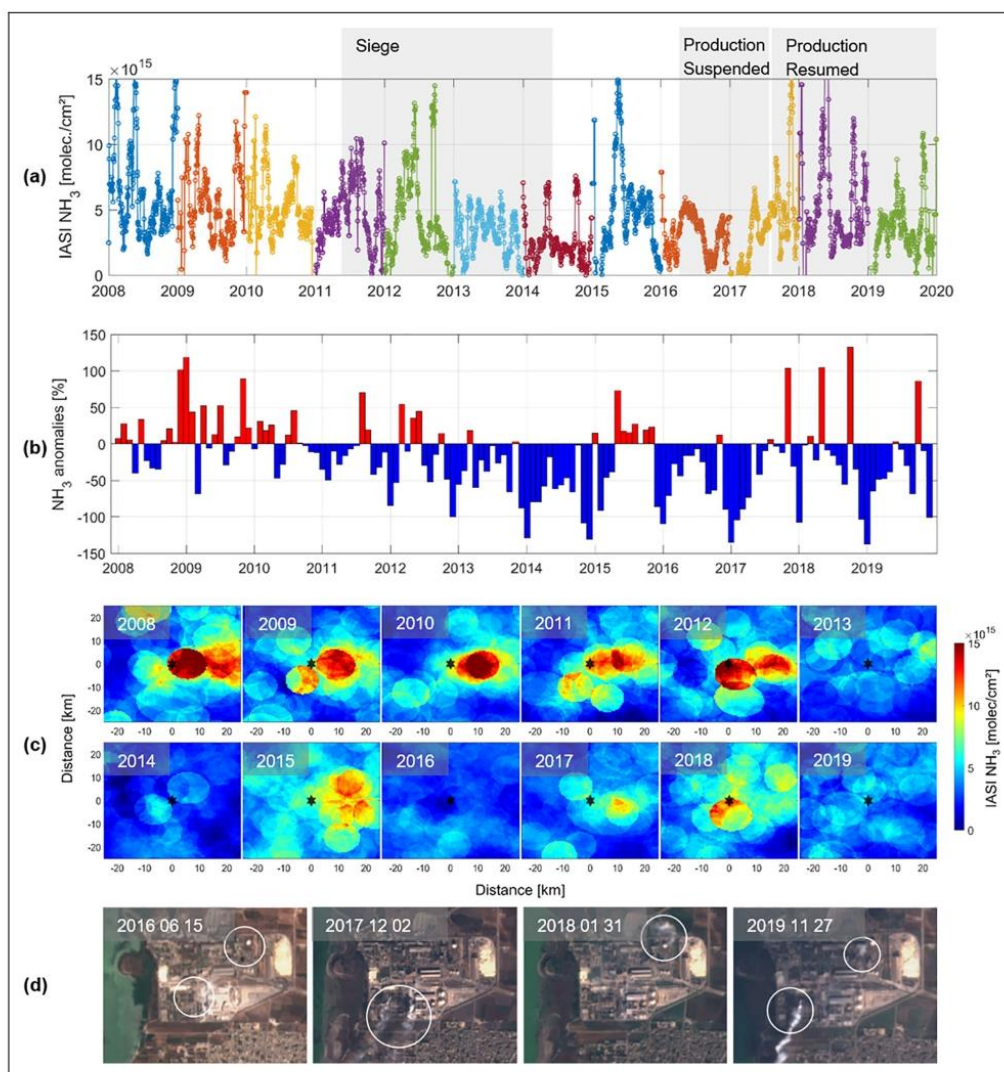


**Figure 2.** (a) 20-day running mean of IASI daily total columns of ammonia ( $\text{molec}/\text{cm}^2$ ) averaged over the fertilizers industry ( $0.5 \times 0.5^\circ$  grid box centered on the factory). (b) Monthly percentage anomalies of IASI total columns of ammonia over the GFC, compared with [2008–2012] monthly averages. (c) Oversampled yearly spatial average of IASI  $\text{NH}_3$  total columns ( $\text{molec}/\text{cm}^2$ ) around the fertilizers industry (indicated with a black star). (d) Sentinel 2 L1C satellite images of the fertilizers company on days of suspension of activities (2016), and resume of production (2017, 2018 and end of 2019). DOI: <https://doi.org/10.1525/elementa.2021.000041.f2>

(a), we show the 20-day running mean of the  $\text{NH}_3$  total columns. It corresponds to the average of a  $0.5 \times 0.5^\circ$  grid box where the GFC is located in the center of the grid cell of data selection. Industries producing nitrogen-based fertilizers are known to be  $\text{NH}_3$  sources, as  $\text{NH}_3$  can be emitted through the synthesis of anhydrous  $\text{NH}_3$ , urea, and ammonium nitrate (EPA, 1995). A report from GFC mentioned that the off-gassing from the  $\text{NH}_3$  production plant has a pungent odor, confirming the presence of  $\text{NH}_3$  as

well (Zammar et al., 2006). It can be seen that IASI  $\text{NH}_3$  daily time series depends on the activity of the plant with clear perturbations that are related to the conflict events (shown in Figure 1 and highlighted in Figure 2). We used the nonconflict years [2008–2012] as years with typical monthly variations, and we show the interannual variability before, during, and after the war (Figure 2b). Panel (b) in Figure 2 shows monthly anomalies of  $\text{NH}_3$  total columns with respect to the months in [2008–2012].



**Figure 2c** shows the yearly spatial average using the over-sampling method discussed in Section 2.1. Panels (a), (b), and (c) of **Figure 2** show a decrease in  $\text{NH}_3$  total columns after 2012, in particular in 2013 and 2014, accounting to  $-17\%$  and  $-47\%$ , respectively, on a yearly average with respect to [2008–2012]. During these 2 years, the armed confrontations in the region included several military and militia groups, and the siege reached its peak by the end of 2013/early 2014.

The main factors that affected the GFC were the control of the gas field, that is essential for the production of the plant, by anti-government forces and ISIS (SANA, 2017; Aita, 2020); the attack on the company itself by anti-government groups during 2016 (as stated in **Figure 1**) which caused the activities to be suspended for a while (FAO/WFP, 2017); and finally, the shortage in employees (Enab Baladi, 2019a). From the monthly anomalies (**Figure 2b**), we can see that the interannual variations during 2013, 2014, and 2016 are larger than the typical variation observed before the intensification of the war events [2008–2012]. **Figure 2c** clearly shows a decrease in  $\text{NH}_3$  columns over the fertilizer industry by  $-32\%$  during 2016 in comparison to [2008–2012]. In mid-July 2017, after the Syrian military along with other militia groups took over Homs city in March (Washington Post, 2017), the GFC's  $\text{NH}_3$  plant started functioning again (SANA, 2017; Enab Baladi, 2019a). To verify the timing of the suspension of activities, we also examined satellite visible images during the year 2016 from June and on, up till 2019. The result is shown in **Figure 2d**. We found that in 2016, the plant's chimney was not showing any visible exhaust plume, suggesting that it wasn't functioning after the attack took place. The figure also shows that in 2017 and 2018, the plant was functioning again with the chimney's typical exhaust (**Figure 2d**). The IASI measurement shows an increase in  $\text{NH}_3$  in 2017 and 2018 in comparison to years without activity (2013, 2014, and 2016). During 2019, the production of the GFC was less than average (**Figure 2a–c**) due to shortage in fuel and electricity and because of the social conflicts in the company (Aita, 2020), with employees protesting against the new Russian investor company, and demanding better work conditions (COAR, 2019; The New Arab, 2019). It was also reported that productions were suspended for rehabilitation purposes during that year (FAO/WFP, 2019). By the end of 2019, the Russian company got in contact with many dismissed and retired employees offering them a job back at GFC with increased salaries and better conditions (Enab Baladi, 2019b). Satellite images at the end of 2019 revealed an increased activity of the industry (see **Figure 2d**); this observation agrees with the  $\text{NH}_3$  concentration anomalies during that year (**Figure 2b**). Looking at a nearby  $\text{NH}_3$  hot spot in the region, the soda ash industry in Turkey (Mersin:  $36.789^\circ\text{N}$ ,  $34.675^\circ\text{E}$ ), we find that while  $\text{NH}_3$  concentrations decreased in 2016 for the GFC, the source in Mersin showed an increase and the  $\text{NH}_3$  concentrations that became constantly higher than previous years (not shown here).

#### 4.2. Land-use change in northeast Syria

Syria is divided into 14 governorates and the region of study, shown in a rectangle in **Figures 1** and **3**, comprises 4 governorates (a part of east Aleppo, half of Ar-Raqqa, most of Al-Hassakah, and a part of northern Deir Ez-Zor). This area was the most affected in comparison to other agricultural regions in Syria (FAO, 2017a; Mohamed et al., 2020). The climate is warm, semiarid with hot and dry summers (Faour et al., 2010; Al-Fares, 2013). From south to north, annual rainfall in the region ranges from 150 to 800 mm (Mohamed et al., 2020). The study region ( $39,889 \text{ km}^2$ ) comprises cultivated lands with livestock, mostly in the northern part close to the Turkish borders. Grains, cotton, fruits, and olives are cultivated, as well as nomadic herding and scattered cultivation take place in the southern part of the study area (Al-Fares, 2013). Syria's north-eastern and southern parts are key regions for the agricultural sector; this is due to the favorable climate and the availability of water resources (Tull, 2017). We looked at MODIS land cover type for the period [2008–2019].

**Figure 3a** shows 4 snapshots of the land cover in northeast Syria for 4 key years that correspond to beginning of the war (2011), maximum control of ISIS (2015), intense clashes between ISIS and Kurdish forces (2017), and improved security conditions (2019). More information on detailed events are listed in Section 3. **Figure 3b** shows 3 snapshots of the change in MODIS croplands for 2015, 2017, and 2019 as compared to 2011. Croplands expansion is represented in red (cultivated croplands) and abandonment of croplands is shown in blue (neglected croplands). We chose 2011 as a reference year since the Syrian civil war began in March of that year. The area cultivated in 2011 did not change drastically from previous years. Despite the fact that we do not see major changes in croplands' area during 2011, farmers were struggling to travel long distances due to security reasons which prevented them from migrating to the southern part of Syria for agricultural labor (FAO, 2012), a pattern reported in previous years (Selby et al., 2017). As a result, the livestock sector has been affected as herders rely on migration to areas with abundant grasslands and water for their herds. We note also that the study region was still under the control of the Syrian government and that the armed oppositions only started later during 2012 (ISW, 2012). Up until 2015, we observed an increase in cultivated area from 2011 by 7%, 9%, and 10.5% in 2013, 2014, and 2015, respectively (only 2015 is shown here). The increase is especially widespread in Al-Hassakah governorate on the east of the study region (location is shown in **Figure 3b**). In fact, by December 2014, farmers in areas controlled by ISIS found themselves obligated to cultivate their lands, as ISIS issued a law stating that it will confiscate any abandoned cropland (Al-Tamimi, 2015). By mid-2015, ISIS started losing its control gradually. This can particularly be seen in 2017's land-use change shown in **Figure 3b** where we observe a decrease in croplands area (by  $-14\%$  as compared to 2011) and an increase in bare lands as well as shrublands. The clashes intensified when the Kurdish forces pushed ISIS fighters out of the region. FAO report states that in 2017, the fighting and airstrikes

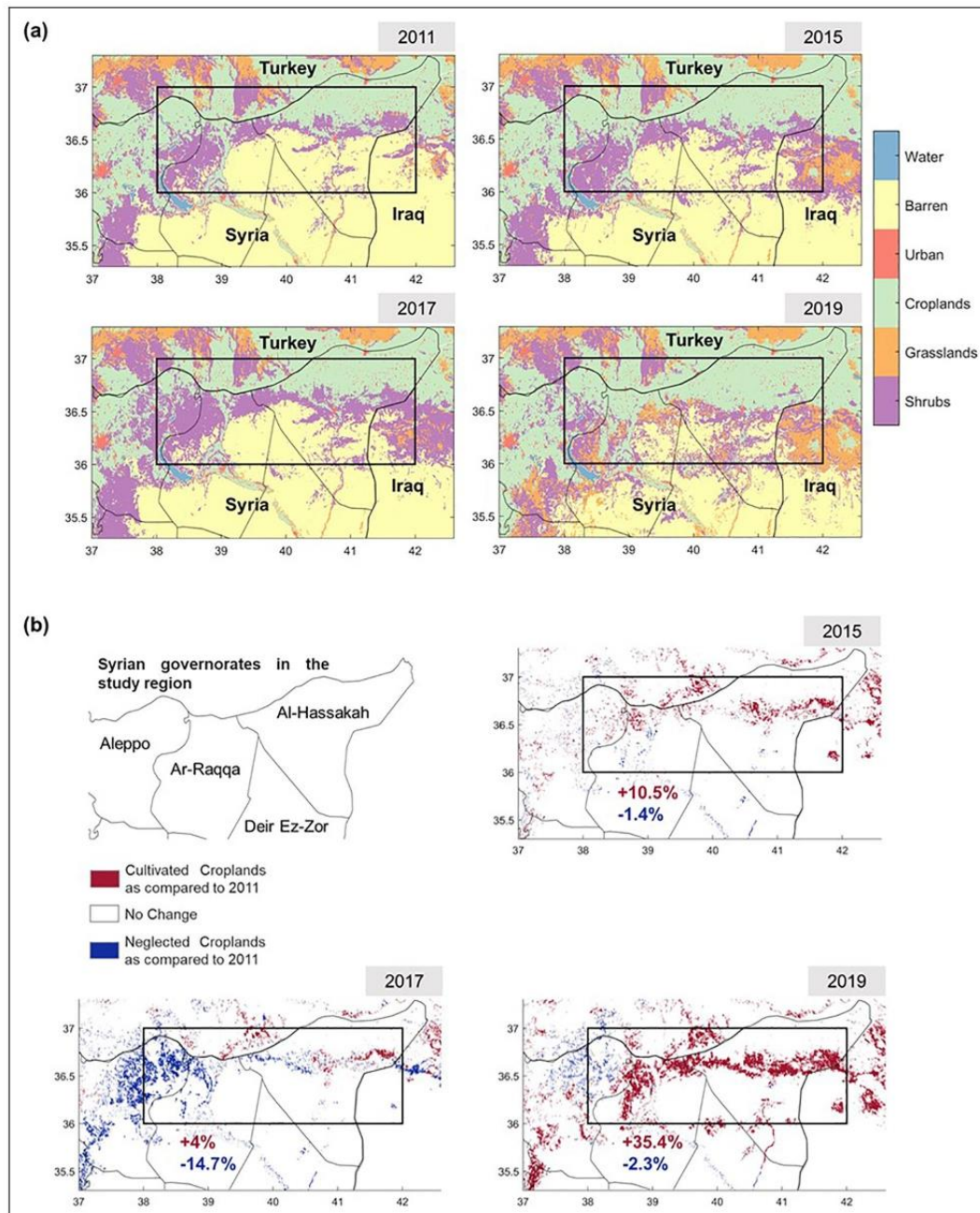


**Figure 3. (a) Yearly distribution of MODIS land cover over northeast Syria ( $500 \times 500 \text{ m}^2$ ).** The region of study is shown in the black rectangle for the years 2011 (start of the war), 2015 (Islamic State in control of most of the region), 2017 (intense clashes between Islamic State, Kurdish forces and other groups), and 2019 (better security conditions). Only relevant land cover classifications are shown here; (b) Yearly evolution (neglected or cultivated) of MODIS croplands as compared to croplands for the year 2011. “Cultivated Croplands” (red pixels)/“Neglected Croplands” (blue pixels) represent croplands that were cultivated/abandoned during the designated year in comparison to 2011. The evolution (expansion/abandonment) of croplands (indicated in red/blue) is calculated in comparison to 2011 and for pixels located in Syria only. DOI: <https://doi.org/10.1525/elementa.2021.000041.f3>



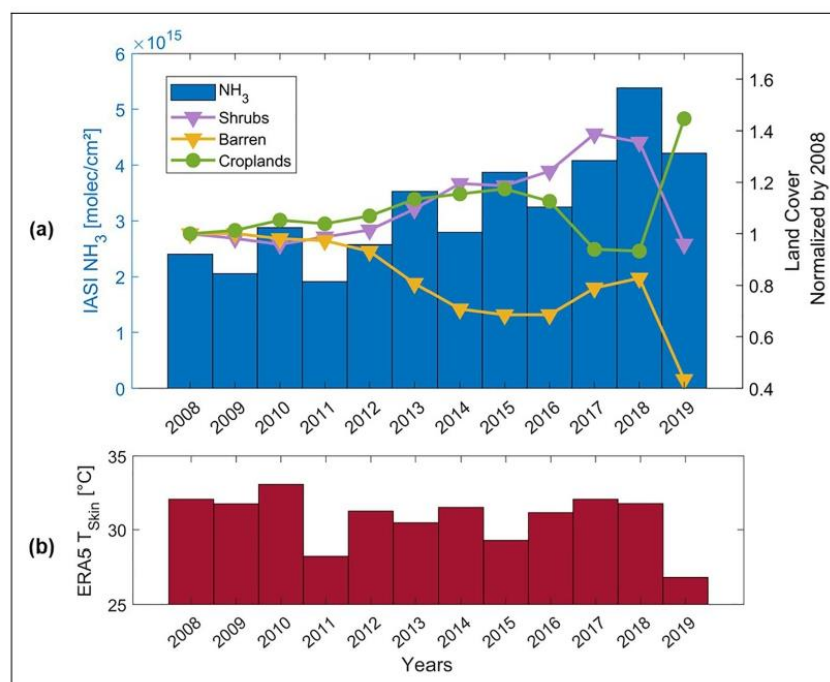


**Figure 4. (a) Spring IASI  $\text{NH}_3$  total columns [March–April–May] over the region of study (in blue), yearly MODIS Land Cover Types normalized by 2008: Shrublands (in purple), bare lands (in yellow), and croplands (in green) for the same region; (b) ERA5  $T_{\text{skin}}$  averaged during the spring season of each year. DOI: <https://doi.org/10.1525/elementa.2021.000041.f4>**

resumed in Ar-Raqqa, which constrained the humanitarian access to civilians (FAO, 2017b). Despite the improvement in security in some parts of the country, the situation in northeast Syria led to displacement of the civilians, and this can explain the abandoned farmlands seen in 2017 in **Figure 3** (FAO, 2017c). In fact, the 4 governorates included in our region of study were classified as regions where agricultural loss exceeds US\$1.5 billion which was considered the highest amount of financial damage in the country (FAO, 2017a).

During 2019, an increase in the cultivated area of approximately +35% compared to 2011 can be seen over the whole Syrian area of study (**Figure 3b**). The change represents shrublands and bare lands that had shifted into croplands (cropland expansion). The improvement in security conditions and the favorable rainfall during 2018/2019 winter season caused an expansion in the area cultivated with cereals (FAO, 2019). During that year, the area cultivated in Al-Hassakah, Aleppo, and Ar-Raqqa represented 70% of the total cultivated wheat area in the whole country (FAO, 2020). Kurdish forces had controlled almost all of the territory of northeast Syria by July 2019 (Liveu-map, 2019), and normal living and farming conditions are restored since.

In **Figure 4a**, we show the  $\text{NH}_3$  evolution in the study region during the spring season (MAM) and over the whole period [2008–2019]. Croplands (in green),

shrublands (in purple), and bare lands (in yellow) changes per year are also added. To assess the effect of soil temperature on  $\text{NH}_3$  concentrations, we also show the  $T_{\text{skin}}$  evolution in **Figure 4b** over the same area from ERA5. It has been shown in previous studies that the rate of emission of  $\text{NH}_3$  from the soil upon the application of fertilizers is mostly affected by temperature and humidity of the soil and air among other factors (Sharpe and Harper, 1995; Anderson et al., 2003; Le Cadre et al., 2005; Dari et al., 2019).

We choose the spring season because we are interested in the  $\text{NH}_3$  change related to agricultural activities and fertilizer use. Generally, 2  $\text{NH}_3$  column peaks are observed per year in the study region; the first and the highest is in spring (between March and mid-May); the second is in autumn and is lower (and not discussed here). Over the period that extends from 2008 to 2019,  $\text{NH}_3$  columns show a general increase in concentrations above the study region. We can see that  $\text{NH}_3$  fluctuations over the years before the war (2011) are dependent on both land cover changes and  $T_{\text{skin}}$  (**Figure 4b**). For example, and in particular during the [2008–2012] period, the  $\text{NH}_3$  interannual variability was mostly governed by temperature fluctuations, as the land cover was mostly constant. However, during the occupation of ISIS [2013–2015], cultivated area increased, and as such, it was an important driver in the  $\text{NH}_3$  variability: the percentage increase in

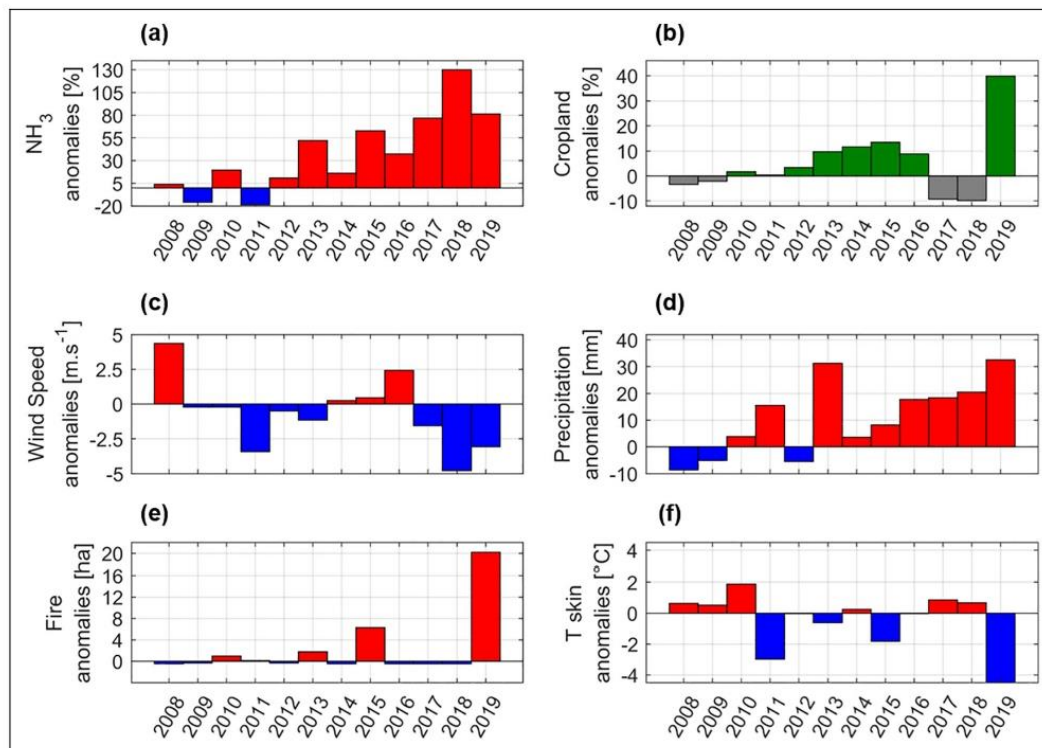


**Figure 5.** Spring anomalies over the region of study compared to the average of the spring season of [2008–2012] for (a) IASI NH<sub>3</sub> total columns [%], (b) cropland anomalies [%], (c) ERA5 wind speed anomalies [m/s], (d) ERA5 total precipitation anomalies [mm], (e) MODIS burned area [ha], and (f) ERA5 T skin anomalies [°C]. DOI: <https://doi.org/10.1525/elementa.2021.000041.f5>

NH<sub>3</sub> concentrations during [2013–2015] is estimated to be +44% in comparison to the average of [2008–2012]. As discussed earlier, the Kurdish forces were pushing ISIS out of the region by mid-2015. We observe an increase in croplands area, and the NH<sub>3</sub> keeps increasing after 2015. Simultaneously, both shrublands and bare lands are observed to be inversely correlated to croplands area. The figure shows that the croplands' expansion/cultivation reaches a maximum in 2019. The difference in NH<sub>3</sub> concentration during the period [2016–2019] in comparison to [2008–2012] average was found to be +81%, while T skin slightly decreased (−0.25%). Finally, croplands, over the same period, showed a decrease in 2017 (−14%) and 2018 (−15%), and an increase in 2019 (+35%) compared to 2011.

In order to check the effect of the different meteorological variables on NH<sub>3</sub> concentrations, we show in **Figure 5** the anomalies of NH<sub>3</sub> in panel (a) in the study region during the spring season (MAM) relative to the average of spring (2008–2012). Panel (b) shows the yearly cropland anomalies with respect to [2008–2012]. Panels (c) and (d) show the spring anomalies of ERA5 wind speed and total precipitation respectively for the same region and relative to the spring average of [2008–2012]. Panel (e) shows MODIS burned area during the spring season,

and panel (f) shows ERA5T skin anomalies for the same season and time period, as compared to the spring average of [2008–2012].

During normal conditions prior to the war (2008–2012), NH<sub>3</sub> anomalies fluctuated between ±20% (**Figure 5a**), temperature anomalies varied between −3°C and +2°C (**Figure 5f**), while croplands anomalies fluctuated between ±3.3% (**Figure 5b**). During the occupation of ISIS that started in 2013 and reached a maximum of land-control by 2015, anomalies in NH<sub>3</sub> concentrations kept increasing (+52%, +16%, and +63% for the years 2013, 2014, and 2015, respectively). The T skin anomalies during these years were relatively normal (see **Figure 5f**). The corresponding T skin anomalies for 2013, 2014, and 2015, respectively, are −0.62°C, +0.24°C, and −1.82°C (−2%, +0.8%, and −6%). While the production of fertilizers in Syria (and in GFC) decreased dramatically during the war, the imported quantity of nitrate-based fertilizers (NPK) increased from 2,634 tons in 2013 to 12,356 tons in 2019 (FAOSTAT, 2021); this explains the continuous availability of nitrogen-based fertilizers in the market.

Precipitation anomalies (**Figure 5d**) for the whole period fluctuated between −10 and +20 mm/season except during 2013 and 2019 (+31 and +32 mm/season respectively). We notice that the croplands' area in 2019 is

higher than that in 2018, but  $\text{NH}_3$  concentrations are lower in 2019. The higher precipitation anomalies (+32 mm/season) in 2019 and the lower T skin anomalies ( $-4.5^\circ\text{C}$ ) are most likely the reason of the reduction in  $\text{NH}_3$  concentrations despite the cropland expanding during that year (due to the solubility of  $\text{NH}_3$  in aqueous phases, precipitation causes the wet deposition of  $\text{NH}_3$  on surfaces). Fires do not occur frequently during the spring season in that region; however, we can see that MODIS burned area product shows +6.3 and +20.2 ha of burned area in 2015 and 2019, respectively (Figure 5e); these fires may have contributed to the concentrations of  $\text{NH}_3$ . In the period before the war (2008–2012), the wind speed anomalies fluctuated between  $-3.4$  and  $+4.4$  m/s (Figure 5c); however, in 2018, wind speed decreased by  $-4.8$  m/s, that is, outside the usual fluctuation during [2008–2012]. As observed,  $\text{NH}_3$  is highest in 2018 (Figure 5a). Fires did not occur during the spring season of 2018, and precipitations were within the usual fluctuation range of [2008–2012]. In fact, the lower wind speed observed in 2018 might have led to the persistence of  $\text{NH}_3$ . To conclude, wind speed, fire events, and precipitation were shown to be within the normal range, except perhaps for 2018 (lower wind speed, higher  $\text{NH}_3$ ) and 2019 (more precipitation, more fire events, but lower skin temperature). As such, the other years are most likely affected by the croplands' expansion. As such, fertilizer use is most likely the main driver for the increase in  $\text{NH}_3$  concentrations.

## 5. Discussion and conclusions

In this study, we discuss the effects of war in breaking the usual  $\text{NH}_3$  interannual variation in the atmosphere. IASI observations show that  $\text{NH}_3$  variability is driven by both natural factors and political events, such as in the case of the Syrian civil war. While the conflict is responsible for the reduced  $\text{NH}_3$  concentrations around the GFC industrial plant due to reduced emissions, it was also responsible for an actual increase of  $\text{NH}_3$  in the northeast due to the expansion of agricultural lands. Our work shows that remote sensing data acquired from space can help the monitoring of socio-ecological changes caused by wars and political conflicts down to a local scale.

We described case studies of 2  $\text{NH}_3$  source regions in Syria and their disruptions due to the conflict. The first is over a fertilizer industry in the city of Homs where industrial activities have been disrupted by the war, and the second over an agricultural region in northeast Syria. A decrease in  $\text{NH}_3$  concentration is observed over the fertilizers industry due to the siege and its consequences reading  $-17\%$ ,  $-47\%$ , and  $-32\%$  in 2013, 2014, and 2016, respectively, as compared to the [2008–2012] average. Even after the fertilizer industry started functioning again in 2017, the seasonal variation and concentration of  $\text{NH}_3$  were never the same as the period that preceded the beginning of the civil war. The activity of the fertilizers industry was affected by shortage in workforce, battles, and politics.

In northeast Syria, the fluctuation in IASI  $\text{NH}_3$  columns is seen to be affected by T skin before the war (2011) and

most likely driven by changes in land cover after 2011. The area witnessed abandonment of croplands in 2017 ( $-14\%$ ), in comparison to 2011, but also a huge croplands expansion in 2019 ( $+35\%$ ). The presence of ISIS in northeast Syria has changed cropping patterns and forced farm owners to cultivate their lands (Jaafar and Woertz, 2016).

We observed clear disruptions in both regions examined in this study. Although the availability of fertilizers in the market would have been affected by the halt of the GFC, the gap in the market was met with imported fertilizers (both legally and illegally). In addition to that, both regions were witnessing different events in different time frames, which makes it hard to draw a connection between the 2 case studies.

This study combines local IASI  $\text{NH}_3$  observations with ERA5 meteorological products (temperatures, total precipitation, and wind speed) and MODIS land cover and burned area. It could be extended to other parts of the world in order to analyze how political changes influence agricultural practices and industrial activities (e.g., in Afghanistan before and after 2021). Current emission inventories do not consider war-related events; we think that they should be adapted according to the results of this study and other studies that show disruptions in emissions that are not related only to climatology. The long-term homogeneous IASI dataset, whose continuity will be ensured with the IASI-NG mission (Crevoisier et al., 2014) that should fly from 2023 to 2050, offer a unique tool to monitor the impact of societal changes and perturbations on the atmospheric composition.

## Data accessibility statement

The IASI- $\text{NH}_3$  used in this study are retrieved from the Aeris data infrastructure (<https://iasi.aeris-data.fr/nh3-era5/>). MODIS land cover data are available for download in the following link: <https://doi.org/10.5067/MODIS/MCD12Q1.006>. MODIS fire data are available for download in the following link: <https://lpdaac.usgs.gov/products/mcd64a1v061/>. Images from Sentinel 2 L1C are available at <https://apps.sentinel-hub.com/sentinel-playground>. ERA5 skin temperature, 10 m u and v wind components, and total precipitation from 1979 to present are available for download in the following DOI: 10.24381/cds.adbb2d47.

## Acknowledgments

The authors acknowledge the Aeris data infrastructure for providing the IASI L1C and L2 data. Rimal Abeed is grateful to CNES for financial support. The IASI mission is a joint mission of Eumetsat and the Centre National d'Etudes Spatiales (CNES, France).

## Funding

The research was funded by the F.R.S.-FNRS and the Belgian State Federal Office for Scientific, Technical and Cultural Affairs (Prodex arrangement HIRS). M. Van Damme is Postdoctoral Researcher (Chargé de Recherche) and L. Clarisse is Research Associate (Chercheur Qualifié) both supported by the Belgian F.R.S.-FNRS.



**Competing interests**

The authors are aware of no competing interests.

**Author contributions**

Contributed to conception and design: RA, SS.

Contributed to acquisition of data: MVD, LC.

Contributed to analysis and interpretation of data: RA.

Drafted and/or revised the article: RA, SS, CC, MVD, LC, PFC.

Approved the submitted version for publication: RA, SS, CC, MVD, LC, PFC.

**References**

- Aita, S.** 2020, Dec. *The unintended consequences of U.S. and European unilateral measures on Syria's economy and its small and medium enterprises*. Atlanta, GA: The Carter Center. Available at [https://www.cartercenter.org/resources/pdfs/peace/conflict\\_resolution/syria-conflict/syria-unintended-consequences-aita-12-20.pdf](https://www.cartercenter.org/resources/pdfs/peace/conflict_resolution/syria-conflict/syria-unintended-consequences-aita-12-20.pdf).
- Al-Allaf, A, Said, S.** 2021. Russian investment in Syrian phosphate: Opportunities and challenges. *Publications Office of the European Union*. (2021/04). DOI: <http://dx.doi.org/10.2870/42382>.
- Al-Fares, W.** 2013. Historical land use/land cover classification using remote sensing: A case study of the Euphrates river basin in Syria. Heidelberg, Germany. *SpringerBriefs in Geography*. DOI: <http://dx.doi.org/10.1007/978-3-319-00624-6>.
- Al-Tamimi, AJ.** 2015. Archive of Islamic State administrative documents. Available at <http://www.aymennjawad.org/2015/01/archive-of-islamic-state-administrative-documents>. Accessed 13 April 2021.
- Anderson, N, Strader, R, Davidson, C.** 2003. Airborne reduced nitrogen: Ammonia emissions from agriculture and other sources. *Environment International* **29**(2–3): 277–286. DOI: [http://dx.doi.org/10.1016/S0160-4120\(02\)00186-1](http://dx.doi.org/10.1016/S0160-4120(02)00186-1).
- BBC.** 2018, 28 Mar. Islamic State and the crisis in Iraq and Syria in maps. *BBC News*. Available at <https://www.bbc.com/news/world-middle-east-27838034>. Accessed 26 March 2021.
- BBC.** 2019, 23 Mar. Islamic State group defeated as final territory lost, US-backed forces say. *BBC News*. Available at <https://www.bbc.com/news/world-middle-east-47678157>. Accessed 26 March 2021.
- Behera, SN, Betha, R, Liu, P, Balasubramanian, R.** 2013. A study of diurnal variations of PM<sub>2.5</sub> acidity and related chemical species using a new thermodynamic equilibrium model. *Science of the Total Environment* **452–453**: 286–295. DOI: <http://dx.doi.org/10.1016/j.scitotenv.2013.02.062>.
- Belward, AS, Estes, JE, Kline, KD.** 1999. The IGBP-DIS global 1-km land-cover data set DIS-Cover: A project overview. *Photogrammetric Engineering & Remote Sensing* **65**(9): 1013–1020.
- Bobbink, R, Hornung, M, Roelofs, JGM.** 1998. The effects of air-borne nitrogen pollutants on species diversity in natural and semi-natural European vegetation. *Journal of Ecology* **86**(5): 717–738. DOI: <http://dx.doi.org/10.1046/j.1365-2745.1998.8650717.x>.
- Chang, Y, Zhang, YL, Kawichai, S, Wang, Q, Van Damme, M, Clarisse, L, Prapamontol, T, Lehmann, MF.** 2021. Convergent evidence for the pervasive but limited contribution of biomass burning to atmospheric ammonia in peninsular Southeast Asia. *Atmospheric Chemistry and Physics* **21**(9): 7187–7198. DOI: <http://dx.doi.org/10.5194/acp-21-7187-2021>.
- Clarisse, L, Van Damme, M, Clerbaux, C, Coheur, PF.** 2019a. Tracking down global NH<sub>3</sub> point sources with wind-adjusted superresolution. *Atmospheric Measurement Techniques* **12**(10): 5457–5473. DOI: <http://dx.doi.org/10.5194/amt-12-5457-2019>.
- Clarisse, L, Van Damme, M, Gardner, W, Coheur, PF, Clerbaux, C, Whitburn, S, Hadji-Lazaro, J, Hurtmans, D.** 2019b. Atmospheric ammonia (NH<sub>3</sub>) emanations from Lake Natrons saline mudflats. *Scientific Reports* **9**(1): 4441. DOI: <http://dx.doi.org/10.1038/s41598-019-39935-3>.
- Clerbaux, C, Boynard, A, Clarisse, L, George, M, Hadji-Lazaro, J, Herbin, H, Hurtmans, D, Pommier, M, Razavi, A, Turquety, S, Wespes, C, Coheur, PF.** 2009. Monitoring of atmospheric composition using the thermal infrared IASI/MetOp sounder. *Atmospheric Chemistry and Physics* **9**(16): 6041–6054. DOI: <http://dx.doi.org/10.5194/acp-9-6041-2009>.
- COAR.** 2019. *Syria update: April 04–April 10, 2019*. Center for Operational Analysis and Research. Available at <https://coar-global.org/2019/04/10/syria-update-between-04-april-to-10-april-2019/>.
- Coheur, PF, Clarisse, L, Turquety, S, Hurtmans, D, Clerbaux, C.** 2009. IASI measurements of reactive trace species in biomass burning plumes. *Atmospheric Chemistry and Physics* **9**(15): 5655–5667. DOI: <http://dx.doi.org/10.5194/acp-9-5655-2009>.
- Corbane, C, Kemper, T, Freire, S, Louvrier, C, Pesaresi, M.** 2016. *Monitoring the Syrian humanitarian crisis with the JRCs global human settlement layer and night-time satellite*. Publications Office of the European Union (EUR 27933). DOI: <http://dx.doi.org/10.2788/48956>.
- Crevoisier, C, Clerbaux, C, Guidard, V, Phulpin, T, Armande, R, Barret, B, Camy-Peyret, C, Chaboureau, JP, Coheur, PF, Crepeau, L, Dufour, G, Labonnote, L, Lavanant, L, Hadji-Lazaro, J, Herbin, H, Jacquinet-Husson, N, Payan, S, Péquignot, E, Pierangelo, C, Sellitto, P, Stubenrauch, C.** 2014. Towards IASI-New Generation (IASI-NG): Impact of improved spectral resolution and radiometric noise on the retrieval of thermodynamic, chemistry and climate variables. *Atmospheric Measurement Techniques* **7**(12): 4367–4385. DOI: <http://dx.doi.org/10.5194/amt-7-4367-2014>.
- Dammers, E, McLinden, CA, Griffin, D, Shephard, MW, Van Der Graaf, S, Lutsch, E, Schaap, M, Gainairu-Matz, Y, Fioletov, V, Van Damme, M,**

- Whitburn, S, Clarisse, L, Cady-Pereira, K, Clerbaux, C, Coheur, PF, Erisman, JW. 2019.  $\text{NH}_3$  emissions from large point sources derived from CrIS and IASI satellite observations. *Atmospheric Chemistry and Physics* **19**(19): 12261–12293. DOI: <http://dx.doi.org/10.5194/acp-19-12261-2019>.
- Dari, B, Rogers, CW, Walsh, OS. 2019. *Understanding factors controlling ammonia volatilization from fertilizer nitrogen applications* (Extension Bulletin 927). University of Idaho. Available at <https://www.extension.uidaho.edu/publishing/pdf/BUL/BUL926.pdf>.
- Eklund, L, Degerald, M, Brandt, M, Prishchepov, AV, Pilesjö, P. 2017. How conflict affects land use: Agricultural activity in areas seized by the Islamic State. *Environmental Research Letters* **12**(5): 054004. DOI: <http://dx.doi.org/10.1088/1748-9326/aa673a>.
- Enab Baladi. 2019a, 31 Jan. *General Fertilizers Company: From Syrian stumbling and Iranian competition to Russian takeover*. Enab Baladi. Available at <https://english.enabbaladi.net/archives/2019/01/general-fertilizers-company-from-syrian-stumbling-and-iranian-competition-to-russian-takeover/>. Accessed 18 March 2021.
- Enab Baladi. 2019b, 12 Sep. *Russia to return dismissed employees to fertilizers company in Homs*. Enab Baladi. Available at <https://english.enabbaladi.net/archives/2019/09/russia-to-return-dismissed-employees-to-fertilizers-company-in-homs/>. Accessed 23 March 2021.
- EPA. 1995. Inorganic chemical industry, in *Stationary point and area sources: AP-42, compilation of air pollutant emissions factors*, Vol. 1, 5th ed. U.S. Environmental Protection Agency. Available at <https://www.epa.gov/air-emissions-factors-and-quantification/ap-42-fifth-edition-volume-i-chapter-8-inorganic-chemical-0>. Accessed 09 April 2021.
- FAO. 2012. GIEWS country briefs: Syrian Arab Republic. Rome. Available at <https://reliefweb.int/report/syrian-arab-republic/giews-country-briefs-syrian-arab-republic-14-march-2012>.
- FAO. 2017a. Counting the cost: Agriculture in Syria after six years of crisis. Rome. Available at [http://www.fao.org/fileadmin/user\\_upload/emergencies/docs/FAO\\_SYRIA-counting-the-cost.pdf](http://www.fao.org/fileadmin/user_upload/emergencies/docs/FAO_SYRIA-counting-the-cost.pdf).
- FAO. 2017b. Syrian Arab Republic situation report. Rome. Available at [http://www.fao.org/fileadmin/user\\_upload/emergencies/docs/FAOSyria\\_SitReport\\_JULY2017.pdf](http://www.fao.org/fileadmin/user_upload/emergencies/docs/FAOSyria_SitReport_JULY2017.pdf).
- FAO. 2017c. Syrian Arab Republic situation report. Rome. Available at [http://www.fao.org/fileadmin/user\\_upload/emergencies/docs/FAOSyriaSitRep\\_Nov2017.pdf](http://www.fao.org/fileadmin/user_upload/emergencies/docs/FAOSyriaSitRep_Nov2017.pdf).
- FAO. 2019. GIEWS country briefs: Syrian Arab Republic. Rome. Available at <https://reliefweb.int/report/syrian-arab-republic/giews-country-brief-syrian-arab-republic-reference-date-05-september>.
- FAO. 2020. 2019 – 2020 Agriculture seasonal performance—key updates. Available at [https://fsccluster.org/sites/default/files/documents/fao\\_presentation-seasonal\\_update\\_july\\_2020.pdf](https://fsccluster.org/sites/default/files/documents/fao_presentation-seasonal_update_july_2020.pdf). Accessed 13 April 2021.
- FAO/WFP. 2017. Special report: Crop and food security assessment mission to the Syrian Arab Republic. Rome. Available at <http://www.fao.org/3/i7578e/i7578e.pdf>.
- FAO/WFP. 2019. Special report: Crop and food security assessment mission to the Syrian Arab Republic. Rome. Available at <https://reliefweb.int/report/syrian-arab-republic/special-report-faowfp-crop-and-food-security-assessment-mission-syrian-3>.
- FAOSTAT. 2021. *FAOSTAT: Fertilizers by Product*. Available at <https://knoema.com/FAORFBFP/faostat-fertilizers-by-product>. Accessed 8 Aug 2021.
- Faour, G, Meslmani, Y, Fayad, A. 2010. Climate-change atlas of Syria. DOI: <http://dx.doi.org/10.13140/RG.2.2.26562.17601>.
- Finch, HJS, Samuel, AM, Lane, GPF. 2002. Fertilisers and manures, in *Lockhart and Wisemans Crop Husbandry Including Grassland*. 8th ed. Cambridge: 52–78 (Woodhead Publishing Series in Food Science, Technology and Nutrition). DOI: <http://dx.doi.org/10.1533/9781855736504.1.52>. Accessed 04 March 2021.
- FOX 32. 2017. ISIS has lost 98 percent of its territory, officials say. *FOX 32 Chicago*. Available at <https://www.fox32chicago.com/news/isis-has-lost-98-percent-of-its-territory-officials-say>. Accessed 26 March 2021.
- Giglio, L, Boschetti, L, Roy, D P, Humber, ML, Justice, CO. 2018. The collection 6 MODIS burned area mapping algorithm and product. *Remote Sensing of Environment* **217**: 72–85. DOI: <http://dx.doi.org/10.1016/j.rse.2018.08.005>.
- Guo, X, Wang, R, Pan, D, Zondlo, MA, Clarisse, L, Van Damme, M, Whitburn, S, Coheur, PF, Clerbaux, C, Franco, B, Golston, LM, Wendt, L, Sun, K, Tao, L, Miller, D, Mikoviny, T, Müller, M, Wisthaler, A, Tevlin, AG, Murphy, JG, Nowak, JB, Roscioli, JR, Volkamer, R, Kille, N, Neuman, JA, Eilerman, SJ, Crawford, JH, Yacovitch, TI, Barrick, JD, Scarino, AJ. 2021. Validation of IASI satellite ammonia observations at the pixel scale using in situ vertical profiles. *Journal of Geophysical Research: Atmospheres* **126**(9). DOI: <http://dx.doi.org/10.1029/2020JD033475>.
- Guthrie, S, Dunkerley, F, Tabaqchali, H, Harshfield, A, Ioppolo, B, Manville, C. 2018. *Impact of ammonia emissions from agriculture on biodiversity: An evidence synthesis*. RAND Corporation. The Royal Society (RR-2695-RS). DOI: <http://dx.doi.org/10.7249/RR2695>.
- Hersbach, H, Bell, B, Berrisford, P, Hirahara, S, Horányi, A, Muñoz-Sabater, J, Nicolas, J, Peubey, C, Radu, R, Schepers, D, Simmons, A, Soci, C, Abdalla, S, Abellan, X, Balsamo, G, Bechtold, P, Gionata Biavati, G, Bidlot, J, Bonavita, M, De Chiara, G, Dahlgren, P, Dee, D, Diamantakis, M, Dragani, R, Flemming, J, Forbes, R, Manuel Fuentes, M, Geer, A, Haimberger, L, Healy, S,

- Hogan, RJ, Elías Hólm, E, Janisková, M, Keeley, S, Laloyaux, P, Lopez, P, Lupu, C, Radnoti, G, de Rosnay, P, Rozum, I, Vamborg, F, Villaume, S, Thépaut, JN. 2020. The ERA5 global reanalysis. *Quarterly Journal of the Royal Meteorological Society* **146**(730): 1999–2049. DOI: <http://dx.doi.org/10.1002/qj.3803>.
- IHS Markit. 2017, 10 Oct. *Islamic State in decline*. IHS Markit. Available at <https://ihsmarkit.com/research-analysis/islamic-state-in-decline.html>.
- ISW. 2012. *Syrias maturing insurgency*. Institute for the Study of War. Available at [http://www.understandingwar.org/sites/default/files/Syrias\\_MaturingInsurgency\\_21June2012.pdf](http://www.understandingwar.org/sites/default/files/Syrias_MaturingInsurgency_21June2012.pdf).
- ISW. 2013. *Syria update: The fall of al-Qusayr*. Institute for the Study of War. Available at <http://www.understandingwar.org/backgrounder/syria-update-fall-al-qusayr>.
- ISW. 2014. *Middle East Security Report 22*. Institute for the Study of War. Available at [http://www.understandingwar.org/sites/default/files/ISIS\\_Governance.pdf](http://www.understandingwar.org/sites/default/files/ISIS_Governance.pdf).
- Jaafar, HH, Woertz, E. 2016. Agriculture as a funding source of ISIS: A GIS and remote sensing analysis. *Food Policy* **64**: 14–25. DOI: <http://dx.doi.org/10.1016/j.foodpol.2016.09.002>.
- Le Cadre, E, Genermont, S, Decuq, C, Recous, S, Cellier, P. 2005. A laboratory system to estimate ammonia volatilization. *Agronomy for Sustainable Development* **25**(1): 101–107. DOI: <http://dx.doi.org/10.1051/agro:2004060>.
- Liveumap. 2019, 31 Aug. *Day of news on live map* (Live Universal Awareness Map). Virginia. Available at <https://syria.liveuamap.com/en/time/31.08.2019>. Accessed 26 March 2021.
- Mohamed, M, Anders, J, Schneider, C. 2020. Monitoring of changes in Land Use/Land Cover in Syria from 2010 to 2018 using multitemporal Landsat imagery and GIS. *Land* **9**(7): 226. DOI: <http://dx.doi.org/10.3390/land9070226>.
- Paulot, F, Jacob, DJ, Johnson, MT, Bell, TG, Baker, AR, Keene, WC, Lima, ID, Doney, SC, Stock, CA. 2015. Global oceanic emission of ammonia: Constraints from seawater and atmospheric observations. *Global Biogeochemical Cycles* **29**(8): 1165–1178. DOI: <http://dx.doi.org/10.1002/2015GB005106>.
- Riddick, SN, Blackall, TD, Dragosits, U, Tang, YS, Morring, A, Daunt, F, Wanless, S, Hamer, KC, Sutton, MA. 2017. High temporal resolution modelling of environmentally-dependent seabird ammonia emissions: Description and testing of the GUANO model. *Atmospheric Environment* **161**: 48–60. DOI: <http://dx.doi.org/10.1016/j.atmosenv.2017.04.020>.
- SANA. 2017, 21 Jul. Governmental delegation continues its visit to Homs, inspecting General Fertilizer Company. *Syrian Arab News Agency (SANA)*. Available at <http://sana.sy/en/?p=110513>. Accessed 23 March 2021.
- Schlesinger, WH, Hartley, AE. 1992. A global budget for atmospheric NH<sub>3</sub>. *Biogeochemistry* **15**(3): 191–211. DOI: <http://dx.doi.org/10.1007/BF00002936>.
- Selby, J, Dahi, OS, Fröhlich, C, Hulme, M. 2017. Climate change and the Syrian civil war revisited. *Political Geography* **60**: 232–244. DOI: <http://dx.doi.org/10.1016/j.polgeo.2017.05.007>.
- Sharpe, RR, Harper, LA. 1995. Soil, plant and atmospheric conditions as they relate to ammonia volatilization. *Fertilizer Research* **42**: 149–158.
- Shephard, MW, Cady-Pereira, KE. 2015. Cross-track Infrared Sounder (CrIS) satellite observations of tropospheric ammonia. *Atmospheric Measurement Techniques* **8**(3): 1323–1336. DOI: <http://dx.doi.org/10.5194/amt-8-1323-2015>.
- Sulla-Menasse, D, Friedl, MA. 2018. User guide to collection 6 MODIS land cover (MCD12Q1 and MCD12C1) product. Available at [https://lpdaac.usgs.gov/documents/101/MCD12\\_User\\_Guide\\_V6.pdf](https://lpdaac.usgs.gov/documents/101/MCD12_User_Guide_V6.pdf).
- Sulla-Menasse, D, Gray, JM, Abercrombie, SP, Friedl, MA. 2019. Hierarchical mapping of annual global land cover 2001 to present: The MODIS Collection 6 Land Cover product. *Remote Sensing of Environment* **222**: 183–194. DOI: <http://dx.doi.org/10.1016/j.rse.2018.12.013>.
- The New Arab. 2019, 8 Apr. Russian military police beat Syrians following workers strike. *The New Arab*. Available at <https://english.alaraby.co.uk/english/news/2019/4/8/russian-military-police-beat-syrians-following-workers-strike>. Accessed 23 March 2021.
- Theobald, MR, Crittenden, PD, Hunt, AP, Tang, YS, Dragosits, U, Sutton, MA. 2006. Ammonia emissions from a cape fur seal colony, Cape Cross, Namibia. *Geophysical Research Letters* **33**(3). DOI: <http://dx.doi.org/10.1029/2005GL024384>.
- Tull, K. 2017. *Agriculture in Syria—K4D Helpdesk Report*. Brighton, UK: Institute of Development Studies. Available at <https://opendocs.ids.ac.uk/opendocs/handle/20.500.12413/13081>.
- UNHCR. 2019. Forced displacement in 2019. Available at <https://www.unhcr.org/be/wp-content/uploads/sites/46/2020/07/Global-Trends-Report-2019.pdf>.
- Van Damme, M, Clarisse, L, Franco, B, Sutton, MA, Erisman, JW, Kruit, RW, van Zanten, M, Whitburn, S, Hadji-Lazaro, J, Hurtmans, D, Clerbaux, C, Coheur, PF. 2021. Global, regional and national trends of atmospheric ammonia derived from a decadal (2008–2018) satellite record. *Environmental Research Letters* **16**: 055017. DOI: <http://dx.doi.org/10.1088/1748-9326/abd5e0>.
- Van Damme, M, Clarisse, L, Whitburn, S, Hadji-Lazaro, J, Hurtmans, D, Clerbaux, C, Coheur, PF. 2018. Industrial and agricultural ammonia point sources exposed. *Nature* **564**(7734): 99–103. DOI: <http://dx.doi.org/10.1038/s41586-018-0747-1>.
- Van Damme, M, Whitburn, S, Clarisse, L, Clerbaux, C, Hurtmans, D, Coheur, PF. 2017. Version 2 of the IASI NH<sub>3</sub> neural network retrieval algorithm; near-real



- time and reanalysed datasets. *Atmospheric Measurement Techniques Discussions*. DOI: <http://dx.doi.org/10.5194/amt-2017-239>.
- Viatte, C, Petit, JE, Yamanouchi, S, Van Damme, M, Doucerain, C, Germain-Piaulenne, E, Gros, V, Faviez, O, Clarisse, L, Coheur, PF, Strong, K, Clerbaux, C.** 2021. Ammonia and PM<sub>2.5</sub> air pollution in Paris during the 2020 COVID lockdown. *Atmosphere* **12**(2): 160. DOI: <http://dx.doi.org/10.3390/atmos12020160>.
- Viatte, C, Wang, T, Van Damme, M, Dammers, E, Meuleux, F, Clarisse, L, Shephard, MW, Whitburn, S, Coheur, PF, Cady-Pereira, KE, Clerbaux, C.** 2020. Atmospheric ammonia variability and link with particulate matter formation: A case study over the Paris area. *Atmospheric Chemistry and Physics* **20**(1): 577–596. DOI: <http://dx.doi.org/10.5194/acp-20-577-2020>.
- Walsh, NP.** 2014, 30 Dec. Life in the rubble of Kobani. *CNN*. Available at <https://www.cnn.com/2014/12/04/world/meast/syria-kobani-civilians/index.html>. Accessed 25 March 2021.
- Washington Post.** 2017, 3 Mar. Hezbollah, Russia and the U.S. help Syria retake Palmyra. *Washington Post*. Available at [https://www.washingtonpost.com/world/syrian-army-retakes-the-ancient-city-of-palmyra-from-the-islamic-state/2017/03/02/fe770c78-ff63-11e6-9b78-824ccab94435\\_story.html](https://www.washingtonpost.com/world/syrian-army-retakes-the-ancient-city-of-palmyra-from-the-islamic-state/2017/03/02/fe770c78-ff63-11e6-9b78-824ccab94435_story.html). Accessed 24 March 2021.
- Whitburn, S, Van Damme, M, Clarisse, L, Bauduin, S, Heald, CL, Hadji-Lazaro, J, Hurtmans, D, Zondlo, MA, Clerbaux, C, Coheur, PF.** 2016. A flexible and robust neural network IASI-NH<sub>3</sub> retrieval algorithm. *Journal of Geophysical Research: Atmospheres* **121**(11): 6581–6599. DOI: <http://dx.doi.org/10.1002/2016JD024828>.
- Whitburn, S, Van Damme, M, Kaiser, JW, van der Werf, GR, Turquety, S, Hurtmans, D, Clarisse, L, Clerbaux, C, Coheur, PF.** 2015. Ammonia emissions in tropical biomass burning regions: Comparison between satellite-derived emissions and bottom-up fire inventories. *Atmospheric Environment* **121**: 42–54. DOI: <http://dx.doi.org/10.1016/j.atmosenv.2015.03.015>.
- Wilson Center.** 2019, 28 Oct. *Timeline: The rise, spread, and fall of the Islamic State*. Wilson Center. Available at <https://www.wilsoncenter.org/article/timeline-the-rise-spread-and-fall-the-islamic-state>.
- Zammar, I, Kurita, H, Kii, A, Matsuo, N.** 2006. Effective use of the waste gas emitted from ammonia production plant in Syria—Clean development mechanism - project design document form CDM PDD. Available at [http://gec.jp/jpn/cdm-fs/2009/200918Shimiz\\_jSyria\\_pdd.pdf](http://gec.jp/jpn/cdm-fs/2009/200918Shimiz_jSyria_pdd.pdf).
- Zhu, L, Jacob, DJ, Mickley, LJ, Marais, EA, Cohan, DS, Yoshida, Y, Duncan, BN, González Abad, G, Chance, KV.** 2014. Anthropogenic emissions of highly reactive volatile organic compounds in eastern Texas inferred from oversampling of satellite (OMI) measurements of HCHO columns. *Environmental Research Letters* **9**(11): 114004. DOI: <http://dx.doi.org/10.1088/1748-9326/9/11/114004>.

**How to cite this article:** Abeed, R, Clerbaux, C, Clarisse, L, Van Damme, M, Coheur, P-F, Safieddine, S. 2021. A space view of agricultural and industrial changes during the Syrian civil war. *Elementa: Science of the Anthropocene* **9**(1). DOI: <https://doi.org/10.1525/elementa.2021.000041>

**Domain Editor-in-Chief:** Detlev Helmig, Boulder AIR LLC, Boulder, CO, USA

**Associate Editor:** Paul Palmer, School of GeoSciences, The University of Edinburgh, Edinburgh, UK

**Knowledge Domain:** Atmospheric Science

**Published:** November 1, 2021    **Accepted:** October 9, 2021    **Submitted:** June 1, 2021

**Copyright:** © 2021 The Author(s). This is an open-access article distributed under the terms of the Creative Commons Attribution 4.0 International License (CC-BY 4.0), which permits unrestricted use, distribution, and reproduction in any medium, provided the original author and source are credited. See <http://creativecommons.org/licenses/by/4.0/>.



*Elem Sci Anth* is a peer-reviewed open access journal published by University of California Press.

OPEN ACCESS

## Chapter 6

### *6 Conclusions and discussions*

Ammonia ( $\text{NH}_3$ ) plays an important role in atmospheric chemical processes and, after deposition, in biogeochemical processes in ecosystems (Rockström et al., 2009). The most significant  $\text{NH}_3$  emissions are from livestock production and the fertilization of cultivated soils with nitrogen fertilizers. The intensification of agricultural practices has significantly perturbed the global nitrogen cycle over the past century, including the increase in ammonia ( $\text{NH}_3$ ) emissions to the atmosphere. The impacts of these emissions include the formation of fine particles, affecting air quality, acidification and eutrophication of ecosystems, and an indirect influence on climate change (Myhre et al., 2013). In order to meet a growing population demand (UN, 2022), the world is facing the challenge of transforming more ecosystems into non-resilient croplands, and/or intensifying the agricultural practices to increase food production. In fact, the volatilization of  $\text{NH}_3$  into the atmosphere and its transformation into suspended fine particulate matter ( $\text{PM}_{2.5}$ ), which is particularly harmful to human health, strongly depend on meteorological parameters. Inorganic  $\text{PM}_{2.5}$  consisting of ammonium ( $\text{NH}_4^+$ ) salts are formed from  $\text{NH}_3$  when available. The changes in the partitioning of  $\text{NH}_3$ - $\text{NH}_4^+$  vary under different ambient conditions and local meteorology (Chen et al., 2021). Changes in meteorological factors affect  $\text{NH}_3$  in several ways, for example:

- Increasing temperatures will increase  $\text{NH}_3$  volatilization and thus its agricultural emissions.
- Changes in temperature, humidity, and other meteorological factors and soil conditions can affect the rate of dissolution, photochemical, oxidative, and other chemical reactions, speeding up or slowing down the conversion of  $\text{NH}_3$  to ammonium  $\text{NH}_4^+$  (which in turn affect the  $\text{PM}_{2.5}$  budget).
- Meteorology affects transport and mixing of atmospheric components, as well as deposition processes. Changes in large-scale weather patterns, which control the dispersion and transport of  $\text{NH}_3$ , can result in changes of the frequency and intensity of air pollution events.

In the US and Europe, approximately half of the  $\text{PM}_{2.5}$  has an inorganic chemical speciation and is composed of ammonium ( $\text{NH}_4^+$ ), nitrate ( $\text{NO}_3^-$ ), and sulfate ( $\text{SO}_4^{2-}$ ) (EPA, 1966; Erisman and Schaap, 2004). For 10%  $\text{NH}_3$  emission reduction in the Eastern US, the reduction in inorganic  $\text{PM}_{2.5}$  was up to 8% in winter (Pinder et al., 2007).

Decreasing the  $\text{N}_r$  input in the environment will benefit not only our heaths, but also ecosystems and biodiversity, (Galloway et al., 2003; Zabel et al., 2019). For example, in the UK, reducing ammonia emissions by 6 % and  $\text{NO}_x$  by 36 %, increases the biodiversity richness by 11 % (Jones et al., 2018). This small percentage is due to the fact that most of the  $\text{N}_r$  damaging the biodiversity originates from ammonia, rather than  $\text{NO}_x$ .

Despite the urgency of the need to reduce  $\text{N}_r$  (Rockström et al., 2009), little is being done on a global scale. The global use of N fertilizers was found to increase significantly, i.e. by a factor of 8 between 1961 and 2013 (Lassaletta et al., 2016). This increase led to positive global trends in  $\text{NH}_3$  concentrations since 2008 that are driven by agriculture in Eastern Asia, (McDuffie et al., 2020; Van Damme et al., 2021). One third of the global N fertilizer use is done in China (31 %), followed by India (15 %), and the United States (11 %) (Lu and Tian, 2017). Cropland expansion and intensification scenarios are expected to increase crop yield, and lower the prices of food in the global market, this however comes with trade-offs to biodiversity (Zabel et al., 2019). Up to 14 % (8 %) of the biodiversity in terrestrial ecosystems are in danger under the cropland expansion (intensification) scenario by 2030, as compared to a reference scenario<sup>27</sup>. Under the stress of climate change (e.g. higher temperatures, increased rain and flooding), it is crucial to understand how ammonia concentrations interact with fluctuating meteorological parameters, especially increasing temperatures.

## ***6.1 Thesis conclusions***

My thesis work shows the importance of understanding the evolution of ammonia concentrations with meteorology, land use, and climate in different parts of the world,. In my work I showed that higher atmospheric columns are driven by increasing air and land surface

---

<sup>27</sup> The reference scenario carries forward current trends in demographic growth, gross domestic products and trade policies considering that with higher incomes preferences change towards livestock products. For details, see Supplementary Note 4, in Zabel et al. (2019).

temperatures, decreasing relative humidity (especially in dry climates), wind speed (up to  $10 \text{ m s}^{-1}$ ) and total precipitation in zones with medium cumulative rainfall per year (up to  $300 \text{ mm yr}^{-1}$ ) (Chapter 3). The correlation between ammonia columns and T skin is lower in warm climate regions, such as in Mexico. In a dry climate, such as Europe, better correlation is seen between increasing relative humidity and decreasing ammonia total columns. By looking at the  $\text{NH}_3$  – T skin relationship, I was able to detect the fertilizers application period from space, by seeing a jump in the concentrations of ammonia when temperatures fall within  $10$  and  $25^\circ\text{C}$  (fall and spring seasons). In most of the regions examined, ammonia increases almost linearly with temperature if the latter is below  $30^\circ\text{C}$ , and exponentially afterwards, especially if the warm periods coincide with the growing season.

In the study shown in Chapter 4, I demonstrated that European croplands, as well as natural habitats (e.g. forests, grasslands), will increasingly emit ammonia by 2100 especially in Eastern Europe. I used a variety of datasets (satellite, reanalysis and model simulation) to calculate the first regional map of ammonia emission potential during the start of the growing season in Europe. The emission potential can be used as a proxy to calculate ammonia columns in the atmosphere, and as such to assess its deposition, atmospheric transport, and contribution to PM formation. This study can help us define a threshold of N input, under future climates, to avoid further rising ammonia emissions and pollution relevant to N contamination.

In Chapter 5 we learned that IASI data are powerful enough to provide an understanding of the impact of geopolitical situations such as the war in Syria. This is particularly useful when access to the region of study is restricted owing to political complications. This study shows that the relationship ammonia – cropland cover is not linear as it depends on other factors. Agricultural activities were seen to intensify, unlike the conventional expectation about agriculture in conflict areas. However, the concentrations of atmospheric ammonia did not depend only on croplands area, but also on the economic situation and the rules set by the political party that was in control of the region at the time of the study period. Meteorology did also play a role in the availability of ammonia, but it was not the main driver of the interannual variability. The current available emissions inventories are likely to underestimate the amount of ammonia emitted. These inventories might not account for the events of war. In northeast Syria, the changes in T skin normally are expected to reduce the volatilization of ammonia, but the results of this study show

the opposite, hence why an in-depth investigation of the political events is needed. The same notion applies to the changes in atmospheric ammonia levels in the industrial region that are solely driven by politics.

## 6.2 *Perspectives and future work*

In order to calculate and assess the effect of ammonia on the biosphere, a comprehensive assessment of its budget on the local, regional, and global scale is needed. It is crucial to apply the method used in Chapter 4 to calculate the emission potential to all seasons of the year; especially in regions with extensive agricultural activities, such as the agricultural regions in the United States, India, and China. In addition to this, more field measurements of ammonia emission potential ( $\Gamma_{soil}$ ) in different land use / cover types are required, this can help us perform better comparison with emission potentials calculated from model and satellite data. Having ammonia columns at different times of the day, from field observations or satellite measurements will allow quantification of daily emission potentials, that will in turn help us understand its diurnal variability. In addition to that, we will be able to understand the meteorological effects by looking at hourly data, and expand our knowledge about night-time ammonia. This for example, will be ensured with the launch of the Infrared Sounder (IRS) on the Meteosat Third Generation (MTG) geostationary satellites scheduled at the end of 2024.

The study presented in Chapter 5 can be expanded to other areas of conflict, such as Ukraine, and Yemen. In addition to studying agricultural changes in conflict areas, monitoring atmospheric composition can help us understand the impacts of economic crises (e.g. Venezuela, Lebanon) on the agricultural sector.

The results of my thesis showed that satellite data, in particular from the IASI instrument, are powerful enough to track ammonia sources and improve the emission inventories, in order to understand further PM forecast. In the light of the scarcity of in-situ measurements of ammonia, satellite-based observations play a major role in our understanding of the nitrogen cycle. IASI can also monitor the trends in ammonia to verify that nations are complying with the current regulations, especially in the context of global warming (EEA, 2010). The IASI-A has been in space since 2006, with IASI-B and -C currently in space, the new generation IASI-NG will be soon launched in 2025 and is expected to last up until 2040. With this, the IASI long-term record

will continue to serve as the longest satellite mission in the world's history. More frequent observation will be secured with the launch of the geostationary satellite MTG, carrying the Infrared Sounder (IRS). Quantifying the relative contribution of agriculture, and the reactive nitrogen to air pollution is key to understand the impacts of N pollution. Gladly, the Nitrosat mission will provide high spatial resolution and sensitivity to ammonia and nitrogen dioxide ( $\text{NO}_2$ ) measurements, both of which are crucial to understanding the N cycle (<https://nitrosat.eu/scirec/>). Future energy transition is set to rely on hydrogen, however potential leakage and the risks attributed to its transportation are alarming (Hauglustaine et al., 2022). However, a promising molecule that can replace hydrogen (during the transportation process) is ammonia, as it can act as a hydrogen carrier (IChemE, 2019). Ammonia, unlike hydrogen, can be compressed and thus it is easier to transport it in the liquid form, which can reduce the leaks relative to transporting hydrogen gas. Later the  $\text{NH}_3$  can be decomposed to hydrogen for energy use, once arrived in the destination (Klerke et al., 2008). Thus, in addition to agriculture, the “so-called” green energy (hydrogen) of the future, will not be so green after all due to increasing  $\text{NH}_3$  emissions and adding to the alarming global budget of  $\text{N}_r$ . Hence, future and current missions are necessary to address nitrogen pollution, under the new energy reforms and a changing climate.



# Appendices

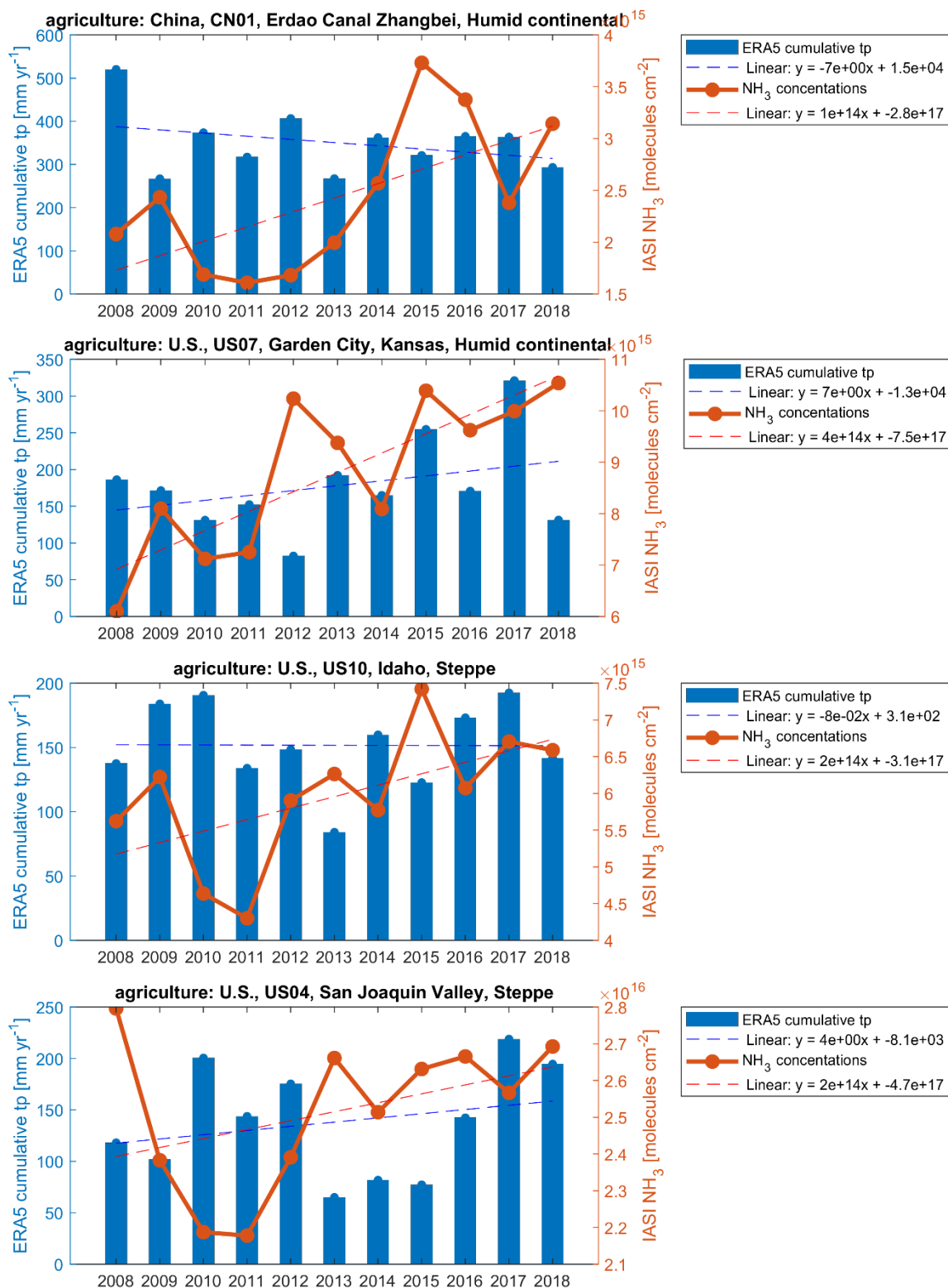


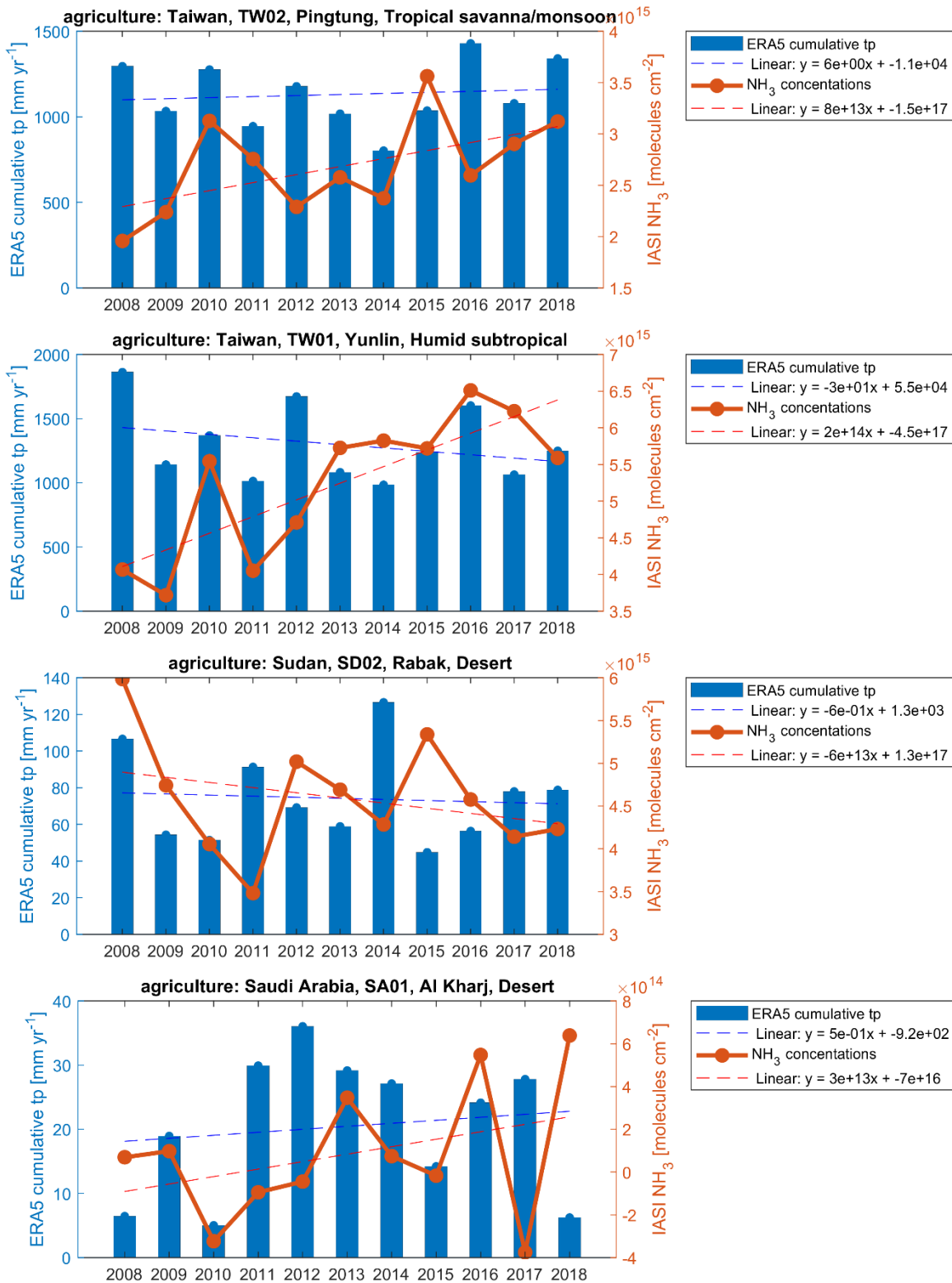
## A. Regions for Chapter 3

id	name	Main source	Country	Longitude		Latitude		climate
AZ01	Azerbaijan	agriculture	Azerbaijan	47	48	39.5	40.5	Steppe
AZ02	Azerbaijan	agriculture	Azerbaijan	48	49	39.4	40.4	Steppe
CN01	Erdao Canal Zhangbei	agriculture	China	114.5	115.5	40.75	41.75	Humid continental
CN02	Xingtai Yong Guyuan	agriculture	China	115.5	116.5	41.5	42.5	Humid continental
EG01	Nile Basin 1	agriculture	Egypt	32.5	33.5	24	25	Desert
EG03	Nile Basin 3	agriculture	Egypt	30	33	26	28	Desert
EG06	Nile Delta 3	agriculture	Egypt	30.7	31.7	29.8	30.8	Desert
EG10	Nile Basin 4	agriculture	Egypt	30.3	31.3	27	28	Desert
ES01	Valladolid	agriculture	Spain	-5	-4	40.75	41.75	Mediterranean
ES02	Vic - Manlleu	agriculture	Spain	1.75	2.75	41.25	42.25	Marine west coast
ES03	Lerida	agriculture	Spain	0.25	1.25	41.25	42.25	Marine west coast
ES04	Manresa	agriculture	Spain	1.5	3	41.5	42.5	Marine west coast
ES07	Lleida	agriculture	Spain	-0.4	1.5	41.3	42.3	Marine west coast
IN01	Hyderabad	agriculture	India	78	79	17	18	Tropical savanna/monsoon
IT01	Cancello e Arnone	agriculture	Italy	14	15	41	42	Mediterranean
IT02	Po Valley	agriculture	Italy	9	10	44.75	45.75	Marine west coast
IT03	North West	agriculture	Italy	7.18	8.18	44.22	45.22	Marine west coast
IT04	Po Valley	agriculture	Italy	10	11	44.5	45.5	Marine west coast
IT05	Po Valley	agriculture	Italy	11	12	44.75	45.75	Marine west coast
IT06	Po Valley	agriculture	Italy	9	11	44.7	45.7	Marine west coast
IT07	Po Valley	agriculture	Italy	8	12	44.5	46	Marine west coast
IT08	Po Valley	agriculture	Italy	7	13	44	46.5	Marine west coast
IT09	Cancello e Arnone	agriculture	Italy	14	15	41	42	Marine west coast
LB01	Bekaa Valley	agriculture	Lebanon	35.2	36.2	33.5	34.5	Mediterranean
SA01	Al Kharj	agriculture	Saudi Arabia	46.9	47.9	23.5	24.5	Desert
SD02	Rabak	agriculture	Sudan	32.5	33.5	12.5	13.5	Desert
TR01	Afyonkarahisar	agriculture	Turkey	30	31	38.5	39.5	Mediterranean
TW01	Yunlin	agriculture	Taiwan	120	121	23.25	24.25	Humid subtropical
TW02	Pingtung	agriculture	Taiwan	120	121	22	23	Tropical savanna/monsoon
US01	San Joaquin Valley	agriculture	U.S.	-123	-118	35	40	Mediterranean
US02	San Joaquin Valley	agriculture	U.S.	-122.5	-121	38.5	40	Mediterranean
US03	San Joaquin Valley	agriculture	U.S.	-122	-120.5	37	38.5	Mediterranean
US04	San Joaquin Valley	agriculture	U.S.	-120	-119	35.5	36.5	Steppe
US07	Garden City, Kansas	agriculture	U.S.	-101.5	-100.5	38	39	Humid continental
US08	San Joaquin Valley	agriculture	U.S.	-120.5	-119	35.5	37	Mediterranean
US09	San Joaquin Valley	agriculture	U.S.	-123	-118	35	38.5	Mediterranean
US10	Idaho	agriculture	U.S.	-115	-114	42.25	43.25	Steppe
CN04	Wucaiwai	industry	China	88.7	89.7	44.2	45.2	Steppe
CN05	Dongfang	industry	China	108.168	109.168	18.578	19.578	Humid subtropical
CN06	Longwen	industry	China	117.144	118.144	24.042	25.042	Humid subtropical
EG08	Al Adabiya Ain Sukhna	industry	Egypt	31.9	32.9	29	30	Desert
ID01	Palembang	industry	Indonesia	104.286	105.286	-3.466	-2.466	Tropical rainforest

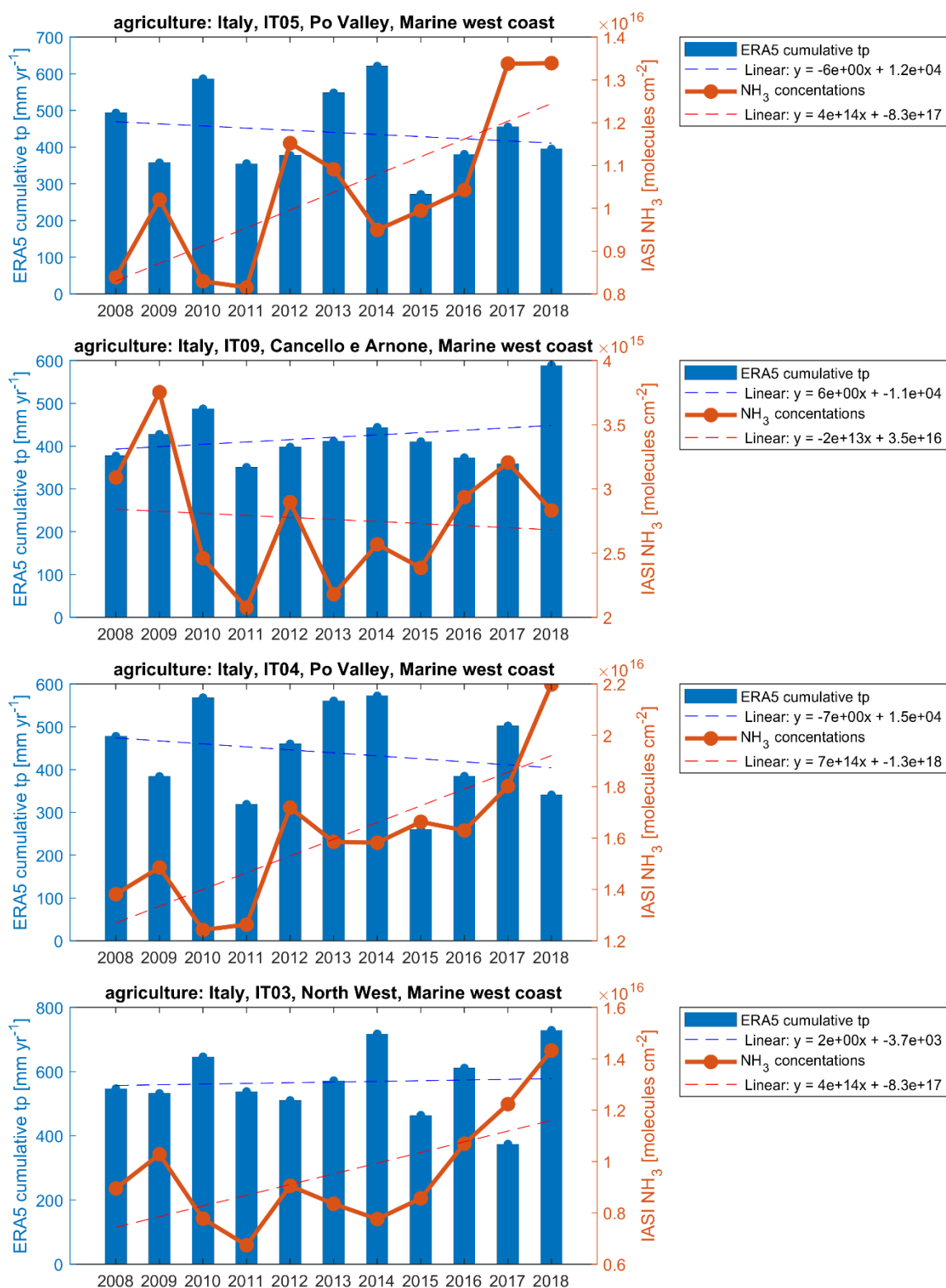
ID02	Lhokseumawe	industry	Indonesia	96.549	97.549	4.726	5.726	Tropical rainforest
LY01	Marsa el Brega	industry	Lybia	19.105	20.105	29.919	30.919	Desert
MX01	Cosoleacaque	industry	Mexico	-95.037	-94.037	17.493	18.493	Tropical savanna/monsoon
OM01	Sur Industrial Estate	industry	Oman	59.2	60.2	22.4	23.4	Desert
RU01	Novgorod	industry	Russia	31	32	58	59	Humid continental
RU02	Berezniki	industry	Russia	56.231	57.231	58.903	59.903	Subarctic
RU03	Togliatti	industry	Russia	49.11	50.11	53.043	54.043	Humid continental
SA03	Haql	industry	Saudi Arabia	34.496	35.496	28.82	29.82	Desert
TT01	Point Lisas	industry	Trinidad and Tobago	-61.975	-60.975	9.903	10.903	Tropical savanna/monsoon
US05	Beech Island	industry	U.S.	-82.442	-81.442	32.939	33.939	Humid subtropical
VE01	El Jose	industry	Venezuela	-65.363	-64.363	9.57	10.57	Tropical savanna/monsoon
AR01	Campana	industry	Argentina	-59.535	-58.535	-34.692	-33.692	Humid subtropical
BR01	Laranjeiras	agriculture	Brazil	-38.677	-37.677	-10.287	-9.287	Steppe
CO01	Cartagena - Mamonal	agriculture	Colombia	-75.989	-74.989	9.808	10.808	Tropical savanna/monsoon
EG04	Nile Delta 1	industry	Egypt	29.5	30.5	30.5	31.5	Desert
EG05	Nile Delta 2	agriculture	Egypt	30.7	31.7	30.8	31.8	Desert
EG09	Nile Delta	industry	Egypt	29.5	32.4	29.7	31.5	Desert
IN02	Gadepan	agriculture	India	76	77	25	26	Steppe
IN03	Phulphur	industry	India	82	83	25	26	Humid subtropical
IN04	Thal	agriculture	India	72.5	73.5	18.5	19.5	Tropical savanna/monsoon
IR01	Marvdasht	industry	Iran	52	53	29	30	Mediterranean
IR02	Bojnourd	agriculture	Iran	57	58	37.2	38.2	Steppe
KZ01	North of Almaty	industry	Kazakhstan	76.3	77.3	43	44	Steppe
SY01	Homs	agriculture	Syria	36.5	37.5	34	35	Mediterranean
US06	Beulah	industry	U.S.	-102.331	-101.331	46.852	47.852	Humid continental
AO01	Luanda	agriculture	Angola	13.3	14.3	-9.8	-8.8	Tropical savanna/monsoon
CG01	Kinshasa	urban	Congo	15	16	-5	-4	Tropical savanna/monsoon
SD01	Khartoum	urban	Sudan	32	33	15	16	Desert

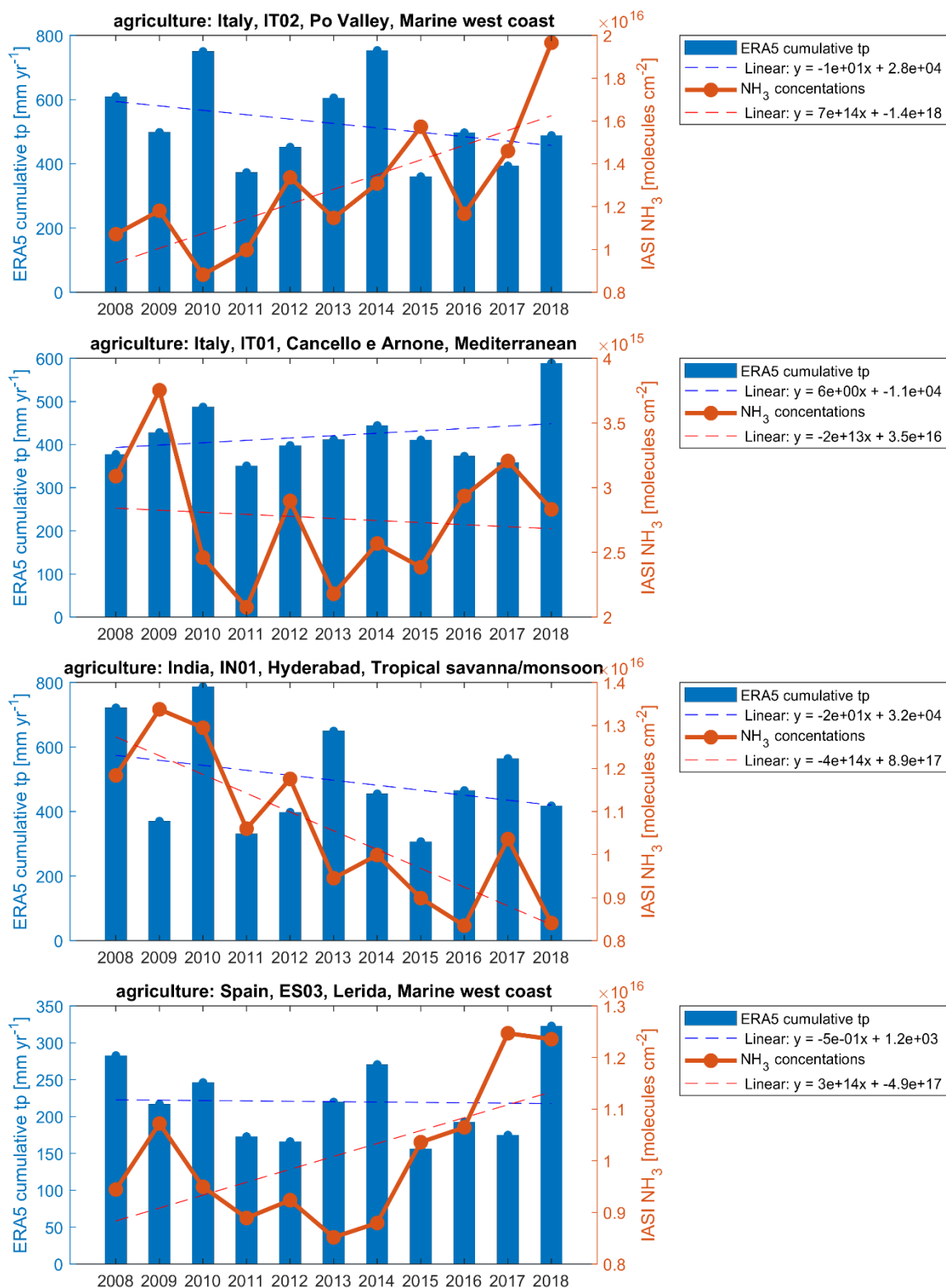
## B. NH<sub>3</sub> – precipitation

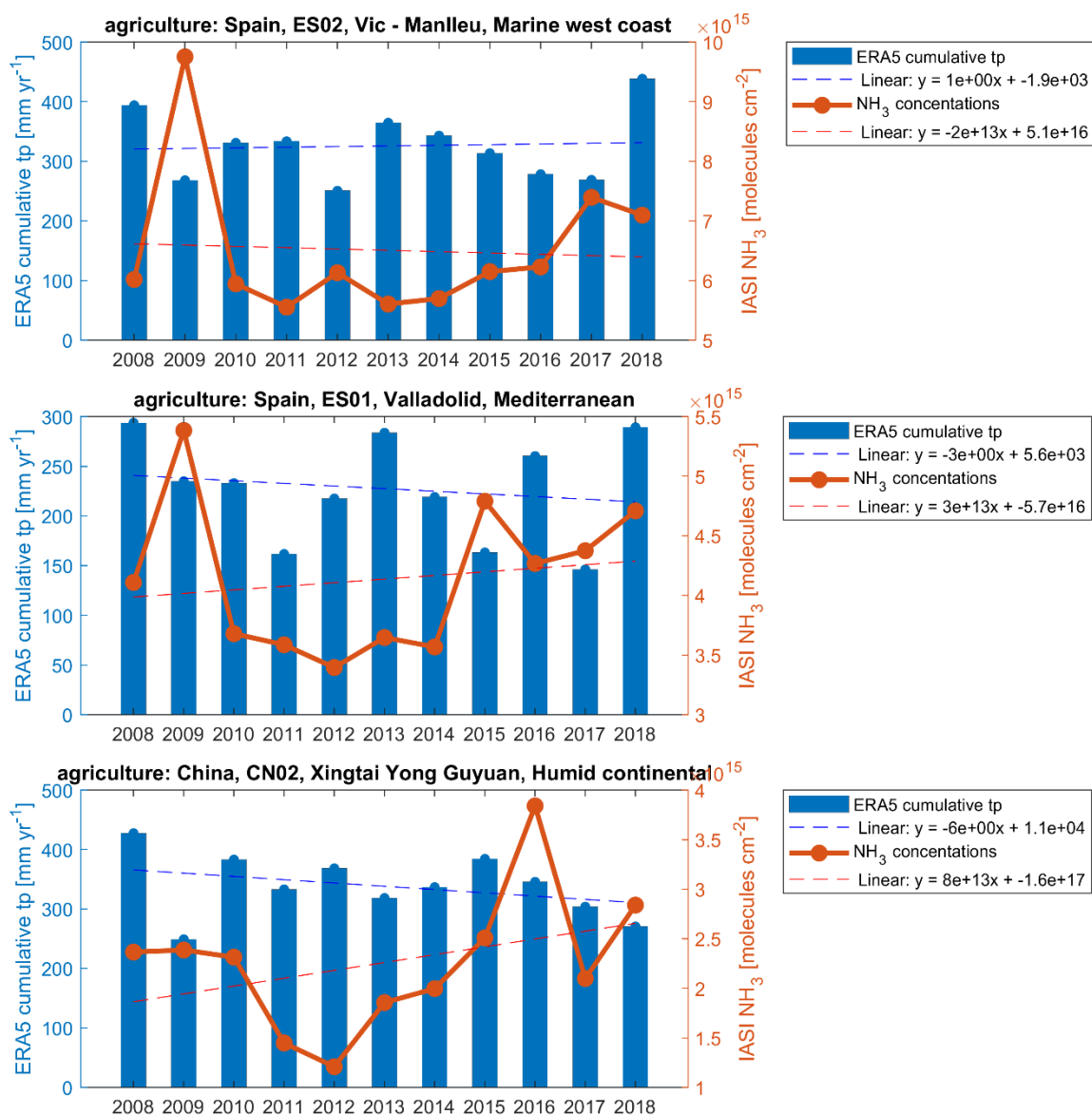


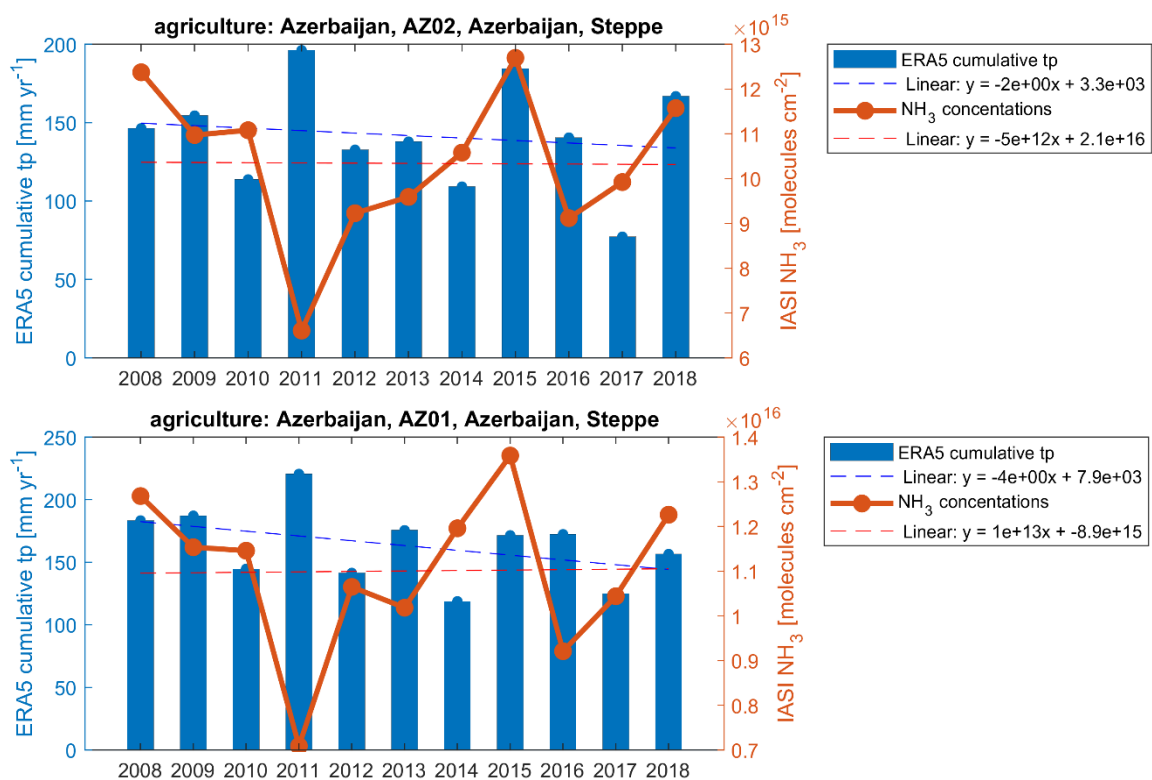




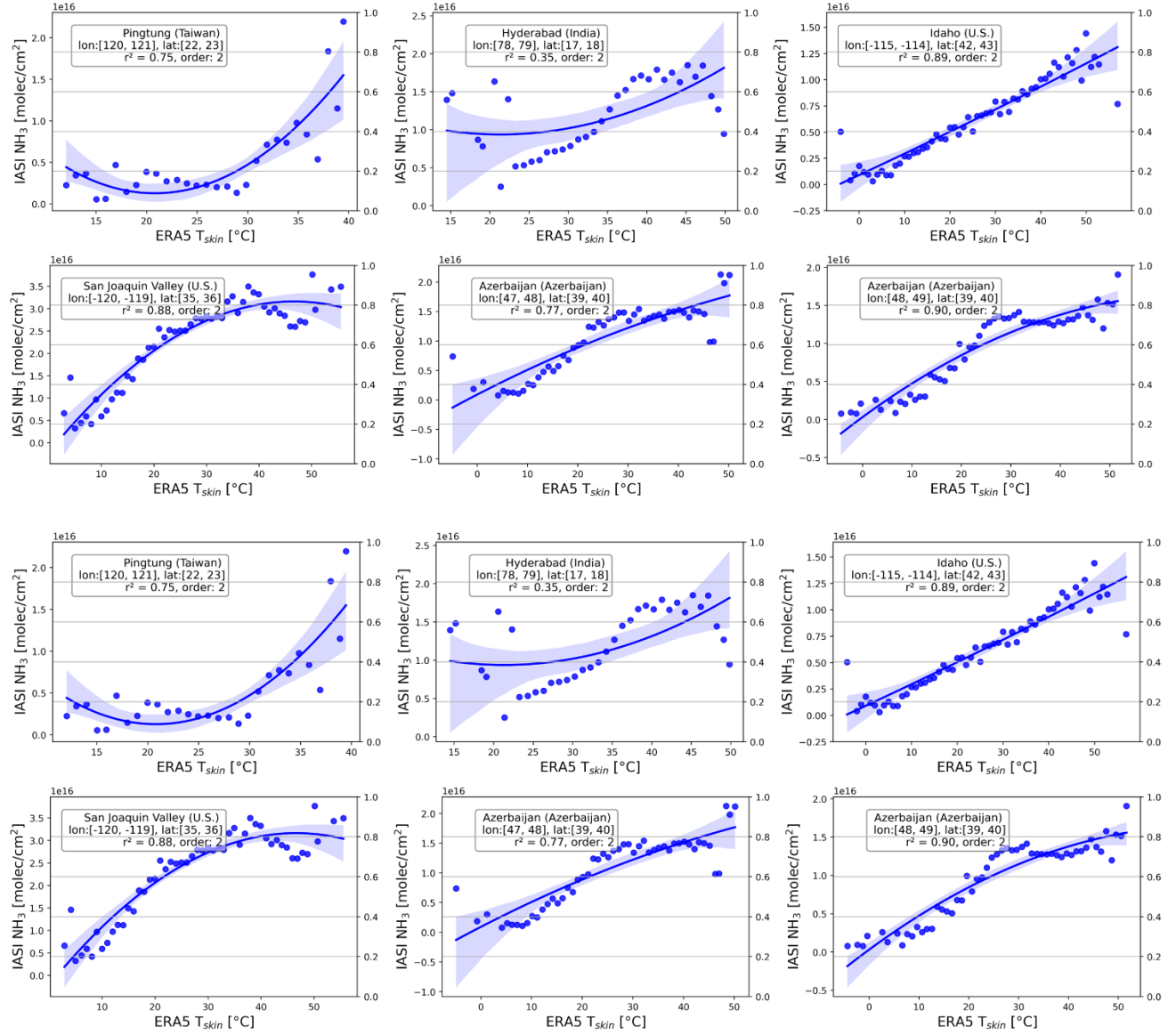


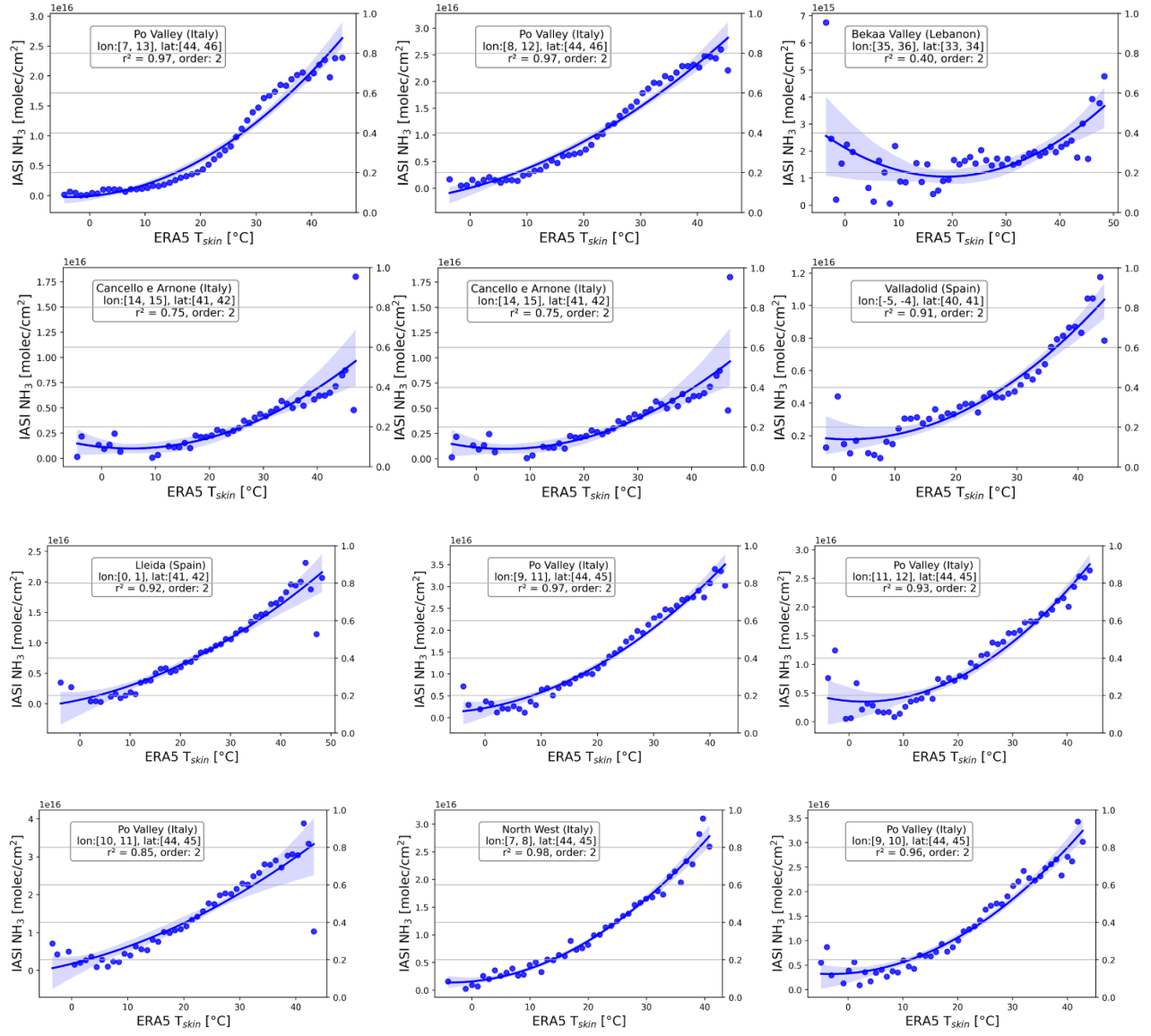




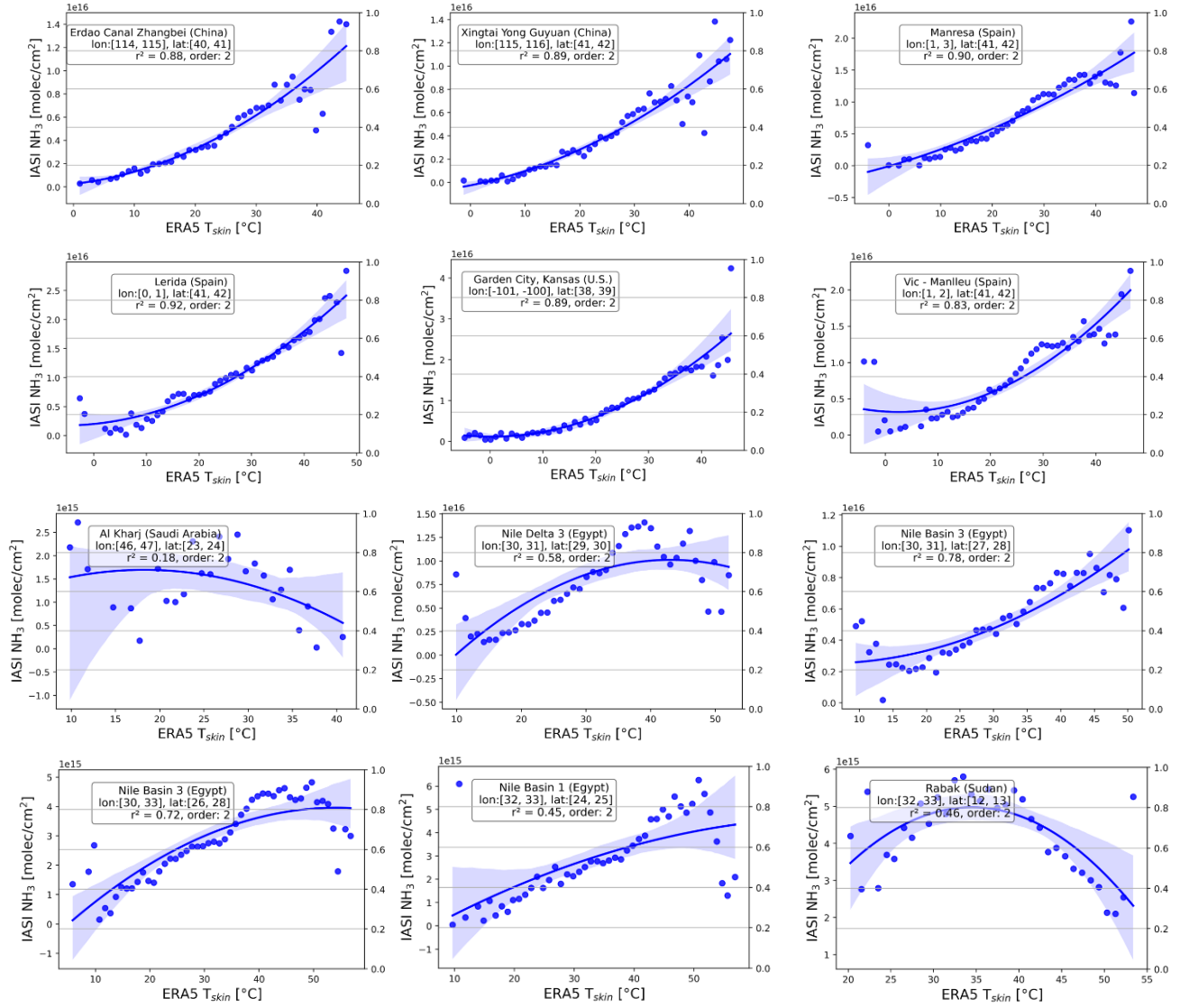


## C. NH<sub>3</sub> – T<sub>skin</sub> binning



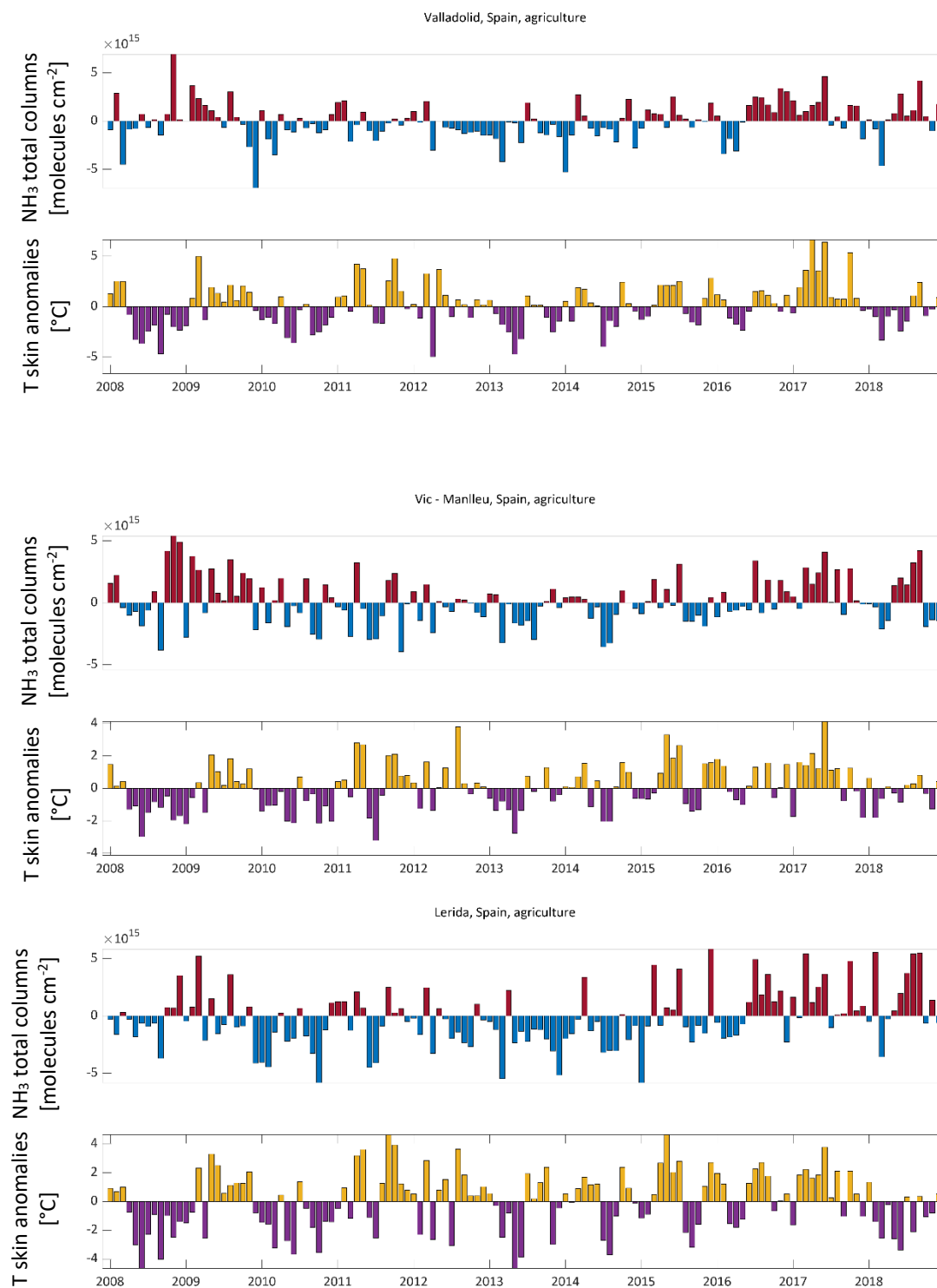


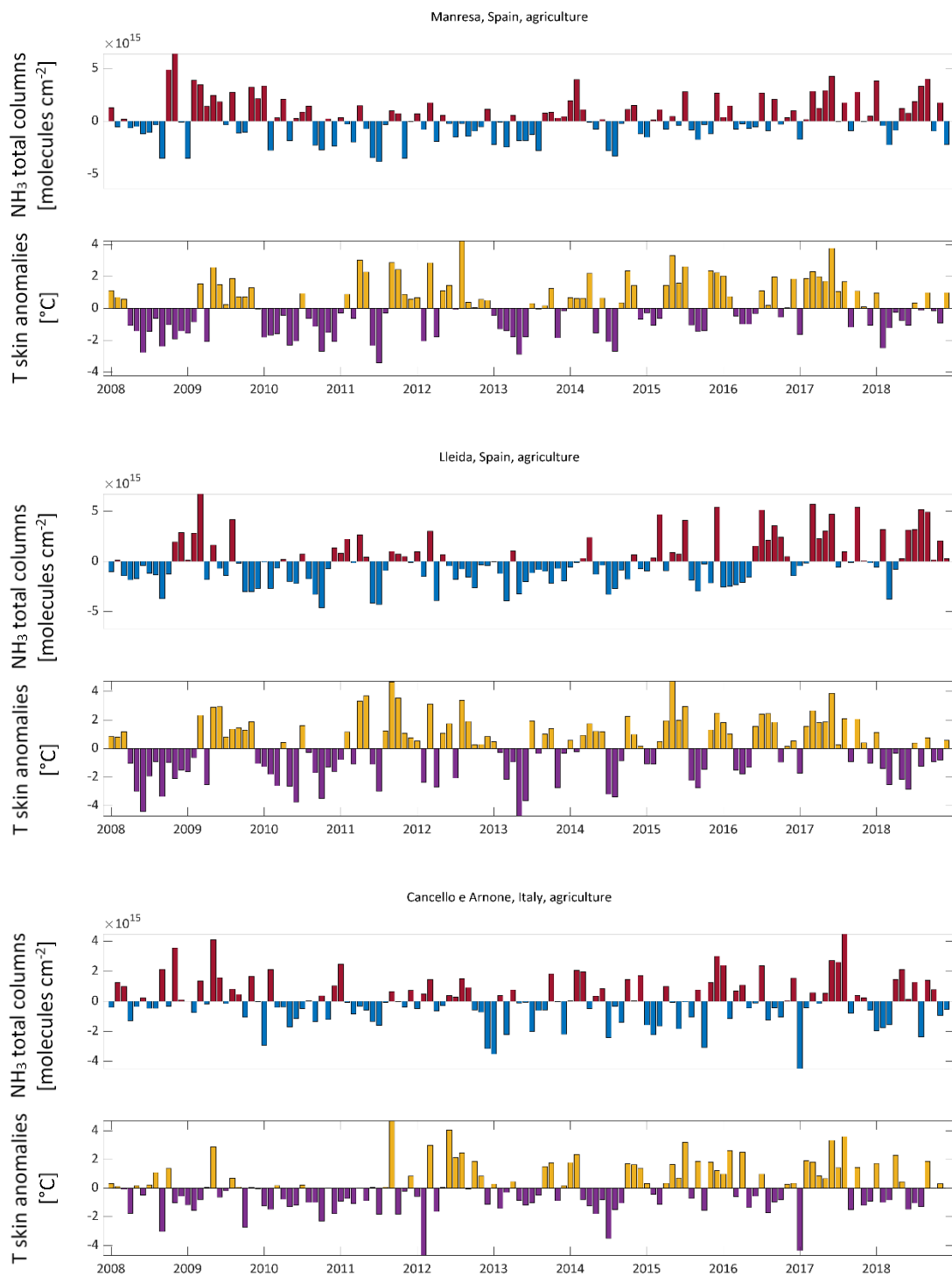


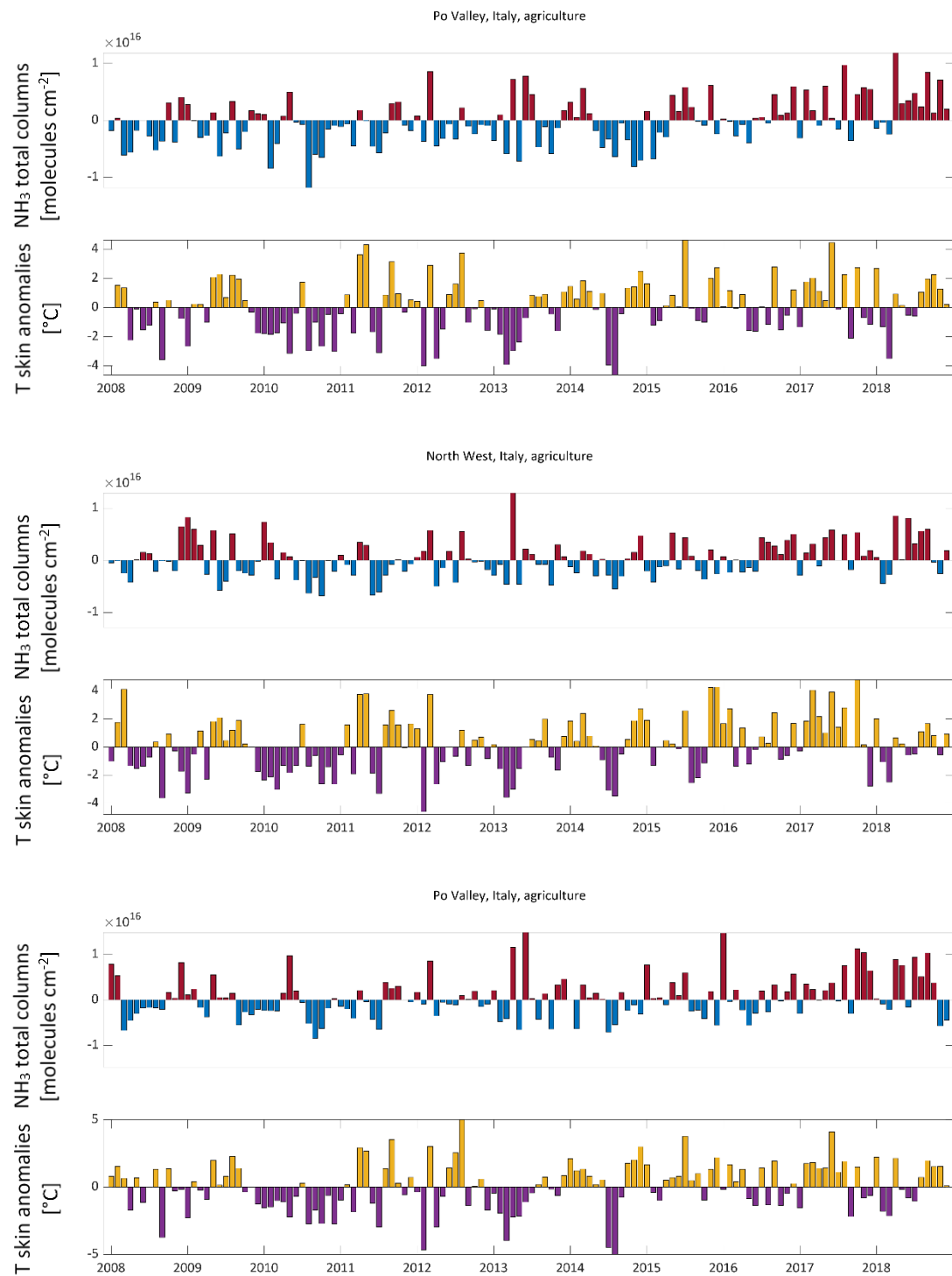


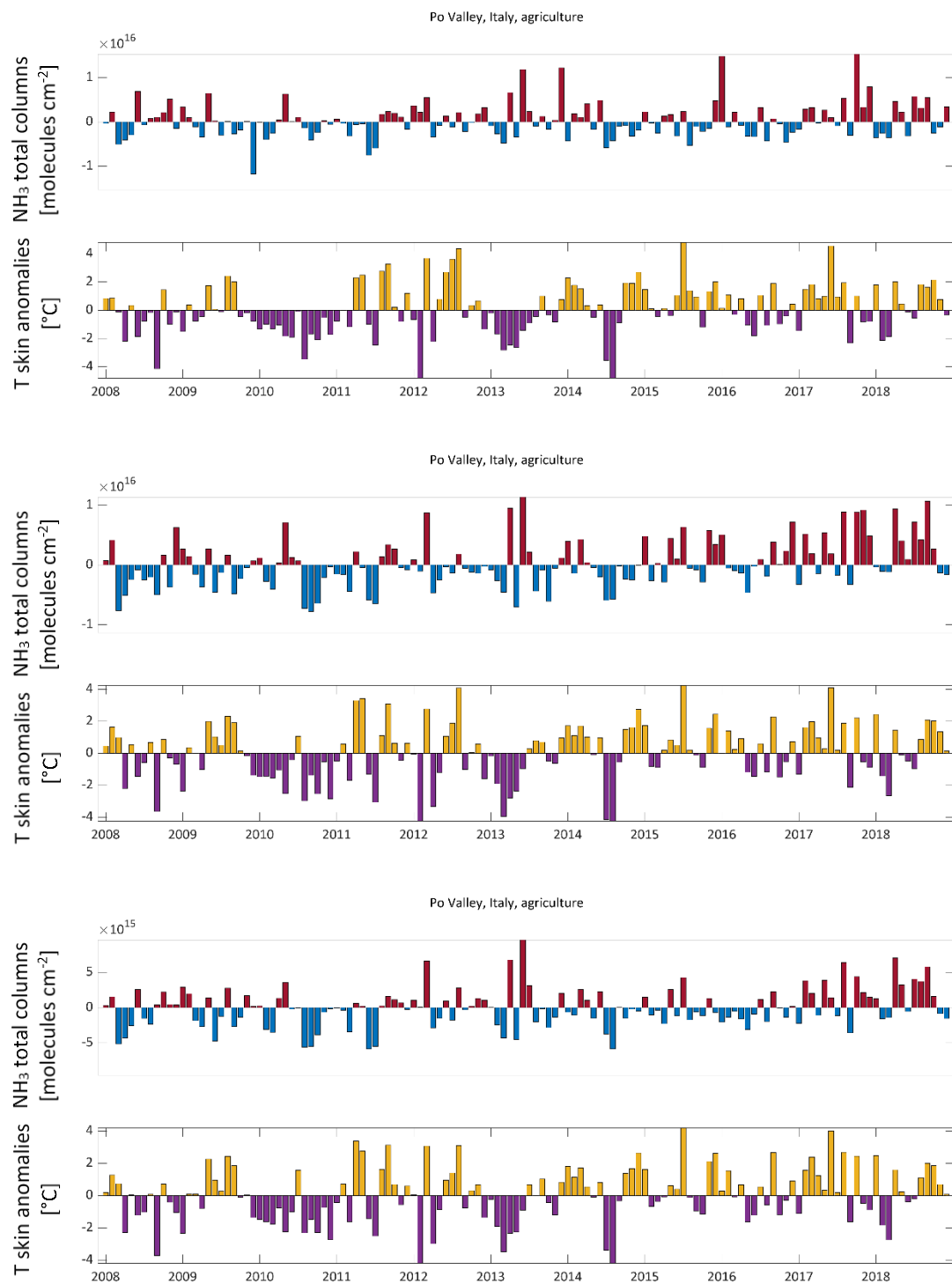
## D. NH<sub>3</sub> – T skin anomalies

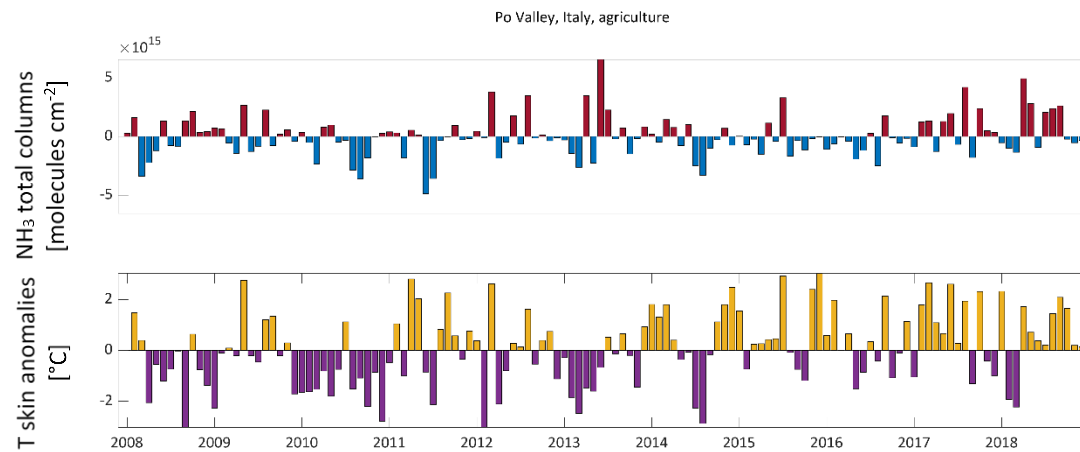
### Agriculture in Europe



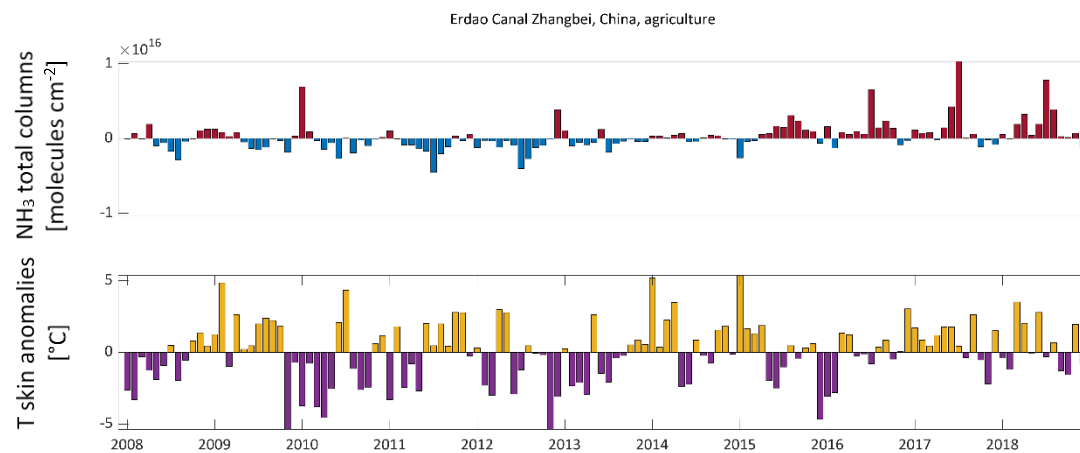
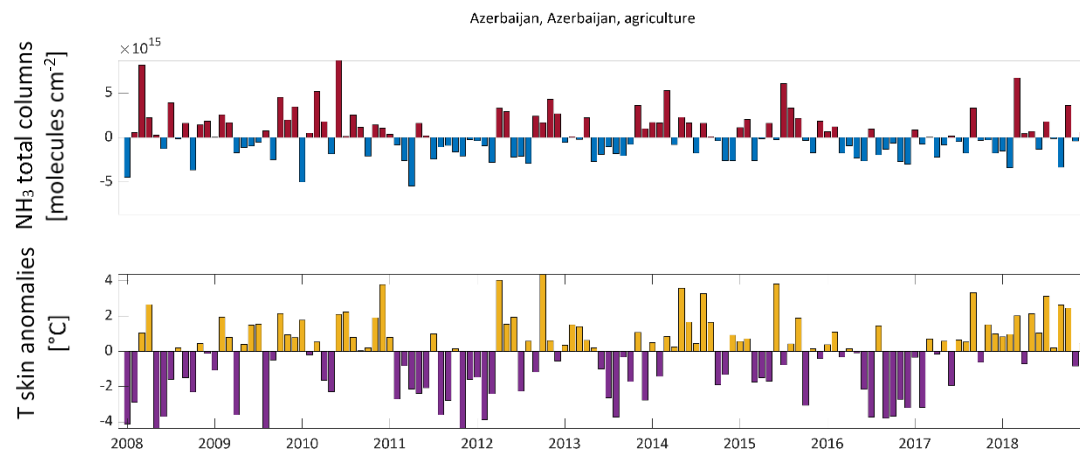




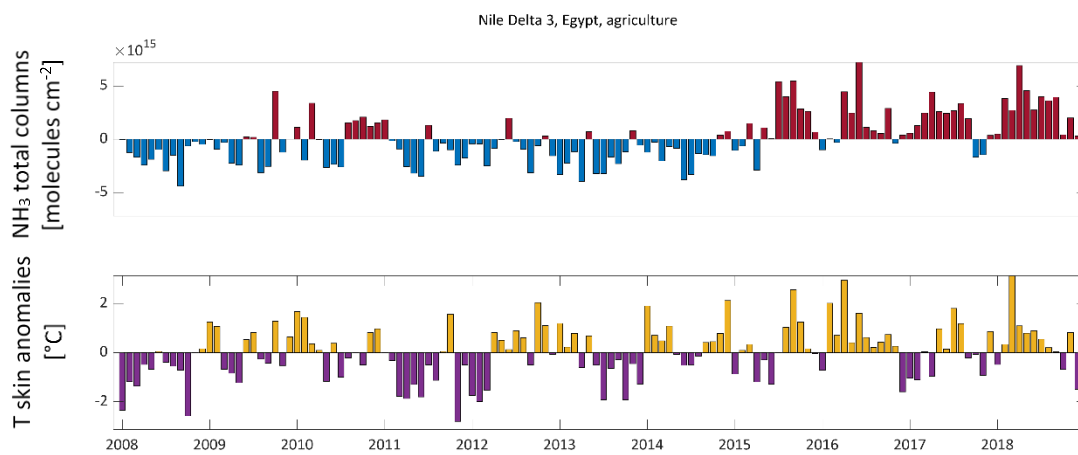
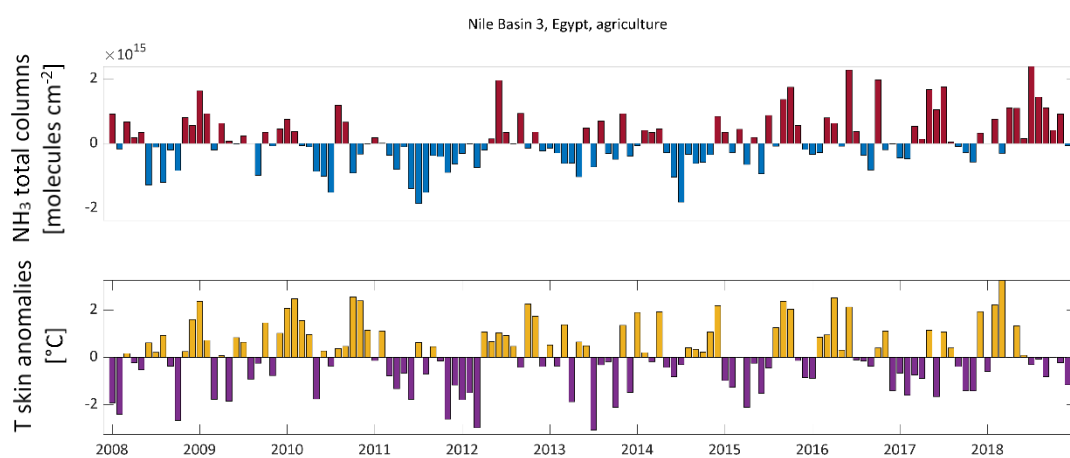
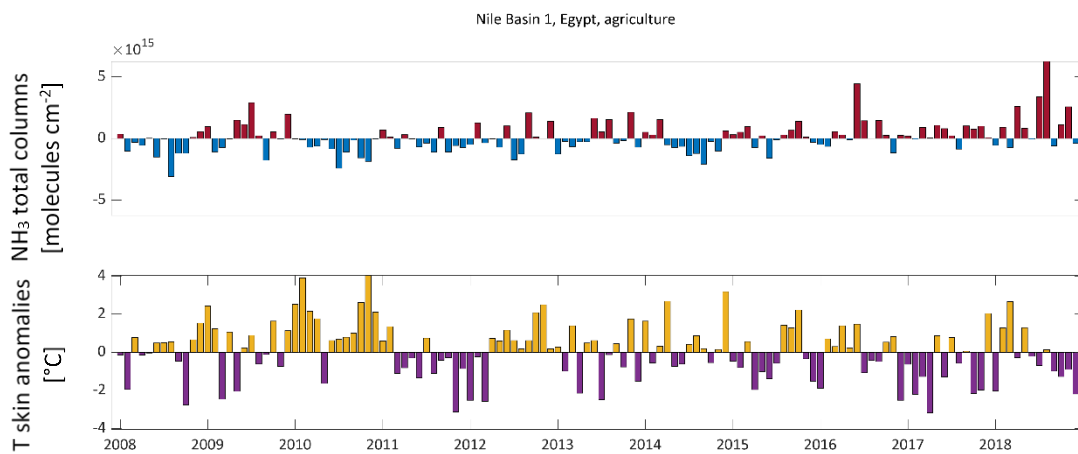


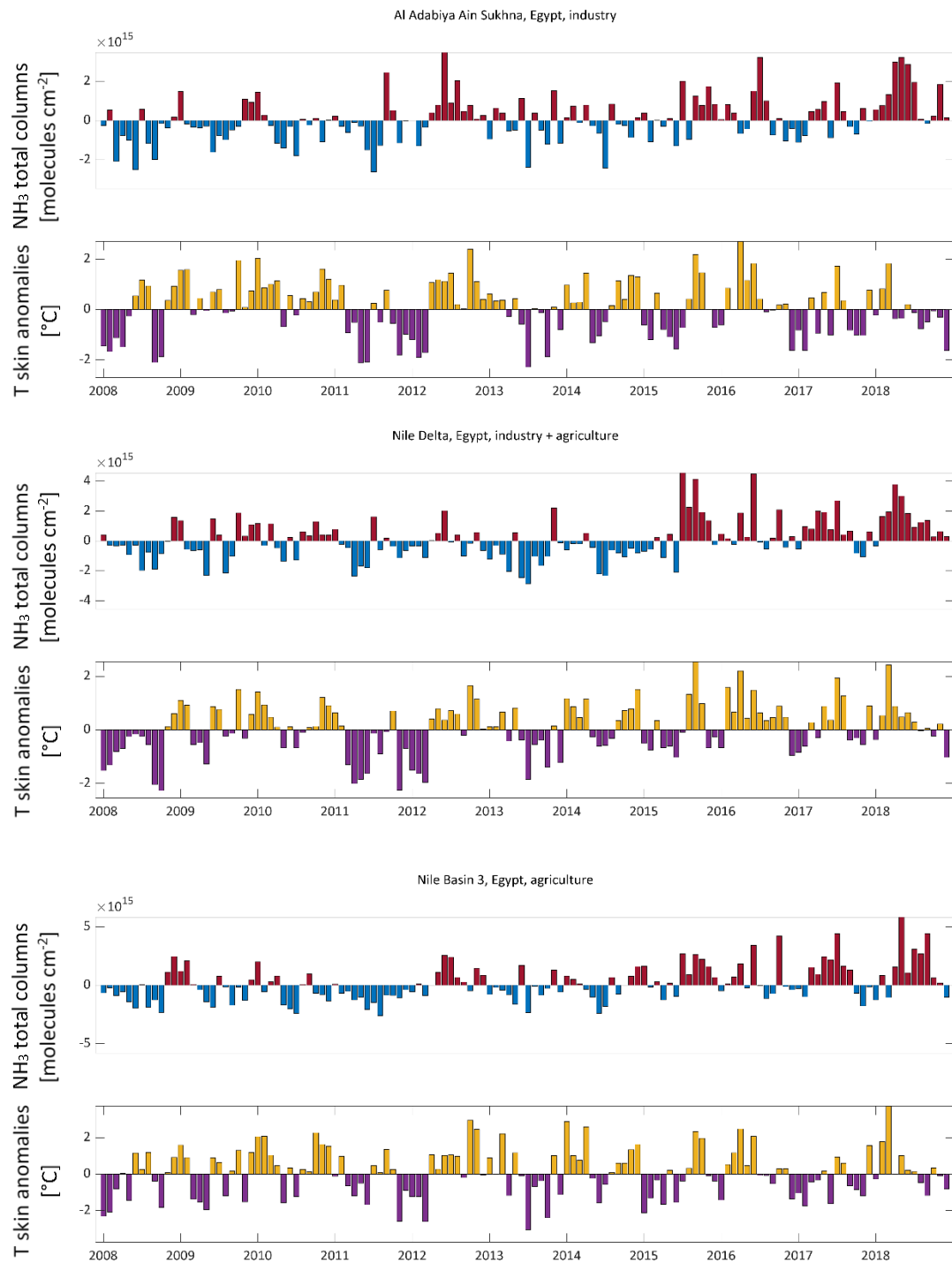


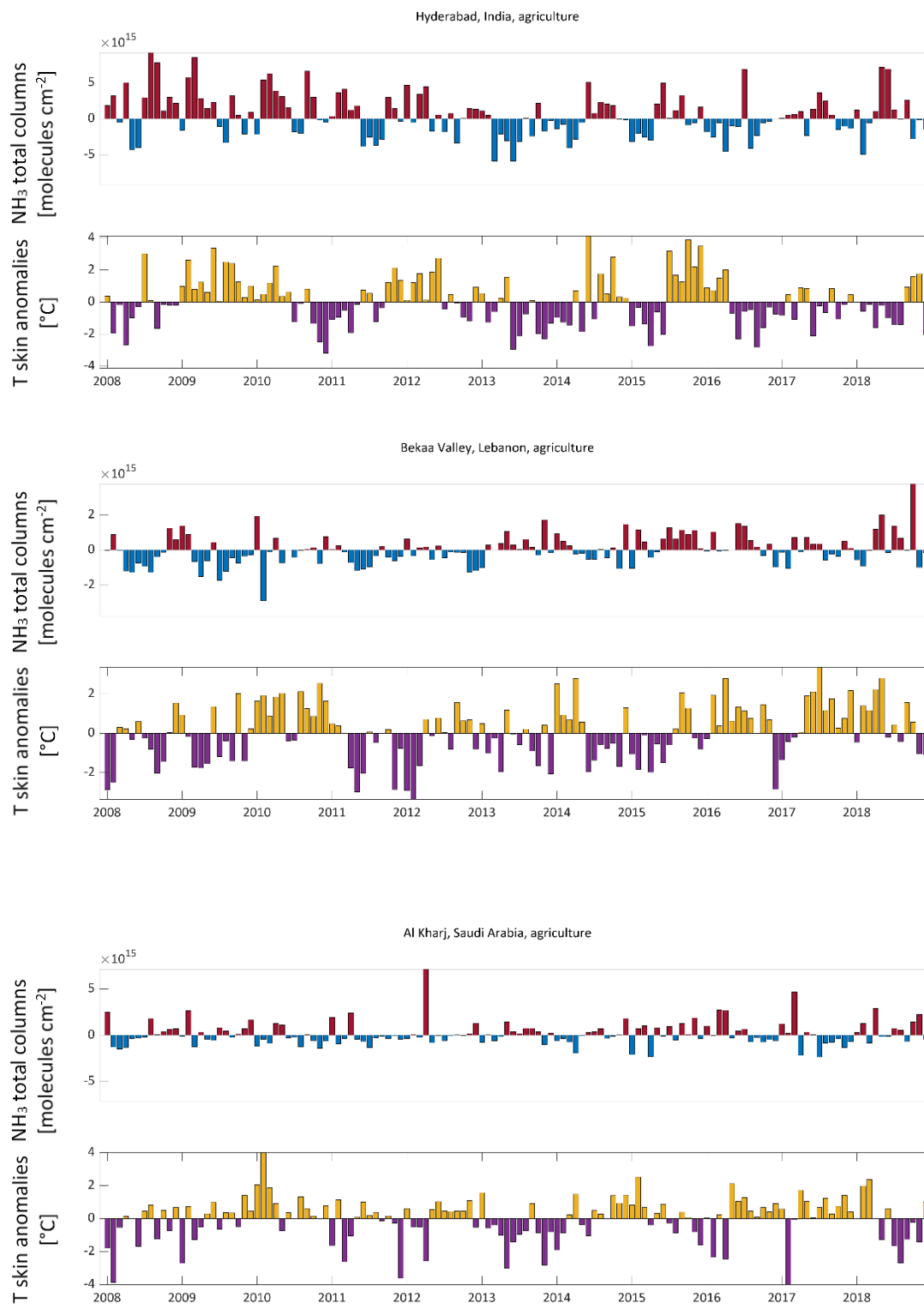
## Agriculture in non-EU regions

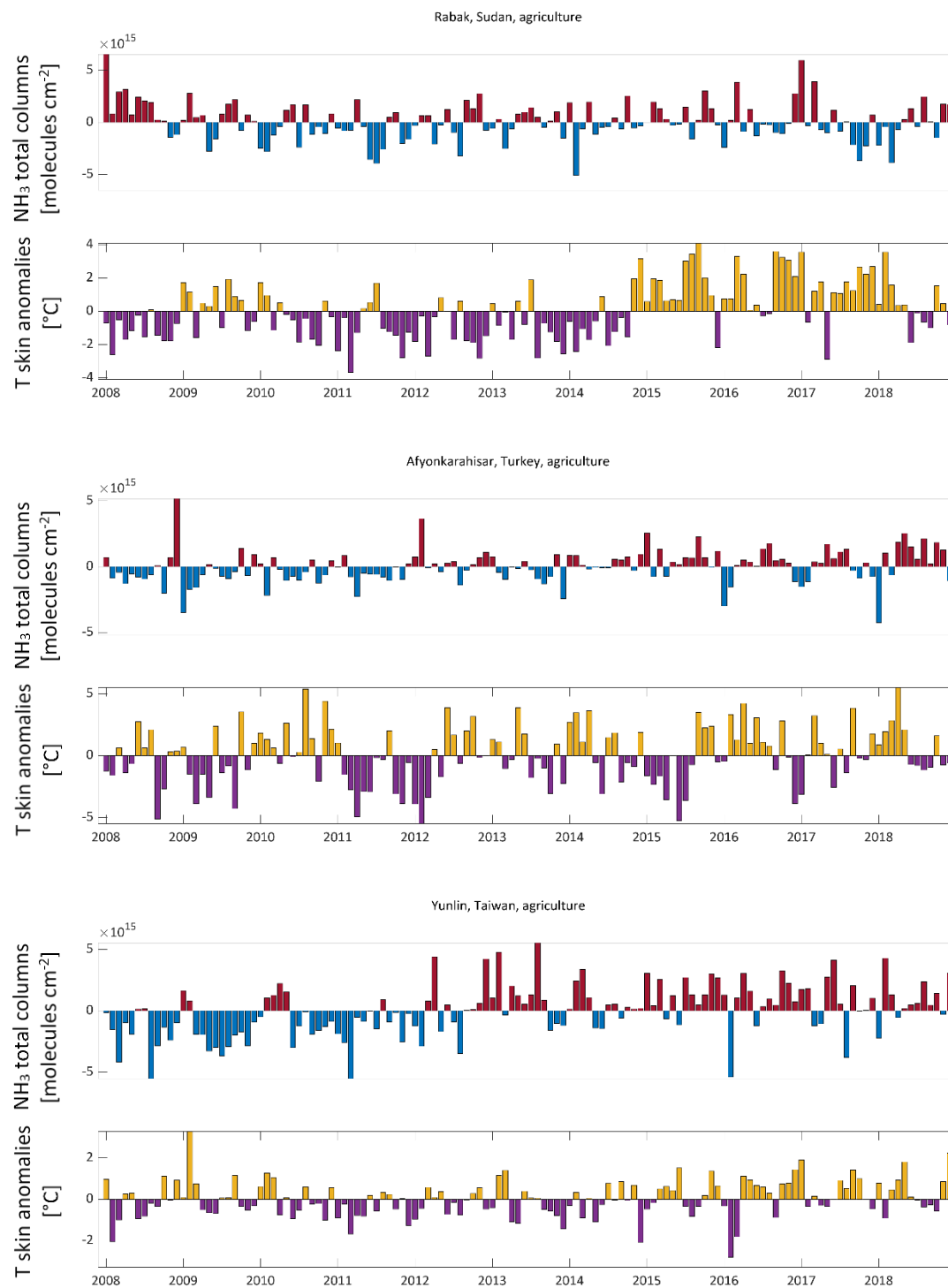


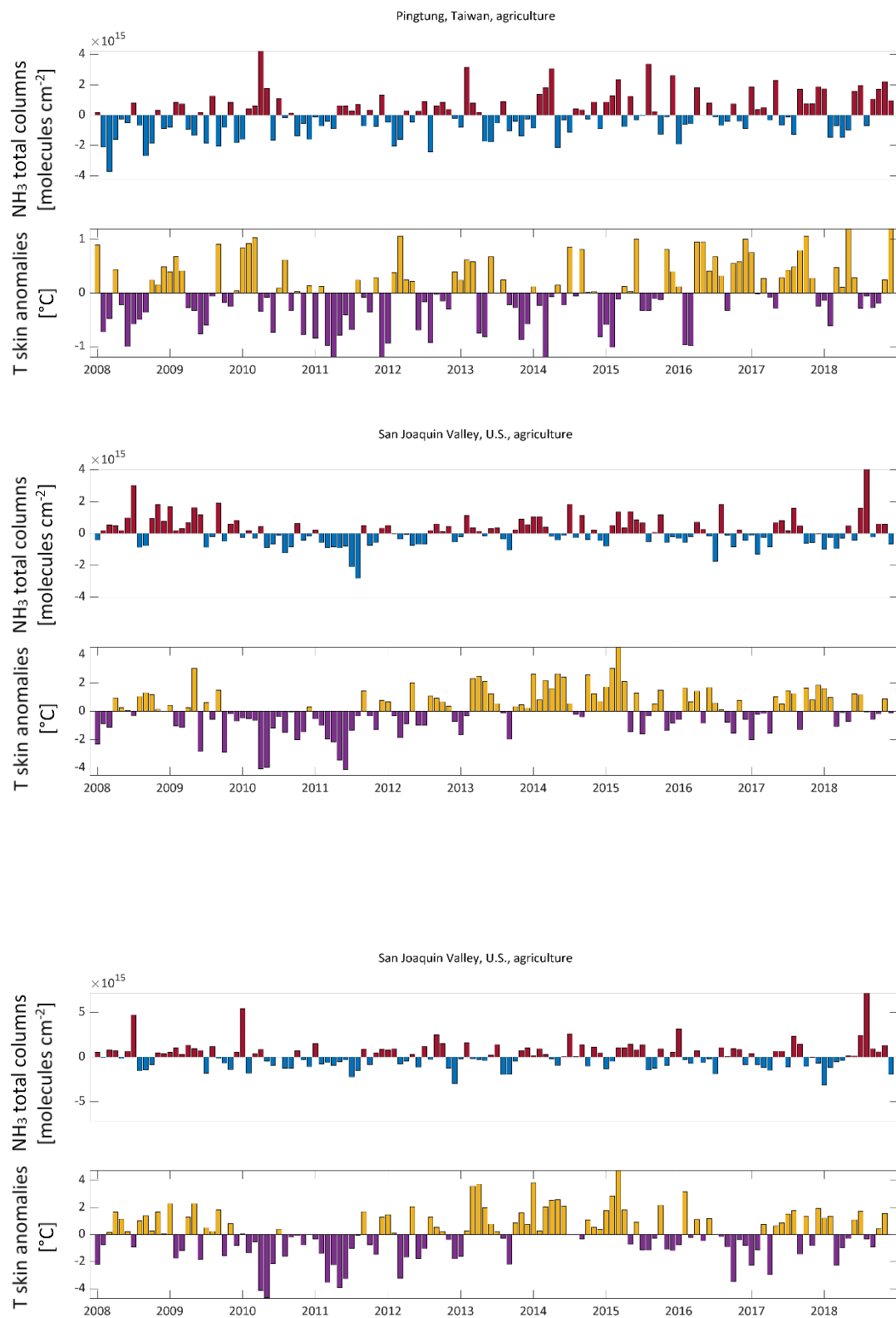


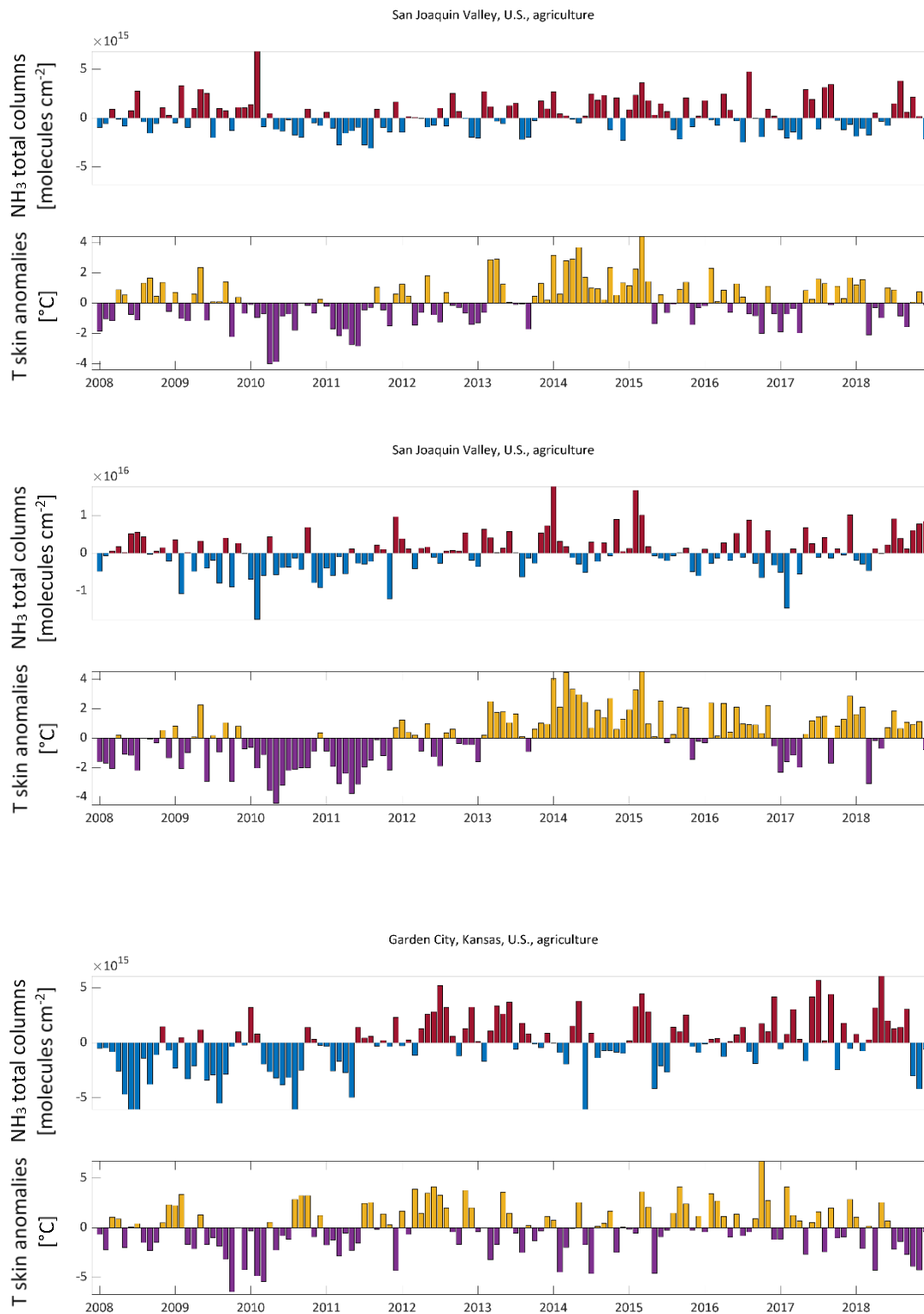




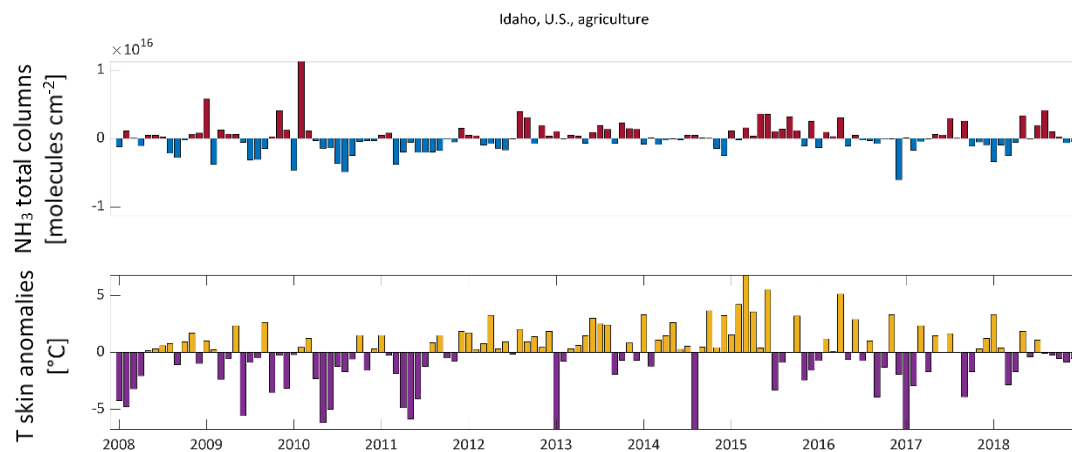




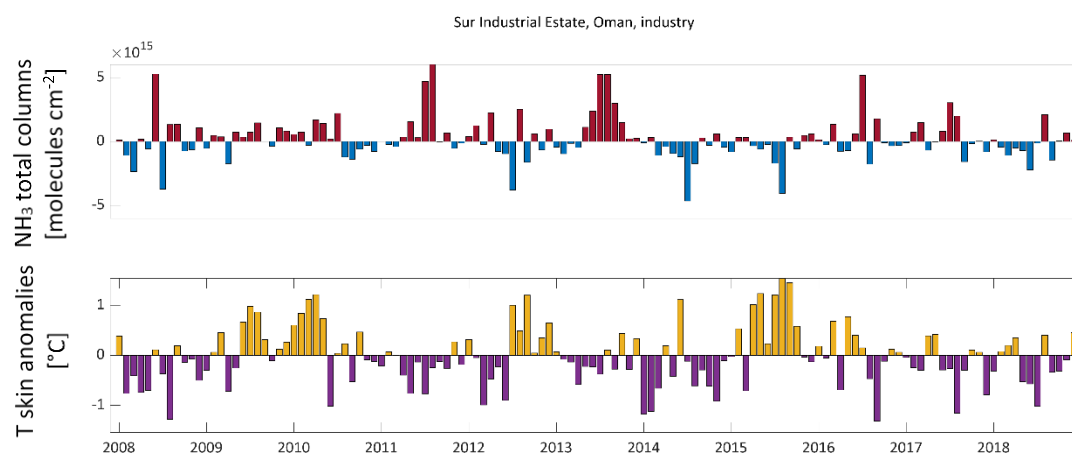
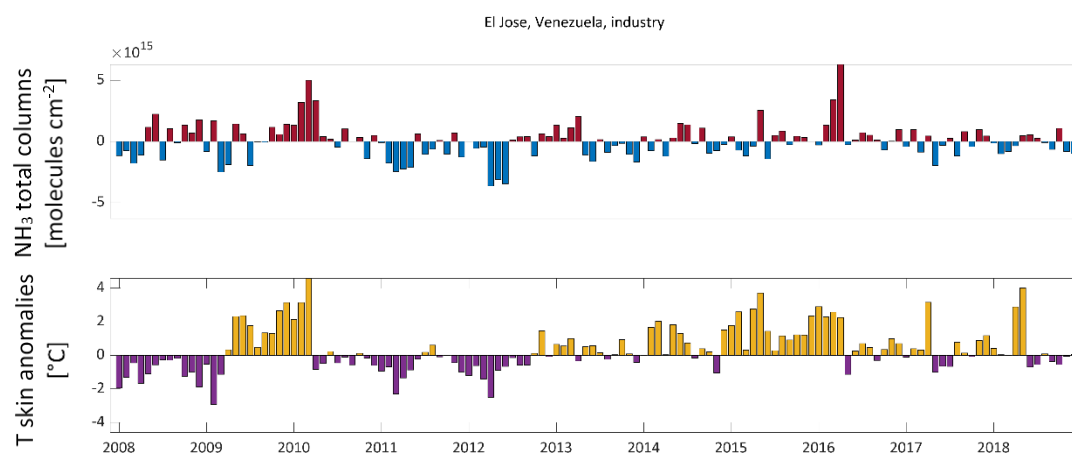


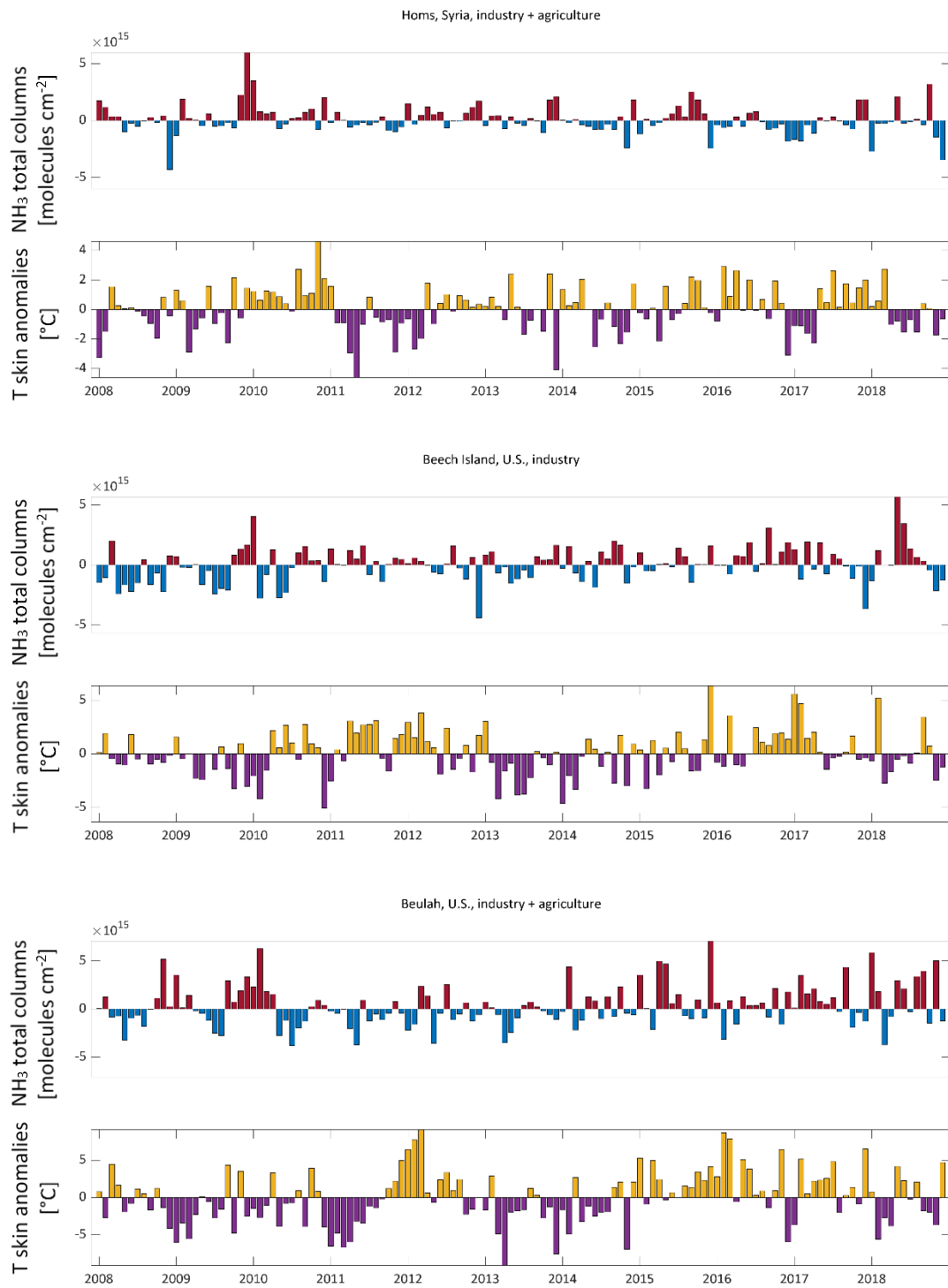


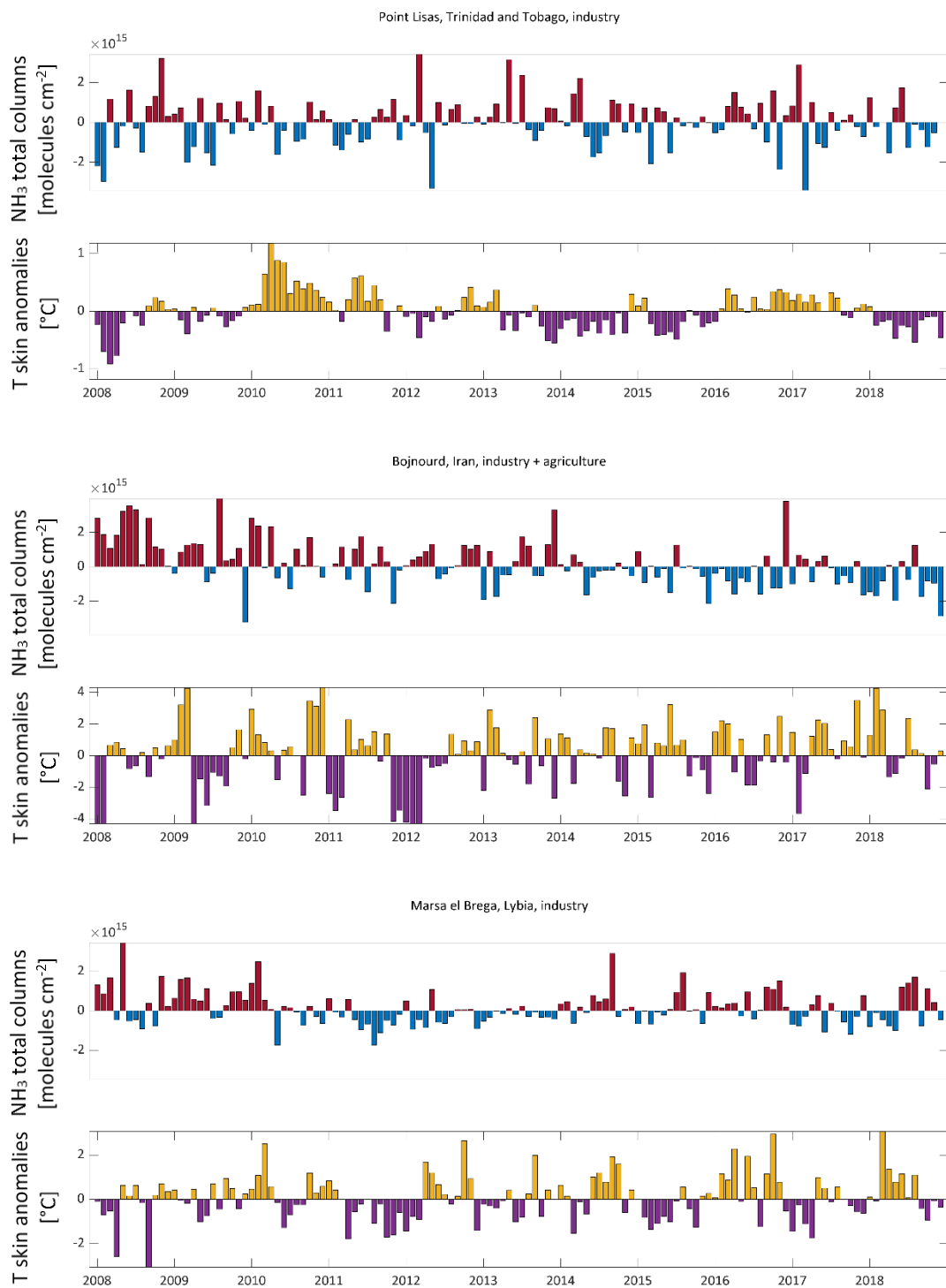


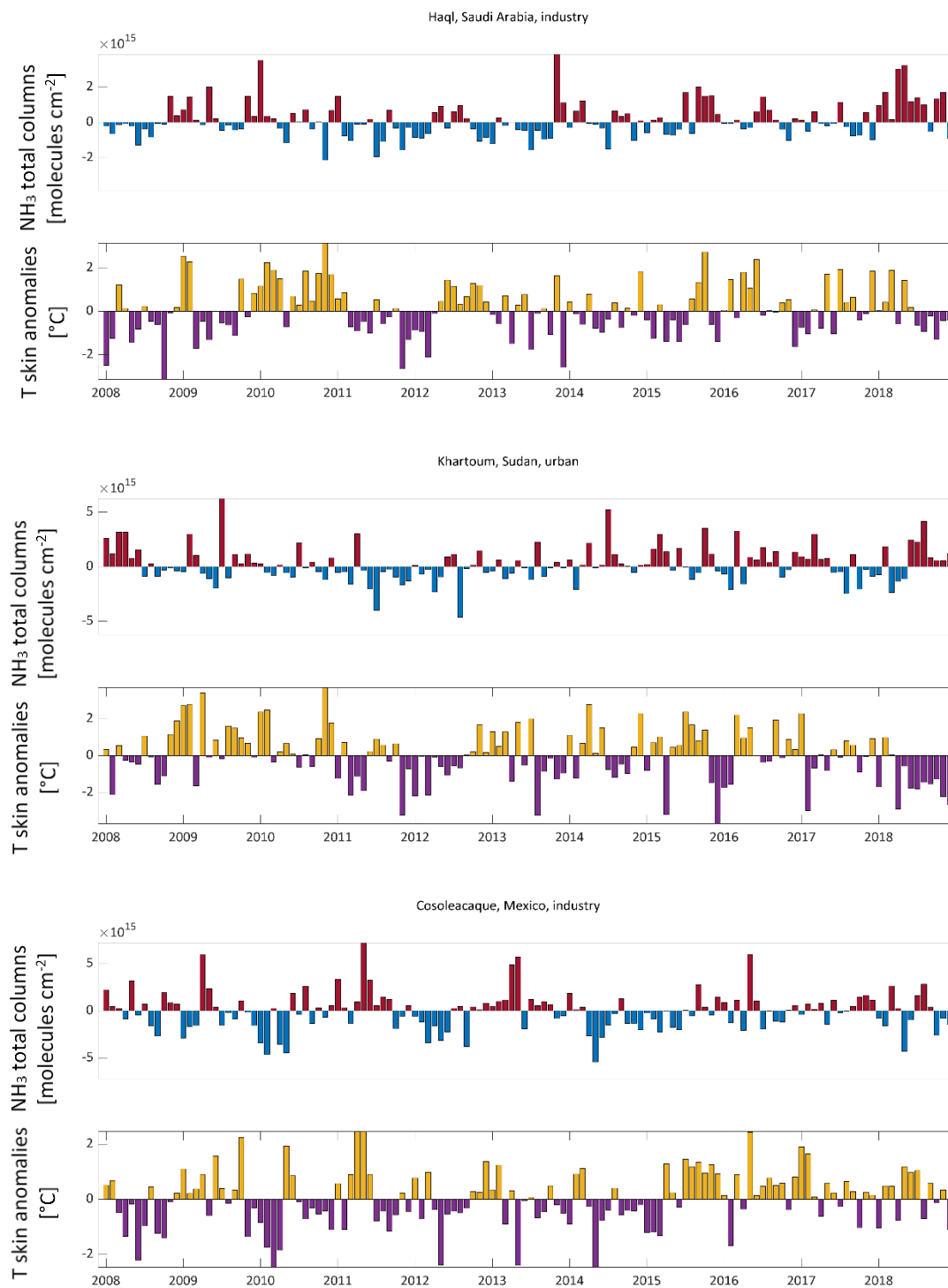


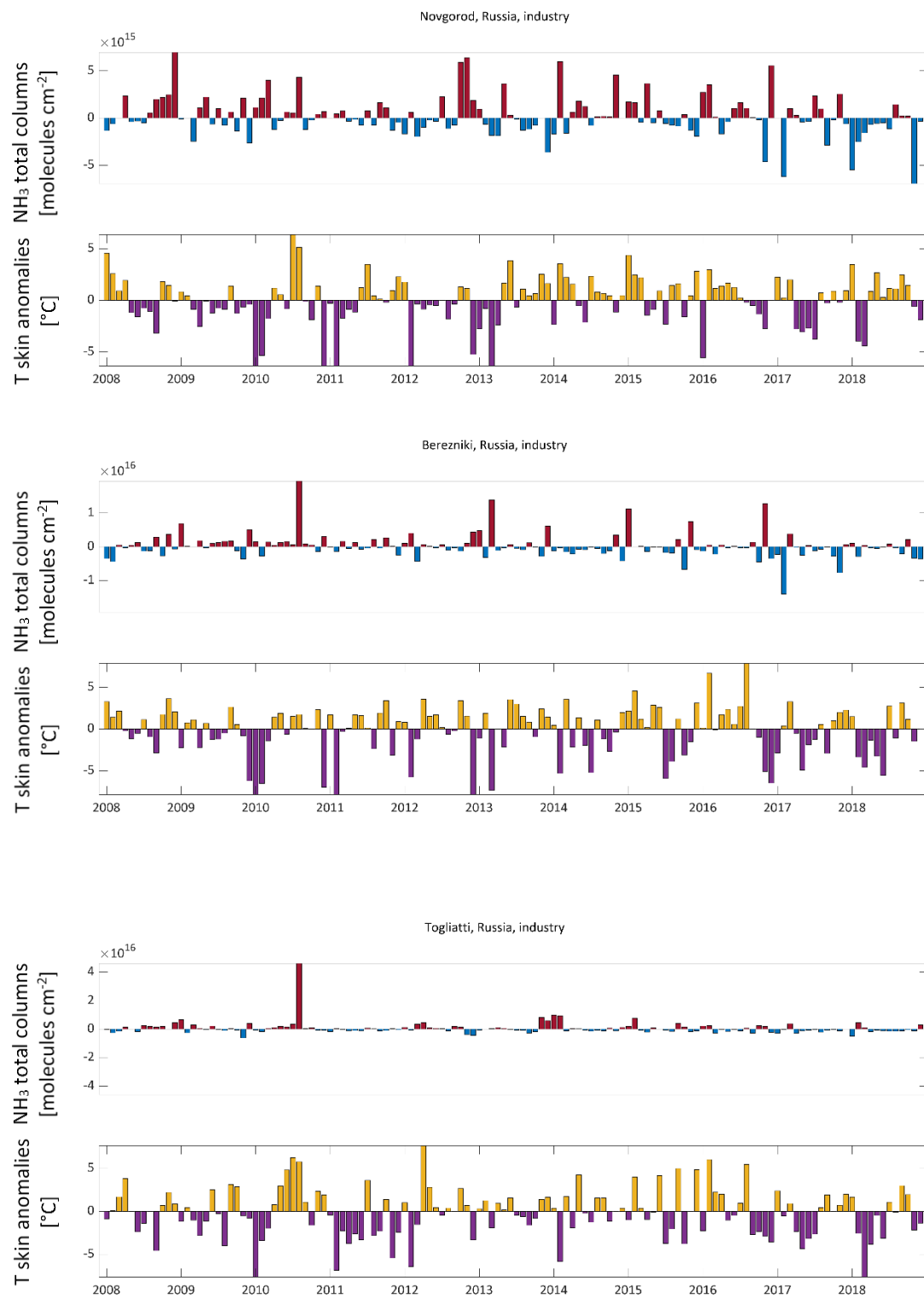
## Industrial, urban and mixed sources

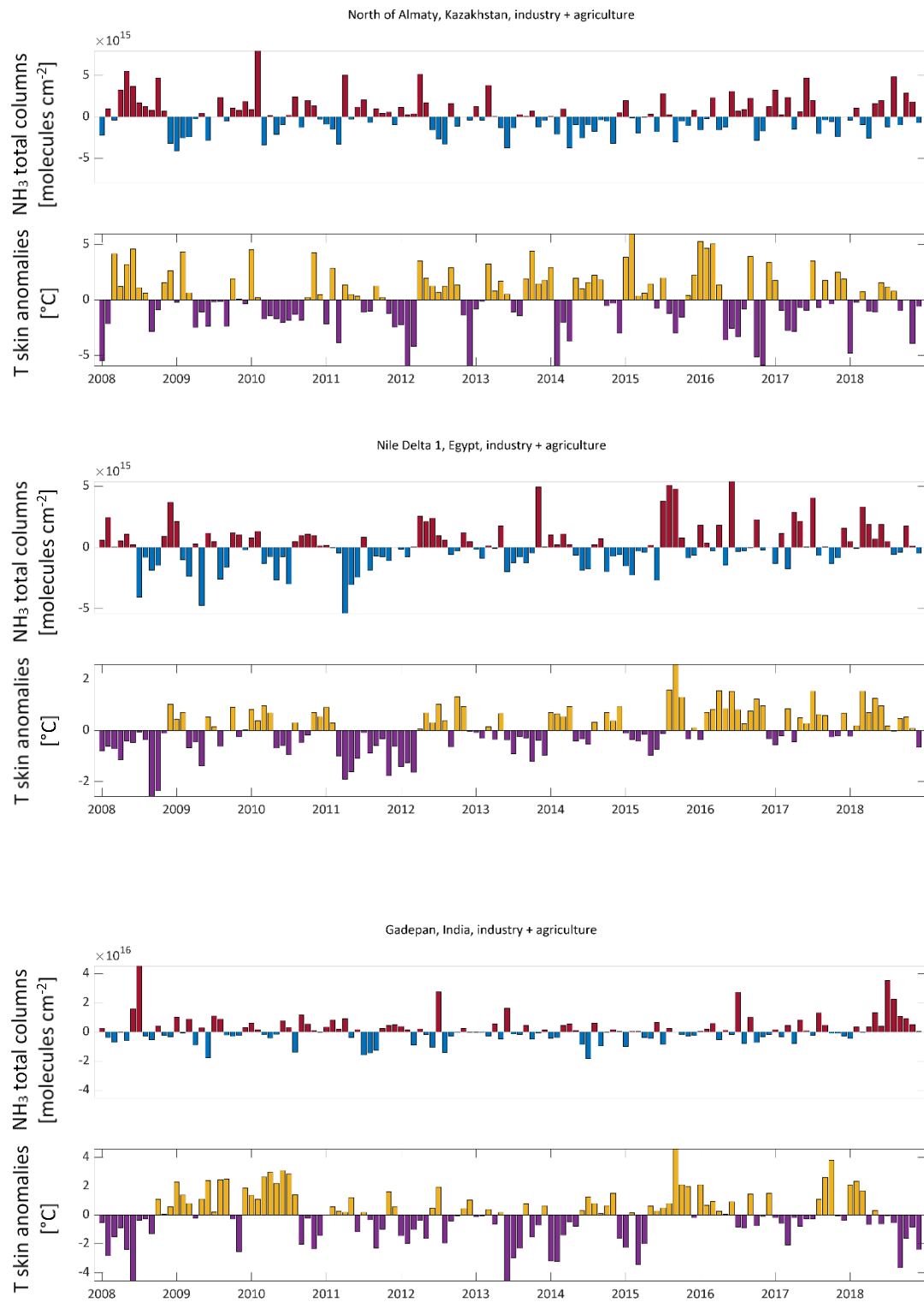




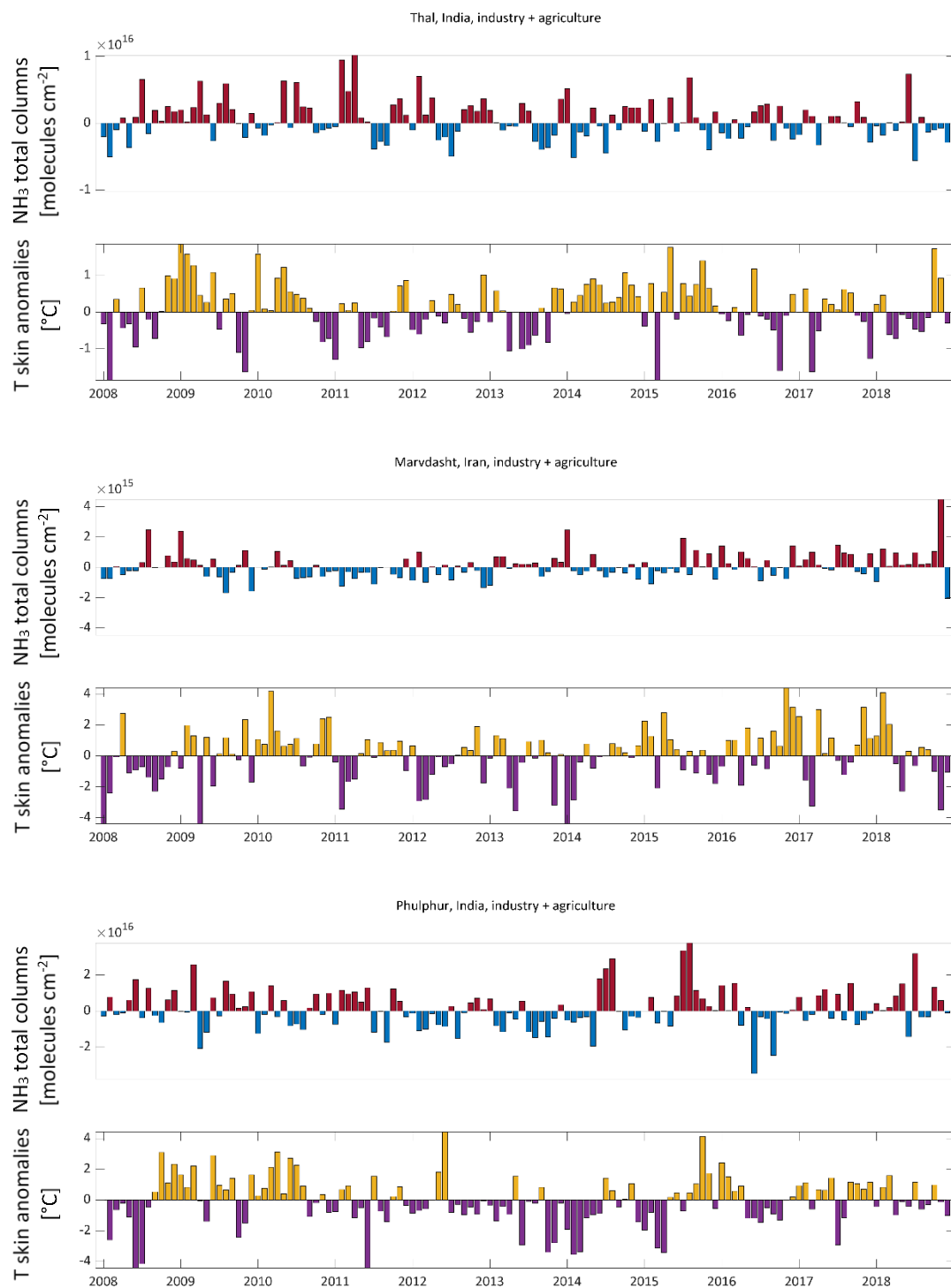


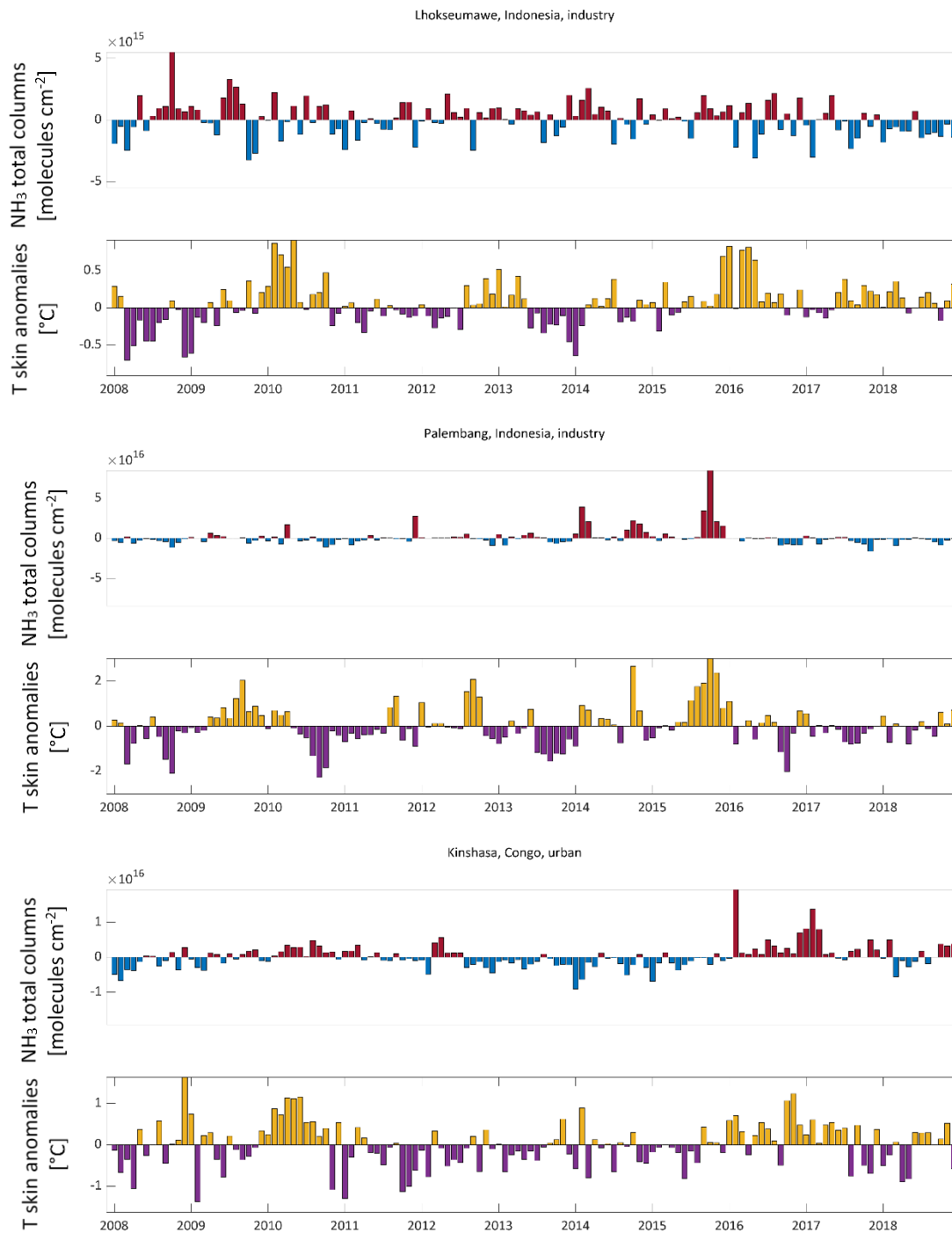


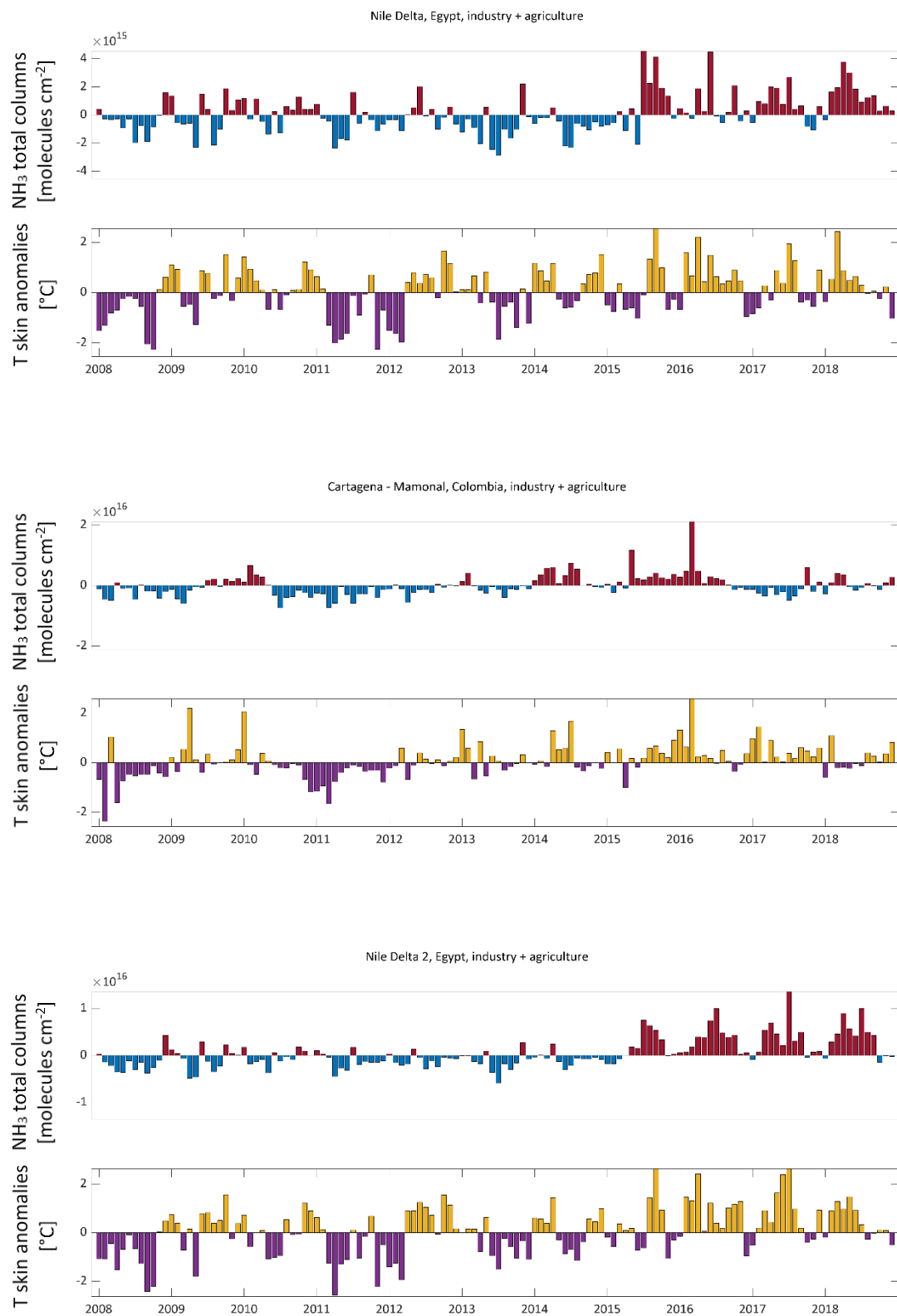


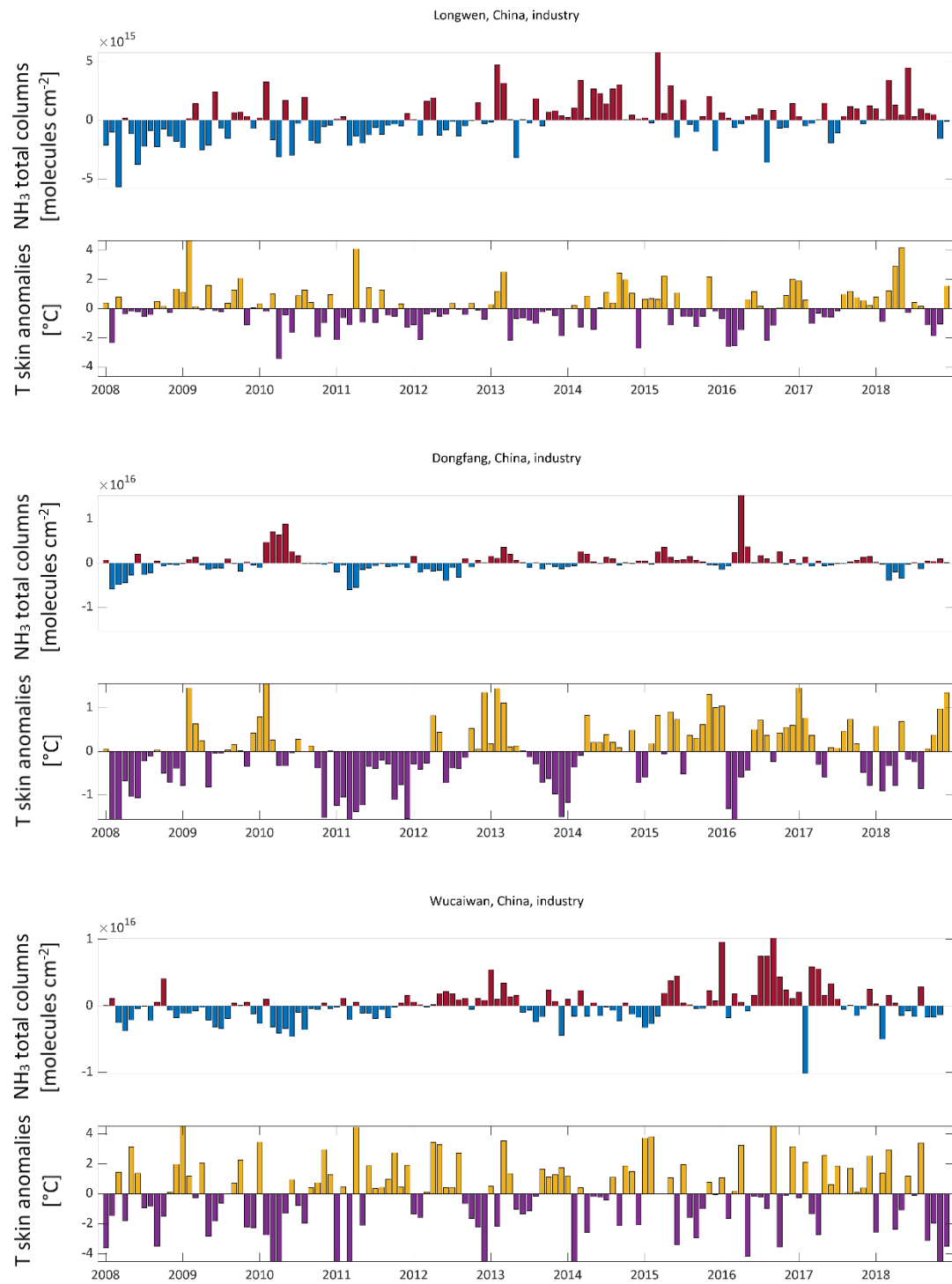


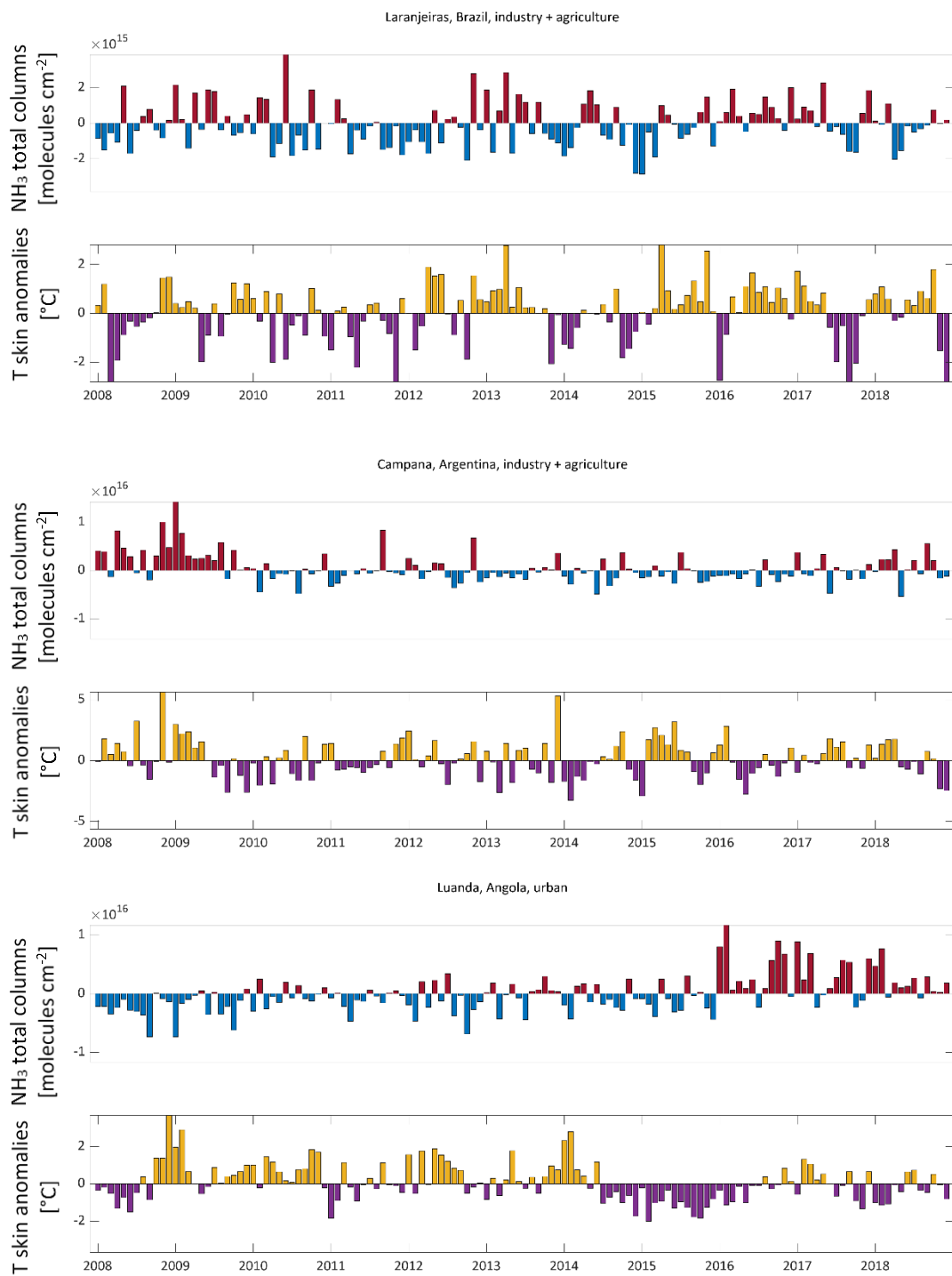












## *References*

- Abeed, R., Clerbaux, C., Clarisse, L., Van Damme, M., Coheur, P.-F., Safieddine, S., 2021. A space view of agricultural and industrial changes during the Syrian civil war. *Elem. Sci. Anthr.* 9, 000041. <https://doi.org/10.1525/elementa.2021.000041>
- Abeed, R., Viatte, C., Porter, W.C., Evangeliou, N., Clerbaux, C., Clarisse, L., Van Damme, M., Coheur, P.-F., Safieddine, S., 2022. Estimating agricultural ammonia volatilization over Europe using satellite observations and simulation data. *EGUsphere* 1–28. <https://doi.org/10.5194/egusphere-2022-1046>
- ACS, 2021. American Chemical Society: Urea [WWW Document]. URL <https://www.acs.org/molecule-of-the-week/archive/u/urea.html> (accessed 12.23.22).
- Adam, D., 2021. How far will global population rise? Researchers can't agree. *Nature* 597, 462–465. <https://doi.org/10.1038/d41586-021-02522-6>
- Adjetei, J., Campbell, L., Searle, P., Saffigna, P., 1999. Studies on depth of placement of urea on nitrogen recovery in wheat grown on a red-brown earth in Australia. *Nutr. Cycl. Agroecosystems* 54, 227–232. <https://doi.org/10.1023/A:1009775622609>
- Al Arabiya News, 2014. Homs evacuation resumes after brief suspension. *Al Arab. Engl.*
- Alexander, B., Sherwen, T., Holmes, C.D., Fisher, J.A., Chen, Q., Evans, M.J., Kasibhatla, P., 2020. Global inorganic nitrate production mechanisms: comparison of a global model with nitrate isotope observations. *Atmospheric Chem. Phys.* 20, 3859–3877. <https://doi.org/10.5194/acp-20-3859-2020>
- Aneja, V.P., Rogers, H.H., Stahel, E.P., 1986. Dry Deposition of Ammonia at Environmental Concentrations on Selected Plant Species. *J. Air Pollut. Control Assoc.* 36, 1338–1341. <https://doi.org/10.1080/00022470.1986.10466183>
- AQEG, 2012. Fine particulate matter (PM<sub>2.5</sub>) in the United Kingdom. Air Quality Expert Group (AQEG), prepared for the Department for Environment, Food and Rural Affairs (Defra), Scottish Executive, Welsh Government and the Department of the Environment in Northern Ireland.
- Barnes, A.P., Svensson, C., Kjeldsen, T.R., 2022. North Atlantic air pressure and temperature conditions associated with heavy rainfall in Great Britain. *Int. J. Climatol.* 42, 3190–3207. <https://doi.org/10.1002/joc.7414>
- Bassett, M.E., Seinfeld, J.H., 1984. Atmospheric equilibrium model of sulfate and nitrate aerosols—II. Particle size analysis. *Atmospheric Environ.* 1967 18, 1163–1170. [https://doi.org/10.1016/0004-6981\(84\)90147-1](https://doi.org/10.1016/0004-6981(84)90147-1)
- Battye, W., Aneja, V.P., Schlesinger, W.H., 2017. Is nitrogen the next carbon? *Earth's Future* 5, 894–904. <https://doi.org/10.1002/2017EF000592>
- BBC News, 2019. Islamic State group defeated as final territory lost, US-backed forces say. *BBC News*.



- BBC News, 2017. Syria government “producing chemical weapons at research facilities.” BBC News.
- BBC News, 2014. Syria conflict: Rebels evacuated from Old City of Homs. BBC News.
- Beck, H.E., Zimmermann, N.E., McVicar, T.R., Vergopolan, N., Berg, A., Wood, E.F., 2018. Present and future Köppen-Geiger climate classification maps at 1-km resolution. *Sci. Data* 5, 180214. <https://doi.org/10.1038/sdata.2018.214>
- Beer, R., Shephard, M.W., Kulawik, S.S., Clough, S.A., Eldering, A., Bowman, K.W., Sander, S.P., Fisher, B.M., Payne, V.H., Luo, M., Osterman, G.B., Worden, J.R., 2008. First satellite observations of lower tropospheric ammonia and methanol. *Geophys. Res. Lett.* 35. <https://doi.org/10.1029/2008GL033642>
- Behera, S.N., Sharma, M., Aneja, V.P., Balasubramanian, R., 2013. Ammonia in the atmosphere: a review on emission sources, atmospheric chemistry and deposition on terrestrial bodies. *Env. Sci Pollut Res* 41. <https://doi.org/10.1007/s11356-013-2051-9>
- Belakovski, D., 2003. Kukhi-Malik area (Kuhi-malik), Yagnob River, Zeravshan Range, Sughd, Tajikistan [WWW Document]. URL <https://www.mindat.org/loc-122085.html> (accessed 11.20.22).
- Belakovski, D., 1990. Mindat.org [WWW Document]. URL <https://www.mindat.org/locentries.php?p=220855&m=1641> (accessed 11.20.22).
- Bell, B., Hersbach, H., Simmons, A., Berrisford, P., Dahlgren, P., Horányi, A., Muñoz-Sabater, J., Nicolas, J., Radu, R., Schepers, D., Soci, C., Villaume, S., Bidlot, J., Haimberger, L., Woollen, J., Buontempo, C., Thépaut, J., 2021. The ERA5 global reanalysis: Preliminary extension to 1950. *Q. J. R. Meteorol. Soc.* 147, 4186–4227. <https://doi.org/10.1002/qj.4174>
- Belward, A.S., Estes, John E., Kline, K.D., 1999. The IGBP-DIS Global 1-Km Land-Cover Data Set DIS-Cover: A Project Overview. *Photogramm. Eng. Remote Sens.* 65, 1013–20.
- Bey, I., Jacob, D.J., Yantosca, R.M., Logan, J.A., Field, B.D., Fiore, A.M., Li, Q., Liu, H.Y., Mickley, L.J., Schultz, M.G., 2001. Global modeling of tropospheric chemistry with assimilated meteorology: Model description and evaluation. *J. Geophys. Res. Atmospheres* 106, 23073–23095. <https://doi.org/10.1029/2001JD000807>
- Bouwman, A.F., Lee, D.S., Asman, W. a. H., Dentener, F.J., Van Der Hoek, K.W., Olivier, J.G.J., 1997. A global high-resolution emission inventory for ammonia. *Glob. Biogeochem. Cycles* 11, 561–587. <https://doi.org/10.1029/97GB02266>
- Bray, C.D., Battye, W.H., Aneja, V.P., Schlesinger, W.H., 2021. Global emissions of NH<sub>3</sub>, NO<sub>x</sub>, and N<sub>2</sub>O from biomass burning and the impact of climate change. *J. Air Waste Manag. Assoc.* 71, 102–114. <https://doi.org/10.1080/10962247.2020.1842822>
- Chakraborty, S.P., Sen Gupta, S.P., 1959. Fixation of Nitrogen by the Rice Plant. *Nature* 184, 2033–2034. <https://doi.org/10.1038/1842033a0>
- Chang, Y., Zhang, Y.-L., Kawichai, S., Wang, Q., Van Damme, M., Clarisse, L., Prapamontol, T., Lehmann, M.F., 2021. Convergent evidence for the pervasive but limited contribution of biomass burning to atmospheric ammonia in peninsular Southeast Asia. *Atmospheric Chem. Phys.* 21, 7187–7198. <https://doi.org/10.5194/acp-21-7187-2021>

- Chen, P., Du, Q., Liu, X., Zhou, L., Hussain, S., Lei, L., Song, C., Wang, X., Liu, W., Yang, F., Shu, K., Liu, J., Du, J., Yang, W., Yong, T., 2017. Effects of reduced nitrogen inputs on crop yield and nitrogen use efficiency in a long-term maize-soybean relay strip intercropping system. *PLoS ONE* 12, e0184503. <https://doi.org/10.1371/journal.pone.0184503>
- Chopra, A., Lineweaver, C.H., 2008. The major elemental abundance differences between life, the oceans and the Sun. *Proc. 8th Aust. Space Sci. Conf.* 2008 7.
- Christopher, S.A., Gupta, P., 2010. Satellite Remote Sensing of Particulate Matter Air Quality: The Cloud-Cover Problem. *J. Air Waste Manag. Assoc.* 60, 596–602. <https://doi.org/10.3155/1047-3289.60.5.596>
- Clarisse, L., Clerbaux, C., Dentener, F., Hurtmans, D., Coheur, P.-F., 2009. Global ammonia distribution derived from infrared satellite observations. *Nat. Geosci.* 2, 479–483. <https://doi.org/10.1038/ngeo551>
- Clarisse, L., R'Honi, Y., Coheur, P.-F., Hurtmans, D., Clerbaux, C., 2011. Thermal infrared nadir observations of 24 atmospheric gases. *Geophys. Res. Lett.* 38. <https://doi.org/10.1029/2011GL047271>
- Clarisse, L., Shephard, M.W., Dentener, F., Hurtmans, D., Cady-Pereira, K., Karagulian, F., Van Damme, M., Clerbaux, C., Coheur, P.-F., 2010. Satellite monitoring of ammonia: A case study of the San Joaquin Valley. *J. Geophys. Res.* 115, D13302. <https://doi.org/10.1029/2009JD013291>
- Clarisse, L., Van Damme, M., Clerbaux, C., Coheur, P.-F., 2019a. Tracking down global NH<sub>3</sub> point sources with wind-adjusted superresolution. *Atmospheric Meas. Tech.* 12, 5457–5473. <https://doi.org/10.5194/amt-12-5457-2019>
- Clarisse, L., Van Damme, M., Gardner, W., Coheur, P.-F., Clerbaux, C., Whitburn, S., Hadji-Lazaro, J., Hurtmans, D., 2019b. Atmospheric ammonia (NH<sub>3</sub>) emanations from Lake Natron's saline mudflats. *Sci. Rep.* 9, 4441. <https://doi.org/10.1038/s41598-019-39935-3>
- Clerbaux, C., Boynard, A., Clarisse, L., George, M., Hadji-Lazaro, J., Herbin, H., Hurtmans, D., Pommier, M., Razavi, A., Turquety, S., Wespes, C., 2009. Monitoring of atmospheric composition using the thermal infrared IASI/MetOp sounder. *Atmospheric Chem. Phys.* 9, 6041–6054. <https://doi.org/10.5194/acp-9-6041-2009>
- Clerbaux, C., Hadji-Lazaro, J., Turquety, S., George, M., Boynard, A., Pommier, M., Safieddine, S., Coheur, P.-F., Hurtmans, D., Clarisse, L., Van Damme, M., 2015. Tracking pollutants from space: Eight years of IASI satellite observation. *Comptes Rendus Geosci.* 347, 134–144. <https://doi.org/10.1016/j.crte.2015.06.001>
- CNN, 2014. Survival in a siege: Leaves become food, faith becomes strength.
- Coheur, P.-F., Barret, B., Turquety, S., Hurtmans, D., Hadji-Lazaro, J., Clerbaux, C., 2005. Retrieval and characterization of ozone vertical profiles from a thermal infrared nadir sounder. *J. Geophys. Res. Atmospheres* 110. <https://doi.org/10.1029/2005JD005845>
- Coheur, P.-F., Clarisse, L., Turquety, S., Hurtmans, D., Clerbaux, C., 2009. IASI measurements of reactive trace species in biomass burning plumes. *Atmospheric Chem. Phys.* 9, 5655–5667. <https://doi.org/10.5194/acp-9-5655-2009>

- Corbane, C., Kemper, T., Freire, S., Louvri r, C., Pesaresi, M., 2016. Monitoring the Syrian humanitarian crisis with the JRC’s global human settlement layer and night-time satellite. Publ. Off. Eur. Union EUR 27933. <https://doi.org/10.2788/48956>
- Crevoisier, C., Ch  din, A., Matsueda, H., Machida, T., Armante, R., Scott, N.A., 2009a. First year of upper tropospheric integrated content of CO<sub>2</sub> from IASI hyperspectral infrared observations. *Atmospheric Chem. Phys.* 9, 4797–4810. <https://doi.org/10.5194/acp-9-4797-2009>
- Crevoisier, C., Nobileau, D., Fiore, A.M., Armante, R., Ch  din, A., Scott, N.A., 2009b. Tropospheric methane in the tropics – first year from IASI hyperspectral infrared observations. *Atmospheric Chem. Phys.* 9, 6337–6350. <https://doi.org/10.5194/acp-9-6337-2009>
- Crutzen, P.J., 2002. Geology of mankind. *Nature* 415, 23–23. <https://doi.org/10.1038/415023a>
- Cui, J., Yu, C., Qiao, N., Xu, X., Tian, Y., Ouyang, H., 2017. Plant preference for NH<sub>4</sub><sup>+</sup> versus NO<sub>3</sub><sup>–</sup> at different growth stages in an alpine agroecosystem. *Field Crops Res.* 201, 192–199. <https://doi.org/10.1016/j.fcr.2016.11.009>
- Dammers, E., McLinden, C.A., Griffin, D., Shephard, M.W., Van Der Graaf, S., Lutsch, E., Schaap, M., Gainairu-Matz, Y., Fioletov, V., Van Damme, M., Whitburn, S., Clarisse, L., Cady-Pereira, K., Clerbaux, C., Coheur, P.F., Erisman, J.W., 2019. NH<sub>3</sub> emissions from large point sources derived from CrIS and IASI satellite observations. *Atmospheric Chem. Phys.* 19, 12261–12293. <https://doi.org/10.5194/acp-19-12261-2019>
- David, M., Loubet, B., Cellier, P., Mattsson, M., Schjoerring, J.K., Nemitz, E., Roche, R., Riedo, M., Sutton, M.A., 2009. Ammonia sources and sinks in an intensively managed grassland canopy. *Biogeosciences* 6, 1903–1915. <https://doi.org/10.5194/bg-6-1903-2009>
- Donnelly, C., Greuell, W., Andersson, J., Gerten, D., Pisacane, G., Roudier, P., Ludwig, F., 2017. Impacts of climate change on European hydrology at 1.5, 2 and 3 degrees mean global warming above preindustrial level. *Clim. Change* 143, 13–26. <https://doi.org/10.1007/s10584-017-1971-7>
- D  scher, R., Acosta, M., Alessandri, A., Anthoni, P., Arsouze, T., Bergman, T., Bernardello, R., Boussetta, S., Caron, L.-P., Carver, G., Castrillo, M., Catalano, F., Cvijanovic, I., Davini, P., Dekker, E., Doblas-Reyes, F.J., Docquier, D., Echevarria, P., Fladrich, U., Fuentes-Franco, R., Gr  ger, M., v. Hardenberg, J., Hieronymus, J., Karami, M.P., Keskinen, J.-P., Koenigk, T., Makkonen, R., Massonnet, F., M  n  goz, M., Miller, P.A., Moreno-Chamarro, E., Nieradzick, L., van Noije, T., Nolan, P., O’Donnell, D., Ollinaho, P., van den Oord, G., Ortega, P., Prims, O.T., Ramos, A., Reerink, T., Rousset, C., Ruprich-Robert, Y., Le Sager, P., Schmith, T., Schr  dner, R., Serva, F., Sicardi, V., Sloth Madsen, M., Smith, B., Tian, T., Tourigny, E., Uotila, P., Vancoppenolle, M., Wang, S., W  r  nd, D., Will  n, U., Wyser, K., Yang, S., Yepes-Arb  s, X., Zhang, Q., 2022. The EC-Earth3 Earth system model for the Coupled Model Intercomparison Project 6. *Geosci. Model Dev.* 15, 2973–3020. <https://doi.org/10.5194/gmd-15-2973-2022>
- ECMWF, 2016. IFS DOCUMENTATION – Cy43r1 Operational implementation PART IV: PHYSICAL PROCESSES.

- EDO, G.D.O., 2011. Drought news in Europe: Situation in April 2011 - Short Analysis of data from the European Drought Observatory (EDO).
- EEA, 2021. Emissions of the main air pollutants in Europe [WWW Document]. URL <https://www.eea.europa.eu/ims/emissions-of-the-main-air> (accessed 11.20.22).
- EEA, 2010. Ammonia (NH<sub>3</sub>) emissions — European Environment Agency.
- Eklund, L., Degerald, M., Brandt, M., Prishchepov, A.V., Pilesjö, P., 2017. How conflict affects land use: agricultural activity in areas seized by the Islamic State. *Environ. Res. Lett.* 12, 054004. <https://doi.org/10.1088/1748-9326/aa673a>
- Enab Baladi, 2019. Russia To Return Dismissed Employees To Fertilizers Company In Homs. Enab Baladi.
- EPA, 1966. Air Quality Criteria for Particulate Matter (Final Report, 1996) [WWW Document]. URL <https://cfpub.epa.gov/ncea/risk/recordisplay.cfm?deid=2832> (accessed 2.28.23).
- Eremenko, M., Dufour, G., Foret, G., Keim, C., Orphal, J., Beekmann, M., Bergametti, G., Flaud, J.-M., 2008. Tropospheric ozone distributions over Europe during the heat wave in July 2007 observed from infrared nadir spectra recorded by IASI. *Geophys. Res. Lett.* 35. <https://doi.org/10.1029/2008GL034803>
- Erismann, J.W., Galloway, J.N., Dise, N.B., Sutton, M.A., Bleeker, A., Grizzetti, B., Leach, A.M., Vries, W. de, 2015. Nitrogen: too much of a vital resource: Science Brief. WWF Netherlands.
- Erismann, J.W., Schaap, M., 2004. The need for ammonia abatement with respect to secondary PM reductions in Europe. *Environ. Pollut.* 129, 159–163. <https://doi.org/10.1016/j.envpol.2003.08.042>
- Erismann, J.W., Sutton, M.A., Galloway, J., Klimont, Z., Winiwarter, W., 2008. How a century of ammonia synthesis changed the world. *Nat. Geosci.* 1, 636–639. <https://doi.org/10.1038/ngeo325>
- Erismann, J.W., Van Pul, A., Wyers, P., 1994. Parametrization of surface resistance for the quantification of atmospheric deposition of acidifying pollutants and ozone. *Atmos. Environ.* 28, 2595–2607. [https://doi.org/10.1016/1352-2310\(94\)90433-2](https://doi.org/10.1016/1352-2310(94)90433-2)
- European Environment Agency, 2022. Global and European temperatures.
- Evangelizou, N., Balkanski, Y., Eckhardt, S., Cozic, A., Van Damme, M., Coheur, P.-F., Clarisse, L., Shephard, M., Cady-Pereira, K., Hauglustaine, D., 2021. 10-year satellite-constrained fluxes of ammonia improve performance of chemistry transport models. *Atmospheric Chem. Phys.* 21, 4431–4451. <https://doi.org/10.5194/acp-21-4431-2021>
- Eyring, V., Bony, S., Meehl, G.A., Senior, C.A., Stevens, B., Stouffer, R.J., Taylor, K.E., 2016. Overview of the Coupled Model Intercomparison Project Phase 6 (CMIP6) experimental design and organization. *Geosci. Model Dev.* 9, 1937–1958. <https://doi.org/10.5194/gmd-9-1937-2016>
- Faisal, M., Hazarika, N., Ganguly, D., Kumar, M., Singh, V., 2022. PM<sub>2.5</sub> bound species variation and source characterization in the post-lockdown period of the Covid-19 pandemic in Delhi. *Urban Clim.* 46, 101290. <https://doi.org/10.1016/j.uclim.2022.101290>

- FAO, 2022. FAO, GIEWS, Earth Observation [WWW Document]. URL <https://www.fao.org/giews/earthobservation/country/index.jsp?lang=en&code=FRA> (accessed 7.5.22).
- FAO, 2017. Counting the Cost: Agriculture in Syria after six years of crisis.
- FAO, 2003. Fertilizer use by crop in the Syrian Arab Republic. Rome, Italy.
- FAO Earth Observation, 2022. Crop-growing season in Ireland [WWW Document]. URL <https://www.fao.org/giews/earthobservation/country/index.jsp?lang=en&code=IRL#> (accessed 2.27.23).
- FAOSTAT, 2020. FAOSTAT - Fertilizers by Nutrient [WWW Document]. URL <https://www.fao.org/faostat/en/#data/RFN/visualize> (accessed 12.25.22).
- FAO/WFP, 2019. Special Report - FAO/WFP Crop and Food Security Assessment Mission to the Syrian Arab Republic. Rome.
- FAO/WFP, 2017. CROP AND FOOD SECURITY ASSESSMENT MISSION TO THE SYRIAN ARAB REPUBLIC - July 2017.
- Farmer, D.K., Matsunaga, A., Docherty, K.S., Surratt, J.D., Seinfeld, J.H., Ziemann, P.J., Jimenez, J.L., 2010. Response of an aerosol mass spectrometer to organonitrates and organosulfates and implications for atmospheric chemistry. *Proc. Natl. Acad. Sci.* 107, 6670–6675. <https://doi.org/10.1073/pnas.0912340107>
- Farquhar, G.D., Firth, P.M., Wetselaar, R., Weir, B., 1980. On the Gaseous Exchange of Ammonia between Leaves and the Environment: Determination of the Ammonia Compensation Point. *Plant Physiol.* 66, 710–714. <https://doi.org/10.1104/pp.66.4.710>
- Farquhar, G.D., Wetselaar, R., Weir, B., 1983. Gaseous nitrogen losses from plants, in: Freney, J.R., Simpson, J.R. (Eds.), *Gaseous Loss of Nitrogen from Plant-Soil Systems, Developments in Plant and Soil Sciences*. Springer Netherlands, Dordrecht, pp. 159–180. [https://doi.org/10.1007/978-94-017-1662-8\\_6](https://doi.org/10.1007/978-94-017-1662-8_6)
- Fertilizers Europe, 2016. Infinite Fertilizers - Nutrient Stewardship.
- Fields, S., 2004. Global Nitrogen: Cycling out of Control. *Environ. Health Perspect.* 112, A556–A563.
- Finch, H.J.S., Samuel, A.M., Lane, G.P.F., 2002. Fertilisers and manures, in: Lockhart and Wiseman's *Crop Husbandry Including Grassland* (8th Edition). Woodhead Publishing, Cambridge, pp. 52–78.
- Fiore, A.M., Horowitz, L.W., Purves, D.W., Levy II, H., Evans, M.J., Wang, Y., Li, Q., Yantosca, R.M., 2005. Evaluating the contribution of changes in isoprene emissions to surface ozone trends over the eastern United States. *J. Geophys. Res. Atmospheres* 110. <https://doi.org/10.1029/2004JD005485>
- Flechard, C.R., Massad, R.-S., Loubet, B., Personne, E., Simpson, D., Bash, J.O., Cooter, E.J., Nemitz, E., Sutton, M.A., 2013. Advances in understanding, models and parameterizations of biosphere-atmosphere ammonia exchange. *Biogeosciences* 10, 5183–5225. <https://doi.org/10.5194/bg-10-5183-2013>



- Flechard, C.R., Nemitz, E., Smith, R.I., Fowler, D., Vermeulen, A.T., Bleeker, A., Erismann, J.W., Simpson, D., Zhang, L., Tang, Y.S., Sutton, M.A., 2011. Dry deposition of reactive nitrogen to European ecosystems: a comparison of inferential models across the NitroEurope network. *Atmospheric Chem. Phys.* 11, 2703–2728. <https://doi.org/10.5194/acp-11-2703-2011>
- Flechard, C.R., Spirig, C., Neftel, A., Ammann, C., 2010. The annual ammonia budget of fertilised cut grassland – Part 2: Seasonal variations and compensation point modeling. *Biogeosciences* 7, 537–556. <https://doi.org/10.5194/bg-7-537-2010>
- Folberth, G.A., Hauglustaine, D.A., Lathière, J., Brocheton, F., 2006. Interactive chemistry in the Laboratoire de Météorologie Dynamique general circulation model: model description and impact analysis of biogenic hydrocarbons on tropospheric chemistry. *Atmospheric Chem. Phys.* 6, 2273–2319. <https://doi.org/10.5194/acp-6-2273-2006>
- Fontoura, S., Bayer, C., 2010. Ammonia volatilization in no-till system in the South-Central region of the State of Paraná, Brazil. *Rev. Bras. Ciênc. Solo* 34, 1677–1684. <https://doi.org/10.1590/S0100-06832010000500020>
- Fortems-Cheiney, A., Dufour, G., Hamaoui-Laguel, L., Foret, G., Siour, G., Van Damme, M., Meleux, F., Coheur, P.-F., Clerbaux, C., Clarisse, L., Favez, O., Wallasch, M., Beekmann, M., 2016. Unaccounted variability in NH<sub>3</sub> agricultural sources detected by IASI contributing to European spring haze episode. *Geophys. Res. Lett.* 43, 5475–5482. <https://doi.org/10.1002/2016GL069361>
- Foulds, A., Khan, M.A.H., Bannan, T.J., Percival, C.J., Lowenberg, M.H., Shallcross, D.E., 2021. Abundance of NO<sub>3</sub> Derived Organo-Nitrates and Their Importance in the Atmosphere. *Atmosphere* 12, 1381. <https://doi.org/10.3390/atmos12111381>
- Fowler, D., Coyle, M., Skiba, U., Sutton, M.A., Cape, J.N., Reis, S., Sheppard, L.J., Jenkins, A., Grizzetti, B., Galloway, J.N., Vitousek, P., Leach, A., Bouwman, A.F., Butterbach-Bahl, K., Dentener, F., Stevenson, D., Amann, M., Voss, M., 2013. The global nitrogen cycle in the twenty-first century. *Philos. Trans. R. Soc. B Biol. Sci.* 368, 20130164. <https://doi.org/10.1098/rstb.2013.0164>
- Fowler, D., Pitcairn, C.E.R., Sutton, M.A., Flechard, C., Loubet, B., Coyle, M., Munro, R.C., 1998. The mass budget of atmospheric ammonia in woodland within 1 km of livestock buildings. *Environ. Pollut., Nitrogen, the Confer-N-s First International Nitrogen Conference 1998* 102, 343–348. [https://doi.org/10.1016/S0269-7491\(98\)80053-5](https://doi.org/10.1016/S0269-7491(98)80053-5)
- Franco, B., Clarisse, L., Stavrou, T., Müller, J.-F., Pozzer, A., Hadji-Lazaro, J., Hurtmans, D., Clerbaux, C., Coheur, P.-F., 2019. Acetone Atmospheric Distribution Retrieved From Space. *Geophys. Res. Lett.* 46, 2884–2893. <https://doi.org/10.1029/2019GL082052>
- Franco, B., Clarisse, L., Stavrou, T., Müller, J.-F., Van Damme, M., Whitburn, S., Hadji-Lazaro, J., Hurtmans, D., Taraborrelli, D., Clerbaux, C., Coheur, P.-F., 2018. A General Framework for Global Retrievals of Trace Gases From IASI: Application to Methanol, Formic Acid, and PAN. *J. Geophys. Res. Atmospheres* 123, 13,963–13,984. <https://doi.org/10.1029/2018JD029633>
- Franzen, D.W., 2017. Nitrogen Extenders and Additives for Field Crops. North Dakota State University.



- Galloway, J.N., Aber, J.D., Erisman, J.W., Seitzinger, S.P., Howarth, R.W., Cowling, E.B., Cosby, B.J., 2003. The Nitrogen Cascade. *BioScience* 53, 341–356. [https://doi.org/10.1641/0006-3568\(2003\)053\[0341:TNC\]2.0.CO;2](https://doi.org/10.1641/0006-3568(2003)053[0341:TNC]2.0.CO;2)
- Galloway, J.N., Dentener, F.J., Capone, D.G., Boyer, E.W., Howarth, R.W., Seitzinger, S.P., Asner, G.P., Cleveland, C.C., Green, P.A., Holland, E.A., Karl, D.M., Michaels, A.F., Porter, J.H., Townsend, A.R., Vöosmarty, C.J., 2004. Nitrogen Cycles: Past, Present, and Future. *Biogeochemistry* 70, 153–226. <https://doi.org/10.1007/s10533-004-0370-0>
- Galloway, J.N., Leach, A.M., Bleeker, A., Erisman, J.W., 2013. A chronology of human understanding of the nitrogen cycle. *Philos. Trans. R. Soc. B Biol. Sci.* 368, 20130120. <https://doi.org/10.1098/rstb.2013.0120>
- Galloway, J.N., Townsend, A.R., Erisman, J.W., Bekunda, M., Cai, Z., Freney, J.R., Martinelli, L.A., Seitzinger, S.P., Sutton, M.A., 2008. Transformation of the Nitrogen Cycle: Recent Trends, Questions, and Potential Solutions. *Science* 320, 889–892. <https://doi.org/10.1126/science.1136674>
- Garrido-Perez, J.M., Ordóñez, C., García-Herrera, R., Barriopedro, D., 2018. Air stagnation in Europe: Spatiotemporal variability and impact on air quality. *Sci. Total Environ.* 645, 1238–1252. <https://doi.org/10.1016/j.scitotenv.2018.07.238>
- Gelaro, R., McCarty, W., Suárez, M.J., Todling, R., Molod, A., Takacs, L., Randles, C.A., Darmenov, A., Bosilovich, M.G., Reichle, R., Wargan, K., Coy, L., Cullather, R., Draper, C., Akella, S., Buchard, V., Conaty, A., Silva, A.M. da, Gu, W., Kim, G.-K., Koster, R., Lucchesi, R., Merkova, D., Nielsen, J.E., Partyka, G., Pawson, S., Putman, W., Rienecker, M., Schubert, S.D., Sienkiewicz, M., Zhao, B., 2017. The Modern-Era Retrospective Analysis for Research and Applications, Version 2 (MERRA-2). *J. Clim.* 30, 5419–5454. <https://doi.org/10.1175/JCLI-D-16-0758.1>
- George, M., Clerbaux, C., Bouarar, I., Coheur, P.-F., Deeter, M.N., Edwards, D.P., Francis, G., Gille, J.C., Hadji-Lazaro, J., Hurtmans, D., Inness, A., Mao, D., Worden, H.M., 2015. An examination of the long-term CO records from MOPITT and IASI: comparison of retrieval methodology. *Atmospheric Meas. Tech.* 8, 4313–4328. <https://doi.org/10.5194/amt-8-4313-2015>
- Giglio, L., Boschetti, L., Roy, D.P., Humber, M.L., Justice, C.O., 2018. The Collection 6 MODIS burned area mapping algorithm and product. *Remote Sens. Environ.* 217, 72–85. <https://doi.org/10.1016/j.rse.2018.08.005>
- Goldberg, M.D., Kilcoyne, H., Cikanek, H., Mehta, A., 2013. Joint Polar Satellite System: The United States next generation civilian polar-orbiting environmental satellite system. *J. Geophys. Res. Atmospheres* 118, 13,463–13,475. <https://doi.org/10.1002/2013JD020389>
- Gross, A., Boyd, C.E., Wood, C.W., 1999. Ammonia Volatilization from Freshwater Fish Ponds. *J. Environ. Qual.* 28, 793–797. <https://doi.org/10.2134/jeq1999.00472425002800030009x>
- Gruber, N., Galloway, J.N., 2008. An Earth-system perspective of the global nitrogen cycle. *Nature* 451, 293–296. <https://doi.org/10.1038/nature06592>
- Guo, X., Wang, R., Pan, D., Zondlo, M.A., Clarisse, L., Damme, M.V., Whitburn, S., Coheur, P.-F., Clerbaux, C., Franco, B., Golston, L.M., Wendt, L., Sun, K., Tao, L., Miller, D., Mikoviny, T., Müller, M., Wisthaler, A., Tevlin, A.G., Murphy, J.G., Nowak, J.B.,

- Roscioli, J.R., Volkamer, R., Kille, N., Neuman, J.A., Eilerman, S.J., Crawford, J.H., Yacovitch, T.I., Barrick, J.D., Scarino, A.J., 2021. Validation of IASI Satellite Ammonia Observations at the Pixel Scale Using In Situ Vertical Profiles. *J. Geophys. Res. Atmospheres* 126, e2020JD033475. <https://doi.org/10.1029/2020JD033475>
- Gurmesa, G.A., Wang, A., Li, S., Peng, S., de Vries, W., Gundersen, P., Ciais, P., Phillips, O.L., Hobbie, E.A., Zhu, W., Nadelhoffer, K., Xi, Y., Bai, E., Sun, T., Chen, D., Zhou, W., Zhang, Y., Guo, Y., Zhu, J., Duan, L., Li, D., Koba, K., Du, E., Zhou, G., Han, X., Han, S., Fang, Y., 2022. Retention of deposited ammonium and nitrate and its impact on the global forest carbon sink. *Nat. Commun.* 13, 880. <https://doi.org/10.1038/s41467-022-28345-1>
- Harper, L.A., 2015. Ammonia: Measurement Issues, in: Hatfield, J.L., Baker, J.M. (Eds.), *Agronomy Monographs*. American Society of Agronomy, Crop Science Society of America, and Soil Science Society of America, Madison, WI, USA, pp. 345–379. <https://doi.org/10.2134/agronmonogr47.c15>
- Hauglustaine, D., Paulot, F., Collins, W., Derwent, R., Sand, M., Boucher, O., 2022. Climate benefit of a future hydrogen economy. *Commun. Earth Environ.* 3, 1–14. <https://doi.org/10.1038/s43247-022-00626-z>
- Heffer, P., Prud'homme, M., 2016. Global nitrogen fertiliser demand and supply: trend, current level and outlook 22.
- Herbin, H., Hurtmans, D., Clarisse, L., Turquety, S., Clerbaux, C., Rinsland, C.P., Boone, C., Bernath, P.F., Coheur, P.-F., 2009. Distributions and seasonal variations of tropospheric ethene (C<sub>2</sub>H<sub>4</sub>) from Atmospheric Chemistry Experiment (ACE-FTS) solar occultation spectra. *Geophys. Res. Lett.* 36. <https://doi.org/10.1029/2008GL036338>
- Hersbach, H., Bell, B., Berrisford, P., Hirahara, S., Horányi, A., Muñoz-Sabater, J., Nicolas, J., Peubey, C., Radu, R., Schepers, D., Simmons, A., Soci, C., Abdalla, S., Abellan, X., Balsamo, G., Bechtold, P., Biavati, G., Bidlot, J., Bonavita, M., Chiara, G.D., Dahlgren, P., Dee, D., Diamantakis, M., Dragani, R., Flemming, J., Forbes, R., Fuentes, M., Geer, A., Haimberger, L., Healy, S., Hogan, R.J., Hólm, E., Janisková, M., Keeley, S., Laloyaux, P., Lopez, P., Lupu, C., Radnoti, G., Rosnay, P. de, Rozum, I., Vamborg, F., Villaume, S., Thépaut, J.-N., 2020. The ERA5 global reanalysis. *Q. J. R. Meteorol. Soc.* 146, 1999–2049. <https://doi.org/10.1002/qj.3803>
- Hilton, F., Armante, R., August, T., Barnet, C., Bouchard, A., Camy-Peyret, C., Capelle, V., Clarisse, L., Clerbaux, C., Coheur, P.-F., Collard, A., Crevoisier, C., Dufour, G., Edwards, D., Faijan, F., Fourrié, N., Gambacorta, A., Goldberg, M., Guidard, V., Hurtmans, D., Illingworth, S., Jacquinet-Husson, N., Kerzenmacher, T., Klaes, D., Lavanant, L., Masiello, G., Matricardi, M., McNally, A., Newman, S., Pavelin, E., Payan, S., Péquignot, E., Peyridieu, S., Phulpin, T., Remedios, J., Schlüssel, P., Serio, C., Strow, L., Stubenrauch, C., Taylor, J., Tobin, D., Wolf, W., Zhou, D., 2012. Hyperspectral Earth Observation from IASI: Five Years of Accomplishments. *Bull. Am. Meteorol. Soc.* 93, 347–370. <https://doi.org/10.1175/BAMS-D-11-00027.1>
- Hoesly, R.M., Smith, S.J., Feng, L., Klimont, Z., Janssens-Maenhout, G., Pitkanen, T., Seibert, J.J., Vu, L., Andres, R.J., Bolt, R.M., Bond, T.C., Dawidowski, L., Kholod, N., Kurokawa, J., Li, M., Liu, L., Lu, Z., Moura, M.C.P., O'Rourke, P.R., Zhang, Q., 2018. Historical

- (1750–2014) anthropogenic emissions of reactive gases and aerosols from the Community Emissions Data System (CEDS). *Geosci. Model Dev.* 11, 369–408. <https://doi.org/10.5194/gmd-11-369-2018>
- Hourdin, F., Musat, I., Bony, S., Braconnot, P., Codron, F., Dufresne, J.-L., Fairhead, L., Filiberti, M.-A., Friedlingstein, P., Grandpeix, J.-Y., Krinner, G., LeVan, P., Li, Z.-X., Lott, F., 2006. The LMDZ4 general circulation model: climate performance and sensitivity to parametrized physics with emphasis on tropical convection. *Clim. Dyn.* 27, 787–813. <https://doi.org/10.1007/s00382-006-0158-0>
- Hurtmans, D., Coheur, P.-F., Wespes, C., Clarisse, L., Scharf, O., Clerbaux, C., Hadji-Lazaro, J., George, M., Turquety, S., 2012. FORLI radiative transfer and retrieval code for IASI. *J. Quant. Spectrosc. Radiat. Transf., Three Leaders in Spectroscopy* 113, 1391–1408. <https://doi.org/10.1016/j.jqsrt.2012.02.036>
- Husted, S., Schjoerring, J.K., 1996. Ammonia Flux between Oilseed Rape Plants and the Atmosphere in Response to Changes in Leaf Temperature, Light Intensity, and Air Humidity (Interactions with Leaf Conductance and Apoplastic  $\text{NH}_4^+$  and  $\text{H}^+$  Concentrations). *Plant Physiol.* 112, 67–74. <https://doi.org/10.1104/pp.112.1.67>
- ICChemE, 2019.  $\text{H}_2$  and  $\text{NH}_3$  – the Perfect Marriage in a Carbon-free Society. *Chem. Eng.*
- IPCC, 2013. Summary for Policymakers. In: *Climate Change 2013: The Physical Science Basis. Contribution of Working Group I to the Fifth Assessment Report of the Intergovernmental Panel on Climate Change*. Cambridge University Press., Cambridge, United Kingdom and New York, NY, USA.
- ISW, 2013. Syria Update: The Fall of al-Qusayr.
- Jaafar, H.H., Woertz, E., 2016. Agriculture as a funding source of ISIS: A GIS and remote sensing analysis. *Food Policy* 64, 14–25. <https://doi.org/10.1016/j.foodpol.2016.09.002>
- Jacob, D., Kotova, L., Teichmann, C., Sobolowski, S.P., Vautard, R., Donnelly, C., Koutroulis, A.G., Grillakis, M.G., Tsanis, I.K., Damm, A., Sakalli, A., van Vliet, M.T.H., 2018. Climate Impacts in Europe Under  $+1.5^\circ\text{C}$  Global Warming. *Earth's Future* 6, 264–285. <https://doi.org/10.1002/2017EF000710>
- Jacob, D.J., 1999. *Introduction to Atmospheric Chemistry*. Princeton University Press.
- Jacobson, M.Z., 2002. *Atmospheric Pollution: History, Science, and Regulation*. Cambridge University Press.
- Jones, L., Milne, A., Hall, J., Mills, G., Provins, A., Christie, M., 2018. Valuing Improvements in Biodiversity Due to Controls on Atmospheric Nitrogen Pollution. *Ecol. Econ.* 152, 358–366. <https://doi.org/10.1016/j.ecolecon.2018.06.010>
- Jung, J., Choi, Y., Souri, A.H., Mousavinezhad, S., Sayeed, A., Lee, K., 2022. The Impact of Springtime-Transported Air Pollutants on Local Air Quality With Satellite-Constrained  $\text{NO}_x$  Emission Adjustments Over East Asia. *J. Geophys. Res. Atmospheres* 127, e2021JD035251. <https://doi.org/10.1029/2021JD035251>
- Keller, C.A., Long, M.S., Yantosca, R.M., Da Silva, A.M., Pawson, S., Jacob, D.J., 2014. HEMCO v1.0: a versatile, ESMF-compliant component for calculating emissions in

- atmospheric models. *Geosci. Model Dev.* 7, 1409–1417. <https://doi.org/10.5194/gmd-7-1409-2014>
- Kissel, D., Cabrera, M., 2005. *Encyclopedia of Soils in the Environment*: Hillel, Daniel: 9780123485304: Amazon.com: Books, Daniel Hillel. ed. New York, NY USA.
- Klaes, K.D., 2018. The EUMETSAT Polar System, in: *Comprehensive Remote Sensing*. Elsevier, pp. 192–219. <https://doi.org/10.1016/B978-0-12-409548-9.10318-5>
- Klerke, A., Christensen, C.H., Nørskov, J.K., Vegge, T., 2008. Ammonia for hydrogen storage: challenges and opportunities. *J. Mater. Chem.* 18, 2304–2310. <https://doi.org/10.1039/B720020J>
- Krinner, G., Viovy, N., de Noblet-Ducoudré, N., Ogée, J., Polcher, J., Friedlingstein, P., Ciais, P., Sitch, S., Prentice, I.C., 2005. A dynamic global vegetation model for studies of the coupled atmosphere-biosphere system. *Glob. Biogeochem. Cycles* 19. <https://doi.org/10.1029/2003GB002199>
- Krupa, S.V., 2003. Effects of atmospheric ammonia (NH<sub>3</sub>) on terrestrial vegetation: a review. *Environ. Pollut.* 124, 179–221. [https://doi.org/10.1016/S0269-7491\(02\)00434-7](https://doi.org/10.1016/S0269-7491(02)00434-7)
- Lachatre, M., Fortems-Cheiney, A., Foret, G., Siour, G., Dufour, G., Clarisse, L., Clerbaux, C., Coheur, P.-F., Van Damme, M., Beekmann, M., 2019. The unintended consequence of SO<sub>2</sub> and NO<sub>2</sub> regulations over China: increase of ammonia levels and impact on PM<sub>2.5</sub> concentrations. *Atmospheric Chem. Phys.* 19, 6701–6716. <https://doi.org/10.5194/acp-19-6701-2019>
- Lamquin, N., Bruniquel, V., Gascon, F., 2018. Sentinel-2 L1C radiometric validation using deep convective clouds observations. *Eur. J. Remote Sens.* 51, 11–27. <https://doi.org/10.1080/22797254.2017.1395713>
- Lassaletta, L., Billen, G., Garnier, J., Bouwman, L., Velazquez, E., Mueller, N.D., Gerber, J.S., 2016. Nitrogen use in the global food system: past trends and future trajectories of agronomic performance, pollution, trade, and dietary demand. *Environ. Res. Lett.* 11, 095007. <https://doi.org/10.1088/1748-9326/11/9/095007>
- Lawes, J.B., 1847. On agricultural chemistry. *J. R. Agric. Soc. Engl.*
- LCAT, 2022. June Crisis Update.
- Lea, P.J., 1985. CHAPTER 14 - AMMONIA ASSIMILATION AND AMINO ACID BIOSYNTHESIS, in: Coombs, J., Hall, D.O., Long, S.P., Scurlock, J.M.O. (Eds.), *Techniques in Bioproductivity and Photosynthesis* (Second Edition), Pergamon International Library of Science, Technology, Engineering and Social Studies. Pergamon, pp. 173–187. <https://doi.org/10.1016/B978-0-08-031999-5.50024-8>
- Lee, W., An, S., Choi, Y., 2020. Ammonia harvesting via membrane gas extraction at moderately alkaline pH: A step toward net-profitable nitrogen recovery from domestic wastewater. *Chem. Eng. J.* 405, 126662. <https://doi.org/10.1016/j.cej.2020.126662>
- Leghari, S.J., Wahocho, N.A., Laghari, G.M., HafeezLaghari, A., MustafaBhabhan, G., HussainTalpur, K., Bhutto, T.A., Wahocho, S.A., Lashari, A.A., 2016. Role of nitrogen for plant growth and development: a review. *Adv. Environ. Biol.* 10, 209–219.

- Lentze, G., 2021. Metop-A satellite retiring after 15 years of huge benefits to forecasting [WWW Document]. ECMWF. URL <https://www.ecmwf.int/en/about/media-centre/news/2021/metop-satellite-retiring-after-15-years-huge-benefits-forecasting> (accessed 6.25.22).
- Liehr, S., Classen, J., Humenik, F., Baird, C., Rice, J.M., 2006. Ammonia Recovery from Swine Belt Separated Liquid. <https://doi.org/10.13031/2013.21123>
- Lin, Y.-C., Yu, M., Xie, F., Zhang, Y., 2022. Anthropogenic Emission Sources of Sulfate Aerosols in Hangzhou, East China: Insights from Isotope Techniques with Consideration of Fractionation Effects between Gas-to-Particle Transformations. *Environ. Sci. Technol.* 56, 3905–3914. <https://doi.org/10.1021/acs.est.1c05823>
- Liu, L., Xu, W., Lu, Xiankai, Zhong, B., Guo, Y., Lu, Xiao, Zhao, Y., He, W., Wang, S., Zhang, X., Liu, X., Vitousek, P., 2022. Exploring global changes in agricultural ammonia emissions and their contribution to nitrogen deposition since 1980. *Proc. Natl. Acad. Sci.* 119, e2121998119. <https://doi.org/10.1073/pnas.2121998119>
- Liu, L., Zhang, X., Xu, W., Liu, X., Wei, J., Wang, Z., Yang, Y., 2020. Global estimates of dry ammonia deposition inferred from space-measurements. *Sci. Total Environ.* 730, 139189. <https://doi.org/10.1016/j.scitotenv.2020.139189>
- Liu, M., Huang, Xin, Song, Y., Tang, J., Cao, J., Zhang, X., Zhang, Q., Wang, S., Xu, T., Kang, L., Cai, X., Zhang, H., Yang, F., Wang, H., Yu, J.Z., Lau, A.K.H., He, L., Huang, Xiaofeng, Duan, L., Ding, A., Xue, L., Gao, J., Liu, B., Zhu, T., 2019. Ammonia emission control in China would mitigate haze pollution and nitrogen deposition, but worsen acid rain. *Proc. Natl. Acad. Sci.* 116, 7760–7765. <https://doi.org/10.1073/pnas.1814880116>
- Loubet, B., Decuq, C., Personne, E., Massad, R.S., Flechard, C., Fanucci, O., Mascher, N., Gueudet, J.-C., Masson, S., Durand, B., Genermont, S., Fauvel, Y., Cellier, P., 2012. Investigating the stomatal, cuticular and soil ammonia fluxes over a growing tritical crop under high acidic loads. *Biogeosciences* 9, 1537–1552. <https://doi.org/10.5194/bg-9-1537-2012>
- Lu, C., Tian, H., 2017. Global nitrogen and phosphorus fertilizer use for agriculture production in the past half century: shifted hot spots and nutrient imbalance. *Earth Syst. Sci. Data* 9, 181–192. <https://doi.org/10.5194/essd-9-181-2017>
- Lubin, A., Saleem, A., 2019. Remote sensing-based mapping of the destruction to Aleppo during the Syrian Civil War between 2011 and 2017. *Appl. Geogr.* 108, 30–38. <https://doi.org/10.1016/j.apgeog.2019.05.004>
- Manunza, B., Deiana, S., Pintore, M., Gessa, C., 1999. The binding mechanism of urea, hydroxamic acid and N-(N-butyl)-phosphoric triamide to the urease active site. A comparative molecular dynamics study. *Soil Biol. Biochem.* 31, 789–796. [https://doi.org/10.1016/S0038-0717\(98\)00155-2](https://doi.org/10.1016/S0038-0717(98)00155-2)
- Marais, E.A., Pandey, A.K., Van Damme, M., Clarisse, L., Coheur, P.-F., Shephard, M.W., Cady-Pereira, K.E., Misselbrook, T., Zhu, L., Luo, G., Yu, F., 2021. UK Ammonia Emissions Estimated With Satellite Observations and GEOS-Chem. *J. Geophys. Res. Atmospheres* 126, e2021JD035237. <https://doi.org/10.1029/2021JD035237>



- Massad, R.-S., Nemitz, E., Sutton, M.A., 2010. Review and parameterisation of bi-directional ammonia exchange between vegetation and the atmosphere. *Atmospheric Chem. Phys.* 10, 10359–10386. <https://doi.org/10.5194/acp-10-10359-2010>
- Mattsson, M., B. H., M. D., Loubet, B., M. R., Theobald, M., Sutton, M., Bruhn, D., Neftel, A., Schjoerring, J., 2008. Temporal variability in bioassays of ammonia emission potential in relation to plant and soil N parameters in intensively managed grassland. *Biogeosciences Discuss.* 5. <https://doi.org/10.5194/bgd-5-2749-2008>
- McDuffie, E.E., Smith, S.J., O'Rourke, P., Tibrewal, K., Venkataraman, C., Marais, E.A., Zheng, B., Crippa, M., Brauer, M., Martin, R.V., 2020. A global anthropogenic emission inventory of atmospheric pollutants from sector- and fuel-specific sources (1970–2017): an application of the Community Emissions Data System (CEDS). *Earth Syst. Sci. Data* 12, 3413–3442. <https://doi.org/10.5194/essd-12-3413-2020>
- Met Office, 2016. Exceptionally warm and dry Spring 2011. Met Office.
- Mohamad, S., 2019. Use of Algae and Cyanobacteria to Assess the State of Pollution in Qattinah Lake. *Fudan Univ. J. Med. Sci*
- Mohamed, M., Anders, J., Schneider, C., 2020. Monitoring of Changes in Land Use/Land Cover in Syria from 2010 to 2018 Using Multitemporal Landsat Imagery and GIS. *Land* 9, 226. <https://doi.org/10.3390/land9070226>
- Murray, L.T., 2016. Lightning NO<sub>x</sub> and Impacts on Air Quality. *Curr. Pollut. Rep.* 2, 115–133. <https://doi.org/10.1007/s40726-016-0031-7>
- Myhre, G., Shindell, D., Bréon, F.-M., Collins, W., Fuglestad, J., Huang, J., Koch, D., Lamarque, J.-F., Lee, D., Mendoza, B., Nakajima, T., Robock, A., Stephens, G., Zhang, H., Aamaas, B., Boucher, O., Dalsøren, S.B., Daniel, J.S., Forster, P., Granier, C., Haigh, J., Hodnebrog, Ø., Kaplan, J.O., Marston, G., Nielsen, C.J., O'Neill, B.C., Peters, G.P., Pongratz, J., Ramaswamy, V., Roth, R., Rotstayn, L., Smith, S.J., Stevenson, D., Vernier, J.-P., Wild, O., Young, P., Jacob, D., Ravishankara, A.R., Shine, K., 2013. 8 Anthropogenic and Natural Radiative Forcing, IPCC. Cambridge University Press, Cambridge, United Kingdom and New York, NY, USA.
- Naeem, E., Abd El-Megeed, T., Emadeldin, Y., Abushady, A.M., Abdelrahman, M., 2022. Injected Anhydrous Ammonia Is More Effective Than Broadcast Urea as a Source of Nitrogen for Drill Seeded Rice. *Agronomy* 12, 942. <https://doi.org/10.3390/agronomy12040942>
- Nemitz, E., Sutton, M.A., Schjoerring, J.K., Husted, S., Paul Wyers, G., 2000. Resistance modelling of ammonia exchange over oilseed rape. *Agric. For. Meteorol.* 105, 405–425. [https://doi.org/10.1016/S0168-1923\(00\)00206-9](https://doi.org/10.1016/S0168-1923(00)00206-9)
- Ni, K., Pacholski, A.S., 2022. Soil Moisture and Temperature Effects on Granule Dissolution and Urease Activity of Urea with and without Inhibitors—An Incubation Study. *Agriculture* 12, 2037. <https://doi.org/10.3390/agriculture12122037>
- Novotny, V., 1999. Diffuse pollution from agriculture — A worldwide outlook. *Water Sci. Technol., Integrated Management of Water Quality: The Role of Agricultural Diffuse Pollution Sources* 39, 1–13. [https://doi.org/10.1016/S0273-1223\(99\)00027-X](https://doi.org/10.1016/S0273-1223(99)00027-X)



- Olesen, J.E., Sommer, S.G., 1993. Modelling effects of wind speed and surface cover on ammonia volatilization from stored pig slurry. *Atmospheric Environ. Part Gen. Top.* 27, 2567–2574. [https://doi.org/10.1016/0960-1686\(93\)90030-3](https://doi.org/10.1016/0960-1686(93)90030-3)
- Ouseley, W., 1800. *The oriental geography of Ebn haukal an Arabian traveller of the tenth century*. London, UK.
- Personne, E., Tardy, F., Générmont, S., Decuq, C., Gueudet, J.-C., Mascher, N., Durand, B., Masson, S., Lauransot, M., Fléchar, C., Burkhardt, J., Loubet, B., 2015. Investigating sources and sinks for ammonia exchanges between the atmosphere and a wheat canopy following slurry application with trailing hose. *Agric. For. Meteorol.* 207, 11–23. <https://doi.org/10.1016/j.agrformet.2015.03.002>
- Phillips, S.B., Arya, S.P., Aneja, V.P., 2004. Ammonia flux and dry deposition velocity from near-surface concentration gradient measurements over a grass surface in North Carolina. *Atmos. Environ.* 38, 3469–3480. <https://doi.org/10.1016/j.atmosenv.2004.02.054>
- Pinder, R.W., Adams, P.J., Pandis, S.N., 2007. Ammonia Emission Controls as a Cost-Effective Strategy for Reducing Atmospheric Particulate Matter in the Eastern United States. *Environ. Sci. Technol.* 41, 380–386. <https://doi.org/10.1021/es060379a>
- Pinder, R.W., Gilliland, A.B., Dennis, R.L., 2008. Environmental impact of atmospheric NH<sub>3</sub> emissions under present and future conditions in the eastern United States. *Geophys. Res. Lett.* 35. <https://doi.org/10.1029/2008GL033732>
- Plumb, R.A., Stolarski, R.S., 2013. Chapter 2: The Theory of Estimating Lifetimes Using Models and Observations, in: *SPARC Lifetimes Report (2013) – SPARC Report No. 6*, 6.
- Potapov, P., Turubanova, S., Hansen, M.C., Tyukavina, A., Zalles, V., Khan, A., Song, X.-P., Pickens, A., Shen, Q., Cortez, J., 2022. Global maps of cropland extent and change show accelerated cropland expansion in the twenty-first century. *Nat. Food* 3, 19–28. <https://doi.org/10.1038/s43016-021-00429-z>
- Randerson, J.T., Van Der Werf, G.R., Giglio, L., Collatz, G.J., Kasibhatla, P.S., 2015. Global Fire Emissions Database, Version 4.1 (GFEDv4). ORNL DAAC. <https://doi.org/10.3334/ORNLDAAAC/1293>
- Reynolds, C.M., Wolf, D.C., 1987. EFFECT OF SOIL MOISTURE AND AIR RELATIVE HUMIDITY ON AMMONIA VOLATILIZATION FROM SURFACE-APPLIED UREA. *Soil Sci.* 143, 144–152.
- Riahi, K., van Vuuren, D.P., Kriegler, E., Edmonds, J., O'Neill, B.C., Fujimori, S., Bauer, N., Calvin, K., Dellink, R., Fricko, O., Lutz, W., Popp, A., Cuaresma, J.C., Kc, S., Leimbach, M., Jiang, L., Kram, T., Rao, S., Emmerling, J., Ebi, K., Hasegawa, T., Havlik, P., Humenöder, F., Da Silva, L.A., Smith, S., Stehfest, E., Bosetti, V., Eom, J., Gernaat, D., Masui, T., Rogelj, J., Strefler, J., Drouet, L., Krey, V., Luderer, G., Harmsen, M., Takahashi, K., Baumstark, L., Doelman, J.C., Kainuma, M., Klimont, Z., Marangoni, G., Lotze-Campen, H., Obersteiner, M., Tabeau, A., Tavoni, M., 2017. The Shared Socioeconomic Pathways and their energy, land use, and greenhouse gas emissions implications: An overview. *Glob. Environ. Change* 42, 153–168. <https://doi.org/10.1016/j.gloenvcha.2016.05.009>

- Ricaud, P., Attié, J.-L., Teyssèdre, H., El Amraoui, L., Peuch, V.-H., Matricardi, M., Schluessel, P., 2009. Equatorial total column of nitrous oxide as measured by IASI on MetOp-A: implications for transport processes. *Atmospheric Chem. Phys.* 9, 3947–3956. <https://doi.org/10.5194/acp-9-3947-2009>
- Rispens, J.R., Jones, S.A., Clemmons, N.S., Ahmed, S., Harduar-Morano, L., Johnson, M.D., Edge, C., Vyas, A., Bourgikos, E., Orr, M.F., 2020. Anhydrous Ammonia Chemical Release — Lake County, Illinois, April 2019. *Morb. Mortal. Wkly. Rep.* 69, 109–113. <https://doi.org/10.15585/mmwr.mm6904a4>
- Rockström, J., Steffen, W., Noone, K., Persson, Å., Chapin, F.S., Lambin, E.F., Lenton, T.M., Scheffer, M., Folke, C., Schellnhuber, H.J., Nykvist, B., de Wit, C.A., Hughes, T., van der Leeuw, S., Rodhe, H., Sörlin, S., Snyder, P.K., Costanza, R., Svedin, U., Falkenmark, M., Karlberg, L., Corell, R.W., Fabry, V.J., Hansen, J., Walker, B., Liverman, D., Richardson, K., Crutzen, P., Foley, J.A., 2009. A safe operating space for humanity. *Nature* 461, 472–475. <https://doi.org/10.1038/461472a>
- Roelle, P.A., Aneja, V.P., 2005. Modeling of Ammonia Emissions from Soils. *Environ. Eng. Sci.* 22, 58–72. <https://doi.org/10.1089/ees.2005.22.58>
- Safieddine, S., Clerbaux, C., Clarisse, L., Whitburn, S., Eltahir, E.A.B., 2022. Present and future land surface and wet bulb temperatures in the Arabian Peninsula. *Environ. Res. Lett.* 17, 044029. <https://doi.org/10.1088/1748-9326/ac507c>
- Sahrawat, K.L., 1948. Effects of temperature and moisture on urease activity in semi-arid tropical soils\*. *Plant Soil* 401–408.
- Sahu, J.N., Mahalik, K., Patwardhan, A.V., Meikap, B.C., 2008. Equilibrium and Kinetic Studies on the Hydrolysis of Urea for Ammonia Generation in a Semibatch Reactor. *Ind. Eng. Chem. Res.* 47, 4689–4696. <https://doi.org/10.1021/ie800481z>
- Schiferl, L.D., Heald, C.L., Nowak, J.B., Holloway, J.S., Neuman, J.A., Bahreini, R., Pollack, I.B., Ryerson, T.B., Wiedinmyer, C., Murphy, J.G., 2014. An investigation of ammonia and inorganic particulate matter in California during the CalNex campaign. *J. Geophys. Res. Atmospheres* 119, 1883–1902. <https://doi.org/10.1002/2013JD020765>
- Schjoerring, J.K., Husted, S., Mattsson, M., 1998. Physiological parameters controlling plant–atmosphere ammonia exchange. *Atmos. Environ.* 32, 491–498. [https://doi.org/10.1016/S1352-2310\(97\)00006-X](https://doi.org/10.1016/S1352-2310(97)00006-X)
- Schumann, U., Huntrieser, H., 2007. The global lightning-induced nitrogen oxides source. *Atmospheric Chem. Phys.* 7, 3823–3907. <https://doi.org/10.5194/acp-7-3823-2007>
- Selman, M., Sugg, Z., Greenhalgh, S., 2008. Eutrophication and Hypoxia in Coastal Areas.
- Shen, H., Chen, Y., Hu, Y., Ran, L., Lam, S.K., Pavur, G.K., Zhou, F., Pleim, J.E., Russell, A.G., 2020. Intense Warming Will Significantly Increase Cropland Ammonia Volatilization Threatening Food Security and Ecosystem Health. *One Earth* 3, 126–134. <https://doi.org/10.1016/j.oneear.2020.06.015>
- Shephard, M.W., Cady-Pereira, K.E., 2015. Cross-track Infrared Sounder (CrIS) satellite observations of tropospheric ammonia. *Atmos Meas Tech* 8, 1323–1336. <https://doi.org/10.5194/amt-8-1323-2015>

- Shephard, M.W., Cady-Pereira, K.E., Luo, M., Henze, D.K., Pinder, R.W., Walker, J.T., Rinsland, C.P., Bash, J.O., Zhu, L., Payne, V.H., Clarisse, L., 2011. TES ammonia retrieval strategy and global observations of the spatial and seasonal variability of ammonia. *Atmospheric Chem. Phys.* 11, 10743–10763. <https://doi.org/10.5194/acp-11-10743-2011>
- Smil, V., 2000. Enriching the Earth: Fritz Haber, Carl Bosch, and the Transformation of World Food Production. <https://doi.org/10.7551/mitpress/2767.001.0001>
- Sommer, S.G., Hutchings, N.J., 2001. Ammonia emission from field applied manure and its reduction—invited paper. *Eur. J. Agron.* 15, 1–15. [https://doi.org/10.1016/S1161-0301\(01\)00112-5](https://doi.org/10.1016/S1161-0301(01)00112-5)
- Steffen, W., Richardson, K., Rockström, J., Cornell, S.E., Fetzer, I., Bennett, E.M., Biggs, R., Carpenter, S.R., Vries, W. de, Wit, C.A. de, Folke, C., Gerten, D., Heinke, J., Mace, G.M., Persson, L.M., Ramanathan, V., Reyers, B., Sörlin, S., 2015. Planetary boundaries: Guiding human development on a changing planet. *Science* 347. <https://doi.org/10.1126/science.1259855>
- Sulla-Menashe, D., Friedl, M.A., 2018. User Guide to Collection 6 MODIS Land Cover (MCD12Q1 and MCD12C1) Product.
- Sulla-Menashe, D., Gray, J.M., Abercrombie, S.P., Friedl, M.A., 2019. Hierarchical mapping of annual global land cover 2001 to present: The MODIS Collection 6 Land Cover product. *Remote Sens. Environ.* 222, 183–194. <https://doi.org/10.1016/j.rse.2018.12.013>
- Sutton, M.A., Burkhardt, J.K., Guerin, D., Nemitz, E., Fowler, D., 1998. Development of resistance models to describe measurements of bi-directional ammonia surface–atmosphere exchange. *Atmos. Environ.* 32, 473–480. [https://doi.org/10.1016/S1352-2310\(97\)00164-7](https://doi.org/10.1016/S1352-2310(97)00164-7)
- Sutton, M.A., Dragosits, U., Tang, Y.S., Fowler, D., 2000. Ammonia emissions from non-agricultural sources in the UK. *Atmos. Environ.* 34, 855–869. [https://doi.org/10.1016/S1352-2310\(99\)00362-3](https://doi.org/10.1016/S1352-2310(99)00362-3)
- Sutton, M.A., Erisman, J.W., Dentener, F., Möller, D., 2008. Ammonia in the environment: From ancient times to the present. *Environ. Pollut.* 156, 583–604. <https://doi.org/10.1016/j.envpol.2008.03.013>
- Sutton, M.A., Howard, C.M., 2018. Satellite pinpoints ammonia sources globally. *Nature* 564, 49–50. <https://doi.org/10.1038/d41586-018-07584-7>
- Sutton, M.A., Reis, S., Riddick, S.N., Dragosits, U., Nemitz, E., Theobald, M.R., Tang, Y.S., Braban, C.F., Viero, M., Dore, A.J., Mitchell, R.F., Wanless, S., Daunt, F., Fowler, D., Blackall, T.D., Milford, C., Flechard, C.R., Loubet, B., Massad, R., Cellier, P., Personne, E., Coheur, P.F., Clarisse, L., Van Damme, M., Ngadi, Y., Clerbaux, C., Skjøth, C.A., Geels, C., Hertel, O., Wichink Kruit, R.J., Pinder, R.W., Bash, J.O., Walker, J.T., Simpson, D., Horváth, L., Misselbrook, T.H., Bleeker, A., Dentener, F., de Vries, W., 2013. Towards a climate-dependent paradigm of ammonia emission and deposition. *Philos. Trans. R. Soc. B Biol. Sci.* 368, 20130166. <https://doi.org/10.1098/rstb.2013.0166>
- Sutton, M.A., van Dijk, N., Levy, P.E., Jones, M.R., Leith, I.D., Sheppard, L.J., Leeson, S., Sim Tang, Y., Stephens, A., Braban, C.F., Dragosits, U., Howard, C.M., Viero, M., Fowler, D., Corbett, P., Naikoo, M.I., Munzi, S., Ellis, C.J., Chatterjee, S., Steadman, C.E.,

- Móring, A., Wolseley, P.A., 2020. Alkaline air: changing perspectives on nitrogen and air pollution in an ammonia-rich world. *Philos. Trans. R. Soc. Math. Phys. Eng. Sci.* 378, 20190315. <https://doi.org/10.1098/rsta.2019.0315>
- Svensson, L., Ferm, M., 1993. Mass Transfer Coefficient and Equilibrium Concentration as Key Factors in a New Approach to Estimate Ammonia Emission from Livestock Manure. *J. Agric. Eng. Res.* 56, 1–11. <https://doi.org/10.1006/jaer.1993.1056>
- Takai, K., 2019. The Nitrogen Cycle: A Large, Fast, and Mystifying Cycle. *Microbes Environ.* 34, 223–225. <https://doi.org/10.1264/jsme2.ME3403rh>
- Todd, L.A., Ramanathan, M., Mottus, K., Katz, R., Dodson, A., Mihlan, G., 2001. Measuring chemical emissions using open-path Fourier transform infrared (OP-FTIR) spectroscopy and computer-assisted tomography. *Atmos. Environ.* 35, 1937–1947. [https://doi.org/10.1016/S1352-2310\(00\)00546-X](https://doi.org/10.1016/S1352-2310(00)00546-X)
- Topp, G.C., Parkin, G.W., Ferré, T.P., Carter, M.R., Gregorich, E.G., 2008. Soil water content. *Soil sampling and methods of analysis*.
- Tournadre, B., Chelin, P., Ray, M., Cuesta, J., Kutzner, R.D., Landsheere, X., Fortems-Cheiney, A., Flaud, J.-M., Hase, F., Blumenstock, T., Orphal, J., Viatte, C., Camy-Peyret, C., 2020. Atmospheric ammonia (NH<sub>3</sub>) over the Paris megacity: 9 years of total column observations from ground-based infrared remote sensing. *Atmospheric Meas. Tech.* 13, 3923–3937. <https://doi.org/10.5194/amt-13-3923-2020>
- UN, 2022. World Population Prospects 2022: Summary of Results 52.
- US EPA, O., 2015. Ammonia. URL <https://www.epa.gov/caddis-vol2/ammonia> (accessed 11.14.22).
- USDA, 2022a. International Agricultural Productivity. U.S. Department of Agriculture.
- USDA, 2022b. Europe - Crop Calendars [WWW Document]. Foreign Agric. Serv. US Dep. Agric. URL [https://ipad.fas.usda.gov/rssiws/al/crop\\_calendar/europe.aspx](https://ipad.fas.usda.gov/rssiws/al/crop_calendar/europe.aspx) (accessed 6.10.22).
- Uwizeye, A., de Boer, I.J.M., Opio, C.I., Schulte, R.P.O., Falcucci, A., Tempio, G., Teillard, F., Casu, F., Rulli, M., Galloway, J.N., Leip, A., Erisman, J.W., Robinson, T.P., Steinfeld, H., Gerber, P.J., 2020. Nitrogen emissions along global livestock supply chains. *Nat. Food* 1, 437–446. <https://doi.org/10.1038/s43016-020-0113-y>
- Van Damme, M., Clarisse, L., Franco, B., Sutton, M.A., Erisman, J.W., Kruit, R.W., Zanten, M. van, Whitburn, S., Hadji-Lazaro, J., Hurtmans, D., Clerbaux, C., Coheur, P.-F., 2021. Global, regional and national trends of atmospheric ammonia derived from a decadal (2008–2018) satellite record. *Environ. Res. Lett.* 16, 055017. <https://doi.org/10.1088/1748-9326/abd5e0>
- Van Damme, M., Clarisse, L., Heald, C.L., Hurtmans, D., Ngadi, Y., Clerbaux, C., Dolman, A.J., Erisman, J.W., Coheur, P.F., 2014. Global distributions, time series and error characterization of atmospheric ammonia (NH<sub>3</sub>) from IASI satellite observations. *Atmospheric Chem. Phys.* 14, 2905–2922. <https://doi.org/10.5194/acp-14-2905-2014>
- Van Damme, M., Clarisse, L., Stavrou, T., Wichink Kruit, R., Sellekaerts, L., Viatte, C., Clerbaux, C., Coheur, P.-F., 2022. On the weekly cycle of atmospheric ammonia over

- European agricultural hotspots. *Sci. Rep.* 12, 12327. <https://doi.org/10.1038/s41598-022-15836-w>
- Van Damme, M., Clarisse, L., Whitburn, S., Hadji-Lazaro, J., Hurtmans, D., Clerbaux, C., Coheur, P.-F., 2018. Industrial and agricultural ammonia point sources exposed. *Nature* 564, 99–103. <https://doi.org/10.1038/s41586-018-0747-1>
- Van Damme, M., Whitburn, S., Clarisse, L., Clerbaux, C., Hurtmans, D., Coheur, P.-F., 2017. Version 2 of the IASI NH<sub>3</sub> neural network retrieval algorithm; near-real time and reanalysed datasets. <https://doi.org/10.5194/amt-2017-239>
- Van Der Molen, J., Beljaars, A.C.M., Chardon, W.J., Jury, W.A., Faassen, H.G. van, 1990. Ammonia volatilization from arable land after application of cattle slurry. 2. Derivation of a transfer model. *Neth. J. Agric. Sci.* 38, 239–254. <https://doi.org/10.18174/njas.v38i3A.16586>
- van Dijk, M., Morley, T., Rau, M.L., Saghai, Y., 2021. A meta-analysis of projected global food demand and population at risk of hunger for the period 2010–2050. *Nat. Food* 2, 494–501. <https://doi.org/10.1038/s43016-021-00322-9>
- Van Hove, L.W.A., Adema, E.H., Vredenberg, W.J., Pieters, G.A., 1989. A study of the adsorption of NH<sub>3</sub> and SO<sub>2</sub> on leaf surfaces. *Atmospheric Environ.* 1967 23, 1479–1486. [https://doi.org/10.1016/0004-6981\(89\)90407-1](https://doi.org/10.1016/0004-6981(89)90407-1)
- Van Hove, L.W.A., Tonk, W.J.M., Pieters, G.A., Adema, E.H., Vredenberg, W.J., 1988. A leaf chamber for measuring the uptake of pollutant gases at low concentrations by leaves, transpiration and carbon dioxide assimilation. *Atmospheric Environ.* 1967 22, 2515–2523. [https://doi.org/10.1016/0004-6981\(88\)90483-0](https://doi.org/10.1016/0004-6981(88)90483-0)
- Veefkind, J.P., Aben, I., McMullan, K., Förster, H., de Vries, J., Otter, G., Claas, J., Eskes, H.J., de Haan, J.F., Kleipool, Q., van Weele, M., Hasekamp, O., Hoogeveen, R., Landgraf, J., Snel, R., Tol, P., Ingmann, P., Voors, R., Kruizinga, B., Vink, R., Visser, H., Levelt, P.F., 2012. TROPOMI on the ESA Sentinel-5 Precursor: A GMES mission for global observations of the atmospheric composition for climate, air quality and ozone layer applications. *Remote Sens. Environ., The Sentinel Missions - New Opportunities for Science* 120, 70–83. <https://doi.org/10.1016/j.rse.2011.09.027>
- Viatte, C., Abeed, R., Yamanouchi, S., Porter, W.C., Safieddine, S., Van Damme, M., Clarisse, L., Herrera, B., Grutter, M., Coheur, P.-F., Strong, K., Clerbaux, C., 2022. NH<sub>3</sub> spatiotemporal variability over Paris, Mexico City, and Toronto, and its link to PM<sub>2.5</sub> during pollution events. *Atmospheric Chem. Phys.* 22, 12907–12922. <https://doi.org/10.5194/acp-22-12907-2022>
- Viatte, C., Wang, T., Van Damme, M., Dammers, E., Meleux, F., Clarisse, L., Shephard, M.W., Whitburn, S., Coheur, P.F., Cady-Pereira, K.E., Clerbaux, C., 2020. Atmospheric ammonia variability and link with particulate matter formation: a case study over the Paris area. *Atmospheric Chem. Phys.* 20, 577–596. <https://doi.org/10.5194/acp-20-577-2020>
- von Wirén, N., Gojon, A., Chaillou, S., Raper, D., 2001. Mechanisms and Regulation of Ammonium Uptake in Higher Plants, in: Lea, P.J., Morot-Gaudry, J.-F. (Eds.), *Plant Nitrogen*. Springer, Berlin, Heidelberg, pp. 61–77. [https://doi.org/10.1007/978-3-662-04064-5\\_3](https://doi.org/10.1007/978-3-662-04064-5_3)



- Vrekoussis, M., Richter, A., Hilboll, A., Burrows, J.P., Gerasopoulos, E., Lelieveld, J., Barrie, L., Zerefos, C., Mihalopoulos, N., 2013. Economic crisis detected from space: Air quality observations over Athens/Greece. *Geophys. Res. Lett.* 40, 458–463. <https://doi.org/10.1002/grl.50118>
- Walker, J.C., Dudhia, A., Carboni, E., 2011. An effective method for the detection of trace species demonstrated using the MetOp Infrared Atmospheric Sounding Interferometer. *Atmospheric Meas. Tech.* 4, 1567–1580. <https://doi.org/10.5194/amt-4-1567-2011>
- Wang, Q., Miao, Y., Wang, L., 2020. Regional Transport Increases Ammonia Concentration in Beijing, China. *Atmosphere* 11, 563. <https://doi.org/10.3390/atmos11060563>
- Wang, S., Nan, J., Shi, C., Fu, Q., Gao, S., Wang, D., Cui, H., Saiz-Lopez, A., Zhou, B., 2015. Atmospheric ammonia and its impacts on regional air quality over the megacity of Shanghai, China. *Sci. Rep.* 5, 15842. <https://doi.org/10.1038/srep15842>
- Warner, J.X., Wei, Z., Strow, L.L., Dickerson, R.R., Nowak, J.B., 2016. The global tropospheric ammonia distribution as seen in the 13-year AIRS measurement record. *Atmospheric Chem. Phys.* 16, 5467–5479. <https://doi.org/10.5194/acp-16-5467-2016>
- Wentworth, G.R., Murphy, J.G., Gregoire, P.K., Cheyne, C.A.L., Tevlin, A.G., Hems, R., 2014. Soil–atmosphere exchange of ammonia in a non-fertilized grassland: measured emission potentials and inferred fluxes. *Biogeosciences* 11, 5675–5686. <https://doi.org/10.5194/bg-11-5675-2014>
- Wesely, M.L., 1989. Parameterization of surface resistances to gaseous dry deposition in regional-scale numerical models. *Atmospheric Environ.* 1967 23, 1293–1304. [https://doi.org/10.1016/0004-6981\(89\)90153-4](https://doi.org/10.1016/0004-6981(89)90153-4)
- Whitburn, S., Damme, M.V., Clarisse, L., Bauduin, S., Heald, C.L., Hadji-Lazaro, J., Hurtmans, D., Zondlo, M.A., Clerbaux, C., Coheur, P.-F., 2016. A flexible and robust neural network IASI-NH<sub>3</sub> retrieval algorithm. *J. Geophys. Res. Atmospheres* 121, 6581–6599. <https://doi.org/10.1002/2016JD024828>
- Whitburn, S., Van Damme, M., Kaiser, J.W., van der Werf, G.R., Turquety, S., Hurtmans, D., Clarisse, L., Clerbaux, C., Coheur, P.-F., 2015. Ammonia emissions in tropical biomass burning regions: Comparison between satellite-derived emissions and bottom-up fire inventories. *Atmos. Environ., Interdisciplinary Research Aspects of Open Biomass Burning and its Impact on the Atmosphere* 121, 42–54. <https://doi.org/10.1016/j.atmosenv.2015.03.015>
- Wichink Kruit, R., 2010. Surface-atmosphere exchange of ammonia.
- Wu, Y., Gu, B., Erisman, J.W., Reis, S., Fang, Y., Lu, X., Zhang, X., 2016. PM<sub>2.5</sub> pollution is substantially affected by ammonia emissions in China. *Environ. Pollut. Barking Essex* 1987 218, 86–94. <https://doi.org/10.1016/j.envpol.2016.08.027>
- Yamanouchi, S., Viatte, C., Strong, K., Lutsch, E., Jones, D.B.A., Clerbaux, C., Van Damme, M., Clarisse, L., Coheur, P.-F., 2021. Multiscale observations of NH<sub>3</sub> around Toronto, Canada. *Atmospheric Meas. Tech.* 14, 905–921. <https://doi.org/10.5194/amt-14-905-2021>



- Yang, S., Yuan, B., Peng, Y., Huang, S., Chen, W., Hu, W., Pei, C., Zhou, J., Parrish, D.D., Wang, W., He, X., Cheng, C., Li, X.-B., Yang, X., Song, Y., Wang, H., Qi, J., Wang, B., Wang, Chen, Wang, Chaomin, Wang, Z., Li, T., Zheng, E., Wang, S., Wu, C., Cai, M., Ye, C., Song, W., Cheng, P., Chen, D., Wang, Xinming, Zhang, Z., Wang, Xuemei, Zheng, J., Shao, M., 2022. The formation and mitigation of nitrate pollution: comparison between urban and suburban environments. *Atmospheric Chem. Phys.* 22, 4539–4556. <https://doi.org/10.5194/acp-22-4539-2022>
- Zabel, F., Delzeit, R., Schneider, J.M., Seppelt, R., Mauser, W., Václavík, T., 2019. Global impacts of future cropland expansion and intensification on agricultural markets and biodiversity. *Nat. Commun.* 10, 2844. <https://doi.org/10.1038/s41467-019-10775-z>
- Zavyalov, V., Esplin, M., Scott, D., Esplin, B., Bingham, G., Hoffman, E., Lietzke, C., Predina, J., Frain, R., Suwinski, L., Han, Y., Major, C., Graham, B., Phillips, L., 2013. Noise performance of the CrIS instrument. *J. Geophys. Res. Atmospheres* 118, 13,108–13,120. <https://doi.org/10.1002/2013JD020457>
- Zhang, B., Shen, H., Yun, X., Zhong, Q., Henderson, B.H., Wang, X., Shi, L., Gunthe, S.S., Huey, L.G., Tao, S., Russell, A.G., Liu, P., 2022. Global Emissions of Hydrogen Chloride and Particulate Chloride from Continental Sources. *Environ. Sci. Technol.* 56, 3894–3904. <https://doi.org/10.1021/acs.est.1c05634>
- Zhang, L., Wright, L.P., Asman, W. a. H., 2010. Bi-directional air-surface exchange of atmospheric ammonia: A review of measurements and a development of a big-leaf model for applications in regional-scale air-quality models. *J. Geophys. Res. Atmospheres* 115. <https://doi.org/10.1029/2009JD013589>
- Zhu, L., Jacob, D.J., Mickley, L.J., Marais, E.A., Cohan, D.S., Yoshida, Y., Duncan, B.N., Abad, G.G., Chance, K.V., 2014. Anthropogenic emissions of highly reactive volatile organic compounds in eastern Texas inferred from oversampling of satellite (OMI) measurements of HCHO columns. *Environ. Res. Lett.* 9, 114004. <https://doi.org/10.1088/1748-9326/9/11/114004>